



Provided by the author(s) and University of Galway in accordance with publisher policies. Please cite the published version when available.

Title	A computational and experimental investigation of tracheobronchial stent performance
Author(s)	McGrath, Donnacha John
Publication Date	2017-05-25
Item record	http://hdl.handle.net/10379/6951

Downloaded 2024-04-26T20:15:26Z

Some rights reserved. For more information, please see the item record link above.



A Computational and Experimental Investigation of Tracheobronchial Stent Performance

Donnacha J. McGrath B.E.



A thesis submitted to the National University of Ireland as fulfilment of
the requirements for the Degree of Doctor of Philosophy

May 2017

Discipline of Biomedical Engineering,
College of Engineering and Informatics,
National University of Ireland, Galway

Supervisors: Prof. Peter E. McHugh and Prof. Mark Bruzzi

For mom and dad,

for always being there.

Contents

Abstract	vii
Personal Acknowledgements	viii
Technical Acknowledgements	ix
List of Publications	x
Declaration of Originality	xi
1. Introduction and Background to the Literature	1
1.1 Introduction	1
1.1.1 Objectives	2
1.2 The Lung	2
1.2.1 Lung Structure	3
1.2.2 Physiology of Lung Motion	5
1.2.3 Lung Constituent Mechanical Properties	9
1.2.4 Animal Models	12
1.3 Tracheobronchial Stenting	13
1.3.1 Tracheobronchial Stent Applications	14
1.3.2 Stent Types	15
1.3.3 Stenting Complications	17
1.4 Stent Properties and Mechanical Analysis	20
1.4.1 Properties of Self-expanding Nitinol Stents	20
1.5 Computational Modelling of Stent Structures	27
1.5.1 Stent Mechanical Performance	28
1.5.2 Airway Analyses	29
1.5.3 Respiratory Motion Modelling	36
1.6 Thesis Structure	41

A.1	Appendix 1.....	44
A.1.1	Constitutive Models	44
	References.....	48
2.	Nitinol Stent Design - Understanding Axial Buckling	62
	Abstract	62
2.1	Introduction.....	62
2.2	Methods and Results.....	66
2.2.1	Stent Fabrication	66
2.2.2	Part 1: Buckling Observation and Determination	66
2.2.3	Part 2: Stability Analysis.....	74
2.2.4	Part 3: Stent Re-design.....	80
2.3	Discussion	83
2.4	Conclusions.....	85
A.2	Appendix 2.....	87
A.2.1	Stent Stiffness Post-buckling.....	87
	References.....	89
3.	Evaluation of Cover Effects on Bare Stent Mechanical Response	92
	Abstract	92
3.1	Introduction.....	92
3.2	Materials and Methods	96
3.2.1	Stent Fabrication	96
3.2.2	Material Properties	97
3.2.3	Stent Experimental Testing	99
3.2.4	Stent Computational Modelling.....	101
3.3	Results	105
3.3.1	Radial Force Testing	105

3.3.2	Flat Plate Testing	110
3.3.3	Non-uniform Force Testing	110
3.4	Discussion	112
3.5	Conclusions.....	115
A.3	Appendix 3.....	117
A.3.1	Mesh convergence and Simulation Run Times	117
A.3.2	Raw Radial Force	118
A.3.3	Adhesive and Friction Effects on Stent Response.....	118
A.3.4	Cover Element Type	119
A.3.5	Radial Force Test Accuracy.....	123
A.3.6	Flat Plate Strain Comparison.....	124
	References	126
4.	An Ovine <i>in-vivo</i> Framework for Tracheobronchial Stent Analysis.....	130
	Abstract	130
4.1	Introduction.....	130
4.2	Materials and Methods	134
4.2.1	Imaging Data	134
4.2.2	Lung Geometry.....	135
4.2.3	Zero-pressure Assembly.....	137
4.2.4	Stent Model.....	139
4.2.5	Material Properties	141
4.2.6	Computational Experiments	143
4.3	Results	148
4.3.1	Lung Deformation Results.....	148
4.3.2	Stenting Results.....	151
4.3.3	Tissue Interaction.....	156

4.4	Discussion	159
4.5	Limitations	162
4.6	Summary and Conclusions	164
A.4	Appendix 4.....	165
A.4.1	Airway Tissue Computational Fit	165
A.4.2	Nodal Displacement Method Accuracy.....	167
	References.....	169
5. Evaluating the Interaction of a Tracheobronchial Stent in an Ovine <i>in-vivo</i>		
Model		174
Abstract		174
5.1 Introduction.....		174
5.2 Materials and Methods		179
5.2.1 Animal Work.....		179
5.2.2 Stent Fabrication		180
5.2.3 Stent Modelling.....		180
5.2.4 Lung Modelling.....		183
5.2.5 Stenting Analyses		187
5.3 Results		189
5.3.1 Animal Study Results.....		189
5.3.2 Simulation Results.....		191
5.4 Discussion		199
5.5 Limitations		202
5.6 Summary and Conclusions		203
References.....		204
6. Conclusions and recommendations		
6.1 Introduction.....		209

6.2	Thesis Summary.....	209
6.3	Recommendations for Future Research.....	213
6.4	Concluding Remarks	216
	References.....	218
A.	Appendix 5.....	219
A.5	Appendix 5: Roles of Co-Authors	219
A.5.1	Chapter 2: Nitinol Stent Design – Understanding Axial Buckling	219
A.5.2	Chapter 3: Evaluation of Cover Effects on Bare Stent Mechanical Response.....	219
A.5.3	Chapter 4: An Ovine <i>in-vivo</i> Framework for Tracheobronchial Stent Analysis	220
A.5.4	Chapter 5: Evaluating the Interaction of a Tracheobronchial Stent in an Ovine <i>in-vivo</i> Model.....	220

Abstract

Tracheobronchial stents are used to relieve blockages in the respiratory tree, typically caused by lung cancer. However, multiple complications can be associated with stents for this indication. In order to be able to improve clinical outcomes, a better understanding of device behaviour must be obtained. The work performed in this thesis investigates the mechanical performance of tracheobronchial stents under *in-vitro* and *in-vivo* conditions, and develops an experimental and computational framework from which future designs may be investigated and improved.

The mechanical performance of bare laser-cut nitinol stents is first investigated through a detailed study on the effect of device geometry and material properties on stent response. It is shown that the non-linear properties of nitinol can have a significant effect on stent stability which should be accounted for during the stent design process. An experimental and computational *in-vitro* testing methodology is then generated to determine the mechanical performance of bare and covered tracheobronchial stents. Through this analysis it is shown that stent response is highly loading specific, suggesting that the loading configuration that a stent is about to be subjected to should be considered pre-implantation.

Ovine lung deformation models are developed to evaluate stent response in physiologically realistic conditions. The generated models account for airway deformation due to a combination of lung motion and pressure loading. It is found that pressure conditions account for the majority of stent loading, but airway deformation due to lung motion can have an appreciable effect on stent mechanical response. Predictions from derived physiological stent deployment models are then compared to ovine pre-clinical implantation outcomes. Results of this suggest that granulation formation may be as a result of high levels of contact associated with lung motion. Indications of other common stent related complications are also highlighted in the models.

In conclusion, the work performed in this thesis has led to an enhanced understanding of the mechanical performance of tracheobronchial stents. The computational models and experimental tests generated in this work form a framework that could be used as an aid for improving tracheobronchial stent design.

Personal Acknowledgements

Firstly, I wish to express my most sincere thanks to both my supervisors Prof. Peter McHugh and Prof. Mark Bruzzi for their unparalleled guidance, motivation and support. I am truly grateful for the countless hours of discussion and deliberation. Your genuine interest, cheerfulness and positivity were paramount in getting me here.

I would also like to offer a big thanks to Dr. Barry O'Brien for his help, knowledge and direction. Your door has always been open and that is very much appreciated. Thanks to all the academic staff that have helped over the years. Thanks too to the technical staff in the university, particularly William Kelly, Pat Kelly, Bony Kennedy and David Connolly who have always been on-hand in a time of need. And to Jane Bowman who has helped in buckets.

Special thanks are due for the entire PulmoStent team. Through this project I met some great people and had wonderful experiences. I'd particularly like to thank Lena, Christian and Stefan for all they've done.

Over the years I've come to know a great bunch of 2nd and 3rd floor postgrads (and postdocs of all floors) who've brought me many a fantastic laugh. Thanks for all the tea breaks, lunches, nights out, burritos, tag craic, laughing, cakes, conference excursions, group trips, and general shenanigans that have made time fly by – Conor, Tarek, Enda, Paddy, Heather, James (x2), Oliver (A promise is a promise), Claire, Myles, Caoimhe, Shane, Brian, Eimear, Eoin, Rosa, Sarah, Noddy, Dave, LizzyG, Fiona, Ed, Orla, Mary, Paul, Conleth, Stefan, Stefaan, Richie, Reyhaneh, Nicola and Sinead.

To the guys in the house at 180 – Elaine, Myles, James, Tom and Ronan – thanks for the good times. The hours of COD, the cube parties and late night antics will never be forgotten!

I am forever grateful to Deirdre and Daniel, who both did their bit to guide me towards a brighter, better path.

Sophie – you have brought so much good to my life. Your belief and encouragement have been astounding. Thank you for listening, caring and comforting. And for bringing so many smiles.

I owe so much to my parents Marian and Eddie. Thank you - for always being there, for your support, for your guidance, for your love, and for the laughs - you're the best. And Sham – you too.

Technical Acknowledgements

The research leading to these results has received funding from the European Union's Seventh Framework Programme (FP7/2007-2013 under grant agreement n° NMP3-SL-2012-280915) - PulmoStent. Funding from the College of Engineering and Informatics at NUI Galway through a College Scholarship is also acknowledged, along with funding support provided by the Structured PhD Programme in Biomedical Engineering and Regenerative Medicine (BMERM). Funded under the Programme for Research in Third-Level Institutions (PRTL) Cycle 5 (Strand 2) and co-funded under the European Regional Development Fund (ERDF). The SFI/HEA Irish Centre for High-End Computing (ICHEC) is also acknowledged for the provision of computational facilities and support.

List of Publications

First-author journal publications

McGrath D.J., O'Brien B., Bruzzi M., McHugh P.E. Nitinol Stent Design - Understanding Axial Buckling. *Journal of the Mechanical Behavior of Biomedical Materials*, 40:252-263, 2014.

McGrath D.J., O'Brien B., Bruzzi M., Kelly N., Clauser J., Steinseifer U., McHugh P.E. Evaluation of Cover Effects on Bare Stent Mechanical Response. *Journal of the Mechanical Behavior of Biomedical Materials*, 61:567-580, 2016.

McGrath D.J., Thiebes A.L., Cornelissen C.G., O'Shea M.B., O'Brien B., Jockenhoevel S., Bruzzi M., McHugh P.E. An ovine *in-vivo* framework for tracheobronchial stent analysis. *Biomechanics and Modeling in Mechanobiology*, In Press, 2017.

McGrath D.J., Thiebes A.L., Cornelissen C.G., O'Brien B., Jockenhoevel S., Bruzzi M., McHugh P.E. Evaluating the interaction of a tracheobronchial stent in an ovine *in-vivo* model. *Biomechanics and Modeling in Mechanobiology*, 2017. Under Review.

Publications not included in this thesis

Thiebes A.L., Kelly N., Sweeney C.A., McGrath D.J., Clauser J., Kurtenbach K., Gesche V.N., Chen W., Jan Kok R., Steinseifer U., Bruzzi M., O'Brien B., McHugh P.E., Jockenhoevel S., Cornelissen C.G. PulmoStent: In Vitro to In Vivo Evaluation of a Tissue Engineered Endobronchial Stent. *Annals of Biomedical Engineering*, 45:873-883, 2016.

Chen W., Clauser J., Thiebes A.L., McGrath D.J., McHugh P.E., Steinseifer U., Jockenhoevel S., Hennink W.E., Jan Kok R. Selection and Fabrication of a non-woven polycarbonate urethane cover for a tissue engineered airway stent. *International Journal of Pharmaceutics*, 514:255-262, 2016.

Chen W., Clauser J., Thiebes A.L., McGrath D.J., Kelly N., van Steenbergen M.J., Jockenhoevel S., Steinseifer U., McHugh P.E., Hennink W.E., Jan Kok R. Gefitinib/ gefitinib microspheres loaded polyurethane constructs as drug-eluting stent coating. *European Journal of Pharmaceutical Sciences*, 103:94-103, 2017.

Chen W., di Carlo C., Devery D., McGrath D.J., McHugh P.E., Kurtenbach K., Jockenhoevel S., Hennink W.E., Jan Kok R. Fabrication and characterisation of gefitinib-releasing polyurethane foam as a coating for drug eluting stent in the treatment of bronchotracheal cancer. *International Journal of Pharmaceutics*, 2017. Under Review.

Declaration of Originality

I certify that the work presented in this thesis is my own¹.

Donnacha McGrath

¹ Please see Appendix 5 for details describing the roles of co-authors.

Chapter 1

Introduction and Background to the Literature

1.1 Introduction

Tracheobronchial stents are used to relieve blockages in the respiratory tree, typically caused by lung cancer. The devices are associated with a high rate of complications which include stent migration, stent strut fracture, mucous plugging and granulation tissue formation. In order to improve stent design and reduce complications it is first necessary to determine how the devices function *in-vitro* and how they interact with the body they are implanted in *in-vivo*.

Until now, little work has been documented in the literature on the analysis of tracheobronchial stent mechanical performance. Self-expanding metallic stents are commonly fabricated from nitinol which exhibits complex material properties like superelasticity and hysteresis, which can cause difficulties in design. Often, the stents are sheathed with a polymeric cover to reduce the effect of some complications. However, the polymeric covering can impact stent mechanical performance. While much work has been performed in the literature on the effects of tracheal stenting on tissue response, little has been undertaken with regard to evaluating the effect of *in-vivo* loading on tracheobronchial stent mechanical performance. Improving our understanding of how tracheobronchial stents function may help improve the next generation of devices.

The work presented in this thesis was primarily driven by the requirements of the FP7 funded PulmoStent Project. Of which the primary goal was to develop a solution to mucous plugging. This was to be accomplished through the amalgamation of tissue engineering and stenting technologies. Where a tissue engineered ciliated epithelium was to be introduced onto the inner lumen of a covered tracheobronchial stent to restore mucociliary clearance to the stented region. As part of this work a covered laser-cut stent needed to be developed and project feasibility investigated

through an *in-vivo* animal study. For more details on the PulmoStent project the reader is referred to http://cordis.europa.eu/result/rcn/173303_en.html.

1.1.1 Objectives

The overall objective of this thesis is to develop a computational and experimental framework that can be used to understand the mechanical performance of tracheobronchial stents, with the aim of being able to facilitate the improvement of future device designs. Specifically, the aims of the current work are:

1. To investigate self-expanding nitinol stent buckling and eliminate it from the design.
2. To evaluate the mechanical effect that adhered covers can have on tracheobronchial stent response.
3. To develop a finite element framework that can be used to evaluate tracheobronchial stent performance *in-vivo*.
4. To correlate pre-clinical observations of granulation tissue formation with computational predictions.

Each of these objectives are investigated and discussed in Chapters 2-5 of this thesis. This chapter introduces the subject matter of the research and outlines the background and literature relevant to tracheobronchial stenting. This includes details on: the lung's structure and its functioning, tracheobronchial stent applications and complications, important stent mechanical properties and, computational modelling of stents and lung motion. The chapter concludes with a summary of the thesis structure.

1.2 The Lung

The primary function of the lung is to exchange gas by introducing oxygen and removing carbon dioxide. This is accomplished at the alveolar surface through simple diffusion where inspired air is introduced into the blood and carbon dioxide is expired (West 2012). The process is driven by the interaction of multiple components where

the lung itself plays a passive role. In this section, a detailed introduction to the lung is described including details on its structure, the physiology of lung motion, the material properties of the primary structural components, and animal models.

1.2.1 Lung Structure

The primary structures in the lungs are the tracheobronchial tree, the pulmonary arterial system, and the lung parenchyma. The tracheobronchial tree is formed from a series of branching airways that end at the alveolar surface. This system begins at the trachea (or windpipe) which extends from below the larynx to the fourth thoracic vertebra where it splits into the left and right main bronchi (Fréchette and Deslauriers 2006). The main bronchi enter their respective lung and subdivide further to form the bronchial tree containing smaller and smaller branches of bronchi which are joined to smaller bronchioles that eventually terminate at the alveoli ducts after approximately 23 generations (McCool 2006) (Fig. 1.1). Airway generations are counted at each branch point of the tracheobronchial tree, with the trachea allocated a generation of zero and each subsequent bifurcation increasing by a value of one as illustrated in Fig. 1.1. The human airways exhibit dichotomous branching, which is described by the airway dividing into two branches with similar diameters and branching angles (Weibel and Gomez 1962; Schlesinger and McFadden 1981).

Each alveolar duct ends in alveoli sacs where gas exchange occurs (West 2012). The blood carrying pulmonary arterial system follows the path of the respiratory tree with the blood vessels branching off into smaller units that end with capillaries in contact with the alveoli (Lawrence et al. 2015). The lung parenchyma is the porous structure that encases the circulation system and is formed from the lung constituents that involve gas transfer including the alveoli, alveolar ducts, capillaries and the respiratory bronchioles (Hyde et al. 2009). Often the larger pulmonary arteries are also considered part of the lung parenchyma, which is what is assumed in Chapters 4 and 5 in this thesis. The lung parenchyma forms the lobes that make up the lungs with the right lung containing three lobes and the left containing two.

The walls of the tracheobronchial tree are complex structures. The trachea and main bronchi are structurally similar, being made up of four sections: the mucosa, the

submucosa, the cartilage and smooth muscle section, and the outer adventitia (Hayward and Reid 1952; Lawrence et al. 2015) (Fig. 1.2 (a)). In these regions the cartilage is formed in c-shaped rings connected at each end by a thin smooth muscle membrane. In the trachea there are between 16 and 22 of such c-shaped cartilage rings connected by annular tissue (Fréchette and Deslauriers 2006; Lawrence et al. 2015). The stiff cartilage supports the airway and allows it to collapse during coughing. This increases the airflow velocity which improves cough efficiency by helping to remove particulates from the airway surface (Kamm 1999). Below the main bronchi the cartilage in the airways begins to become more irregular, first forming patches and then completely disappearing in the bronchioles at around the 12th division (Hayward and Reid 1952). An example of the cross-section of a secondary bronchus is provided in Fig. 1.2 (b).



Fig. 1.1: Idealised airway tree generations. Reproduced with permission from Weibel (1963).

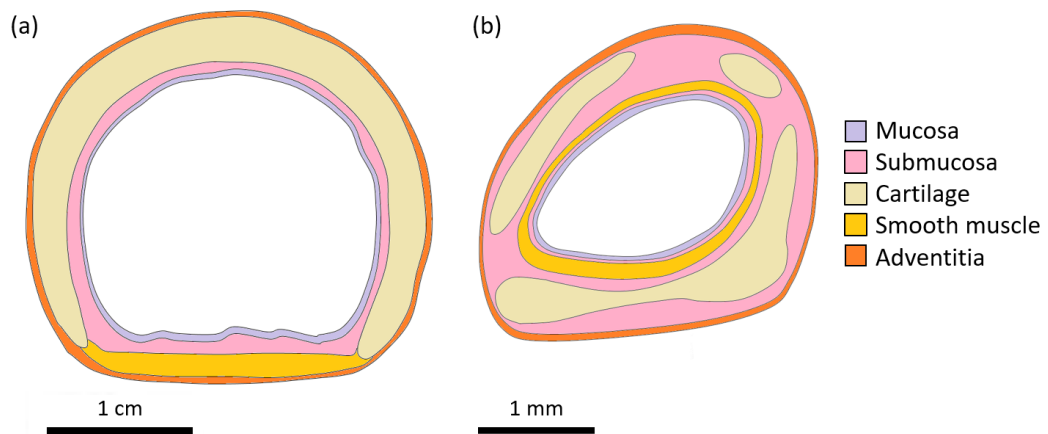


Fig. 1.2: Schematic representation of airway structure of (a) the trachea (b) secondary bronchus. Adapted from Krstic (1984).

1.2.2 Physiology of Lung Motion

The lungs are found in the thoracic cavity surrounded by the rib cage and diaphragm. Each lung is encased within a thin membrane called a pleura, which surrounds all the lobes individually and also lines the diaphragm and mediastinum, forming a sac within the thoracic cavity. The pleural sac contains a thin fluid-filled space 5-35 μm thick, with the pleural fluid acting as a lubricant allowing near frictionless sliding of the components within the thoracic cavity during respiration (Lai Fook 2004). The pleural space maintains a negative intrapleural pressure which acts on the outer surfaces of the lung, keeping them inflated at all times. Before inspiration the intrapleural pressure is around $-5 \text{ cmH}_2\text{O}$ (West 2012). Respiratory motion is initiated with contraction of the diaphragm and intercostal muscles which causes the diaphragm to move downwards and the chest wall to shift outwards. This enlarges the pleural cavity and decreases the intrapleural pressure acting on the lung surface. The change in pressure expands the lung, causing a drop in internal lung pressure which forces air to enter through the trachea and down to the alveolar sacs where gas exchange occurs (West 2012). Exhalation during normal breathing occurs through natural recoil of the lung. In effect the lungs remain passive and inflate and deflate with the expansion and contraction of the thoracic cavity during normal breathing (Werner et al. 2009). However, expiratory muscles such as the internal intercostals and abdominal muscles can be used when increased demand is required of the ventilatory system, such as when exercising (Bates 2009). There is a hysteresis effect

in the lung where the pressure-volume (PV) relationships during inhalation and exhalation differ, so that the pressure at a specific lung volume is always lower during inhalation (West 2012) (Fig. 1.3). The pressures in the lung during breathing are summarised in Fig. 1.4. More detailed information on breathing mechanics can be found in (West 2012).

Coughing is performed by the lung to clear the airways of unwanted particulates, mucus and other secretions (McCool 2006). Clearance of the respiratory tree is achieved by forcing air out through the airways at high speeds, which tears particulates from the airway walls and adds them to the expiratory gas (Langlands 1967; Irwin 1977). The cough sequence occurs over three phases which are classified as inspiratory, compressive and expiratory (Irwin 1977). During the inspiration phase air is inhaled and the expiratory muscles are lengthened by the increased air volume which can be as much as 90% of inspiratory capacity (Park et al. 2010). The compressive phase begins when the glottis closes and the expiratory muscles contract. Closure of the glottis retains the air in the lung as intrapleural pressures build from muscle contraction (Irwin 1977). During closure of the glottis the intrapleural pressure can increase to over 400 cmH₂O (McCool 2006). The final phase of coughing, the expiratory phase, begins with the opening of the glottis and the release of high expiratory flows due to the pressure developed during the compressive phase (McCool 2006). This expiratory flow begins with an initial peak flow lasting 30 to 50 ms followed by 200 to 500 ms of sustained flows during which time lung volume and pressure drop (McCool 2006) (Fig. 1.5). During the expiratory phase the larger airways collapse, resulting in an increased airflow velocity that improves cough efficiency (Kamm 1999).

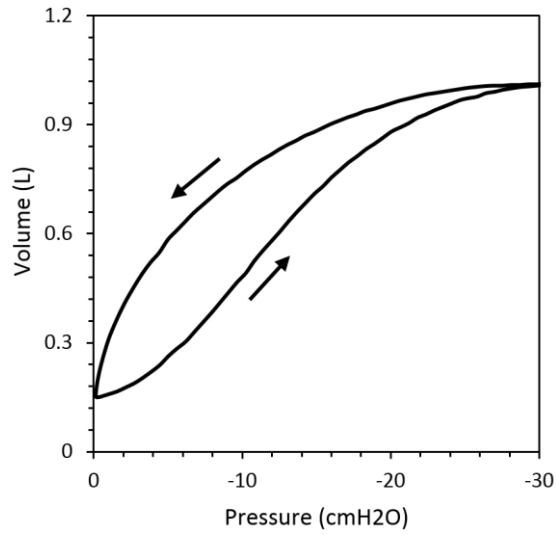


Fig. 1.3: Example of lung hysteresis in pressure-volume curves for excised lungs. Adapted from West (2012).

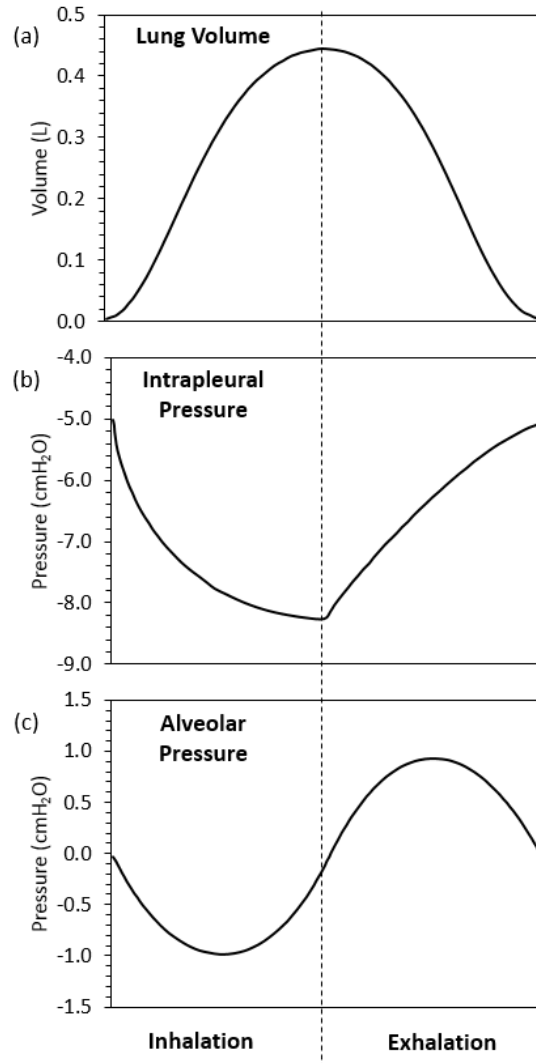


Fig. 1.4: Example of normal breathing (a) lung volume, (b) intrapleural pressure, (c) alveolar pressure. Adapted from West (2012).

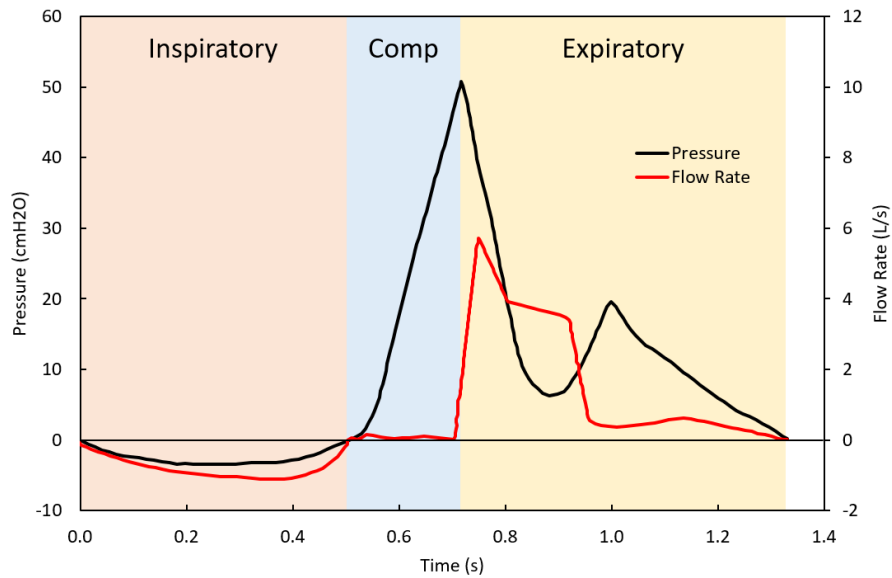


Fig. 1.5: Schematic illustrating variations in pressure and flow during the three phases of coughing. Adapted from McCool (2006).

In Fig. 1.6 some important lung volumes are summarised. Tidal volume is the amount of air inhaled over the course of a typical breath. The total lung capacity (TLC) is the largest volume of air that can be inhaled into the lungs, and the residual volume is the amount of air that remains in the lungs after a full forced exhalation. The difference in volume between TLC and residual volume is known as vital capacity, and the lung volume at the end of a passive exhalation is called the functional residual capacity (FRC) (West 2012).

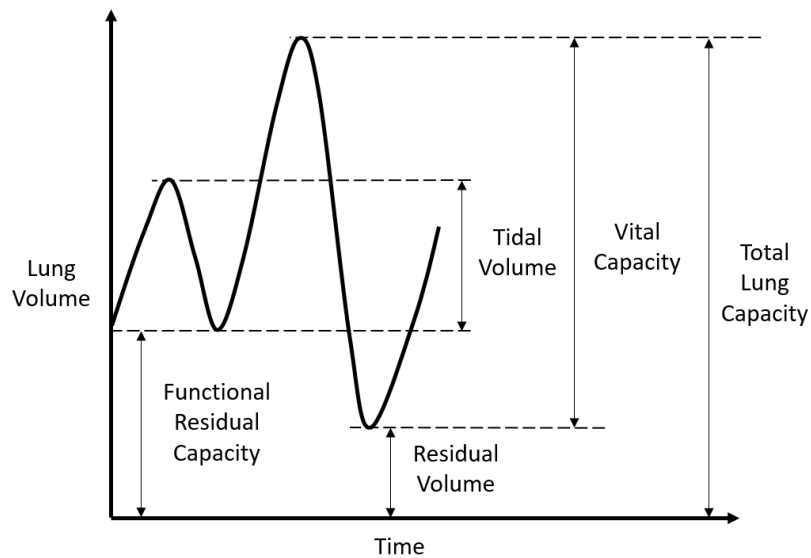


Fig. 1.6: Breathing volumes of the lung. Adapted from Bates (2009).

1.2.3 Lung Constituent Mechanical Properties

1.2.3.1 Lung Parenchyma

As discussed previously, the lung parenchyma is primarily composed of the smaller lung structures concerned with gas transfer (the alveoli, alveolar ducts, capillaries and respiratory bronchioles) which form a complex porous structure. Apart from housing the primary structures involved in gas transfer, the parenchyma plays a vital role in the mechanics of breathing due to its elastic recoil (Suki and Bates 2011). This makes the mechanical properties of the parenchyma extremely important for lung function, particularly as most lung diseases are associated with irregular tissue mechanics (Suki and Bates 2008; Suki and Bates 2011). The general behaviour of the lung parenchyma can be seen in the PV relationship in Fig. 1.3, with a non-linear viscoelastic response and hysteresis which is common among biological tissues (Bates 2009; Lokshin and Lanir 2009). It should be noted that the PV plot shown here (Fig. 1.3) also includes the combined effects of the tracheobronchial tree and the pulmonary vasculature. The quasi-static behaviour of isolated strips of dog lung parenchymal tissue is shown in Fig. 1.7 where material strain stiffening is observed. This is believed to be primarily driven by the interaction between fibres of collagen and elastin, the tissue's main structural constituents (Mead 1961). At lower strains, the stress is taken up by the elastin fibres which have a linear stress-strain relationship up to at least 200% (Fung 1993). The collagen fibres, which are stiffer, are folded and loose at these lower strains, but begin to take up the stress steadily as the strain increases. This results in a steady escalation in stress which is observed as the asymptotic shape seen in Fig. 1.7.

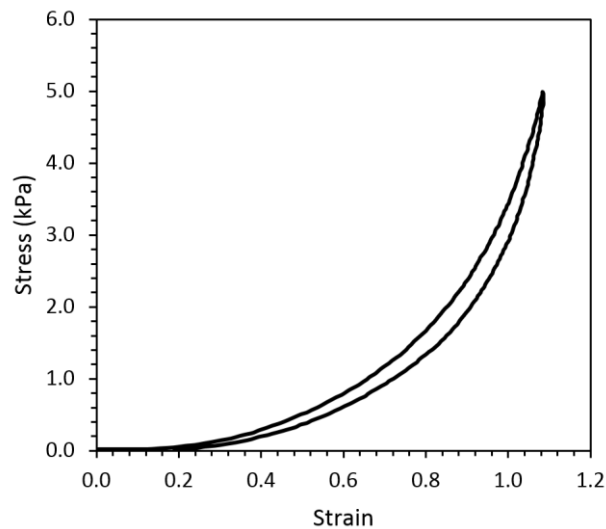


Fig. 1.7: Stress versus strain of strips of dog lung parenchyma. Adapted from Bates et al. (1994).

1.2.3.2 Tracheobronchial Tree

Due to the large motions that the lung undergoes during respiration the tracheobronchial tree needs to be able to stretch and accommodate considerable changes in both length and diameter (Kamm 1999). This compliance is also essential for the first few airway generations during coughing, where dynamic collapse of the airway occurs (Kamm 1999). Owing to these requirements, the airways, like the parenchyma are complex structures with multifaceted material properties. In general, the experimental analyses performed on the tracheobronchial tree for both animals and humans can be separated into two categories: measurement of mechanical relationships for intact airway structures (Martin and Proctor 1958; Croteau and Cook 1961; Hughes et al. 1972; Brown and Mitzner 1998; Tiddens et al. 1999) and calculation of the mechanical properties of individual tissue layers (Panitch et al. 1989; Rains et al. 1992; Codd et al. 1994; Teng et al. 2008; Teng et al. 2009; Trabelsi et al. 2010; Bagnoli et al. 2013; Safshekan et al. 2016a; Safshekan et al. 2016b). The effect of pressure on airway diameter and length shows an increase in airway compliance with each new branching generation due to a gradual decrease in cartilage content, airway thickness and diameter (Martin and Proctor 1958; Croteau and Cook 1961; Prakash and Hyatt 1978). Testing on individual components of the tracheal wall including cartilage, trachealis muscle, connective tissue, mucosal layers and the adventitia have generally shown the airway materials to exhibit non-linear, viscoelastic and anisotropic properties (Teng et al. 2008; Trabelsi et al. 2010; Teng et

al. 2012; Safshekan et al. 2016a; Safshekan et al. 2016b). Cartilage, which provides the majority of the structural support to the upper airways is a fibre-reinforced composite of randomly oriented collagen fibres encasing hydrated proteoglycans (Rains et al. 1992; Trabelsi et al. 2010). The tissue is often considered isotropic and non-linear (Trabelsi et al. 2010; Safshekan et al. 2016a), though it can remain relatively linear below a strain of 20% (Lambert et al. 1991; Safshekan et al. 2016a) (Fig. 1.8). Tracheal cartilage produces a stiff response with an elastic modulus between 1 and 40 MPa (Rains et al. 1992; Roberts et al. 1998; Trabelsi et al. 2010; Safshekan et al. 2016a), where stiffness has been shown to increase with age (Rains et al. 1992; Safshekan et al. 2016a). The smooth muscle in the airways contains two orthogonal collagen families that give it anisotropic characteristics (Trabelsi et al. 2010; Teng et al. 2012). The fibres run in the longitudinal and transverse directions, with the longitudinal producing a tissue tangent modulus (at 5% strain) around 1.4 times stiffer than the circumferential direction (Teng et al. 2012). The trachealis muscle is significantly more compliant than the airway cartilage as illustrated in Fig. 1.8, and similarly, has also been shown to increase in stiffness with age in sheep (Panitch et al. 1989). The connective tissue between the cartilage rings in the trachea has been shown to have similar tensile properties to the smooth muscle (Safshekan et al. 2016a). Other soft tissues in the tracheobronchial tree like the adventitial membrane, mucosa and submucosa are not thought to significantly affect the mechanical attributes of the airway (Teng et al. 2012). It should be noted that all of the above experimental studies focused on tracheal tissue constituents and never considered tissue within the smaller airways where cartilage formation is more irregular (Hayward and Reid 1952). Residual stresses within excised airways have also been investigated through the recording of the opening angle observed when a radial cut is made through intact rings of the tissue (McKay et al. 2002). McKay et al. (2002) found that a zero-stress state for human and porcine airways could be assumed, while sheep and rabbit airways contained residual stress. Interestingly, opening angles were significantly lower in ovine airways originating within the lung parenchyma, suggesting that these intraparenchymal airways contain a much lower residual stress state than the larger airways outside of the parenchyma.

It should be noted that while the tissues in the lung exhibit viscoelastic properties, these are not considered in Chapters 4 and 5 of this thesis as is common in the literature. In this work dynamic effects are not considered and so it is reasonable to assume that tissue viscoelasticity can be ignored. Additionally, Teng et al. (2012) found that the hysteresis associated with airway tissue loading and unloading was small enough to be considered hyperelastic.

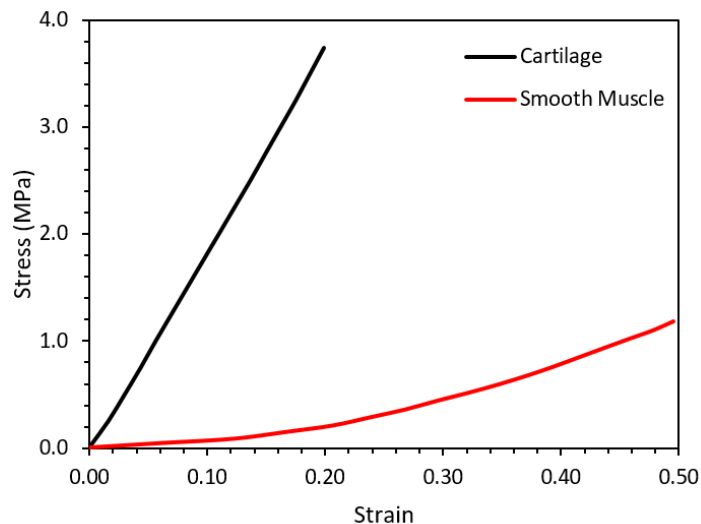


Fig. 1.8: Comparison of tensile stress-stretch curves for human cartilage and smooth muscle. Note cartilage is tested in the radial direction while smooth muscle is tested in the longitudinal direction. Adapted from Safshaken 2016.

1.2.4 Animal Models

A range of animal models are used in the research of respiratory diseases including rats, rabbits, pigs, dogs and sheep (Allen et al. 2009; Bähr and Wolf 2012). Although no animal model is suitable to capture all aspects of human lung behaviour, large animals are particularly suitable for evaluating cases where airway structure and function play an important role (Scheerlinck et al. 2008; Van der Velden and Snibson 2011). Animals with similar lung capacities to humans include dogs, sheep and pigs. However, sheep are seen as the large animal of choice for respiratory physiology (Scheerlinck et al. 2008; Bähr and Wolf 2012). Sheep have similar lung function to humans with airflow, compliance, breathing rates and tidal volumes all falling within normal human ranges, which can allow for lung function testing to be implemented using the same techniques as used for spontaneous human breathing (Van der Velden and Snibson 2011). The ovine (and porcine) lung is structurally similar to the

human lung consisting of two left lobes and four right lobes, and the airways are also similar in the distribution of epithelial cells and smooth muscle (Meeusen et al. 2009). Although the branching pattern of the lower airways of sheep are similar to the dichotomous pattern seen in humans (Meeusen et al. 2009), the branching of the larger ovine airways is monopodial, meaning that the airway produces two branches that extend out at differing angles (Schlesinger and McFadden 1981). This results in a more asymmetric airway tree than the human respiratory tree (Fig. 1.9). One of the most noticeable differences in the animal lung structure is the tracheal bronchus that extends from the trachea into the right upper lobe which is rarely seen in humans (Doolittle and Mair 2002) (Fig. 1.9). Although there are differences between animal and human lungs, animal models are especially important for the development and analysis of interventional medical devices such as tracheobronchial stents (Hugo Marquette et al. 1995; Bolliger et al. 1999; Puma et al. 2000; Hwang et al. 2001; Fiorentino et al. 2016; Chaure et al. 2016).



Fig. 1.9: Tracheobronchial tree of (a) human lungs (b) ovine lungs. Notice the tracheal bronchus in the ovine airway. Adapted from Tawhai et al. (2004).

1.3 Tracheobronchial Stenting

Respiratory diseases are responsible for around 1 million European deaths per year, with an estimated total cost in the region of €96 billion (Gibson et al. 2013). The most prevalent respiratory disease is lung cancer, which accounted for 1.4 million worldwide deaths and was the most diagnosed form of cancer for males in 2008

(WHO 2011; Jemal et al. 2011). It is estimated that about 30% of people with lung cancer go on to acquire difficulties with central airway blockages associated with extrinsic or intrinsic tumour growth hampering airflow through the airways, and require stenting for alleviation (Bolliger et al. 2006; Lee et al. 2010). Tracheobronchial stents are stiff scaffolds which are delivered to diseased airways to provide support and maintain lumen patency. Tracheobronchial stents are indicated for five principal indications: support for airways compressed by external tumours; ensuring lumen patency after the removal of intraluminal cancer; alleviating benign strictures; supporting lumen collapse due to malacia; and sealing fistulas (airway tears) (Freitag 2010). In this section airway stent applications, types and complications are discussed.

1.3.1 Tracheobronchial Stent Applications

The leading use for tracheobronchial stents is in the re-establishment of patency to narrowed airways caused by benign and malignant stenoses (Freitag 2010). Typically, stents are utilised when obstruction is >50% of the airway lumen and suffocation is imminent (Bolliger et al. 1993; Furukawa et al. 2010). Malignant stenosis is most often caused by external compression from bronchogenic, oesophageal, or thyroid carcinomas (Ernst et al. 2004), and less frequently by intraluminal tumour growth (Macchiarini 2006). While intraluminal tumour tissue can be removed using methods like laser resection and argon plasma coagulation, stenoses formed from external compression can only be treated with stent placement (Bolliger et al. 2006). In malignant cases tracheobronchial stents are typically used for palliative purposes, and patient survival times are short (Dutau et al. 2015; Lin and Chung 2016). Benign strictures are primarily caused by intubation, tracheostomy and lung transplant, though any damage to the inner lumen can result in the development of stenoses (Murthy et al. 2007; Thistlethwaite et al. 2008; Puchalski and Musani 2013). With benign stenosis tracheal sleeve resection is the preferred treatment (Grillo et al. 1992), but where surgical intervention is not possible, stenting is often the only option (Strausz 1997; Freitag 2010).

Stents are also used to treat cases of airway collapse called malacia. In these instances weakening of the cartilage causes the airways to collapse (Murgu and Colt

2006). Here, stents are often used as a short-term action, before other long term treatments such as external splinting or physiotherapy and continuous positive airway pressure therapy (Murgu and Colt 2006; Freitag 2010). Another common use for these devices is in the treatment of tracheoesophageal fistulas which occur primarily due to infiltration by oesophageal carcinomas (Hürtgen and Herber 2014). The opening formed between the trachea and airway can cause choking, severe coughing and pneumonia (Gudovsky et al. 1993). Currently, the treatment of choice is to seal the fistula using a combination of airway and oesophageal stents, where the stent covers form a suitable seal (Ke et al. 2015).

1.3.2 Stent Types

One of the first examples of a tracheobronchial stent was the Montgomery T-tube which was developed in 1965 (Montgomery 1965). This stent, which is still in use today, requires a tracheotomy to accommodate an external limb (Guibert et al. 2015). Since the development of the T-tube, a wide variety of airway stents have been developed that are typically divided into three categories based on their material: polymeric, metal or covered metal. The ideal airway stent should: return luminal patency; be cost effective; be easily placed and removed if necessary; resist migration; cause minimal granulation tissue formation; not inhibit mucociliary clearance; and be compliant enough to mimic airway physiology (Saito and Imamura 2005; Chin et al. 2008; Guibert et al. 2015). Many of these requirements are contrasting and so no ideal tracheobronchial stent currently exists (Saito and Imamura 2005; Guibert et al. 2016).

1.3.2.1 Polymeric Stents

Currently available polymeric stents include the Dumon (Novatech, France), the Hood stent (Hood Laboratories, USA), the Polyflex (Boston Scientific, USA), and the Noppen stent (Reynders Medical Supply, Belgium). Of these, the most popular is the Dumon (Freitag 2010; Lin and Chung 2016) (Fig. 1.10). Fabricated from coated silicone, it looks like a hollow tube with small studs radiating outwards to help fixate the stent (Freitag 2010). The Dumon is also available in bifurcated form for stenoses near the carina (Guibert et al. 2015). Polymeric stents are often considered the best option for benign and malignant tumours as they are easy to place and remove

(Puma et al. 2000), they are considered safe, and produce little granulation formation (Dumon 1990; Chin et al. 2008). These stents do have their drawbacks though, such as the requirement for general anaesthesia and rigid bronchoscopy for implantation, high migration rates, reduced mucociliary clearance, and a narrow internal lumen due to the wall thickness required to support the airway (Chin et al. 2008; Serrano et al. 2013; Guibert et al. 2015).



Fig. 1.10: Various Dumon stent types. Adapted from Dutau 2013.

1.3.2.2 Metal and Covered Metal Stents

Some bare metal and covered metal stents consist of the Ultraflex (Boston Scientific) (Fig. 1.11 (a)), the AERO (Merit Medical, USA) (Fig. 1.11 (b)), and the Aerstent (Leufen, Germany). Typically, these stents are self-expanding and fabricated from nitinol (Chin et al. 2008) by either being laser-cut from a thin tube or created from the knitting or braiding of wire filaments. Stent covers are commonly made from silicone, PTFE (polytetrafluoroethylene) or polyurethane (Farhatnia et al. 2013). The advantages given by metal stents include easy insertion with flexible bronchoscopy, better fixation and improved clearance of secretions (Saito and Imamura 2005; Godoy et al. 2014; Guibert et al. 2015). Bare stents have become less popular due to issues with incorporation into the airway wall and granulation formation (Murthy et al. 2004; Noppen et al. 2005; Godoy et al. 2014), but are still used in cramped, severely deformed stenoses (Puma et al. 2000; Guibert et al. 2015). Covered stents are used to prevent tumour ingrowth through open stent struts, they are also more favoured than bare stents in benign cases where stent removal after long periods may be

necessary (Godoy et al. 2014). They are also ideally suited to sealing airway fistulas (Hürtgen and Herber 2014). Common risks associated with metallic stents include granuloma formation (Husain et al. 2007), stent fracture, and airway perforation (Puma et al. 2000). Covered stents can reduce mucociliary clearance and increase the risk of migration (Madden et al. 2002; Shin et al. 2003).



Fig. 1.11: (a) Ultraflex stent examples (Madden et al. 2002), (b) Aero Stent example (Mehta 2008)).

1.3.2.3 New Developments

Recently the development of biodegradable and drug eluting tracheobronchial stents has gained much interest. In benign cases, stents are often only needed for a temporary period before needing to be removed (Galluccio et al. 2009; Dutau et al. 2010). The necessity for a procedure to remove a stent in these instances adds cost, and so a biodegradable stent that would maintain airway patency for a set amount of time before eventually vanishing is appealing (Dutau et al. 2015). Although much work is being carried out in this area, there have been few trials in humans and little sign of a biodegradable airway stent coming on the market soon (Dutau et al. 2015; Lin and Chung 2016). Drug eluting stents have been proposed as a possible way of preventing granulation formation, but these too are still in the developmental stage (Guibert et al. 2016; Hohenforst-Schmidt et al. 2016).

1.3.3 Stenting Complications

Currently, there is no ideal tracheobronchial stent as all stents are associated with complications (Rafanan and Mehta 2000; Godoy et al. 2014). As a group, airway

stents have a relatively high complication rate of around 15% (Colt et al. 1992; Dechambre et al. 1998; Lemaire et al. 2005; Makris and Marquette 2007; Godoy et al. 2014). The primary complications related to stenting include stent migration, granulation tissue formation, stent strut fracture and mucous plugging.

Stent migration can be a serious complication of airway stenting. All stent designs that are not fixed in position can migrate either proximally or distally along the airways (Freitag 2010). Although the coughing out of stents have been recorded (Aggarwal et al. 1999), the more life-threatening cases are when stents migrate and completely occlude an airway, which can lead to asphyxiation (Hautmann et al. 2000). To mitigate migration stents should be oversized so that when deployed they apply a suitable expansion force (Ernst and Herth 2013). However, even if proper sizing is used, factors like the cyclic loading from respiration and coughing, tissue viscoelasticity, and the effects of tumour specific treatments can result in stents becoming loose and migrating (Freitag 2010). Migration has been observed in around 10% of malignant stenoses and in twice as many cases for benign conditions (Freitag 2010). Polymeric and fully covered metal stents tend to migrate more than their bare metal counterparts (Wood et al. 2003; Abdel-Rahman et al. 2014; Godoy et al. 2014).

Tumour growth and granulation formation can lead to restenosis of the stented airway which can result in lumen blockage (Fig. 1.12). If the stent is bare then the tumour can grow directly through the open structure, and if the stent doesn't suitably extend past the tumour then the tumour can grow in over the stent ends (Freitag 2010). This is not a common problem for malignant cases as the stents are typically used for palliative care where life expectancy is short (Dutau et al. 2015; Lin and Chung 2016). Conversely, the use of bare stents for treatment of benign conditions is discouraged, primarily due to stent embedding and the subsequent formation of granulation tissue. This can result in serious complications and has prompted the Food and Drug Administration (FDA) to publish a notification recommending that metal stents are only used in benign cases when surgical options or polymeric stent placement is not viable (Food and Drug Administration 2005; Sosa and Michaud 2012; Serrano et al. 2013). Granulation tissue is believed to be formed from a combination of mechanical irritation caused by scratching of the stent surface

against the airway wall, excessive expansion pressures, and bacterial infection (Schmäl et al. 2003; Ost et al. 2012), and can result in the formation of stenoses which can lead to loss of airway patency. The granulation tissue is formed from a mass of fibrous connective tissue which can adopt functional characteristics of smooth muscle (Brown and Montgomery 1996; Thiebes et al. 2017). Typically, granulation tissue forms at the proximal and distal stent ends (Burningham et al. 2002; Schmäl et al. 2003; Lemaire et al. 2005; Hu et al. 2011). It has been recorded in over half of all stenting cases, and has been seen as clinically significant in around 25% of all cases (Freitag 2010). All stent types can produce some form of granulation tissue, though bare metal stents are considered the worst (Ost et al. 2012; Sosa and Michaud 2012).



Fig. 1.12: Granulation tissue formation at distal stent end. Reproduced from Freitag (2010).

Stent fracture is a major complication of airway stents as it can potentially cause airway obstruction and perforation (Rousseau et al. 1993; Chung et al. 2008; Godoy et al. 2014) (Fig. 1.13). The cause of the fractures are thought to be from cyclic loading due to coughing, compression during swallowing, granulation, shearing forces or tortuous airways (Burningham et al. 2002; Zakaluzny et al. 2003; Chung et al. 2008). Fracture is most commonly found in benign airway obstruction, rather than in malignant cases, where patient survival time most likely plays an important role (Chung et al. 2008; Chung et al. 2011). Fracture, in one study, was shown to most likely occur between 500 and 1000 days after implantation, revealing fracture rates of 2.1%, 9.4%, 13.9% and 11.1% over the first four years after implantation (Chung

et al. 2008). The removal of damaged airway stents is possible, but there is a significant risk of further complications, such as tearing of the mucosa, perforation, pneumothorax and return of lumen blockage (Lunn et al. 2005; Godoy et al. 2014).



Fig. 1.13: Example of metallic stent fracture. Adapted from Zakaluzny et al. (2003).

Observed in over a third of all tracheobronchial stenting cases, mucostasis is one of the most prevalent complications (Freitag 2010). For the most part this occurs in patients as halitosis (bad breath), which is caused by the emergence of bacteria and fungi colonies surrounding the stent (Noppen et al. 1999; Freitag 2010). Of more clinical importance though, is the problem of retained secretions that can build up and occlude the stent lumen. This is a common problem with polymeric and covered metal stents, believed to be due to the blocking of the respiratory epithelium causing distal mucous build up (Swanson et al. 2007). Typically, this is treated with antibiotics and repeated suctioning (Freitag 2010). To effectively combat the complications associated with these devices it is necessary to understand the principal properties of airway stents and how mechanical performance is determined.

1.4 Stent Properties and Mechanical Analysis

1.4.1 Properties of Self-expanding Nitinol Stents

The primary focus of this thesis is on bare and covered self-expanding nitinol tracheobronchial stents and so this section focuses on the properties associated with these devices. Nitinol self-expanding stents are ideal for use in tracheobronchial

applications due to properties such as crushability and biased stiffness, which are adopted from the special characteristics associated with nitinol (O'Brien and Bruzzi 2011).

1.4.1.1 Nitinol Shape Memory and Superelasticity

Nitinol is an alloy of near-equiatomic levels of nickel and titanium which exhibits superelastic and shape memory characteristics. Superelasticity allows the alloy to reach strains in excess of 10% without plastically deforming, while shape memory permits it to regain its original shape following an external (plastic) deformation by applying heat (Duerig et al. 2000; Stoeckel et al. 2004). Its unusual properties stem from a change in stress or temperature inducing a solid state transformation between austenite and martensite (O'Brien and Bruzzi 2011).

Shape memory utilises thermally induced reversible phase transformation in nitinol, where cooling it in its austenitic phase changes the crystal structure to form twinned martensite, without shape change (Fig. 1.14). At this lower temperature (M_f) the twinned martensite forms a stable martensitic phase, where mechanical loading can induce permanent deformation up to a strain of approximately 8% through a process called detwinning (O'Brien and Bruzzi 2011). The addition of heat at a higher temperature (A_f) can then return the material to its austenitic phase and original undeformed shape (Duerig et al. 1990).

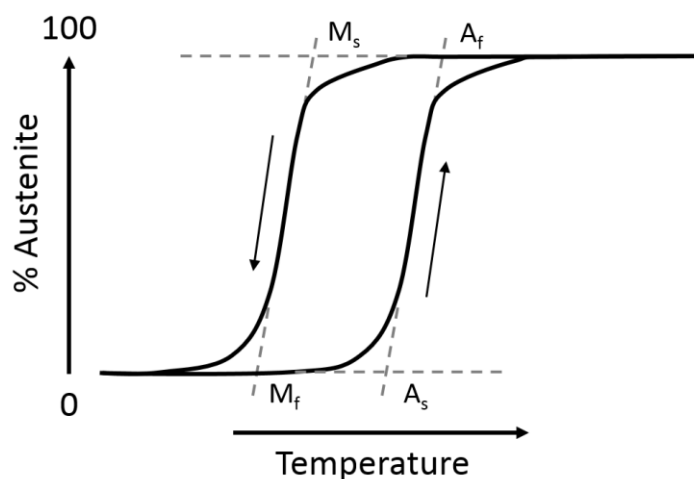


Fig. 1.14: Schematic representation of austenite transformation and hysteresis over a change in temperature. A and M correspond to the austenite and martensite phases, and subscript s and f refer to the start and finish temperatures of the respective transformation. Adapted from O'Brien and Bruzzi (2011).

Superelasticity is induced in nitinol when an external stress above a critical level causes phase transformation (Duerig et al. 1990; Stoeckel et al. 2004). A stress-induced detwinned martensite is formed which is unstable at high temperatures (above A_f), allowing the material to revert back to its austenitic structure and original undeformed shape upon removal of the external force (Robertson et al. 2012). In this way large strain recovery is possible. Loading and unloading of the material at this temperature results in a stress-strain plot similar to that presented in Fig. 1.15. The austenitic state is represented by a stiff linear response up to around 1% strain, after which transformation to martensite begins at a critical stress (point A). Further loading from this point increases the martensitic volume fraction until the transformation is complete at point B. In the fully martensitic state additional loading initially results in an essentially linear elastic response (with a lower stiffness than the austenitic state), which if strained excessively can result in plastic deformation. Unloading of the material in the martensitic state allows elastic strain recovery and transformation back to austenite. The critical stresses during unloading are lower (between points C and D), resulting in material hysteresis (O'Brien and Bruzzi 2011).

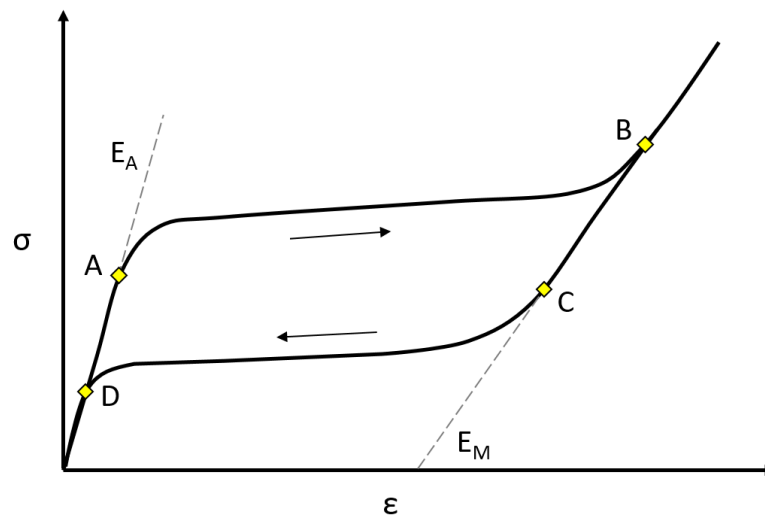


Fig. 1.15: Schematic representation of a typical nitinol stress-strain curve. E_A and E_M refer to austenitic stiffness and martensitic stiffness respectively.

1.4.1.2 Nitinol Stent Characteristics

The superelastic property of nitinol is the feature most often employed in self-expanding stents. The ability to reach high strains without plastic deformation allows nitinol devices to be crimped down to small diameter profiles, permitting them to be

loaded into delivery systems which can be tracked to the desired location in the body's network of airways or arteries. Once positioned the stent can be deployed by retracting an outer sheath or pushing the stent out of the delivery system, where upon release the stent expands using its stored-up elastic energy. A typical crimping and deployment procedure is illustrated with a schematic of radial force (or hoop force) versus diameter in Fig. 1.16. The first thing to notice is that nitinol stent loading response is similar to that of the nitinol stress-strain curve with stiff austenitic and martensitic responses joined by upper and lower plateaus. As the stent is crimped into the delivery catheter the radial force increases as far as point A. From here the device is deployed into the vessel which increases the diameter and produces a drop in force showing the hysteresis associated with the reverse transformation from stress induced martensite to austenite. At point B the stent reaches an equilibrium position with the vessel wall and expansion stops. In this position the force exerted by the stent is determined by the unload plateau which is commonly termed the chronic outward force (COF) (Duerig et al. 2000). If further unloading of the stent occurs the COF follows along the unloading plateau, providing gentle loading (Duerig et al. 2000). However, if the stent undergoes further radial loading (e.g. during coughing or normal breathing) the stent resists the loading along the line between points B and C, returning to the upper loading plateau. This increased stress resistance is termed radial resistive force (RRF) (Duerig et al. 2000), and provides nitinol stents with a certain amount of crush resistance (O'Brien and Bruzzi 2011). The ability of nitinol stents to vary stiffness (between COF and RRF) has been referred to as "biased stiffness" (Duerig et al. 2000).

The concept of biased stiffness is particularly important for tracheobronchial applications. When nitinol stents are deployed in the tracheobronchial tree to combat malignant stenoses the malignancy can press against the device, but the stent resists the increased compression due to the stiff RRF. At the same time a lower COF is applied to the healthy tissue that is not applying a compressive load (O'Brien and Bruzzi 2011). Another important aspect of nitinol stenting in the airways is that the superelastic properties allow airway stents to collapse during coughing and return to their initial configuration without plastic deformation, which can aid

mucocilliary clearance as well as ensuring stent patency (Freitag et al. 1995; Miyazawa et al. 2000; Sosa and Michaud 2012).

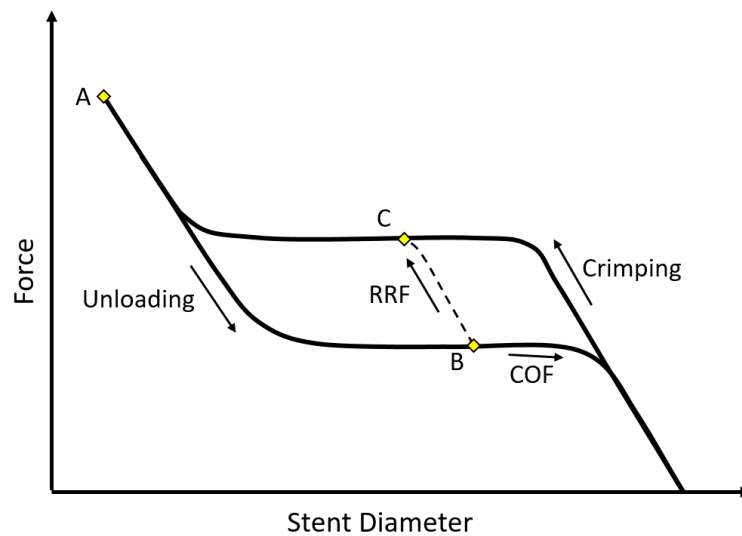


Fig. 1.16: Schematic of radial force versus stent diameter mimicking stent loading and deployment. Adapted from Duerig et al. (2000).

Other properties of nitinol that are worth mentioning in the context of stenting are its temperature dependant stiffness and biocompatibility. The mechanical properties of nitinol are particularly temperature dependent as can be appreciated from the shape memory and superelastic features that can be obtained from the application of mechanical loading at different temperatures. Similarly, the stiffness of nitinol is temperature dependent, with stiffness increasing with increasing temperature (Pelton et al. 2000; Henderson et al. 2011). To ensure self-expanding stents perform at an optimal stiffness at body temperature an A_f around 30 °C is typically used (Stoeckel et al. 2004; O'Brien and Bruzzi 2011). This guarantees that the stent (in its unconfined state) is fully austenitic at body temperature and capable of applying a suitable force against the lumen wall. This temperature dependence requires that any testing performed on nitinol for stent implantation should be performed at body temperature to ensure meaningful results. Although nitinol contains a high nickel content which can have toxic effects at elevated concentrations it is considered a highly biocompatible material with low concentrations of nickel release after initial implantation and corrosion resistance better than stainless steel (Putters et al. 1992; Ryhänen 2000; Stoeckel et al. 2004).

1.4.1.3 Stent Performance

Stent performance is typically assessed through *in-vitro* benchtop testing and *in-vivo* analyses. While there are no specific requirements for stent evaluation, the FDA has published guidance on the type of non-clinical engineering tests that should be performed for applications submitted for premarket approval of intravascular stents (Food and Drug Administration 2010) and premarket notification for tracheobronchial prostheses (Food and Drug Administration 1998). These documents recommend benchtop testing such as deployment testing, radial force testing, crush testing, and fatigue analyses for self-expanding devices. Deployment testing is performed to ensure the device can be accurately and repeatedly deployed at the target location. This is often accomplished by deploying the stent in a tube with similar properties to the target location (Food and Drug Administration 1998). Radial force testing is performed using an iris-like mechanism to reduce the diameter of the stent while simultaneously recording radial force. This produces a curve of radial force versus diameter (as presented in Fig. 1.16) from which important stent attributes such as the COF, RRF and maximum crimping force for stent loading can be obtained. Crush testing or flat plate testing is also routinely performed on superelastic devices to evaluate the ability of the stent to return to a desired configuration after the application of a large external load. Often, this is performed by crushing and unloading the device between two platens while recording the generated out-of-plane bending forces.

The super-elasticity of nitinol stents allow them to undergo larger cyclic strain deformations than other elastic-plastic devices (Duerig et al. 2000), which allows for collapsibility. However, they still suffer from fatigue fracture which can cause multiple complications such as airway perforation and blockage (Rousseau et al. 1993). Fatigue characterisation is routinely performed on diamond samples as well as on entire stent devices (Pelton et al. 2008; Robertson et al. 2012). To ensure patency of a device over its lifetime nitinol stents are evaluated for fatigue using strain based techniques rather than more commonly employed stress based methods. This is due to the large range of strains for which stress remains almost constant over the plateau region associated with nitinol detwinning (Fig. 1.15)

(Robertson et al. 2012). Constant life diagrams like that shown in Fig. 1.17 are employed as they take account of the mean strain caused by stent oversizing and variations in strain amplitude due to the cyclic loading of the lungs (Pelton 2011). A remarkable characteristic of nitinol in fatigue is the increase in fatigue resistance with increasing mean strain above 1.5% mean strain which is illustrated in Fig. 1.17. In general a device is considered “safe” with a strain amplitude below 0.4% for 10^7 cycles (Pelton et al. 2008).

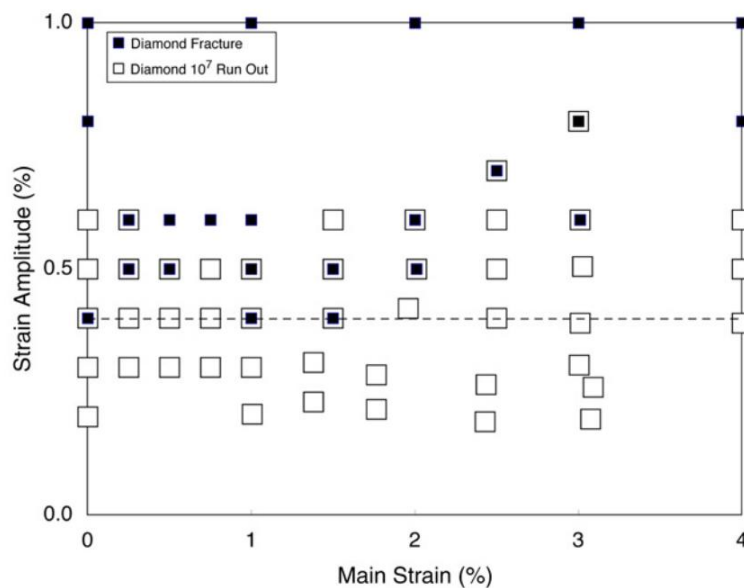


Fig. 1.17: Constant life plot of diamond stent samples. Samples that did not survive to 10^7 cycles are shown with closed squares. Open squares are for samples that did not fail before 10^7 cycles. Reproduced with permission from (Pelton et al. 2008).

Remarkably, from a mechanical perspective only a comparison between an existing device and the proposed device with regard to deployment and radial force are required for tracheobronchial devices (Food and Drug Administration 1998). However, if significant differences are present then animal testing and clinical data may be required.

To the authors knowledge there are only two studies presented in the literature investigating *in-vitro* properties of tracheobronchial stent designs: Freitag et al. (1994, 1995). The studies considered a number of tracheobronchial stents with sizing related to both the trachea and bronchus. Stents were deployed into excised human and porcine airways and the influence of cough loading and extrinsic tumour

compression were evaluated. Coughing was simulated using rapid pressure changes driven by a vacuum pump, while changes in cross-sectional area were recorded. The effect of extrinsic tumour compression on stent response was evaluated using the end of a small rod to load the devices which were either deployed in an excised trachea or tested in an unconfined configuration. Cross-sectional area, rod displacement and the force applied were recorded. These test methods provide practical information in relation to how different stent designs affect the natural collapse of the airway and how stents resist local loading. However, the use of excised tissue makes repeatability an issue, and stent loading in a freely expanded condition does not adequately represent the *in-vivo* condition where the stent is constrained by the airway.

Animal studies on tracheobronchial stents are more common in the literature (Hugo Marquette et al. 1995; Bolliger et al. 1999; Korpela et al. 1999; Puma et al. 2000; Hwang et al. 2001; Serrano et al. 2016). The animal models considered for stenting include sheep (Puma et al. 2000), dogs (Hwang et al. 2001), rabbits (Korpela et al. 1998; Korpela et al. 1999; Serrano et al. 2016) and, piglets and mini-pigs (Hugo Marquette et al. 1995; Bolliger et al. 1999). The effects of implanting tracheobronchial stents in healthy animals was investigated by Puma et al. (2000), Hwang et al. (2001) and Serrano et al. (2016), while Korpela et al. (1999), Bolliger et al. (1999) and Hugo Marquette et al. (1995) deployed stents in animals with surgically created stenoses. These studies provide detailed insight into how different stent designs operate in *in-vivo* conditions, reporting complications such as migration, secretion retention, granulation formation and airway distension. However, repeatability and cost are significant issues with such testing. In addition, quantitative comparisons of stent performance is difficult to obtain from such analyses. Computational modelling provides another route to quantitatively investigate the stent implant under *in-vitro* and *in-vivo* conditions.

1.5 Computational Modelling of Stent Structures

Computational modelling has become an indispensable tool within the biomedical field. It is commonly used to improve device design, and is a basic requirement of the FDA to demonstrate stent safety and effectiveness (Food and Drug Administration

2010). Computational analyses can also be utilised in a clinical environment to aid in providing improved treatment. A common example of this in relation to respiratory applications is the tracking of tumour motion during radiotherapy treatment for lung cancer. In this section an overview of *in-vitro* and *in-vivo* stent modelling, and respiratory motion modelling described in the literature is provided.

1.5.1 Stent Mechanical Performance

For many years finite element modelling has been used to assess and enhance stent mechanical performance. Numerous publications exist in the literature on various important aspects of stent design (Rebelo and Perry 2000; McGarry et al. 2004; Donnelly et al. 2007; García et al. 2012; Grogan et al. 2012; Conway et al. 2012; Nematzadeh and Sadrnezhad 2012; Azaouzi et al. 2013; Meoli et al. 2014; Ghriallais and Bruzzi 2014; Gökgöl et al. 2015). Though, primarily focused on cardiovascular and endovascular stenting applications, many of these studies cover topics that can be directly applied to self-expanding tracheobronchial stenting applications, such as the effects of varying strut dimensions (García et al. 2012), appropriate simulation conditions for accurately capturing radial force (Ghriallais and Bruzzi 2014), and the effects of stent oversizing (Gökgöl et al. 2015).

One of the first finite element studies on nitinol stent mechanics was performed by Gong et al. (2004). In this study constitutive models developed to represent nitinol's superelastic behaviour were shown to be capable of suitably capturing the mechanical performance of a self-expanding nitinol stent under radial force and crush loading conditions. More recently, García et al. (2012) examined the effect that variations in strut dimensions and stent diameter can have on stent radial force. Findings of the study showed that strut width has a greater influence on stent reaction force than strut thickness, and demonstrated how a stent with variable radial force (along its length) could potentially be employed to limit tissue damage outside of stenosed regions. A study by Ní Ghriallais and Bruzzi (2012) investigated suitable modelling techniques for evaluating radial force accuracy. The choice of boundary conditions and other modelling assumptions was shown to effect stent radial force, highlighting in particular that entire stent lengths were required to negate end effects. The impact of stent oversizing in arteries was studied by Gökgöl

et al. (2015), where larger oversizing was found to negatively affect stent fatigue life, while securing only a minimal increase in lumen gain.

Abdominal aortic aneurism (AAA) stent grafts are typically larger than airway stents in both diameter and length, though the effect the graft material has on stent mechanical performance would be expected to be similar. One of the first analyses on stent grafts was performed by Kleinstreuer et al. (2008), where it was shown that different graft materials can affect stent fatigue life differently. De Bock et al. (2013) experimentally tested and computationally modelled various stent grafts, and showed that the inclusion of the graft material was necessary for accurately modelling stent interactions. A more in depth discussion on covered stent modelling is provided in Chapter 3.

With regards to tracheobronchial stent modelling, to the authors knowledge there has been no study directly examining their mechanical performance. However, a wealth of studies have evaluated the effect of stenting on local airway mechanics from a biomechanical aspect (Perez del Palomar et al. 2010; Trabelsi et al. 2011; Malvè et al. 2011d; Malvè et al. 2014; Trabelsi et al. 2015; Chaure et al. 2016). Stent material properties in these studies are considered linear-elastic, even for materials like nitinol that exhibit complex non-linear behaviours (Malvè et al. 2011c; Malvè et al. 2014; Chaure et al. 2016). Furthermore, stent deployment is often not considered (Malvè et al. 2011a; Malvè et al. 2011c; Malvè et al. 2014), or modelled using a radial expansion boundary condition that rigidly stiffens the stent when deployed (Perez del Palomar et al. 2010; Trabelsi et al. 2011; Chaure et al. 2016). Stent geometrical representations have also been simplified, particularly for braided or warp knitted stents (Malvè et al. 2011c; Chaure et al. 2016). Many of the simplifications performed in these analyses are due to the complexities associated with fluid structure interaction (FSI) modelling.

1.5.2 Airway Analyses

One of the first computational studies to evaluate the effect of tracheobronchial stenting on local respiratory mechanics was performed by Malvè et al. (2010). While the main focus of the study was on accurately capturing radial deformation of the

trachea during normal breathing and coughing, the effects of a “virtual” stent were also considered. Using CT images from a 70 year old healthy man a tracheal geometry was developed that incorporated cartilage c-shaped rings and connective smooth muscle components, two of the primary structural constituents of the trachea. Tissue material properties were obtained from tensile testing of human samples obtained at autopsy. The cartilage properties were modelled using an isotropic Neo-Hookean constitutive model, while the smooth muscle was described using an anisotropic Holzapfel constitutive model which considered the contributions of two orthogonal fibre families. A FSI model was used to model the interaction between the tracheal tissue and air flow for normal breathing and coughing. Through this analysis realistic physiological radial deformation which qualitatively captured the collapsibility of the airway was obtained. The effects of stent introduction were then evaluated by deforming part of the trachea to conform to a cylindrical surface, which represented a “virtual” silicone Dumon stent. The “virtual” stent was assigned linear-elastic properties with a Young’s modulus of 1 MPa, and the FSI analysis for normal breathing and coughing was repeated. Results showed that the stiff stent reduced the velocity of air exiting the airway by preventing muscular membrane collapse, which results in a reduction of cough efficiency.

Malvè et al. (2011c) went on to compare the stress and deformation induced for normal breathing and mechanical ventilation in an unstented trachea. Using a similar approach to their previous work, it was shown that mechanical ventilation affected the normal physiological deformation of the trachea by not inducing tracheal collapse. This was attributed to the fact that in mechanical ventilation only positive pressure is applied to induce flow, while in normal ventilation positive and negative pressure swings are present. While the maximum deformations induced by the two loading conditions were shown to be similar, the stresses produced by the mechanical ventilation condition were over twice that of normal breathing.

The effects of stenting the trachea with two different stent designs were considered in Malvè et al. (2011b). A silicone Dumon and nitinol Ultraflex stent design were compared. The Dumon stent was modelled as a 2 mm thick cylinder, and the Ultraflex was modelled with a simplified repeating pattern with a 0.25 mm thickness. Stented

assemblies were obtained by radially expanding stent surfaces into a tracheal geometry using displacement boundary conditions. A fluid mesh was then introduced to the cavity and a FSI analysis was performed on the stented geometry from a stress-free configuration. Linear-elastic properties were assumed for both nitinol and silicone, and a perfect adhesion was assumed between the stents and tissue surface. As before, the stents were shown to affect the natural deformation of the airway, though the Ultraflex stent allowed more deformation than the Dumon. To examine the likelihood of stent migration the ratio of nodal axial force to radial force was compared, where areas with higher axial force were considered to have a pre-disposition to migrate. It was shown that when using this comparison the Dumon stent may have a higher tendency to migrate due to over 50% of the surface having a greater axial force.

A FSI comparison of a healthy and stenotic trachea was performed in Malvè et al. (2011d) using geometry obtained from a healthy and a diseased subject. The stenosis was modelled using a hyperelastic representation with properties twice as stiff as the muscular membrane. The stiff stenosis was found to reduce tracheal deflections and induce a significant pressure drop. The influence of stenting on a stenotic trachea was later explored (Malvè et al. 2011a). Diseased tracheal geometries pre and post stenting were obtained from CT. The Dumon stent used in the stenting procedure was modelled with a perfect adhesion to the tracheal wall, with the analysis initiating with the stent in the expanded condition. The stenosis reduced the airflow, again inducing a large drop in pressure, while the stented geometry exhibited more normal physiologic pressures. As in previous studies, the stent stiffened the tissue and reduced tracheal deflections. High stresses at the stent ends were detected during simulated respiration which were taken as an indication of possible future granulation formation. An interesting finding of the study was that local flow recirculation occurred at the stent ends which was postulated as a possible cause for the formation of mucous plugs.

The influence of stent shape on flow recirculation was further investigated in a follow-up study (Malvè et al. 2012). The ends of a Dumon stent which are normally perpendicular to the cylindrical surface were altered to have a slope of 45°, 60°, or a

parabolic transition and their corresponding impact on recirculation was inspected. All alterations were found to improve the local flow without affecting tracheal stresses, with the parabolic transition having the most profound effect.

A final study by Malvè et al. (2014) simulated Zilver Flex stent (Cook Medical) implantation in a healthy rabbit trachea. Tracheal geometries were obtained from CT taken before and after stent implantation, and the cartilage rings and muscular membrane were visualised as previously described. Rabbit material properties and pressure distributions were also attained. Cartilage and muscle were both modelled as isotropic and fit to a Demiray strain energy density function. The stent geometry was obtained directly from the CT, and assumed to be in perfect adhesion with the tissue. The nitinol properties of the laser-cut stent were assumed linear-elastic, with a Young's modulus corresponding to nitinol's stiffer austenitic phase (40 GPa). Normal breathing was simulated in both the unstented and stented trachea models using FSI analysis, and results were visually compared to stented animals. As before, only radial deformation was considered. High stresses throughout the stent implantation site were shown to correlate with granulation formation and tissue reactivity experimentally. Low wall shear stresses (WSS) were also identified in these areas. Low values of WSS have previously been proposed as having a role in tissue inflammation in cardiovascular applications (LaDisa et al. 2005; Balossino et al. 2008; Morlacchi et al. 2011).

The influence of tracheal stenting on swallowing was investigated by Pérez del Palomar et al. (2010) using the finite element method. A tracheal model from a healthy man was used to create a tracheal computational model geometry which contained cartilage ring and muscle membrane representations. Material properties were obtained from experiments previously performed by the group (Trabelsi et al. 2010). A Holzapfel constitutive model was used to model the muscle membrane and a Neo-Hookean constitutive model was used to represent cartilaginous properties. A mesh adaptation algorithm was utilised to deform the obtained tracheal geometry to fit the tracheas of two patients before stent implantation. The swallowing motion of each patient before and after stent implantation was recorded by tracking the thyroid cartilage motion using fluoroscopy. Stent implantation was simulated by

radially deforming a cylindrical surface representing a Dumon stent to a diameter slightly larger than the trachea to capture the stress in the tissue from stent expansion. This method rigidly stiffens the stent. A coefficient of friction of 0.1 was used between the stent and tissue surfaces. To simulate the swallowing motion displacement boundary condition were applied to the top surface of the trachea, while the distal end of the trachea was fixed. The recorded displacements before implantation were applied to the unstented tracheal geometries, and the stented measurements were applied to the stented geometries. The stress for one patient model almost tripled after stent implantation and their ability to swallow was predicted to be reduced by around 28%. The high stress was associated with granulation tissue formation at the proximal end of the stent which was observed experimentally. The stenting procedure simulation had little predicted effect on the second patient, which also correlated clinically, as the second patient did not require further intervention after stent implantation.

This work on the influence of stenting on swallowing was further investigated by Trabelsi et al. (2011). A reference geometry was obtained from the CT of a healthy man, and cartilage, smooth muscle and annular ligaments were all modelled. Material properties were obtained from the same study as before (Trabelsi et al. 2010). In this instance an analysis undertaken showed that a Neo-Hookean constitutive model was a suitable substitute for the more complex Holzapfel constitutive model previously used for modelling smooth muscle, showing very little effect on predicted stresses. Cartilage was modelled using a linear-elastic representation and the annular ligaments were modelled with a Neo-Hookean constitutive model. Again, stent implantation simulations for two patients were considered. However in both cases the geometry from a healthy patient was used for modelling and only the deformation applied to the tracheal surface was varied depending on patient-specific displacement data. Stent implantation was simulated as before. Results showed a significant increase in stress for one patient model at the proximal stent end, while the second patient model presented little change in maximum stress, even with the stresses associated with stent expansion. Another

finding of the study was that the simulations predict that patients can lose their natural ability to swallow by over 18.9% after stent implantation.

Modelling of the implantation of a Montgomery T-tube and its impact on swallowing and mechanical ventilation was subsequently investigated (Trabelsi et al. 2015). A healthy tracheal geometry was attained for computational simulation as earlier. A circular perforation with an 8 mm diameter was introduced to the tracheal geometry (below the second cartilaginous ring) to represent the tracheotomy required to insert the external limb of the Montgomery T-tube stent. The stent was modelled as two perpendicular cylindrical tubes which were radially deformed to their clinical diameters to capture the stress in the tissue from expansion. A coefficient of friction of 0.5 was used in this analysis. The swallowing motion was then modelled by applying a force to the superior surface of the trachea corresponding to values presented in previous work (Trabelsi et al. 2011). Results from the stented trachea simulation were compared to results for the corresponding healthy trachea previously reported. The simulations predicted that the patient model was found to lose 75% and 63% of his natural motion in the z and y directions respectively. The maximal principal stress was found to be three times higher after stenting, indicating the possible formation of granulation tissue. A CFD (computational fluid dynamics) analysis evaluating mechanical ventilation of the stented geometry was performed in addition. The boundary conditions associated with a FSI analysis were considered too complex to implement in the analysis. The CFD results indicated that due to the high pressures associated with mechanical ventilation the trachea may be in a constant state of high stress.

More recently, Chaure et al. (2016) modelled the implantation of two stent types in a rabbit model using FSI analyses. Zilver Flex and WallStent (Boston Scientific) stents were experimentally implanted in a number of rabbits. The tracheal geometry was idealised as a cylindrical tube with cartilaginous and muscular membrane regions measured from a dissected sample. Tissue properties were obtained from tensile testing and fit to the Demiray strain energy density function. The laser-cut Zilver Flex geometry was attained from CT of an implanted stent. The WallStent (a braided stainless steel stent) geometry was approximated, with contact between individual

wires neglected and cross-over points modelled as solid hinges. A perfect adhesion was assumed between the stent surfaces and the tissue surface, and stent material properties were represented using linear-elastic representations. FSI of normal breathing for the unstented and stented conditions was evaluated using conditions determined from spirometry performed on a rabbit. Only tracheal motion in the radial direction was considered. Stent deployment was simulated using a radial displacement boundary condition that allows tissue stresses to be obtained, but results in rigid stiffening of the stent. Results of the analyses were compared with experimental findings from the stent implantations. Inflammation, epithelial thickening and granulation were experimentally reported, and compared to computational results of maximum principal stress and WSS. High levels of inflammation, epithelial thickening and granulation tissue were found for the WallStent, while lower levels were found for the Zilver Flex stent. This corresponded well with the computational stress prediction with the WallStent producing higher stresses than the Zilver Flex stent. Low values of WSS were obtained for both stented geometries along the stent edges, where higher WSS was predicted for the stent-free geometry. The study concluded that the computational results suggest that the stress induced from stent deployment may have a greater influence on tissue response than fluid dynamics.

To summarise, much work has been performed on the computational modelling of tracheal stenting analyses. Complex anatomical geometries are often employed that consider the heterogeneity of the trachea, with cartilage and smooth muscle representations. Isotropic and anisotropic properties are commonly employed. While complex FSI models considering normal breathing, coughing and mechanical ventilation have been employed (Malvè et al. 2011c; Malvè et al. 2014; Chaure et al. 2016), these do not consider the out-of-plane motions associated with respiratory motion. Although, work performed in some studies did consider the out-of-plane motion associated with swallowing (Perez del Palomar et al. 2010; Trabelsi et al. 2011; Trabelsi et al. 2015). In all the presented works, the stents and associated interactions were significantly simplified. Often, the stresses related to the stenting procedure in both the stent and the tissue were not considered. Or, the stent was

modelled as a rigid structure which was unable to deform under physiological loading due to the enforcement of displacement boundary conditions. The interaction between the stent and tissue was often simplified by assuming a perfect adhesion between the two structures, though contact was considered in some instances. In the presented literature, stent properties are modelled using linear-elastic relations which would fail to capture the complex behaviour of the stent, and its effects on airway physiology. Finally, stent analyses below the trachea have not been considered.

1.5.3 Respiratory Motion Modelling

Lung motion modelling is used to describe the motion of the organ or structures within the organ for a motion of interest, such as a respiratory cycle (McClelland et al. 2013). Typical clinical applications of lung motion modelling include reducing motion-induced artefacts to help improve image quality for diagnosis and treatment planning (Lamare et al. 2007; Wolthaus et al. 2008), and simulating lung motion for tumour motion prediction for more efficient radiotherapy treatment (Sharp et al. 2004; Seppenwoolde et al. 2007). Lung motion has been measured in a large variety of ways, including 4D CT, ultrasound, fluoroscopy, optical sensors and 4D MRI (Davies et al. 1994; Kubo and Hill 1996; Vedam et al. 2001; Plathow et al. 2004; Mageras et al. 2004). With CT being the preferred modality in recent years.

The two primary methods for lung CT acquisition is from static breath hold and dynamic CT (4D CT) scans during normal breathing (Werner et al. 2009; Tawhai et al. 2009). For static breath hold acquisition, the lungs are often imaged at Total Lung Capacity (TLC) and Functional Residual Capacity (FRC). Static scans are usually of high quality as motion-induced artefacts are less of a problem. 4D CT scans are obtained over the course of several breaths (Castillo et al. 2010). An external monitor is used to record breathing phase so that corresponding phases can be reconstructed, or average motion can be attained (Vedam et al. 2003; Pan et al. 2004). Any time point can be reconstructed, but typically end-inspiration (EI) and end-exhalation (EE) are most often used. Dynamic images tend to be lower quality than static images due to the combination of lung motion and the grouping of images from different breaths.

The principal methods used to model lung motion are image registration and biomechanical modelling. Due to the highly deformable nature of the lungs, non-rigid registration procedures known as deformable image registrations (DIR) are used. DIR algorithms map lung motion between separate images by matching geometric features or pixel intensity (Crum et al. 2004; Tustison et al. 2011). This involves finding a transformation that minimises the difference between the two images once deformed by the transformation (Bel-Brunon et al. 2014). Many different DIR algorithms have been proposed, and their advantages and disadvantages are discussed in greater detail in Brock (2010) and Murphy et al. (2011). However, the greatest universal disadvantage of DIR algorithms is that they neglect the physical properties and physiological processes associated with the lung as motion is extracted directly from the image data (Klinder et al. 2008; Werner et al. 2009). DIR methods are then more suited to applications where physiological changes in respiratory mechanics are not critical for the success of the analysis, such as the inclusion of airway deformation during CFD analysis (Yin et al. 2013; Ibrahim et al. 2015).

Biomechanical modelling uses the laws of physics to take account of the variability in respiratory motion (Fuerst et al. 2015). Typically, an anatomical model is created, which is used to simulate lung motion during respiration using the finite element method. Changes in input parameters can then be used to predict lung deformation under differing conditions. It has previously been applied to applications such as determining the effect gravity has on respiratory physiology (West and Matthews 1972; Tawhai et al. 2009), and tumour tracking and prediction of tumour deformation (Al-Mayah et al. 2008; Werner et al. 2009). Two common strategies utilised to realise lung motion are surface projection and pressure loading. For both methods the lung geometry at a particular phase is obtained, typically as a continuous and homogenous solid. Then for the surface projection method the lung surface is projected onto the corresponding surface at another respiratory phase, and respiration motion is simulated through contact constraints (Al-Mayah et al. 2008; Tawhai et al. 2009; Al-Mayah et al. 2010). While for pressure loading, the solid lung geometry is expanded by applying a pressure directly to the lung surface, with

the overall deformation being limited to a corresponding surface phase (Villard et al. 2005; Werner et al. 2009; Eom et al. 2010).

While biomechanical lung models were first introduced in the 1970's (Mead et al. 1970; West and Matthews 1972), it wasn't until more recently that studies began evaluating realistic lung geometries through the use of CT (Zhang et al. 2004; Villard et al. 2005). To simplify the complex lung geometry the lung was considered a homogenous and isotropic solid, and the airways, vascular system and fissures between lobes were neglected. The solid lungs were expanded from End Exhalation (EE) to End Inhalation (EI) using uniform pressure applied to the EE surface, and the final volume was limited by contact with a shell representation of the EI lung. Both studies considered the lung to behave linear-elastically. Villard et al. (2005) evaluated the influence of varying Young's modulus and Poisson's ratio, and found that while Young's modulus only affected the pressure required to suitably inflate the lung, Poisson's ratio affected shear stresses and so should not be chosen arbitrarily.

Tawhai et al. (2006) investigated soft-tissue deformation and ventilation in the ovine lung. CT was obtained at six static pressures between 0 and 25 cmH₂O in 5 cmH₂O increments. The lung was modelled as homogenous and isotropic, and separate lung lobes were not considered. To account for the *in-vivo* stresses present in imaging data due to intrapleural pressure a uniform scaling of the 25 cmH₂O (or TLC) volume was performed to around 25% of the initial volume. Lung motion was modelled by using identifiable landmarks at the various pressures to displace the nodes on the outer surface. However, this method is not ideal as inaccurate tracking can result in errors in lung deformation. Airway tree motion was determined in the model by tracking the deformation of nodes corresponding to airway branching points and produced an RMS error of around 4 mm. Tawhai et al. (2009) performed further biomechanical lung modelling on human lungs. *In-vivo* stresses were accounted for by implementing a uniform scaling of a homogenous lung volume from TLC to 50% of FRC. This time lung inflation was achieved using a surface projection method, where the outer surface of the lung was constrained to remain in frictionless contact with a surface representing the deforming pleural cavity. Pleural cavity deformation was determined by projecting the cavity surface at TLC onto the surface at FRC.

Landmark error was not considered. The study evaluated the effect of position on density gradient, and showed that the magnitude in the supine position was almost twice that of the prone.

Al-Mayah et al. (2008) also used a surface projection approach. In this case, the initial lung position was taken at EI and the surfaces between the left and right lung cavities were used to deform the lungs to EE using either a frictionless sliding contact condition or a no-contact condition. The deformation was controlled by projecting the cavity surface at EI onto the EE lung surface, hence compressing the lung. Linear-elastic and hyperelastic material properties were evaluated, with experimental test data (Zeng et al. 1987) fit to a Marlow hyperelastic constitutive model. Hyperelastic properties with contact were seen to dramatically improve results of the non-contact models. However, a linear-elastic contact model was not evaluated. Al-Mayah et al. (2009) went on to evaluate the effect of Poisson's ratio and the coefficient of friction for sliding contact, proposing a Poisson's ratio of 0.4 and frictionless contact as optimum parameters. Further enhancements were performed in a later study which investigated the effect of including the bronchial tree on lung deformation (Al-Mayah et al. 2010). The airways were discretised using a shell element representation, and only the volume outside of the bronchial tree was meshed. A variety of linear-elastic material representations with Young's moduli between 0.01 and 18 MPa were considered for the bronchial tree. Global model accuracy was found to not be affected by the inclusion of the bronchial tree. However, it was shown to have some effect at a local level. Al-Mayah concluded that the assumption of lung homogeneity was adequate. A final study explored model optimisation with respect to element type and material constitutive representation (Al-Mayah et al. 2011). Four model variations were investigated, consisting of linear or quadrilateral tetrahedral elements and linear-elastic or hyperelastic material properties with a homogenous lung representation. An average landmark error of around 2.8 mm was obtained for all combinations, resulting in the proposal that linear material properties and linear element representations are favoured.

Lung motion was again modelled using a uniform pressure applied to the outer surface of a homogenous lung volume by Werner et al. (2009). The lung tissue was

assumed homogenous and Young's modulus and Poisson's ratio were varied between 0.1 and 7.8 kPa and 0.2 and 0.45 respectively. Results showed that variation of either of the elastic parameters had little effect on lung motion fields. Here it was suggested that this may be due to the assumption of a homogenous lung volume and the gross motion of the lung being limited to a fixed geometry. An average landmark error of 3.3 mm was observed for an average landmark motion of 6.6 mm.

Uniform pressure applied to the exterior of a homogenous, hyperelastic lung volume was used by Eom et al. (2010). However, unlike other similar models pressure was determined based on the instantaneous lung volume described by PV curves. Lung motion was modelled for both inspiration and expiration allowing lung hysteresis to be captured. Average landmark error was found to be in the region of 3.4 mm between EE and EI. Interestingly, landmark error at breathing phases between EE and EI and between EI and EE was not shown to be dependent on degree of lung expansion.

More recently, Fuerst et al. (2015) proposed a model to predict lung motion without the need for a limiting geometry at EI by applying patient-specific thoracic pressures. The lung, thorax and diaphragm are obtained and divided into a number of different pressure zones to allow for non-uniform pressure application. Lung motion is realised through a collision model which ensures the lung surface remains within a set distance of the pressurised zones. An iterative process is used to determine the thoracic pressure needed to expand the assembly to the required position. After each iteration landmark position is compared at EI and pressures are adjusted to improve the fit. A homogenous and isotropic lung model is used together with a linear-elastic material representation. Landmark error over the entire respiratory cycle was shown to be around 3.4 mm.

In summary, lung motion modelling can be performed in a variety of ways. CT is the most common method for geometry acquisition. While deformable image registration is commonly used, the rigid deformations required for its use make it unsuitable for stenting analyses. Biomechanical lung models have been proposed using a wide selection of inputs. The lung is typically modelled as a homogenous and

isotropic solid with a linear-elastic material representation. Material properties can vary within the evaluated ranges without overly-affecting landmark error which is usually in the order of 3 mm. The *in-vivo* stresses present in image data are generally not considered, though uniform scaling of the lung volume has been considered. The bronchial tree has also rarely been considered in previous analyses, having been shown to have little effect on global lung deformation. No modelling of lung respiratory motion for stenting applications has been studied.

1.6 Thesis Structure

This thesis is structured as an “Article-Based” thesis with three published journal papers (Chapters 2-4) and one journal paper under review (Chapter 5). Chapters 2-4 are reproduced with minimal modification to the published subject matter. In each technical chapter (Chapters 2-5) a focused analysis of relevant literature is also provided. The chapters within the thesis are summarised below.

Please note that the details on constitutive models utilised in Chapters 2-5 are discussed in Appendix 1.

Chapter 1:

The present chapter outlined the background and literature relevant to tracheobronchial stenting. This included details on: the lung’s structure and its functioning, tracheobronchial stent applications and complications, stent properties and, computational modelling of stents and lung motion. In each technical chapter (chapters 2-5) a focused analysis of relevant literature is also provided.

Chapter 2: *From Article by McGrath et al. entitled “Nitinol Stent Design - Understanding Axial Buckling”, Published in the Journal of the Mechanical Behavior of Biomedical Materials, 2014.*

The superelastic properties of nitinol allow self-expanding stents to be crimped over large diameter ranges without plastic deformation, but its nonlinear properties can contribute towards stent buckling. In this study the axial buckling of a prototype tracheobronchial stent is investigated. It is shown that the transitional plateau region of the nitinol stress-strain curve can have a significant effect on stent stability, and

by reducing the amount of transitional material within the stent hinges the stent stability can be considerably improved.

Chapter 3: *From Article by McGrath et al. entitled "Evaluation of Cover Effects on Bare Stent Mechanical Response", Published in the Journal of the Mechanical Behavior of Biomedical Materials, 2016.*

Covered tracheobronchial stents are used to prevent tumour growth from re-occluding the airways. In this study a combination of experimental and computational methods are used to present the mechanical effects that adhered covers can have on stent performance. It is shown that an adhered cover can significantly alter mechanical performance, and that the loading configuration that a stent is about to be subjected to should be considered before stent implantation.

Chapter 4: *From Article by McGrath et al. entitled "An ovine in-vivo framework for tracheobronchial stent analysis", Published in Biomechanics and Modeling in Mechanobiology, 2017*

This study develops a computational framework to evaluate tracheobronchial stent designs in an ovine *in-vivo* model. Results of the analysis indicate that three of the major complications associated with tracheobronchial stents can potentially be analysed with this framework, which can be readily applied to the human case. Airway deformation caused by lung motion is shown to have a significant effect on stent mechanical performance, including implications for stent migration, granulation formation and stent fracture.

Chapter 5: *From Article by McGrath et al. entitled "Evaluating the interaction of a tracheobronchial stent in an ovine in-vivo model", Submitted to Biomechanics and Modeling in Mechanobiology, 2017*

This study evaluates the effect of stent interaction on granulation formation in an ovine *in-vivo* model. Results of the analysis indicate a correlation between contact pressure variation and granulation tissue formation, where the change in contact pressure provides a quantitative assessment of tissue irritation due to stent interaction.

Chapter 6:

The primary conclusions of the presented work are summarised and recommendations for future work are discussed.

A.1 Appendix 1

A.1.1 Constitutive Models

In Chapters 2, 3, 4 and 5 of this thesis simulations are described that required the solving of continuum mechanics problems using the commercial finite element solver Abaqus (DS SIMULIA, USA). This section outlines the constitutive formulations implemented in Abaqus which are used to describe the mechanical behaviour of the polymeric stent cover materials, the lung tissues and the nitinol stent material utilised. Additional information on the theoretical framework can be found in Malvern (Malvern 1969), Belytschko et al. (Belytschko et al. 2000), and the Abaqus Theory Manual (DS SIMULIA, USA).

A.1.1.1 Hyperelastic Constitutive Models

Typically hyperelastic materials display a non-linear stress-strain relationship that cannot be suitably captured utilising a linear stress-strain response. Instead, hyperelastic material behaviour is derived from a strain energy density potential, U , which defines the strain energy stored in the material per unit of reference volume as a function of deformation. The polynomial strain energy potential is given by:

$$U = \sum_{i+j=1}^N C_{ij} (\bar{I}_1 - 3)^i (\bar{I}_2 - 3)^j + \sum_{i=1}^N \frac{1}{D_i} (J^{el} - 1)^{2i} \quad (1.1)$$

where C_{ij} and D_i are material constants, J^{el} is the elastic volume ratio, \bar{I}_1 and \bar{I}_2 are the first and second invariants respectively, and N determines the number of terms in the polynomial. For more information see the Abaqus Theory Manual (DS SIMULIA, USA).

In this thesis, two different polynomial forms were used to model the polymers for the stent cover and the lung tissues. The Neo-Hookean form, which is a reduced order polynomial hyperelastic model is used in this work for modelling the isotropic deformation of the polymers used as part of the stent cover in Chapters 3 and 5:

$$U = C_{10} (\bar{I}_1 - 3) + \frac{1}{D_1} (J^{el} - 1)^2 \quad (1.2)$$

A second order reduced polynomial was used to model the parenchymal and airway tissue in Chapters 4 and 5 as given by

$$U = C_{10}(\bar{I}_1 - 3) + C_{20}(\bar{I}_1 - 3)^2 + \frac{1}{D_1}(J^{el} - 1)^2 + \frac{1}{D_2}(J^{el} - 1)^4 \quad (1.3)$$

A.1.1.2 Nitinol Constitutive Model

Nitinol was modelled in this work using the in-built superelastic user material in Abaqus/Standard (UMAT) and Abaqus/Explicit (VUMAT) based on the constitutive model proposed by Auricchio and Taylor (Auricchio et al. 1997; Auricchio and Taylor 1997). The theory is based on general plasticity, where the change in strain, $\Delta\boldsymbol{\varepsilon}$, is broken into two components, a linear elastic component, $\Delta\boldsymbol{\varepsilon}^{el}$, and a transformational component $\Delta\boldsymbol{\varepsilon}^{tr}$, as described by:

$$\Delta\boldsymbol{\varepsilon} = \Delta\boldsymbol{\varepsilon}^{el} + \Delta\boldsymbol{\varepsilon}^{tr} \quad (1.4)$$

The transformation from austenite to martensite occurs between a range of stresses ($\boldsymbol{\sigma}_{tL}^S$ to $\boldsymbol{\sigma}_{tL}^E$ (Fig. A1.1)) determined by alloy specific characteristics, where the transformation component is defined by:

$$\Delta\boldsymbol{\varepsilon}^{tr} = \alpha\Delta\zeta \frac{\partial F}{\partial \boldsymbol{\sigma}} \quad (1.5)$$

$$F^S \leq F \leq F^E \quad (1.6)$$

where α is a scalar value denoting the upper limit of the martensite detwinning deformation, ζ is the fraction of martensite, and F is the transformation potential. The reverse transformation component follows the same expression but at lower stress levels ($\boldsymbol{\sigma}_{tU}^S$ to $\boldsymbol{\sigma}_{tU}^E$ (Fig. A1.1)). A stress potential law is used to determine the intensity of the transformation:

$$\Delta\zeta = f(\boldsymbol{\sigma}, \zeta) \Delta F \quad (1.7)$$

As there is a small volume change associated with the stress induced martensite transformation, a lower level of stress is needed to generate the transformation in tension than in compression. Similarly, the stress levels at which transformation

occurs can be affected by temperature alterations, which produce a linear change in the required stresses. To account for these effects a linear Drucker-Prager approach is utilised for the transformation potential:

$$F = \sigma_e - p \tan \beta + CT \quad (1.8)$$

where σ_e is the von Mises equivalent stress, p is the pressure stress, β and C are material constants and T is temperature. The material parameters required to model the superelastic behaviour of nitinol in Abaqus are provided in Table A1.1. The specific parameters used to model nitinol in this thesis are given in Chapters 2-5. A more detailed discussion on the constitutive model can be obtained in the studies performed by Auricchio and Taylor et al. (Auricchio et al. 1997; Auricchio and Taylor 1997).

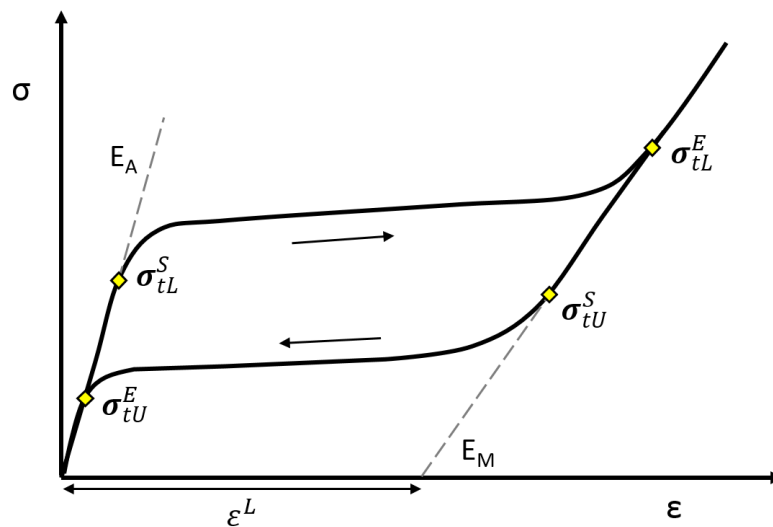


Fig. A1.1: Schematic representation of a nitinol stress-strain curve highlighting points of interest for the inbuilt subroutine. Characters described in Table A1.1.

Table A1.1: Nitinol material properties required for the Abaqus nitinol constitutive model.

Parameter
Austenite Elasticity (E_A)
Austenite Poisson's Ratio (ν_A)
Martensite Elasticity (E_M)
Martensite Poisson's Ratio (ν_M)
Transformation Strain (ε^L)
Start of Transformation Loading (σ_{tL}^S)
End of Transformation Loading (σ_{tL}^E)
Reference Temperature (T_0)
Start of Transformation Unloading (σ_{tU}^S)
End of Transformation Unloading (σ_{tU}^E)
Start of Transformation Stress During Loading in Compression (σ_{CL}^S)
Volumetric Transformation Strain (ε_V^L)

References

- Abdel-Rahman N, Kramer MR, Saute M, Raviv Y, Fruchter O (2014) Metallic stents for airway complications after lung transplantation: long-term follow-up. *Eur J Cardiothorac Surg* 45:854–8. doi: 10.1093/ejcts/ezt458
- Aggarwal A, Dasgupta A, Mehta AC (1999) Metalloptysis expulsion of wire stent fragments. *Chest* 115:1484–1485. doi: 10.1378/chest.115.5.1484-a
- Al-Mayah A, Moseley J, Brock KK (2008) Contact surface and material nonlinearity modeling of human lungs. *Phys Med Biol* 53:305–17. doi: 10.1088/0031-9155/53/1/022
- Al-Mayah A, Moseley J, Velec M, Brock K (2011) Toward efficient biomechanical-based deformable image registration of lungs for image-guided radiotherapy. *Phys Med Biol* 56:4701–13. doi: 10.1088/0031-9155/56/15/005
- Al-Mayah A, Moseley J, Velec M, Brock KK (2009) Sliding characteristic and material compressibility of human lung: Parametric study and verification. *Med Phys* 36:4625–4633. doi: 10.1118/1.3218761
- Al-Mayah A, Moseley J, Velec M, Hunter S, Brock K (2010) Deformable image registration of heterogeneous human lung incorporating the bronchial tree. *Med Phys* 37:4560–4571. doi: 10.1118/1.3471020
- Allen JE, Bischof RJ, Sucie Chang HY, Hirota JA, Hirst SJ, Inman MD, Mitzner W, Sutherland TE (2009) Animal models of airway inflammation and airway smooth muscle remodelling in asthma. *Pulm Pharmacol Ther* 22:455–465. doi: 10.1016/j.pupt.2009.04.001
- Auricchio F, Taylor R, Lubliner J (1997) Shape-memory alloys: macromodelling and numerical simulations of the superelastic behavior. *Comput methods Appl ...* 146.3:281–312.
- Auricchio F, Taylor RL (1997) Shape-memory alloys: modelling and numerical simulations of the finite-strain superelastic behavior. *Comput Methods Appl Mech Eng* 143:175–194. doi: 10.1016/S0045-7825(96)01147-4
- Azaouzi M, Lebaal N, Makradi a., Belouettar S (2013) Optimization based simulation of self-expanding Nitinol stent. *Mater Des* 50:917–928. doi: 10.1016/j.matdes.2013.03.012
- Bagnoli P, Acocella F, Di Giancamillo M, Fumero R, Costantino ML (2013) Finite element analysis of the mechanical behavior of preterm lamb tracheal bifurcation during total liquid ventilation. *J Biomech* 46:462–9. doi: 10.1016/j.jbiomech.2012.10.036
- Bähr A, Wolf E (2012) Domestic animal models for biomedical research. *Reprod Domest Anim* 47:59–71. doi: 10.1111/j.1439-0531.2012.02056.x
- Balossino R, Gervaso F, Migliavacca F, Dubini G (2008) Effects of different stent designs on local hemodynamics in stented arteries. *J Biomech* 41:1053–61. doi: 10.1016/j.jbiomech.2007.12.005
- Bates JHT (2009) Lung mechanics. An inverse modeling approach. Cambridge University Press, New York
- Bates JHT, Maksym GN, Navajas D, Suki B (1994) Lung tissue rheology and 1/f noise. *Ann Biomed Eng* 22:674–681. doi: 10.1007/BF02368292
- Bel-Brunon A, Kehl S, Martin C, Uhlig S, Wall WA (2014) Numerical identification method for

the non-linear viscoelastic compressible behavior of soft tissue using uniaxial tensile tests and image registration – Application to rat lung parenchyma. *J Mech Behav Biomed Mater* 29:360–374. doi: 10.1016/j.jmbbm.2013.09.018

Belytschko T, Liu W, Moran B (2000) *Nonlinear finite elements for continua and structures*. 2000. Chichester, New York, John Wiley 16:650.

Bolliger CT, Probst R, Tschopp K, Soler M, Perruchoud AP (1993) Silicone stents in the management of inoperable tracheobronchial stenoses: Indications and limitations. *Chest* 104:1653–1659. doi: 10.1378/chest.104.6.1653

Bolliger CT, Sutedja TG, Strausz J, Freitag L (2006) Therapeutic bronchoscopy with immediate effect: laser, electrocautery, argon plasma coagulation and stents. *Eur Respir J* 27:1258–71. doi: 10.1183/09031936.06.00013906

Bolliger CT, Wyser C, Wu X, Hauser R, Studer W, Dalquen P, Perruchoud AP (1999) Evaluation of a new self-expandable silicone stent in an experimental tracheal stenosis. *Chest* 115:496–501. doi: 10.1378/chest.115.2.496

Brock KK (2010) Results of a multi-institution deformable registration accuracy study (MIDRAS). *Int J Radiat Oncol Biol Phys* 76:583–596. doi: 10.1016/j.ijrobp.2009.06.031

Brown MT, Montgomery WW (1996) Microbiology of tracheal granulation tissue associated with silicone airway prosthesis. *Ann Otol Rhinol Laryngol* 105:624–627.

Brown RH, Mitzner W (1998) The myth of maximal airway responsiveness in vivo. *J Appl Physiol* 85:2012–7.

Burningham AR, Wax MK, Andersen PE, Everts EC, Cohen JI (2002) Metallic tracheal stents: complications associated with long-term use in the upper airway. *Ann Otol Rhinol Laryngol* 111:285–90.

Castillo E, Castillo R, Martinez J, Shenoy M, Guerrero T (2010) Four-dimensional deformable image registration using trajectory modeling. *Phys Med Biol* 55:305–27. doi: 10.1088/0031-9155/55/1/018

Chauré J, Serrano C, Fernández-Parra R, Peña E, Lostalé F, De Gregorio MA, Martínez MA, Malvè M (2016) On studying the interaction between different stent models and rabbit tracheal tissue: numerical, endoscopic and histological comparison. *Ann Biomed Eng* 44:368–381. doi: 10.1007/s10439-015-1504-3

Chin CS, Litle V, Yun J, Weiser T, Swanson SJ (2008) Airway stents. *Ann Thorac Surg* 85:S792-6. doi: 10.1016/j.athoracsur.2007.11.051

Chung FT, Chen HC, Chou CL, Yu CT, Kuo CH, Kuo HP, Lin SM (2011) An outcome analysis of self-expandable metallic stents in central airway obstruction: a cohort study. *J Cardiothorac Surg* 6:46. doi: 10.1186/1749-8090-6-46

Chung FT, Lin SM, Chen HC, Chou CL, Yu CT, Liu CY, Wang CH, Lin HC, Huang CD, Kuo HP (2008) Factors leading to tracheobronchial self-expandable metallic stent fracture. *J Thorac Cardiovasc Surg* 136:1328–1335. doi: 10.1016/j.jtcvs.2008.05.039

Codd SL, Lambert RK, Alley MR, Pack RJ (1994) Tensile stiffness of ovine tracheal wall. *J Appl Physiol* 76:2627–2635.

- Colt HG, Janssen JP, Dumon JF, Al E (1992) Endoscopic management of bronchial stenosis after lung transplantation. *Chest* 102:10–16. doi: <http://dx.doi.org/10.1378/chest.102.1.10>
- Conway C, Sharif F, McGarry JP, McHugh PE (2012) A computational test-bed to assess coronary stent implantation mechanics using a population-specific approach. *Cardiovasc Eng Technol* 3:374–387. doi: [10.1007/s13239-012-0104-8](https://doi.org/10.1007/s13239-012-0104-8)
- Croteau JR, Cook CD (1961) Volume-pressure and length-tension measurements in human tracheal and bronchial segments. *J Appl Physiol* 16:170–172.
- Crum WR, Hartkens T, Hill DLG (2004) Non-rigid image registration: theory and practice. *Br J Radiol* 77:S140–S153. doi: [10.1259/bjr/25329214](https://doi.org/10.1259/bjr/25329214)
- Davies SC, Hill AL, Holmes RB, Halliwell M, Jackson PC (1994) Ultrasound quantitation of respiratory organ motion in the upper abdomen. *Br J Radiol* 67:1096–1102. doi: [10.1259/0007-1285-67-803-1096](https://doi.org/10.1259/0007-1285-67-803-1096)
- De Bock S, Iannaccone F, De Beule M, Van Loo D, Vermassen F, Verhegghe B, Segers P (2013) Filling the void: a coalescent numerical and experimental technique to determine aortic stent graft mechanics. *J Biomech* 46:2477–82. doi: [10.1016/j.jbiomech.2013.07.010](https://doi.org/10.1016/j.jbiomech.2013.07.010)
- Dechambre S, Dorzee J, Fastrez J, Hanzen C, Van Houtte P, D’Odémont JP (1998) Bronchial stenosis and sclerosing mediastinitis: An uncommon complication of external thoracic radiotherapy. *Eur Respir J* 11:1188–1190. doi: [10.1183/09031936.98.11051188](https://doi.org/10.1183/09031936.98.11051188)
- Donnelly EW, Bruzzi MS, Connolley T, McHugh PE (2007) Finite element comparison of performance related characteristics of balloon expandable stents. *Comput Methods Biomech Biomed Engin* 10:103–110. doi: [10.1080/10255840601086234](https://doi.org/10.1080/10255840601086234)
- Doolittle AM, Mair EA (2002) Tracheal bronchus: Classification, endoscopic analysis, and airway management. *Otolaryngol - Head Neck Surg* 126:240–243. doi: [10.1067/mhn.2002.122703](https://doi.org/10.1067/mhn.2002.122703)
- Duerig TW, Melton KN, Stoeckel D, Wayman CM (1990) *Engineering Aspects of Shape Memory Alloys*. Butterworth-Heinemann Limited
- Duerig TW, Tolomeo DE, Wholey M (2000) An overview of superelastic stent design. *Minim Invasive Ther Allied Technol* 9:235–46. doi: [10.1080/13645700009169654](https://doi.org/10.1080/13645700009169654)
- Dumon JF (1990) A dedicated tracheobronchial stent. *Chest* 97:328–332. doi: [10.1378/chest.97.2.328](https://doi.org/10.1378/chest.97.2.328)
- Dutau H, Cavailles A, Sakr L, Badier M, Gaubert JY, Boniface S, Doddoli C, Thomas P, Reynaud-Gaubert M (2010) A retrospective study of silicone stent placement for management of anastomotic airway complications in lung transplant recipients: Short- and long-term outcomes. *J Hear Lung Transplant* 29:658–664. doi: [10.1016/j.healun.2009.12.011](https://doi.org/10.1016/j.healun.2009.12.011)
- Dutau H, Musani AI, Laroumagne S, Darwiche K, Freitag L, Astoul P (2015) Biodegradable airway stents - bench to bedside: a comprehensive review. *Respiration* 90:512–521. doi: [10.1159/000442054](https://doi.org/10.1159/000442054)
- Eom J, Xu XG, De S, Shi C (2010) Predictive modeling of lung motion over the entire respiratory cycle using measured pressure-volume data, 4DCT images, and finite-element analysis. *Med Phys* 37:4389. doi: [10.1118/1.3455276](https://doi.org/10.1118/1.3455276)

- Ernst A, Feller-Kopman D, Becker HD, Mehta AC (2004) Central airway obstruction. *Am J Respir Crit Care Med* 169:1278–1297. doi: 10.1164/rccm.200210-1181SO
- Ernst A, Herth FJF (2013) Principles and practice of interventional pulmonology. *Princ Pract Interv Pulmonol* 1–757. doi: 10.1007/978-1-4614-4292-9
- Farhatnia Y, Tan A, Motiwala A, Cousins BG, Seifalian AM (2013) Evolution of covered stents in the contemporary era: clinical application, materials and manufacturing strategies using nanotechnology. *Biotechnol Adv* 31:524–42. doi: 10.1016/j.biotechadv.2012.12.010
- Fiorentino A, Piazza C, Ceretti E (2016) Anti-migration enhanced tracheal stent design, rapid manufacturing and experimental tests. *Rapid Prototyp J* 22:178–188. doi: 10.1108/RPJ-06-2014-0072
- Food and Drug Administration (2005) FDA public health notification: complications from metallic tracheal stents in patients with benign airway disorders. In: Food Drug Adm. <http://www.fda.gov/MedicalDevices/Safety/AlertsandNotices/PublicHealthNotifications/ucm062115.htm>. Accessed 24 Jan 2017
- Food and Drug Administration (2010) Non-clinical engineering tests and recommended labeling for intravascular stents and associated delivery systems.
- Food and Drug Administration (1998) Guidance for the content of premarket notifications for esophageal and tracheal prostheses.
- Fréchette E, Deslauriers J (2006) Surgical anatomy of the bronchial tree and pulmonary artery. *Semin Thorac Cardiovasc Surg* 18:77–84. doi: 10.1053/j.semtcvs.2006.06.002
- Freitag L (2010) Airway stents. In: Strausz J, Bolliger CT (eds) *Interventional Pulmonology*. European Respiratory Society Journals Ltd, Sheffield, pp 190–217
- Freitag L, Eicker K, Donovan TJ, Dimov D (1995) Mechanical properties of airway stents. *J Bronchol* 2:270–278. doi: 10.1097/00128594-199510000-00003
- Freitag L, Eicker R, Linz B, Greschuchna D (1994) Theoretical and experimental basis for the development of a dynamic airway stent. *Eur Respir J* 7:2038–2045. doi: 10.1183/09031936.94.07112038
- Fuerst B, Mansi T, Carnis F, Salzle M, Zhang J, Declerck J, Boettger T, Bayouth J, Navab N, Kamen A (2015) Patient-specific biomechanical model for the prediction of lung motion from 4-D CT images. *IEEE Trans Med Imaging* 34:599–607. doi: 10.1109/TMI.2014.2363611
- Fung Y (1993) *Biomechanics: mechanical properties of living tissues*. Springer Science & Business Media
- Furukawa K, Ishida J, Yamaguchi G, Usuda J, Tsutsui H, Saito M, Konaka C, Kato H (2010) The role of airway stent placement in the management of tracheobronchial stenosis caused by inoperable advanced lung cancer. *Surg Today* 40:315–20. doi: 10.1007/s00595-008-4058-2
- Galluccio G, Lucantoni G, Battistoni P, Paone G, Batzella S, Lucifora V, Iacono R Dello (2009) Interventional endoscopy in the management of benign tracheal stenoses: definitive treatment at long-term follow-up. *Eur J Cardio-thoracic Surg* 35:429–433. doi:

10.1016/j.ejcts.2008.10.041

García A, Peña E, Martínez MA (2012) Influence of geometrical parameters on radial force during self-expanding stent deployment. Application for a variable radial stiffness stent. *J Mech Behav Biomed Mater* 10:166–75. doi: 10.1016/j.jmbbm.2012.02.006

Ghriallais RN, Bruzzi M (2014) Self-expanding stent modelling and radial force accuracy. *Comput Methods Biomech Biomed Engin* 17:318–333. doi: 10.1080/10255842.2012.683427

Gibson GJ, Loddenkemper R, Lundbäck B, Sibille Y (2013) Respiratory health and disease in Europe: the new European Lung White Book. *Eur Respir J* 42:559–563. doi: 10.1183/09031936.00105513

Godoy MCB, Saldana DA, Rao PP, Vlahos I, Naidich DP, Benveniste MF, Erasmus JJ, Marom EM, Ost D (2014) Multidetector CT evaluation of airway stents: what the radiologist should know. *RadioGraphics* 34:1793–1806. doi: 10.1148/rg.347130063

Gökgöl C, Diehm N, Nezami FR, Büchler P (2015) Nitinol stent oversizing in patients undergoing popliteal artery revascularization: a finite element study. *Ann Biomed Eng.* doi: 10.1007/s10439-015-1358-8

Gong X, Pelton A, Duerig TW, Rebelo N, Perry K (2004) Finite element analysis and experimental evaluation of superelastic Nitinol stent. SMST, Society, Menlo Park, CA

Grillo HC, Mathisen DJ, Wain JC (1992) Laryngotracheal resection and reconstruction for subglottic stenosis. *Ann Thorac Surg* 53:54–63. doi: 10.1016/0003-4975(92)90757-U

Grogan J a, Leen SB, McHugh PE (2012) Comparing coronary stent material performance on a common geometric platform through simulated bench testing. *J Mech Behav Biomed Mater* 12:129–38. doi: 10.1016/j.jmbbm.2012.02.013

Gudovsky LM, Koroleva NS, Biryukov YB, Chernousov AF, Perelman MI (1993) Tracheoesophageal fistulas. *Ann Thorac Surg* 55:868–875. doi: 10.1016/0003-4975(93)90108-T

Guibert N, Mazieres J, Marquette CH, Rouviere D, Didier A, Hermant C (2015) Integration of interventional bronchoscopy in the management of lung cancer. *Eur Respir Rev* 24:378–391. doi: 10.1183/16000617.00010014

Guibert N, Mhanna L, Droneau S, Plat G, Didier A, Mazieres J, Hermant C (2016) Techniques of endoscopic airway tumor treatment. *J Thorac Dis* 8:3343–3360. doi: 10.21037/jtd.2016.11.49

Hautmann H, Bauer M, Pfeifer KJ, Huber RM (2000) Flexible bronchoscopy: a safe method for metal stent implantation in bronchial disease. *Ann Thorac Surg* 69:398–401.

Hayward J, Reid LM (1952) The cartilage of the intrapulmonary bronchi in normal lungs, in bronchiectasis, and in massive collapse. 98–111.

Henderson E, Nash DH, Dempster WM (2011) On the experimental testing of fine Nitinol wires for medical devices. *J Mech Behav Biomed Mater* 4:261–8. doi: 10.1016/j.jmbbm.2010.10.004

Hohenforst-Schmidt W, Zarogoulidis P, Pitsiou G, Linsmeier B, Tsavlis D, Kioumis I, Papadaki

- E, Freitag L, Tsiouda T, Turner JF, Browning R, Simoff M, Sachpekidis N, Tsakiridis K, Zaric B, Yarmus L, Baka S, Stratakos G, Rittger H (2016) Drug eluting stents for malignant airway obstruction: A critical review of the literature. *J Cancer* 7:377–390. doi: 10.7150/jca.13611
- Hu HC, Liu YH, Wu YC, Hsieh MJ, Chao YK, Wu CY, Ko PJ, Liu CY (2011) Granulation tissue formation following dumon airway stenting: the influence of stent diameter. *Thorac Cardiovasc Surg* 59:163–168.
- Hughes JM, Hoppin FG, Mead J (1972) Effect of lung inflation on bronchial length and diameter in excised lungs. *J Appl Physiol* 32:25–35.
- Hugo Marquette C, Mensier E, Copin MC, Desmidt A, Freitag L, Witt C, Petyt L, Ramon P (1995) Experimental models of tracheobronchial stenoses: A useful tool for evaluating airway stents. *Ann Thorac Surg* 60:651–656. doi: 10.1016/0003-4975(95)00460-3
- Hürtgen M, Herber SCA (2014) Treatment of malignant tracheoesophageal fistula. *Thorac Surg Clin* 24:117–127.
- Husain SA, Finch D, Ahmed M, Morgan A, Hetzel MR (2007) Long-term follow-up of ultraflex metallic stents in benign and malignant central airway obstruction. *Ann Thorac Surg* 83:1251–6. doi: 10.1016/j.athoracsur.2006.11.066
- Hwang JC, Song HY, Kang SG, Suh JH, Ko GY, Lee DH, Kim TH, Jeong YK, Lee JH (2001) Covered retrievable tracheobronchial hinged stent: an experimental study in dogs. *J Vasc Interv Radiol* 12:1429–1436. doi: 10.1016/S1051-0443(07)61704-7
- Hyde DM, Hamid Q, Irvin CG (2009) Anatomy, pathology, and physiology of the tracheobronchial tree: emphasis on the distal airways. *J Allergy Clin Immunol* 124:S72-7. doi: 10.1016/j.jaci.2009.08.048
- Ibrahim G, Rona A, Hainsworth S V. (2015) Modeling the nonlinear motion of the rat central airways. *J Biomech Eng* 138:11007. doi: 10.1115/1.4032051
- Irwin RS (1977) Cough. *Arch Intern Med* 137:1186. doi: 10.1001/archinte.1977.03630210060019
- Jemal A, Bray F, Center MM, Ferlay J, Ward E, Forman D (2011) Global cancer statistics. *CA Cancer J Clin* 61:69–90. doi: 10.3322/caac.20107
- Kamm RD (1999) Airway wall mechanics. *Annu Rev Biomed Eng* 1:47–72. doi: 10.1146/annurev.bioeng.1.1.47
- Ke M, Wu X, Zeng J (2015) The treatment strategy for tracheoesophageal fistula. *J Thorac Dis* 7:S389–S397. doi: 10.3978/j.issn.2072-1439.2015.12.11
- Kleinstreuer C, Li Z, Basciano C a, Seelecke S, Farber M a (2008) Computational mechanics of Nitinol stent grafts. *J Biomech* 41:2370–8. doi: 10.1016/j.jbiomech.2008.05.032
- Klinder T, Lorenz C, von Berg J, Renisch S, Blaffert T, Ostermann J (2008) 4DCT image-based lung motion field extraction and analysis. *Proc SPIE* 6914:69141L–69141L–11. doi: 10.1117/12.769407
- Korpela A, Aarnio P, Sariola H, Törmälä P, Harjula A (1999) Bioabsorbable self-reinforced poly-l-lactide, metallic, and silicone stents in the management of experimental tracheal

stenosis. *Chest* 115:490–495. doi: 10.1378/chest.115.2.490

Korpela A, Aarnio P, Sariola H, Törmälä P, Harjula A (1998) Comparison of tissue reactions in the tracheal mucosa surrounding a bioabsorbable and silicone airway stents. *Ann Thorac Surg* 66:1772–1776. doi: 10.1016/S0003-4975(98)00763-2

Krstic R V (1984) *Illustrated encyclopedia of human histology*. Springer Berlin Heidelberg, Berlin, Heidelberg

Kubo HD, Hill BC (1996) Respiration gated radiotherapy treatment: a technical study. *Phys Med Biol* 41:83–91. doi: 10.1088/0031-9155/41/1/007

LaDisa JF, Olson LE, Molthen RC, Hettrick DA, Pratt PF, Hardel MD, Kersten JR, Warltier DC, Pagel PS (2005) Alterations in wall shear stress predict sites of neointimal hyperplasia after stent implantation in rabbit iliac arteries. *Am J Physiol Heart Circ Physiol* 288:H2465-75. doi: 10.1152/ajpheart.01107.2004

Lai Fook SJ (2004) Pleural mechanics and fluid exchange. *Physiol Rev* 84:385–410. doi: 10.1152/physrev.00026.2003

Lamare F, Carbayo MJL, Cresson T, Kontaxakis G, Santos A, Rest CC Le, Reader AJ, Visvikis D (2007) List-mode-based reconstruction for respiratory motion correction in PET using non-rigid body transformations. *Phys Med Biol* 52:5187–5204. doi: 10.1088/0031-9155/52/17/006

Lambert RK, Baile EM, Moreno R, Bert J, Paré PD (1991) A method for estimating the Young's modulus of complete tracheal cartilage rings. *J Appl Physiol* 70:1152–9.

Langlands J (1967) The dynamics of cough in health and in chronic bronchitis. *Thorax* 22:88–96.

Lawrence DA, Branson B, Oliva I, Rubinowitz A (2015) The wonderful world of the windpipe: a review of central airway anatomy and pathology. *Can Assoc Radiol J* 66:30–43. doi: 10.1016/j.carj.2014.08.003

Lee P, Kupeli E, Mehta AC (2010) Airway stents. *Clin Chest Med* 31:141–150. doi: 10.1016/j.ccm.2009.08.002

Lemaire A, Burfeind WR, Toloza E, Balderson S, Petersen RP, Harpole DH, D'Amico TA (2005) Outcomes of tracheobronchial stents in patients with malignant airway disease. *Ann Thorac Surg* 80:434–438. doi: 10.1016/j.athoracsur.2005.02.071

Lin CY, Chung FT (2016) Central airway tumors: interventional bronchoscopy in diagnosis and management. *J Thorac Dis* 8:E1168–E1176. doi: 10.21037/jtd.2016.10.101

Lokshin O, Lanir Y (2009) Micro and macro rheology of planar tissues. *Biomaterials* 30:3118–3127. doi: 10.1016/j.biomaterials.2009.02.039

Lunn W, Feller-Kopman D, Wahidi M, Ashiku S, Thurer R, Ernst A (2005) Endoscopic removal of metallic airway stents. *Chest* 127:2106–2112. doi: 10.1378/chest.127.6.2106

Macchiarini P (2006) Primary tracheal tumours. *Lancet Oncol* 7:83–91. doi: 10.1016/S1470-2045(05)70541-6

Madden BP, Datta S, Charokopos N (2002) Experience with Ultraflex expandable metallic stents in the management of endobronchial pathology. *Ann Thorac Surg* 73:938–944.

doi: 10.1016/S0003-4975(01)03460-9

- Mageras GS, Pevsner A, Yorke ED, Rosenzweig KE, Ford EC, Hertanto A, Larson SM, Lovelock DM, Erdi YE, Nehmeh SA, Humm JL, Ling CC (2004) Measurement of lung tumor motion using respiration-correlated CT. *Int J Radiat Oncol* 60:933–941. doi: 10.1016/j.ijrobp.2004.06.021
- Makris D, Marquette CH (2007) Tracheobronchial stenting and central airway replacement. *Curr Opin Pulm Med* 13:278–283. doi: 10.1097/MCP.0b013e32816b5c3b
- Malvè M, Barreras I, López-Villalobos JL, Ginel A, Doblaré M (2012) Computational fluid-dynamics optimization of a human tracheal endoprosthesis. *Int Commun Heat Mass Transf* 39:575–581. doi: 10.1016/j.icheatmasstransfer.2012.03.014
- Malvè M, Pérez del Palomar A, Chandra S, López-Villalobos JL, Finol E a, Ginel A, Doblaré M (2011a) FSI analysis of a human trachea before and after prosthesis implantation. *J Biomech Eng* 133:71003. doi: 10.1115/1.4004315
- Malvè M, Pérez del Palomar A, Chandra S, López-Villalobos JL, Mena A, Finol E a, Ginel A, Doblaré M (2011b) FSI Analysis of a healthy and a stenotic human trachea under impedance-based boundary conditions. *J Biomech Eng* 133:21001. doi: 10.1115/1.4003130
- Malvè M, Pérez del Palomar A, López-Villalobos JL, Ginel A, Doblaré M (2010) FSI analysis of the coughing mechanism in a human trachea. *Ann Biomed Eng* 38:1556–65. doi: 10.1007/s10439-010-9951-3
- Malvè M, Pérez del Palomar A, Mena A, Trabelsi O, López-Villalobos JL, Ginel A, Panadero F, Doblaré M (2011c) Numerical modeling of a human stented trachea under different stent designs. *Int Commun Heat Mass Transf* 38:855–862. doi: 10.1016/j.icheatmasstransfer.2011.04.012
- Malvè M, Pérez del Palomar A, Trabelsi O, López-Villalobos JL, Ginel A, Doblaré M (2011d) Modeling of the fluid structure interaction of a human trachea under different ventilation conditions. *Int Commun Heat Mass Transf* 38:10–15. doi: 10.1016/j.icheatmasstransfer.2010.09.010
- Malvè M, Serrano C, Peña E, Fernández Parra R, Lostalé F, De Gregorio M a., Martínez M a. (2014) Modelling the air mass transfer in a healthy and a stented rabbit trachea: CT-images, computer simulations and experimental study. *Int Commun Heat Mass Transf* 53:1–8. doi: 10.1016/j.icheatmasstransfer.2014.02.001
- Malvern LE (1969) *Introduction to the Mechanics of a Continuous Medium*, 1st edn. Prentice-Hall, Inc
- Martin HB, Proctor DF (1958) Pressure-volume measurements on dog bronchi. *J Appl Physiol* 13:337–43.
- McClelland JR, Hawkes DJ, Schaeffter T, King AP (2013) Respiratory motion models: A review. *Med Image Anal* 17:19–42. doi: 10.1016/j.media.2012.09.005
- McCool FD (2006) Global physiology and pathophysiology of cough: ACCP evidence-based clinical practice guidelines. *Chest* 129:48S–53S. doi: 10.1378/chest.129.1_suppl.48S
- McGarry JP, O'Donnell BP, McHugh PE, McGarry JG (2004) Analysis of the mechanical

- performance of a cardiovascular stent design based on micromechanical modelling. *Comput Mater Sci* 31:421–438. doi: 10.1016/j.commat.2004.05.001
- McKay KO, Wiggs BR, Paré PD, Kamm RD (2002) Zero-stress state of intra- and extraparenchymal airways from human, pig, rabbit, and sheep lung. *J Appl Physiol* 92:1261–1266. doi: 10.1152/jap.2001.92.4.1261
- Mead J (1961) Mechanical properties of lungs. *Physiol Rev* 41:281–330.
- Mead J, Takishima T, Leith D (1970) Stress distribution in lungs: a model of pulmonary elasticity. *J Appl Physiol* 28:596–608.
- Meeusen EN, Snibson KJ, Hirst SJ, Bischof RJ (2009) Sheep as a model species for the study and treatment of human asthma and other respiratory diseases. *Drug Discov Today Dis Model* 6:101–106. doi: 10.1016/j.ddmod.2009.12.002
- Mehta AC (2008) AERO self-expanding hybrid stent for airway stenosis. *Expert Rev Med Devices* 5:553–557. doi: 10.1586/17434440.5.5.553
- Meoli A, Dordoni E, Petrini L, Migliavacca F, Dubini G, Pennati G (2014) Computational study of axial fatigue for peripheral nitinol stents. *J Mater Eng Perform* 23:2606–2613. doi: 10.1007/s11665-014-0965-0
- Miyazawa T, Yamakido M, Ikeda S, Furukawa K, Takiguchi Y, Tada H, Shirakusa T (2000) Implantation of Ultraflex nitinol stents in malignant tracheobronchial stenoses. *Chest* 118:959–965. doi: 10.1378/chest.118.4.959
- Montgomery WW (1965) T-tube tracheal stent. *Arch Otolaryngol* 82:320–321.
- Morlacchi S, Keller B, Arcangeli P, Balzan M, Migliavacca F, Dubini G, Gunn J, Arnold N, Narracott A, Evans D, Lawford P (2011) Hemodynamics and In-stent restenosis: Micro-CT images, histology, and computer simulations. *Ann Biomed Eng* 39:2615–2626. doi: 10.1007/s10439-011-0355-9
- Murgu SD, Colt HG (2006) Tracheobronchomalacia and excessive dynamic airway collapse. *Chest* 2005:388–406. doi: 10.1111/j.1400-1843.2006.00862.x
- Murphy K, van Ginneken B, Reinhardt JM, Kabus S, Kai Ding, Xiang Deng, Kunlin Cao, Kaifang Du, Christensen GE, Garcia V, Vercauteren T, Ayache N, Commowick O, Malandain G, Glocker B, Paragios N, Navab N, Gorbunova V, Sporring J, de Bruijne M, Xiao Han, Heinrich MP, Schnabel JA, Jenkinson M, Lorenz C, Modat M, McClelland JR, Ourselin S, Muenzing SEA, Viergever MA, De Nigris D, Collins DL, Arbel T, Peroni M, Rui Li, Sharp GC, Schmidt-Richberg A, Ehrhardt J, Werner R, Smeets D, Loeckx D, Gang Song, Tustison N, Avants B, Gee JC, Staring M, Klein S, Stoel BC, Urschler M, Werlberger M, Vandemeulebroucke J, Rit S, Sarrut D, Pluim JPW (2011) Evaluation of registration methods on thoracic CT: the EMPIRE10 challenge. *IEEE Trans Med Imaging* 30:1901–1920. doi: 10.1109/TMI.2011.2158349
- Murthy SC, Blackstone EH, Gildea TR, Gonzalez-Stawinski G V, Feng J, Budev M, Mason DP, Pettersson GB, Mehta AC (2007) Impact of anastomotic airway complications after lung transplantation. *Ann Thorac Surg* 84:401–409. doi: 10.1016/j.athoracsur.2007.05.018
- Murthy SC, Gildea TR, Mehta AC (2004) Removal of self-expandable metallic stents: is it possible? *Semin Respir Crit Care Med* 25:381–385. doi: 10.1055/s-2004-832711

- Nematzadeh F, Sadrnezhad SK (2012) Effects of material properties on mechanical performance of Nitinol stent designed for femoral artery: Finite element analysis. *Sci Iran* 19:1564–1571. doi: 10.1016/j.scient.2012.10.024
- Noppen M, Piérard D, Meysman M, Claes I, Vincken W (1999) Bacterial colonization of central airways after stenting. *Am J Respir Crit Care Med* 160:672–677. doi: 10.1164/ajrccm.160.2.9812081
- Noppen M, Stratakos G, D’Haese J, Meysman M, Vinken W (2005) Removal of covered self-expandable metallic airway stents in benign disorders: indications, technique, and outcomes. *Chest* 127:482–7. doi: 10.1378/chest.127.2.482
- O’Brien B, Bruzzi M (2011) Shape memory alloys for use in medicine. In: *Comprehensive Biomaterials*. Elsevier, pp 49–72
- Ost DE, Shah AM, Lei X, Godoy MCB, Jimenez C a, Eapen G a, Jani P, Larson AJ, Sarkiss MG, Morice RC (2012) Respiratory infections increase the risk of granulation tissue formation following airway stenting in patients with malignant airway obstruction. *Chest* 141:1473–81. doi: 10.1378/chest.11-2005
- Pan T, Lee TY, Rietzel E, Chen GTY (2004) 4D-CT imaging of a volume influenced by respiratory motion on multi-slice CT. *Med Phys* 31:333–340. doi: 10.1118/1.1639993
- Panitch HB, Allen JL, Ryan JP, Wolfson MR, Shaffer TH (1989) A comparison of preterm and adult airway smooth muscle mechanics. *J Appl Physiol* 66:1760–5.
- Park JH, Kang SW, Lee SC, Choi WA, Kim DH (2010) How respiratory muscle strength correlates with cough capacity in patients with respiratory muscle weakness. *Yonsei Med J* 51:392–397. doi: 10.3349/ymj.2010.51.3.392
- Pelton AR (2011) Nitinol fatigue: A review of microstructures and mechanisms. *J Mater Eng Perform* 20:613–617. doi: 10.1007/s11665-011-9864-9
- Pelton AR, Dicello J, Miyazaki S (2000) Optimisation of processing and properties of medical grade Nitinol wire. *Minim Invasive Ther Allied Technol* 9:107–118. doi: 10.3109/13645700009063057
- Pelton AR, Schroeder V, Mitchell MR, Gong XY, Barney M, Robertson SW (2008) Fatigue and durability of Nitinol stents. *J Mech Behav Biomed Mater* 1:153–164. doi: 10.1016/j.jmbbm.2007.08.001
- Perez del Palomar A, Trabelsi O, Mena A, Lopez-Villalobos JL, Ginel A, Doblare M (2010) Patient-specific models of human trachea to predict mechanical consequences of endoprosthesis implantation. *Philos Trans R Soc A Math Phys Eng Sci* 368:2881–2896. doi: 10.1098/rsta.2010.0092
- Plathow C, Ley S, Fink C, Puderbach M, Hosch W, Schmähl A, Debus J, Kauczor H-U (2004) Analysis of intrathoracic tumor mobility during whole breathing cycle by dynamic MRI. *Int J Radiat Oncol* 59:952–959. doi: 10.1016/j.ijrobp.2003.12.035
- Prakash UB, Hyatt RE (1978) Static mechanical properties of bronchi in normal excised human lungs. *J Appl Physiol* 45:45–50.
- Puchalski J, Musani AI (2013) Tracheobronchial stenosis. causes and advances in management. *Clin Chest Med* 34:557–567. doi: 10.1016/j.ccm.2013.05.002

- Puma F, Farabi R, Urbani M, Santoprete S, Daddi N, Di Meo a, Gialletti R, Tocchi a, Daddi G (2000) Long-term safety and tolerance of silicone and self-expandable airway stents: an experimental study. *Ann Thorac Surg* 69:1030–4.
- Putters JLM, Kaulesar Sukul DMKS, de Zeeuw GR, Bijma A, Besselink PA (1992) Comparative cell culture effects of shape memory metal (nitinol®), nickel and titanium: a biocompatibility estimation. *Eur Surg Res* 24:378–382. doi: 10.1159/000129231
- Rafanan AL, Mehta AC (2000) Stenting of the tracheobronchial tree. *Radiol Clin North Am* 38:395–408.
- Rains JK, Bert JL, Roberts CR, Paré PD (1992) Mechanical properties of human tracheal cartilage. *J Appl Physiol* 72:219–25.
- Rebelo N, Perry M (2000) Finite element analysis for the design of Nitinol medical devices. *Minim Invasive Ther Allied Technol* 9:75–80. doi: 10.3109/13645700009063053
- Roberts CR, Rains JK, Paré PD, Walker DC, Wiggs B, Bert JL (1998) Ultrastructure and tensile properties of human tracheal cartilage. *J Biomech* 31:81–6.
- Robertson SW, Pelton AR, Ritchie RO (2012) Mechanical fatigue and fracture of Nitinol. *Int Mater Rev* 57:1–37. doi: 10.1179/1743280411Y.0000000009
- Rousseau H, Dahan M, Lauque D, Carré P, Didier A, Bilbao I, Herrero J, Blancjouvant F, Joffre F (1993) Self-expandable prostheses in the tracheobronchial tree. *Radiology* 188:199–203. doi: 10.1148/radiology.188.1.8511297
- Ryhänen J (2000) Biocompatibility of nitinol. *Minim Invasive Ther Allied Technol* 9:99–105. doi: 10.3109/13645700009063056
- Safshekan F, Tafazzoli-Shadpour M, Abdouss M, Shadmehr MB (2016a) Mechanical characterization and constitutive modeling of human trachea: Age and gender dependency. *Materials (Basel)*. doi: 10.3390/ma9060456
- Safshekan F, Tafazzoli-Shadpour M, Abdouss M, Shadmehr MB (2016b) Viscoelastic properties of human tracheal tissues. *J Biomech Eng* 139:1–9. doi: 10.1115/1.4034651
- Saito Y, Imamura H (2005) Airway stenting. *Surg Today* 35:265–70. doi: 10.1007/s00595-004-2942-y
- Scheerlinck JPY, Snibson KJ, Bowles VM, Sutton P (2008) Biomedical applications of sheep models: from asthma to vaccines. *Trends Biotechnol* 26:259–266. doi: 10.1016/j.tibtech.2008.02.002
- Schlesinger RB, McFadden LA (1981) Comparative morphometry of the upper bronchial tree in six mammalian species. *Anat Rec* 199:99–108. doi: 10.1002/ar.1091990110
- Schmäl F, Fegeler W, Terpe HJ, Hermann W, Stoll W, Becker K (2003) Bacteria and granulation tissue associated with Montgomery T-tubes. *Laryngoscope* 113:1394–1400. doi: 10.1097/00005537-200308000-00024
- Seppenwoolde Y, Berbeco RI, Nishioka S, Shirato H, Heijmen B (2007) Accuracy of tumor motion compensation algorithm from a robotic respiratory tracking system: A simulation study. *Med Phys* 34:2774–2784. doi: 10.1118/1.2739811
- Serrano C, Laborda A, Lozano JM, Caballero H, Sebastián A, Lopera J, De Gregorio MÁ (2013)

- Metallic stents for tracheobronchial pathology treatment. *Cardiovasc Intervent Radiol* 36:1614–1623. doi: 10.1007/s00270-013-0602-6
- Serrano C, Lostalé F, Rodríguez-Panadero F, de Blas I, Laborda A, Gregorio MA De (2016) Tracheal self-expandable metallic stents: a comparative study of three different stents in a rabbit model. *Arch Bronconeumol (English Ed)* 52:123–130. doi: 10.1016/j.arbr.2015.06.012
- Sharp GC, Jiang SB, Shimizu S, Shirato H (2004) Prediction of respiratory tumour motion for real-time image-guided radiotherapy. *Phys Med Biol* 49:425–440. doi: 10.1088/0031-9155/49/3/006
- Shin JH, Kim SW, Shim TS, Jung GS, Kim TH, Ko GY, Song HY (2003) Malignant tracheobronchial strictures: palliation with covered retrievable expandable nitinol stent. *J Vasc Interv Radiol* 14:1525–1534. doi: 10.1097/01.RVI.0000099525.29957.34
- Sosa AF, Michaud GC (2012) Metallic stents in the airway: should we continue to use them and can we remove them? *Curr Respir Care Rep* 2:54–60. doi: 10.1007/s13665-012-0036-7
- Stoeckel D, Pelton A, Duerig T (2004) Self-expanding nitinol stents: material and design considerations. *Eur Radiol* 14:292–301. doi: 10.1007/s00330-003-2022-5
- Strausz J (1997) Management of postintubation tracheal stenosis with stent implantation. *J Bronchol* 4:294–296. doi: 10.1097/00128594-199710000-00005
- Suki B, Bates JHT (2008) Extracellular matrix mechanics in lung parenchymal diseases. *Respir Physiol Neurobiol* 163:33–43. doi: 10.1016/j.resp.2008.03.015
- Suki B, Bates JHT (2011) Lung tissue mechanics as an emergent phenomenon. 1111–1118. doi: 10.1152/jappphysiol.01244.2010.
- Swanson KL, Edell ES, Prakash UBS, Brutinel WM, Midthun DE, Utz JP (2007) Complications of metal stent therapy in benign airway obstruction. *J Bronchol* 14:90–94. doi: 10.1097/LBR.0b013e318053d445
- Tawhai MH, Hunter P, Tschirren J, Reinhardt J, McLennan G, Hoffman E a (2004) CT-based geometry analysis and finite element models of the human and ovine bronchial tree. *J Appl Physiol* 97:2310–2321. doi: 10.1152/jappphysiol.00520.2004
- Tawhai MH, Nash MP, Hoffman EA (2006) An imaging-based computational approach to model ventilation distribution and soft-tissue deformation in the ovine lung. *Acad Radiol* 13:113–120. doi: 10.1016/j.acra.2005.09.088
- Tawhai MH, Nash MP, Lin CL, Hoffman EA (2009) Supine and prone differences in regional lung density and pleural pressure gradients in the human lung with constant shape. *J Appl Physiol* 107:912–20. doi: 10.1152/jappphysiol.00324.2009
- Teng Z, Ochoa I, Li Z, Liao Z, Lin Y, Doblare M (2009) Study on tracheal collapsibility, compliance, and stress by considering nonlinear mechanical property of cartilage. *Ann Biomed Eng* 37:2380–2389. doi: 10.1007/s10439-009-9765-3
- Teng Z, Ochoa I, Li Z, Lin Y, Rodriguez JF, Bea JA, Doblare M (2008) Nonlinear mechanical property of tracheal cartilage: A theoretical and experimental study. *J Biomech* 41:1995–2002. doi: 10.1016/j.jbiomech.2008.03.032

- Teng Z, Trabelsi O, Ochoa I, He J, Gillard JH, Doblare M (2012) Anisotropic material behaviours of soft tissues in human trachea: an experimental study. *J Biomech* 45:1717–23. doi: 10.1016/j.jbiomech.2012.04.002
- Thiebes AL, Kelly N, Sweeney CA, McGrath DJ, Clauser J, Kurtenbach K, Gesche VN, Chen W, Kok RJ, Steinseifer U, Bruzzi M, O'Brien BJ, McHugh PE, Jockenhoevel S, Cornelissen CG (2017) PulmoStent: in vitro to in vivo evaluation of a tissue engineered endobronchial stent. *Ann Biomed Eng* 45:873–883. doi: 10.1007/s10439-016-1737-9
- Thistlethwaite PA, Yung G, Kemp A, Osbourne S, Jamieson SW, Channick C, Harrell J (2008) Airway stenoses after lung transplantation: Incidence, management, and outcome. *J Thorac Cardiovasc Surg* 136:1569–1575. doi: 10.1016/j.jtcvs.2008.08.021
- Tiddens HAWM, Hofhuis W, Bogaard JM, Hop WCJ, De Bruin H, Willems LNA, De Jongste JC (1999) Compliance, hysteresis, and collapsibility of human small airways. *Am J Respir Crit Care Med* 160:1110–1118. doi: 10.1164/ajrccm.160.4.9709004
- Trabelsi O, Malve M, Mena Tobar A, Doblare M (2015) Simulation of swallowing dysfunction and mechanical ventilation after a Montgomery T-tube insertion. *Comput Methods Biomech Biomed Engin* 18:1596–1605. doi: 10.1080/10255842.2014.930448
- Trabelsi O, Pérez del Palomar A, López-villalobos JL, Ginel A, Doblare M (2010) Experimental characterization and constitutive modeling of the mechanical behavior of the human trachea. *Med Eng Phys* 32:76–82. doi: 10.1016/j.medengphy.2009.10.010
- Trabelsi O, Pérez del Palomar A, Mena Tobar A, López-Villalobos JL, Ginel A, Doblare M (2011) FE simulation of human trachea swallowing movement before and after the implantation of an endoprosthesis. *Appl Math Model* 35:4902–4912. doi: 10.1016/j.apm.2011.03.041
- Tustison NJ, Cook TS, Song G, Gee JC (2011) Pulmonary kinematics from image data: a review. *Acad Radiol* 18:402–417. doi: 10.1016/j.acra.2010.10.019
- Van der Velden J, Snibson KJ (2011) Airway disease: The use of large animal models for drug discovery. *Pulm Pharmacol Ther* 24:525–532. doi: 10.1016/j.pupt.2011.02.001
- Vedam SS, Keall PJ, Kini VR, Mohan R (2001) Determining parameters for respiration-gated radiotherapy. *Med Phys* 28:2139–2146. doi: 10.1118/1.1406524
- Vedam SS, Keall PJ, Kini VR, Mostafavi H, Shukla HP, Mohan R (2003) Acquiring a four-dimensional computed tomography dataset using an external respiratory signal. *Phys Med Biol* 48:45–62. doi: 10.1088/0031-9155/48/1/304
- Villard PF, Beuve M, Shariat B, Baudet V, Jaillet F (2005) Simulation of lung behaviour with finite elements: influence of bio-mechanical parameters. In: *Third International Conference on Medical Information Visualisation--BioMedical Visualisation*. IEEE, pp 9–14
- Weibel ER (1963) Morphometry of the human lung. *Anesthesiol Bookshelf* 26:367. doi: 10.1016/B978-1-4832-0076-7.50005-3
- Weibel ER, Gomez M (1962) Architecture of the human lung. *Science* 137:577–585.
- Werner R, Ehrhardt J, Schmidt R, Handels H (2009) Patient-specific finite element modeling of respiratory lung motion using 4D CT image data. *Med Phys* 36:1500. doi:

10.1118/1.3101820

West JB (2012) *Respiratory physiology: the essentials*. Lippincott Williams & Wilkins

West JB, Matthews FL (1972) Stresses, strains, and surface pressures in the lung caused by its weight. *J Appl Physiol* 32:332–45.

WHO (2011) *World Health Statistics 2011*. WHO Libr Cat Data 1:170. doi: 978 92 4 156419 9

Wolthaus JWH, Sonke JJ, van Herk M, Damen EMF (2008) Reconstruction of a time-averaged midposition CT scan for radiotherapy planning of lung cancer patients using deformable registration). *Med Phys* 35:3998–4011. doi: 10.1118/1.2966347

Wood DE, Liu YH, Vallie E, Karmy-Jones R, Mulligan MS (2003) Airway stenting for malignant and benign tracheobronchial stenosis.

Yin Y, Choi J, Hoffman EA, Tawhai MH, Lin C-L (2013) A multiscale MDCT image-based breathing lung model with time-varying regional ventilation. *J Comput Phys* 244:168–192. doi: 10.1016/j.jcp.2012.12.007

Zakaluzny SA, Lane JD, Mair EA (2003) Complications of tracheobronchial airway stents. *Otolaryngol Head Neck Surg* 128:478–88. doi: 10.1016/mhn.2003.107

Zeng YJ, Yager D, Fung YC (1987) Measurement of the mechanical properties of the human lung tissue. *J Biomech Eng* 109:169–174.

Zhang T, Orton NP, Mackie TR, Paliwal BR (2004) Technical note: A novel boundary condition using contact elements for finite element based deformable image registration. *Med Phys* 31:2412–2415. doi: 10.1118/1.1774131

Chapter 2

Nitinol Stent Design - Understanding Axial Buckling

Published in: The Journal of the Mechanical Behavior of Biomedical Materials, 2014

DOI: 10.1016/j.jmbbm.2014.08.029

Abstract

Nitinol's superelastic properties permit self-expanding stents to be crimped without plastic deformation, but its nonlinear properties can contribute towards stent buckling. This study investigates the axial buckling of a prototype tracheobronchial nitinol stent design during crimping, with the objective of eliminating buckling from the design. To capture the stent buckling mechanism a computational model of a radial force test is simulated, where small geometric defects are introduced to remove symmetry and allow buckling to occur. With the buckling mechanism ascertained, a sensitivity study is carried out to examine the effect that the transitional plateau region of the nitinol loading curve has on stent stability. Results of this analysis are then used to redesign the stent and remove buckling. It is found that the transitional plateau region can have a significant effect on the stability of a stent during crimping, and by reducing the amount of transitional material within the stent hinges during loading the stability of a nitinol stent can be increased.

2.1 Introduction

Tracheobronchial stenting is indicated for many applications in the lung (Saito and Imamura 2005; Chin et al. 2008; Freitag 2010), of which the most common is the restoration of lumen patency due to narrowing caused by tumour growth (Freitag 2010). In the majority of cases this is a palliative procedure used to avoid suffocation

and improve the patient's quality of life. The affected area is accessed through the use of a rigid (or sometimes flexible) bronchoscope inserted through the mouth and guided fluoroscopically. Once the bronchoscope is in position it creates a direct path for the stent catheter to track through, where the stent is then expanded to re-open the occluded airway. Numerous polymeric and metallic stent designs using various deployment mechanisms have been commercially launched for use in the tracheobronchial region, and much literature exists on the complications associated with the use of these stents (Bolliger et al. 1996; Madden et al. 2004; Ryu et al. 2006; Bolliger et al. 2006; Dooms et al. 2009; Furukawa et al. 2010; Fernández-Bussy et al. 2011). But nothing to the authors' knowledge has been published with regard to complications observed during stent design.

Nitinol is a widely used material for the manufacture of self-expanding (SE) tracheobronchial stents, due to its superelastic properties and excellent biocompatibility (Duerig et al. 2000; Stoeckel et al. 2004). Nitinol can reach strains in excess of 10% without plastically deforming (Duerig et al. 2000; Stoeckel et al. 2004), making it possible to crimp and deploy a stent in a self-expanding manner. Nitinol is a complex engineering material that can exhibit both shape memory and superelastic properties. At temperatures above which nitinol is completely austenitic, superelastic behaviour can be achieved by stress induced transformation from the austenitic phase to the martensitic phase, where removal of the applied stress results in complete strain recovery (Otsuka and Ren 2005; Robertson et al. 2012). Loading and unloading of the material at this temperature results in a stress-strain plot similar to that shown in Fig. 2.1, where the loading response can be divided into three distinct sections: austenitic, transitional and martensitic. The austenitic stage is represented by a stiff linear stress-strain relationship during the initial loading of the austenitic phase. After <1% strain, nitinol enters the transitional stage during which large increases in strain result in only small changes in stress. During this transitional stage the austenite begins to transform to martensite, where continued loading increases the volume fraction of stress induced martensite until the transformation is complete. Finally, in the martensitic stage additional loading initially results in an

essentially linear elastic martensitic response, which if strained excessively can result in plastic deformation.

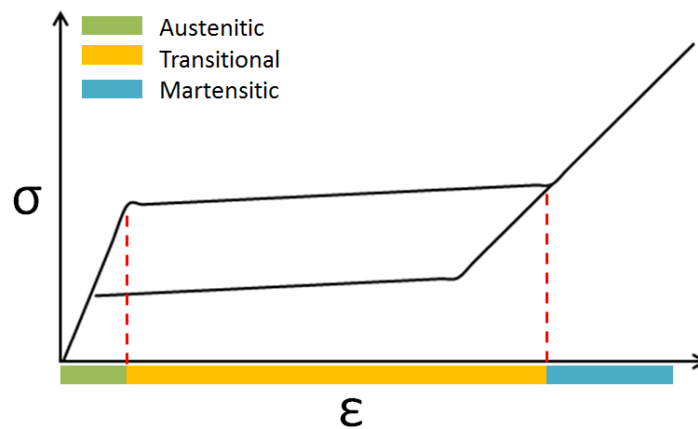


Fig. 2.1: Schematic stress-strain curve for load and unload of nitinol highlighting the three stages during loading: austenitic, transitional and martensitic.

Self-expanding nitinol stents must undergo large deformations when being loaded into the delivery system and this can lead to problems with stent buckling during device design - associated with the compliant transitional plateau stage. This buckling effect has been observed during the development of a prototype nitinol tracheobronchial stent; sudden asymmetric axial displacement of stent struts during crimping has resulted in the loss of mechanical stability of the stent. If the stent remains in the buckled configuration after deployment it can have a number of undesirable side-effects. A buckled stent will have a lower overall stiffness resulting in less mechanical support during extreme loading conditions (e.g. during coughing) which can lead to increased chance of stent migration. Reduced stiffness can result in larger strut displacements which can reduce the fatigue life of the stent owing to increased strain amplitudes. Additional relative axial displacement of stent rings can cause unnecessary irritation to the surrounding tissue causing unwanted inflammatory responses. To the authors' knowledge no literature exists on the cause behind the buckling of nitinol stents.

Nitinol's complex material properties are commonly represented in Abaqus using the Auricchio constitutive model (Auricchio et al. 1997), which captures each aspect of the nitinol load-unload curve based on generalized plasticity theory. Many computational studies have been performed to investigate various aspects of SE

stent design including: fatigue life, *in-vivo* loading and radial force optimisation (Rebelo and Perry 2000; Gong et al. 2004; Kleinstreuer et al. 2008; Chen et al. 2012; García et al. 2012; Azaouzi et al. 2012; Azaouzi et al. 2013; Ghriallais and Bruzzi 2014). Kleinstreuer et al. (2008) investigated the effect of stent crimping, deployment and cyclic loading on stent-graft fatigue life and radial force of diamond shaped specimens. Ghriallais and Bruzzi (2014) studied the effect that boundary conditions and assumptions have on SE stent modelling and radial force accuracy. Azaouzi et al. (2012; 2013) performed a design optimisation focusing on improving the fatigue life of a Cordis SMART stent and also examined the effect that stent dimensions have on a SE stent deployed within an artery. García et al. (2012) investigated the effects of varying strut width and thickness on variable radial force of an Abbott Acculink device. Chen et al. (2012) performed a numerical analysis on the effect of strut length on radial force and fatigue performance. These studies investigated different aspects of nitinol stent design but have not reported stent buckling during loading, although Azaouzi et al. (2012; 2013) did use a static stabilization coefficient to reduce dynamic effects brought on by buckling. Nitinol stent buckling was detected by Gong et al. (2004) experimentally during crush testing which was computationally replicated, however no explanation for the buckling was provided.

Balloon expandable (BE) stents are often tested to collapse during radial strength testing. Normally BE stents undergo a small decrease in stent diameter before losing mechanical stability and buckling (Rieu et al. 1999; Shen et al. 2008). For these stents, the collapse is caused when the stent struts reach a limit load and plastic flow ensues, where a small increase in load results in a large displacement before eventual failure (Dumoulin and Cochelin 2000). Analogously, it is proposed in this work that the non-linear material properties of nitinol can lead to buckling, due to an unstable softening of the stent hinges caused by the low stiffness in the transitional stage.

The objective of the present study is to investigate axial buckling observed during crimping of a large diameter nitinol stent and through elucidation of the buckling mechanism to eliminate it from the design. This is accomplished in three steps. Firstly, the experimentally observed buckling is replicated computationally to identify the main buckling mechanism. Then a stability analysis is carried out on a repeating

unit to evaluate the effect that transitional strain distribution has on stent unit stability, using the buckling mechanism determined. Finally the results of the stability analysis are used to design a stent capable of resisting axial buckling, which is then validated experimentally.

2.2 Methods and Results

2.2.1 Stent Fabrication

All stents were laser-cut from a single nitinol tube lot with 5.0 mm OD and thickness of 0.23 mm. The stents were expanded and shape set over a cylindrical mandrel to approximately 15 mm OD x 30 mm length after which electropolishing was performed. The fabricated stents contained typical defects observed during stent production, including a non-uniform radial unit angle (Fig. 2.2) which occurs due to the friction between the laser-cut stent and the mandrel during expansion. These defects are commonly found during fabrication and would not be considered significant enough to inhibit the mechanical performance of the stents.

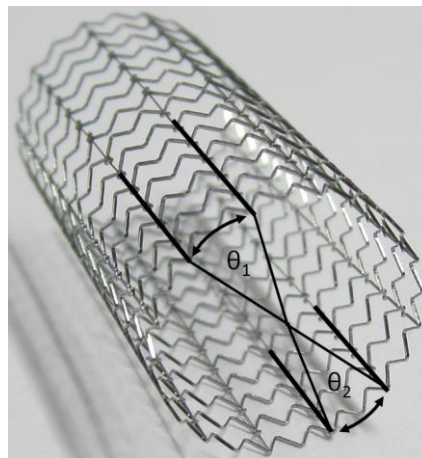


Fig. 2.2: Image of the fabricated prototype stent highlighting the non-uniform radial unit angle defect. The parallel lines mark the outer edges of a repeating unit along the axial length of the stent. The radial angle of these unit lengths are not equal with θ_1 being slightly larger than θ_2 as can be seen from the distance between the lines.

2.2.2 Part 1: Buckling Observation and Determination

In this section the prototype stent buckling mechanism is determined from experimentally validated computational models. Axially buckling stents are experimentally crimped and unloaded during a radial force test. Quantitative and qualitative experimental test results are then used to validate a computational model

which uses geometric and material defects to allow the axial buckling mechanism to be determined.

2.2.2.1 Experimental Testing

Radial force testing is carried out on five stents using a 12-faced crimping head (RX500-102 Radial Force Expansion Force Gauge -Machine Solutions Inc.). The stent is crimped and unloaded at a rate of 0.1 mm/s from its nominal 15 mm OD to 5 mm OD at 37 °C.

2.2.2.2 Nitinol Material Properties

Material properties are obtained by performing tensile tests on samples cut from the same nitinol tubing lot used for stent fabrication. The tube is cut and heat-treated under similar conditions to the stents. Three tube samples are strained to 6%, completely unloaded and subsequently re-loaded to failure, at a rate of 3 mm/min. The results of the tensile test are used to calibrate the material model for nitinol in Abaqus (DS SIMULIA, USA) using the in-built Auricchio constitutive model. Nitinol material properties are fit to the average curve of the tensile tested samples as shown in Fig. 2.3 and the parameters used can be found in Table 2.1. The material model is assumed to be symmetric in tension and compression as is common in the literature (García et al. 2012; Ghriallais and Bruzzi 2014). In this study the effects of plastic deformation are not considered.

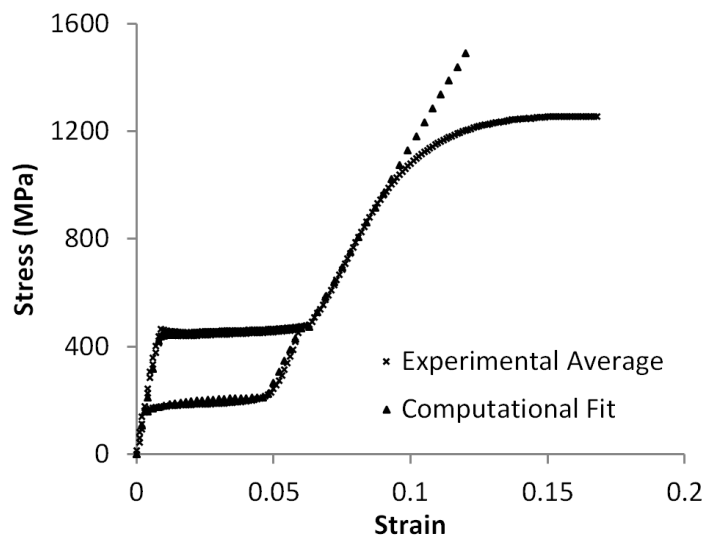


Fig. 2.3: Average experimental tensile result versus computational fit.

2.2.2.3 Stent Model

The initial as-cut stent geometry comprises of a repeating unit structure as shown in Fig. 2.4. The stent contains 12 units circumferentially and 14 longitudinally, and is symmetric about a section located at the centre of the axial length. Each repeating unit contains 5 hinges, of which 2 are attached to a longitudinal connector that spans the length of the stent. This initial design is referred to as A1 in later sections.

To allow buckling to occur in the model, imperfections are introduced to the stent geometry during the expansion step to remove symmetry and allow asymmetric axial displacement. This is a similar approach to that undertaken by Asprone et al. (2013) and Lagaros and Papadopoulos (2006) on the buckling of honeycomb structures. A small non-uniform radial angle defect (described in Section 2.2.1) is used to remove symmetry in the model which creates a bias that forces the axial buckling to initiate.

Table 2.1: Material properties used in the Abaqus UMAT/VUMAT.

Parameter	Value
Austenite Elasticity (MPa)	53001
Austenite Poisson's Ratio	0.3
Martensite Elasticity (MPa)	21500
Martensite Poisson's Ratio	0.3
Transformation Strain	0.038
Start of Transformation Loading (MPa)	434
End of Transformation Loading (MPa)	500
Reference Temperature (°C)	37
Start of Transformation Unloading (MPa)	210.3
End of Transformation Unloading (MPa)	138.7
Start of Transformation Stress During Loading in Compression (MPa)	434
Volumetric Transformation Strain	0.038

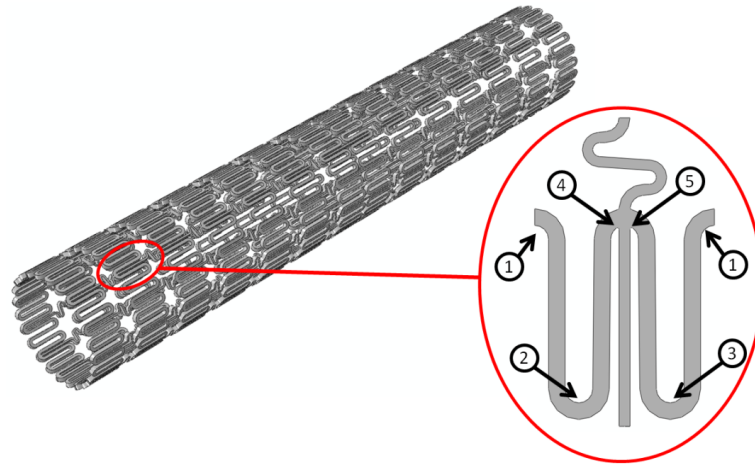


Fig. 2.4: Illustration of the as-cut A1 stent geometry. Inset: As-cut repeating unit highlighting the 5 hinges in the repeating unit. Hinges 4 and 5 are connected to the longitudinal connector.

Stent expansion is accomplished using Abaqus/Standard (V6.11) in three steps as illustrated in Fig. 2.5. Firstly, as is common in the literature, the as-cut stent geometry is placed over a rigid cylinder and radial boundary conditions are used to expand the cylinder (García et al. 2012; Ghriallais and Bruzzi 2014). Surface-to-surface hard normal and tangential penalty contact with a coefficient of friction of 0.1 is defined between the outside surface of the cylinder and the inside surface of the stent, which results in a symmetrical partially-expanded stent after the first step (Fig. 2.5 (b)). The radial angle defect is introduced in the second step and is accomplished by holding all nodes on 6 radial units through the length of the stent in the z-direction while continuing to expand the rigid cylinder (Fig. 2.5 (c)). By holding the nodes in this way the unit angle is restricted while keeping the stent cylindrical. In the third step the process is repeated holding 10 radial units as shown in Fig. 2.5 (d). This results in 3 different unit radial angles around the circumference of the stent of 28.3° , 31.2° and 32.7° .

2.2.2.4 Radial Force Simulation

Radial force testing is simulated using Abaqus/Explicit to enable large sudden deformations caused by asymmetric displacement during buckling to be captured. The defected expanded stent geometry is placed in the centre of the crimper head assembly (Fig. 2.6) which consists of 12 rigid body plates. Displacement boundary conditions on the rigid plates are used to reduce and subsequently increase the diameter of the stent. The radial force is measured using the sum of the magnitude

of the reaction force at the crimper plates reference points for one load and unload cycle. The ratio of kinetic to internal energy is maintained below 5% for the entire simulation apart for an increase to 8% at the point of buckling (Chung and Cho 1998). Semi-automatic mass scaling is used with a target time increment of $5.8E-7$ and a lowest stable time increment of $6.1E-8$. The typical simulation run time for this type of analysis is 1010 CPU hours performed on a SGI ICE X HPC cluster at the Irish Centre for High Performance Computing. A mesh convergence study was carried out and showed the max percentage Von Mises stress difference between the mesh used in the analysis and a finer mesh with a 7.73 fold increase in mesh density to be 2.13%. A mesh detail is shown in the inset in Fig. 2.6.

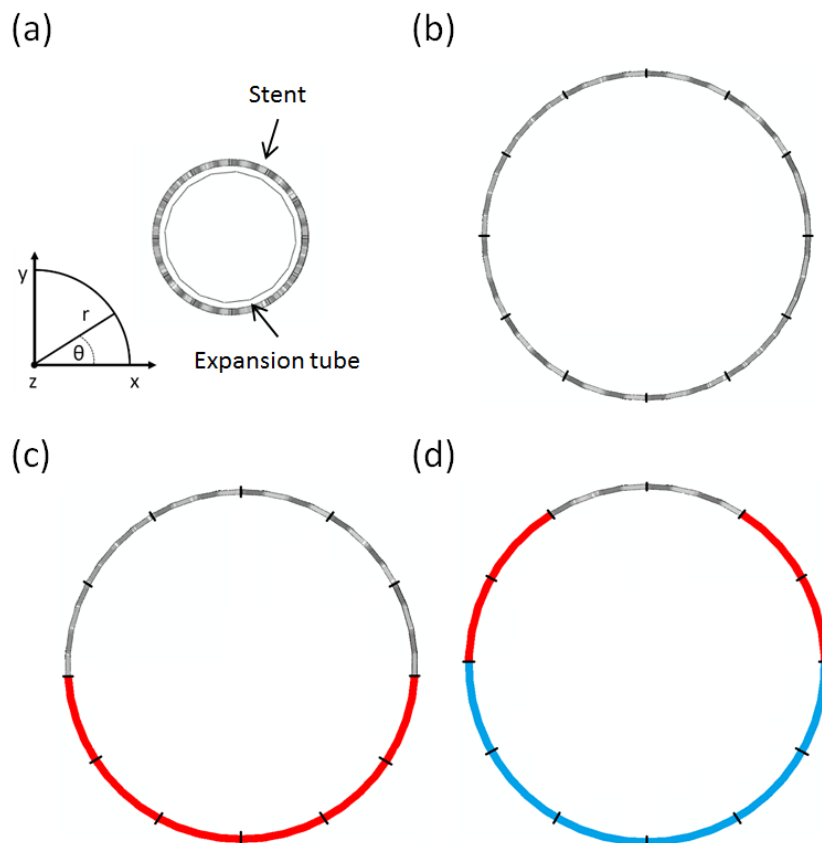


Fig. 2.5: (a) Stent expansion model setup in as-cut configuration. The expansion tube material is defined with a Young's Modulus of 2 GPa and a Poisson's Ratio of 0.3, and is meshed with M3D4R elements. The stent is meshed using 575,424 C3D8R elements and a single node is held in the z-direction to remove rigid body movement. (b) Step 1: The stent is expanded uniformly by expanding the tube radially. Radial units marked in black. (c) Step 2: A non-uniform radial angle defect is introduced by holding all the nodes on 6 radial units (highlighted red) in the z-direction, while expanding the tube radially. (d) Step 3: Step 2 is repeated holding the highlighted blue (6 radial units) and red nodes (4 radial units). The resulting average unit radial angles are 28.3° (Blue), 31.2° (Red) and 32.7° (Grey).

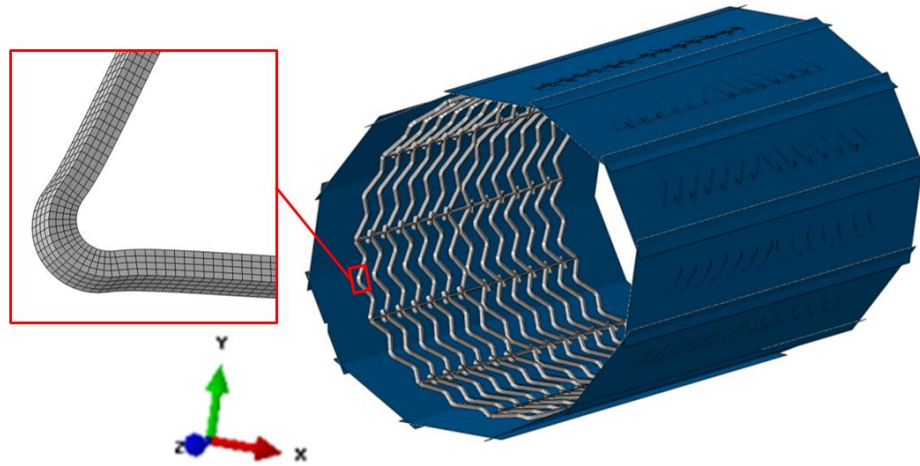


Fig. 2.6: Stent positioned within crimper plates. For all radial force simulations, general contact is defined with frictionless tangential and hard normal contact. Contact between the crimper plates is ignored. One node on the stent is held in the z-direction to remove rigid body motion. Inset shows mesh detail. The stent is meshed using four elements through the width and thickness.

2.2.2.5 Results

The results of the experimental and computational radial force testing are shown in Fig. 2.7. A good correlation exists between the experimental and computational results where a sudden significant drop in radial force signals the onset of axial buckling. Upon unloading the stents fully recover suggesting that the buckling observed is essentially a pseudo-elastic mechanism (Further analysis of the radial loading of a buckled stent is provided in Appendix 2).

A good match between the model and experiment can also be seen in Fig. 2.8, where axial deformation (Fig. 2.8 (a) and (b)) and radial deformation (Fig. 2.8 (c) and (d)) are compared.

In Fig. 2.9 the steps leading up to axial buckling during a crimping simulation are summarised using two repeating units at one stent end. It can be seen that Unit 1 (Fig. 2.9 (a)) initially experiences higher strain levels than Unit 2, with more hinges within the transitional strain region at a radial displacement of 0.689 mm (Fig. 2.9 (b)). This leads to bending of the longitudinal connector (Fig. 2.9 (c)) and eventual axial displacement caused by hinge closure (Fig. 2.9 (d)).

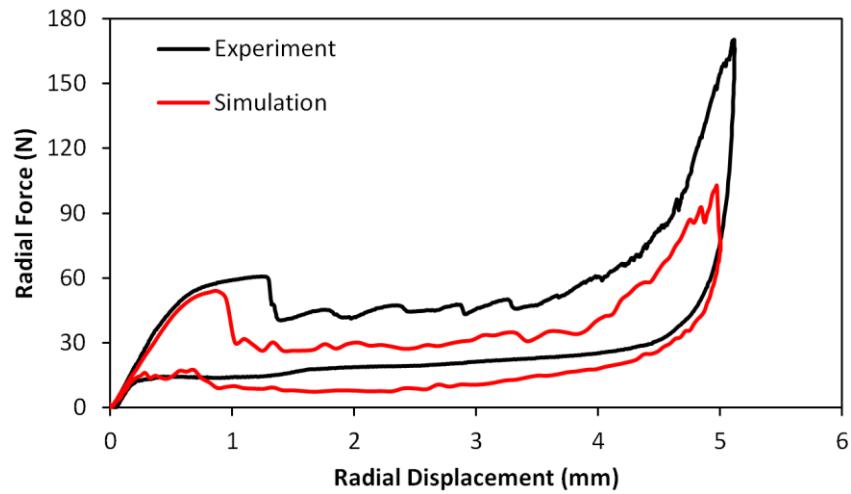


Fig. 2.7: Experimental and computational results for the radial force testing of the A1 stent design. The experimental result is typical of the tested stents.

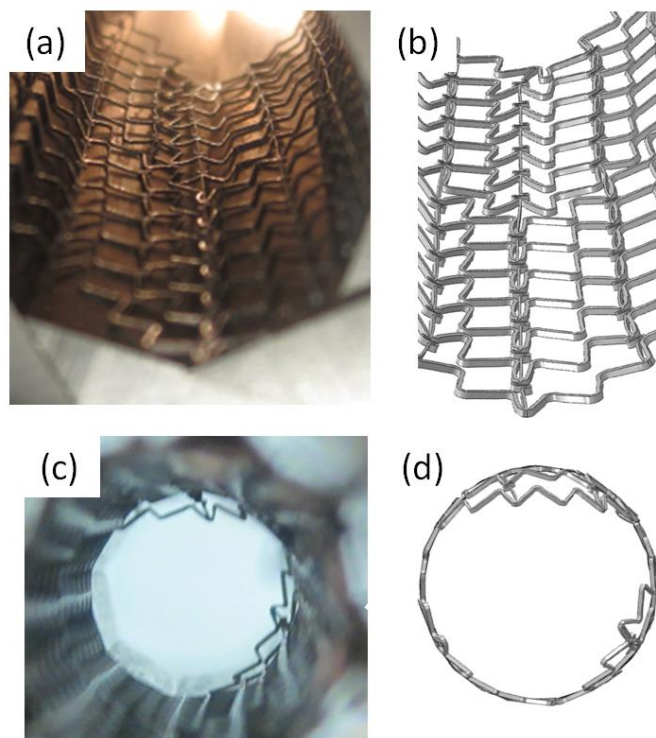


Fig. 2.8: Experimental and computational results of the radial force test. (a) Experimental skewed axial view after occurrence of buckling. (b) The corresponding computational skewed axial view. (c) Experimental radial view after occurrence of buckling. (d) The corresponding computational radial view.

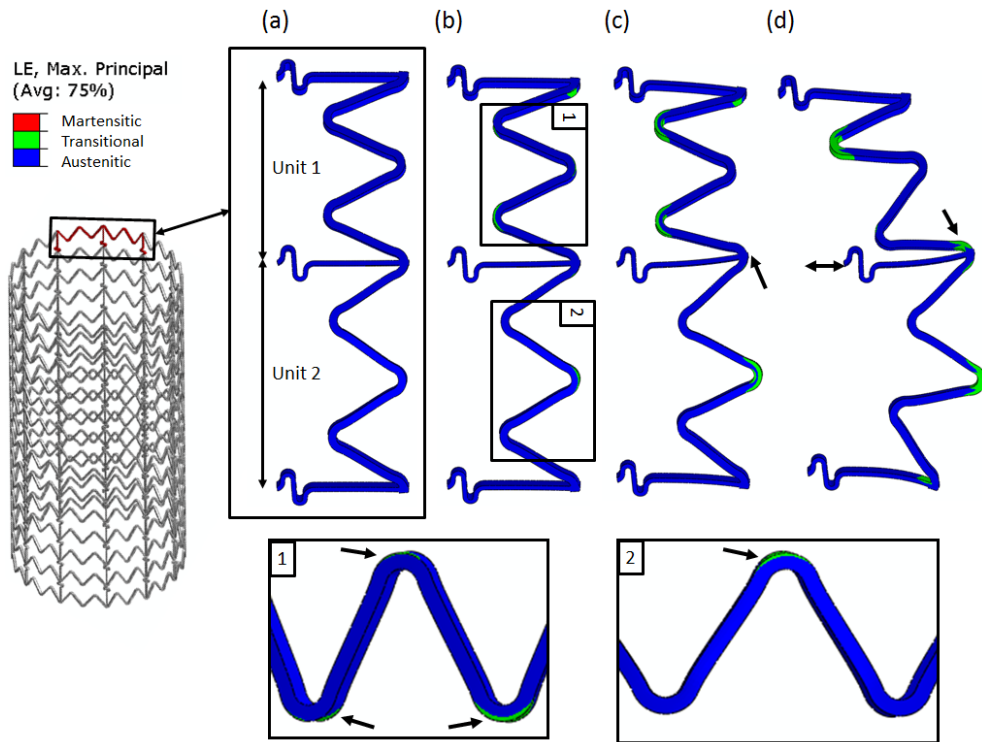


Fig. 2.9: Initiation of buckling in stent model focusing on two end units. Initial radial angles of the two units are 28.3° (Unit 1) and 31.2° (Unit 2). Maximum principal logarithmic strain is shown at radial displacements of (a) 0.573 mm (b) 0.689 mm (c) 0.817 mm and (d) 0.954 mm.

The percentage transitional material (i.e. the percentage of material in the transitional strain range) through a hinge in Unit 1 during loading is shown in Fig. 2.10. A significant increase in the percentage of transitional material is seen between 0.5 mm and 0.75 mm just before buckling occurs at 0.817 mm.

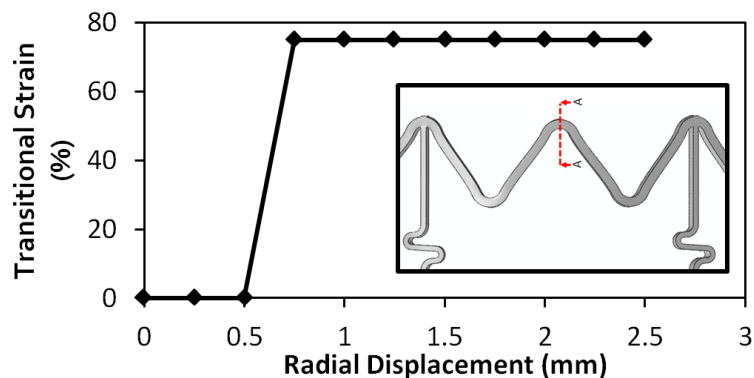


Fig. 2.10: Percentage transitional material in the transitional strain range through A-A of Unit 1 is plot against radial displacement. Percentage based on number of nodes within absolute transitional strain region.

2.2.3 Part 2: Stability Analysis

Due to its repeating unit structure, the stability of the stent during crimping depends on the stability of the repeating unit itself. A stability analysis is carried out using Abaqus/Standard to investigate how transitional strain distribution in a repeating unit affects its ability to resist axial displacement by varying geometric and material properties. This is performed using two 2D models: (i) a crimp analysis to determine the transitional strain levels within the unit during normal loading and, (ii) a sensitivity analysis to determine how sensitive the unit is to the observed buckling mechanism.

2.2.3.1 Unit Geometry and Material Properties

As the stent strut width and thickness (120 x 200 μm respectively) are small in comparison to the stent diameter (15 mm) it is possible to represent the repeating unit using 2D plane stress elements. During stent expansion (before heat setting) and crimping, the normal force applied to the surface of the stent results in the stent hinges being loaded tangentially, which can be replicated easily using the 2D configuration assuming all loads remain planar. A similar approach was used in the work of McGarry et al. (2004) and Donnelly et al. (2007). The as-cut unit is expanded to its equivalent nominal diameter through the use of displacement boundary conditions as described in Fig. 2.11. A mesh convergence analysis was performed in which the percentage difference Von Mises stress between the mesh used and a 2.3 times finer mesh was 0.68%.

The transitional strain distribution through the stent hinges is varied in the analyses in two ways. Strut length (L) is increased according to Table 2.2 to reduce the hinge angle (θ), which results in a reduction of the maximum strains experienced by the hinges during loading, and hence reduces the transitional strain distribution within the hinge. To remove the effect that a change in geometry may have on stent stability the austenitic Young's modulus (E_A) is varied according to Table 2.3. Changing E_A alters the strain at which the material enters the transitional stage, demonstrating how varying the amount of transitional strain within the same unit cell affects its stability. It should be noted that changes to E_A is for demonstration purposes only, to

compare the effects of varying transitional strain distributions within the same geometry.

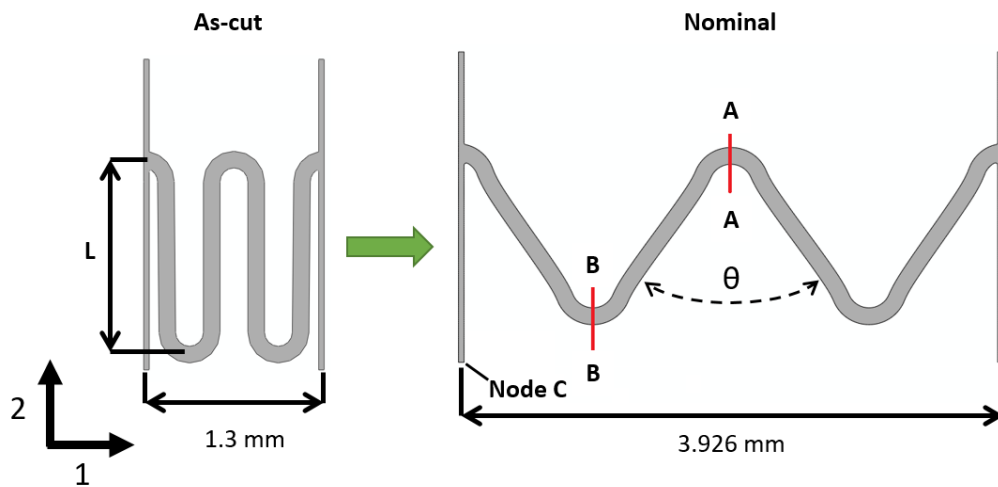


Fig. 2.11: Schematic diagram of the as-cut geometry deforming to the nominal repeating unit cell geometry. One edge of the unit cell is held in the horizontal direction while a horizontal displacement condition is placed on the opposite edge to expand it from 1.3 mm to 3.926 mm. One node is held in the vertical direction to remove rigid body motion. L is the strut length and θ is the hinge angle. Material properties used in the unit cell expansion are taken from Table 1. The geometry is meshed with 4,529 CPS4R plane stress elements.

Table 2.2: Summary of unit strut length (L) variation and corresponding hinge angle (θ) used in the stability analyses.

Unit	L (mm)	$\theta/2$ ($^\circ$)
A1	1.08	35.68
A2	1.98	19.69
A3	2.08	18.86
A4	2.38	16.52
A5	2.68	14.83
A6	3.18	12.95
A7	3.68	11.65

Table 2.3: Summary of material variation used in stability analysis showing the variation in: Austenitic Modulus (E_A) and Austenitic strain range (ϵ_A). For three different material models M1, M2 and M3.

Property/Material	M1	M2	M3
E_A (GPa)	53.0	80.0	20.0
ϵ_A (%)	0.82	0.54	2.17

2.2.3.2 Crimp Analysis

An analysis is performed to evaluate the transitional strain within the stent hinges during crimp. The expanded geometry is imported in its stress-free configuration and crimped to an equivalent diameter of 5 mm by reversing the displacement boundary conditions applied to expand the stent. During the crimping step the normal reaction force and logarithmic strain in the 1-1 direction along line A-A (Fig. 2.11) are recorded. The percentage of transitional material in the hinge is calculated along A-A assuming a symmetric tensile and compressive nitinol response. This assumption may result in a slight under/over-prediction of the amount of line A-A in the compressive transitional region during crimp but should not overtly affect the model results (Nagl et al. 2011). The analysis is repeated for each unit in Table 2.2 with each material variation in Table 2.3, resulting in 21 models in total.

2.2.3.3 Sensitivity Analysis

To evaluate the effect of the transitional strain region on stent unit stability, a defect or perturbation similar to that used in the 3D analysis is introduced into the simulations to remove symmetry so as to allow for a resulting axial displacement.

It is common to apply random geometric or material property variations to remove symmetry and introduce buckling to an analysis (Lagaros and Papadopoulos 2006; Asprone et al. 2013), but this can result in the defects driving the analysis, causing the simulations to over-predict the buckling effect. Instead a perturbation analysis can be performed to observe the sensitivity of the stent unit to buckling (Dumoulin and Cochelin 2000).

By applying a controlled perturbation displacement which mimics the deformation observed from Part 1 it is possible to evaluate the effect that the transitional strain has on unit cell stability in a repeatable manner. This sensitivity assessment model is

setup with the same boundary conditions as the crimp analysis and the perturbation is introduced half-way through the crimp step by placing a displacement boundary condition of -0.4 mm in the 1-1 direction on the nodes along the line B-B in Fig. 2.11. This forces the hinge at the left connector to close at a faster rate and increases the strain through the hinge, simulating the buckling mechanism. The axial displacement of node 'A' (Fig. 2.11) is recorded during the analysis to indicate the unit's ability to resist buckling. To easily compare the results of the various models, an instability parameter is assigned to each unit, which is evaluated using:

$$I_U = \frac{\Delta y}{\Delta x} \quad (2.1)$$

where I_U is the instability of the unit, Δy is the change in axial displacement of Node C (Fig. 2.11) and Δx is the change in horizontal displacement.

2.2.3.4 Results

2.2.3.4.1 Crimp Analysis

The percentage of hinge unit cross-section within the transitional strain range for a selection of models is shown in Fig. 2.12. It can be seen that the maximum percentage of transitional strain and its rate of increase are largest for shorter strut lengths (Fig. 2.12 (b)). In Fig. 2.12 (c) a similar trend can be seen for a reduction in E_A , with the longer ϵ_A significantly reducing the amount of transitional strain within the hinge during loading as expected.

Increasing strut length decreases the maximum strains through the stent hinges but it also results in a significant decrease in radial force as illustrated in Fig. 2.13.

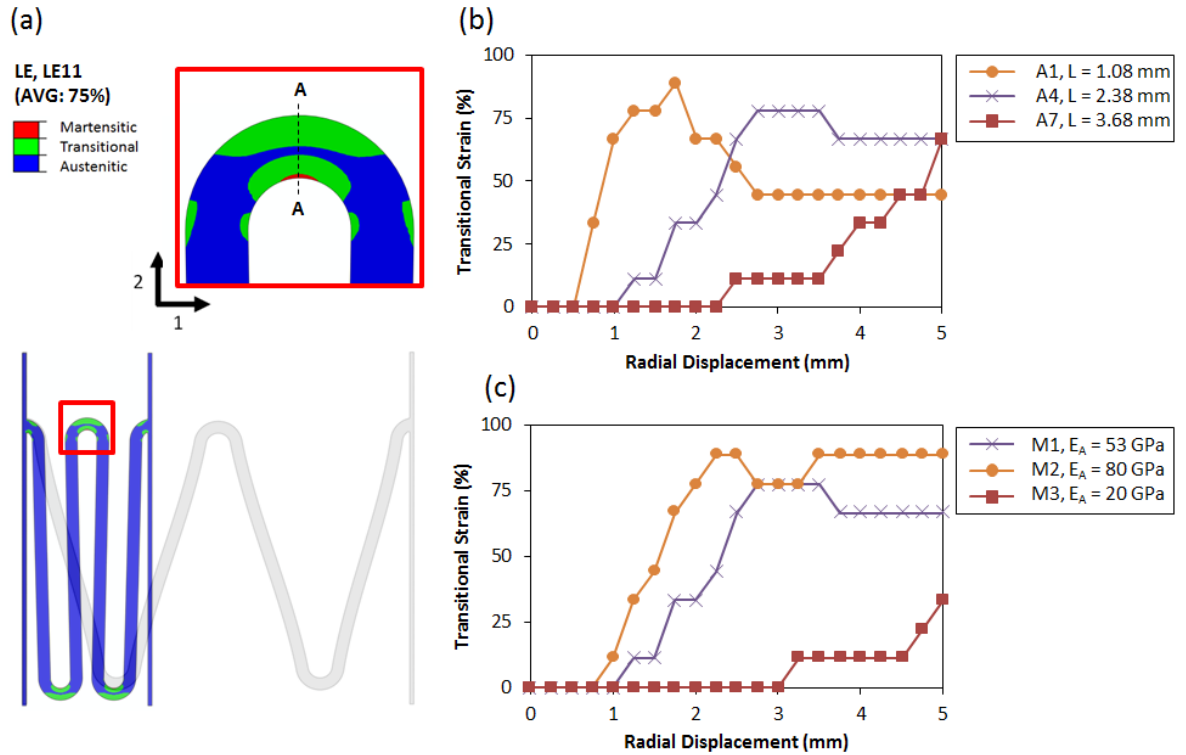


Fig. 2.12: (a) Contour plot of logarithmic strain in the 1-1 direction for A4 geometry and M1 material. Transitional strain percentage through the hinge during crimping of: (b) models with varying strut length (A1, A4 and A7) with material M1 properties (c) models with varying material properties (M1, M2 and M3) with A4 geometry. Transitional strain percentage through the hinge based on the number of nodes within the transitional strain region along line A-A in the 1-1 direction. It should be noted that a drop in the percentage of transitional strain occurs when a node passes into the martensitic strain range during crimping.

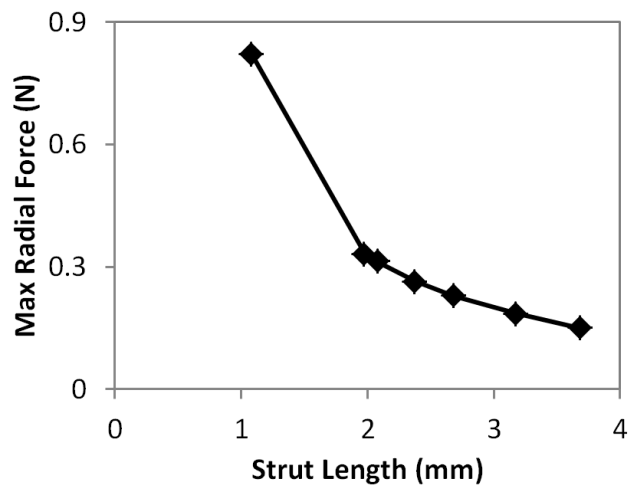


Fig. 2.13: Plot of maximum radial force versus strut length for all geometries in Table 2 using M1 properties (Table 3).

2.2.3.4.2 Sensitivity Analysis

From the results of the sensitivity analysis it can be seen that as strut length increases the maximum axial displacement and the rate of axial displacement decrease (Fig. 2.14 (a)). In Fig. 2.14 (b) a significant decrease is also shown for these values with increasing ϵ_A .

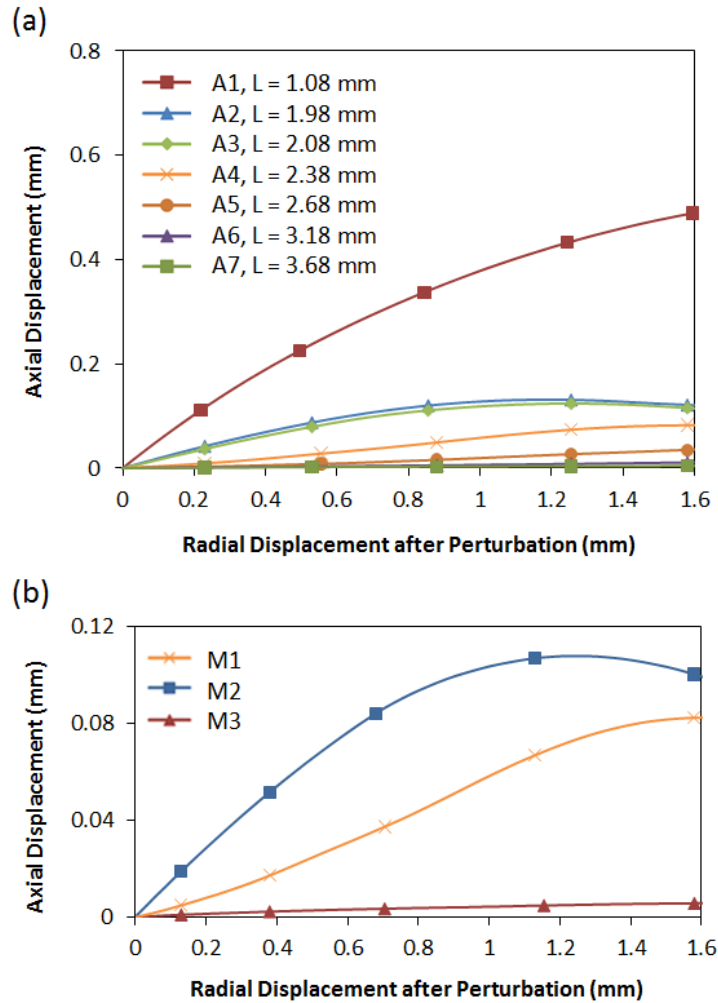


Fig. 2.14: Axial displacement plotted against radial displacement after applying the perturbation at a radial displacement of 2.5 mm. Results are shown for: (a) changes in strut length (Table 2) and material M1 (Table 3) (b) Changes in material properties (Table 3) for A4 geometry (Table 2).

The curves in Fig. 2.15 summarise the combined effects of geometric and material property changes. The plot shows that for shorter struts, with a shorter transitional range (or larger austenitic range (Table 2.3)), the instability of a unit can decrease significantly, and that for longer strut lengths material property changes become much less significant.

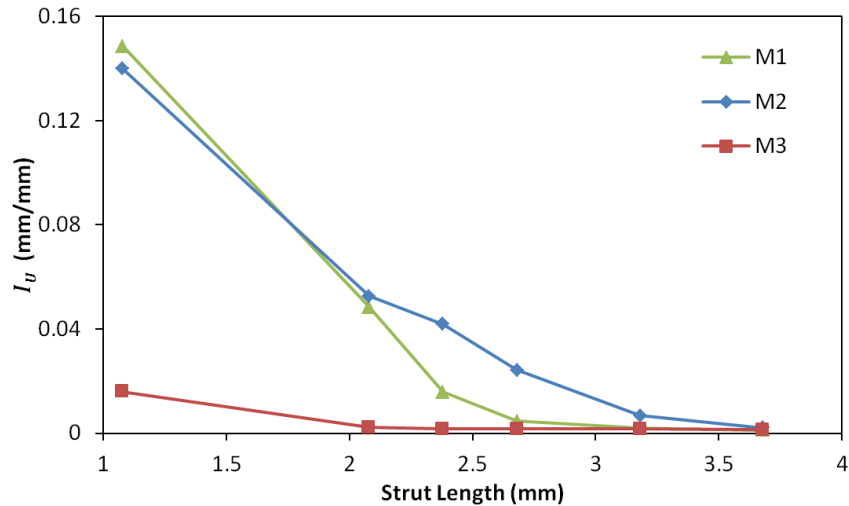


Fig. 2.15: Instability (I_v) of each model was calculated using Eq. 2.1 at a radial displacement of 3 mm.

2.2.4 Part 3: Stent Re-design

Part 2 of the study investigated the effect that transitional strain distribution had on the stability of a repeating unit cell. It is shown in these results that an increase in strut length can significantly increase the stability of the unit, but this can result in a considerable reduction in radial force, which may be unacceptable. In this section the findings of Part 2 are implemented to increase the stability of the stent unit. The effect of small changes to strut width and hinge radii on radial force and instability are then observed, with the aim of designing and fabricating a buckling resistant stent with an adequate radial force. Radial force can also be improved by increasing tubing thickness, but this was not considered in this study as new nitinol tubing and material data would be required to validate the finite element models.

2.2.4.1 Unit Re-design

To perform the stent re-design a base unit first needs to be selected. Ideally the unit should have an instability tending towards zero and have a reasonable radial force. In this instance unit A6 is chosen as it has a low instability index (almost three times smaller than that of unit A5 and only just over 50% greater than unit A7 (Fig. 2.15)). The maximum radial force of unit A6 is almost 20% more than unit A7 and only 6% smaller than unit A5 (Fig. 2.13). However, further modification is required to unit A6 as the predicted radial force is much lower than the original unit. In this instance the effect of small changes to strut width and hinge radii are examined as per Table 2.4 and Fig. 2.16. A stability analysis similar to that described in Sections 2.2.3.2 and

2.2.3.3 is carried out to select an appropriate modified geometry with increased radial force but low instability (I_U). It should be noted that the reduction in R1 between unit A6 and B1 (Table 2.4) may introduce stress concentrations that would not be ideal in fatigue. However, this aspect was not considered as the main goal of the work was to remove buckling from the stent design.

Table 2.4: Summary of changes made to the A6 unit, modified units labelled B 1-4. R1 is the inner hinge radius, R2 is the outer hinge radius, X1 is the vertical distance between the centres of the hinge radii and W1 is the strut width (Figure 16). The strut length and unit radial angle remain constant for each unit. *Ends were squared.

Variables/Units	A6	B1	B2	B3	B4
R1 (mm)	0.1	0.01	0.01	0.01	0.01
R2 (mm)	0.22	0.19	0.19	0.19	0.19
X1 (mm)	0	0	0	0.15	0.11*
W1 (mm)	0.12	0.12	0.18	0.18	0.18

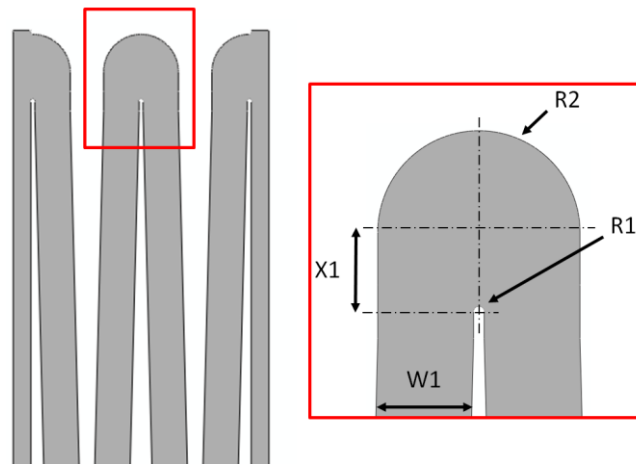


Fig. 2.16: Schematic of unit B4 (Table 4) highlighting the relevant variables. R1 is the inner hinge radius, R2 is the outer hinge radius, X1 is the vertical distance between the centres of the hinge radii and W1 is the strut width.

2.2.4.2 Radial Force

Following on from the analysis in Section 2.2.4.1 above, the B4 geometry is selected from Table 2.4 to create a full stent geometry containing 12 radial and 8 longitudinal units, which is symmetric about the centre as with the A1 stent. The as-cut geometry is expanded using the same angular variation applied in Section 2.2.2.3 and material properties from Table 2.4 are used. A radial force test of the stent is simulated as per

Section 2.2.2.4. A B4 stent is also fabricated and experimentally tested to validate the simulation and show that the stent resists axial buckling.

2.2.4.3 Results

The effect that the changes make to the radial force and instability (I_U) of the A6 unit are shown in Fig. 2.17 (a) and (b) respectively. Each incremental change results in an increase in radial force, while changes to the instability (I_U) varied but improved overall. The B4 expanded unit and full 3D stent geometry are shown in Fig. 2.18.

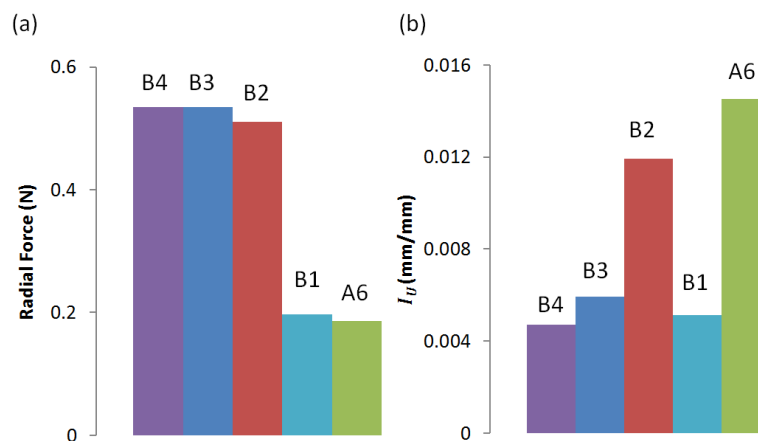


Fig. 2.17: Summary results for stent re-design showing (a) Maximum radial force (b) Instability.

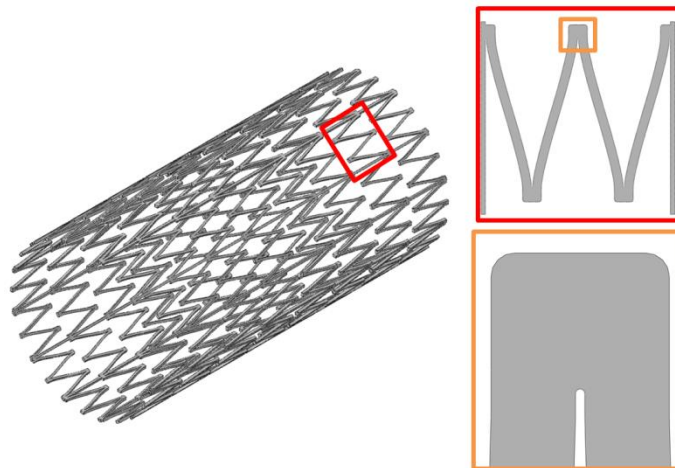


Fig. 2.18: Schematic of the expanded B4 stent and repeating unit with the final hinge configuration highlighted.

The results of the radial force analysis on the B4 unit model are shown in Fig. 2.19. The computational and experimental match well and no sudden drop in radial force is recorded. However, the radial force exerted by the redesigned stent is significantly lower than that of the original buckling stent (Fig. 2.7). This is discussed further in the

Discussion (Section 2.3). The resulting stent design is also expected to decrease stent flexibility due to the increase in strut length and reduction in longitudinal units. This is not expected to affect the trackability or performance of the stent due to its delivery with the use of a bronchoscope and deployment into a relatively straight geometry in the tracheobronchial region.

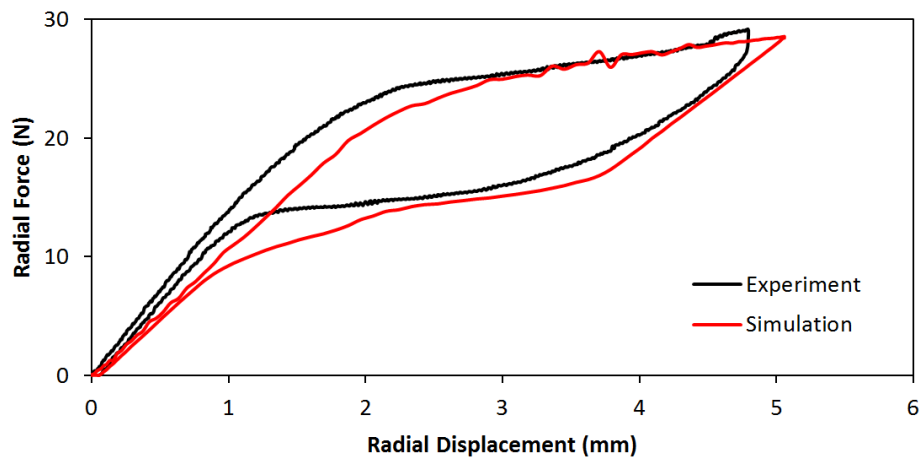


Fig. 2.19: Experimental and computational results for the radial force testing of the B4 stent. There is a good match between the experimental and computational results with no indication of stent buckling.

2.3 Discussion

Nitinol's super-elasticity allows stents to reach large enough strains to be crimped from an expanded configuration to a delivery diameter without plastically deforming the stent hinges, but the design of a functional nitinol stent can be hampered by the materials non-linear properties. Above $\sim 1\%$ strain austenite begins to transform to martensite, resulting in a load plateau with a large change in strain for a small increase in load. It is proposed in this study that the plateau region could be responsible for destabilising the hinges in a stent which can ultimately lead to buckling of the stent.

The finite element method is used to identify the buckling mechanism observed in a prototype tracheobronchial stent by replicating the crimping of the stent during radial force testing. The introduction of small defects to the stent geometry removes symmetry within the model and allows the asymmetric loading and displacement of the stent. A good match between the experiment and computational model is shown

in Fig. 2.7 and Fig. 2.8, where the experimental buckling is captured by a sudden drop in radial force and axial displacement of stent units.

A possible explanation for the buckling observed in this work is provided here. Firstly, consider a stent hinge during crimping. Initially all of the material within the stent hinge is austenitic, but as the stent diameter reduces and the strain within the hinge increases part of this hinge enters the transitional stage. As the transitional stage has a much lower stiffness than the austenitic (or even martensitic) stage (Fig. 2.1), a reduction in stiffness is to be expected similar to that observed in plastic hinges for elastic-perfectly-plastic materials. While the overall stiffness of the hinge is also dependent on factors like the hinge curvature and strut length, the stiffness of the base material can have a significant effect. If the amount of transitional material within the hinge tends towards 100% then the stiffness tends towards zero. This means that large displacement will be allowed under relatively small changes in force which makes the hinge unstable. If you consider that each repeating unit is made up of five hinges, and if all of these hinges are unstable then the unit itself is unstable. This can result in sudden stent buckling as observed. Which can be seen in Fig. 2.9 where the reduction in stiffness of Unit 1 results in connector bending, followed by stent buckling.

The effect of nitinol's transitional plateau region on stent stability is highlighted through the use of a stability analysis where geometric and material properties are varied to alter the strain experienced by the repeating unit hinges. Upon comparing the effect that altering strut length has on stent axial displacement (Fig. 2.14(a)) with the strains observed in the stent hinges during loading (Fig. 2.12(b)) it can be seen that high maximum transitional strains, accompanied by high rates of transitional strain, show a susceptibility to buckling. The same observation is true for increasing the strain to the transitional range (Fig. 2.12 (c)), resulting in increasing axial displacement (Fig. 2.14(b)).

In this study an instability parameter (I_U) was introduced to indicate how unstable stent units are through the use of a single scalar. Using this value allows easy comparison between the effects that geometric and material properties have on

stent unit stability. From Fig. 2.15 it can be seen that a large increase in strut length significantly reduces the instability of the stent unit, this reduction is also observed for a longer strain to the transitional plateau (Table 2.3) for all units. These decreases in instability are expected as both modifications result in a reduction in the amount of transitional strain within the hinge during crimp. However, a large increase in strut length (decrease in hinge angle) also introduces an unexpected geometric effect whereby below a certain angle, the stability of the unit no longer depends on the amount of transitional material within the hinge, because the unit has limited room in which to axially displace. Shorter strut lengths and larger hinge angles reach higher strains faster leaving more room for compliant hinges to rotate and cause axial displacement. This cannot happen with longer struts and smaller angles due to the restricted angles within which the hinges can rotate and displace.

The A6 unit geometry is initially selected to be used in the stent re-design due to its low instability (Fig. 2.15) and slightly higher radial force than the A7 geometry (Fig. 2.13). However the radial force of this unit is lower than acceptable and so a second stability analysis is performed to increase the radial force while maintaining a low instability. From the results of this analysis (Fig. 2.17) it can be seen that an increase in radial force can be accomplished by making relatively small changes to the stent unit hinges and strut width while also reducing the stent unit instability. The B4 unit (Table 2.4) is used to fabricate a stent that successfully resists axial buckling both computationally and experimentally (Fig. 2.19), showing that axial buckling is successfully removed from the new design. The radial force of the B4 stent is lower than that of the original A1 stent (Fig. 2.7), but the chronic outward force based on a typical 20% oversizing is adequate compared to a commercially available tracheobronchial device which was found to have a chronic outward force of 11 N. If a stent with comparable radial force was required this could be easily implemented by increasing stent tube thickness, which increases radial force with little change to the in-plane strain distributions.

2.4 Conclusions

This study has shown that the transitional stage of nitinol loading can have an effect on the stability of a stent during crimp. If the amount of transitional strain within the

stent hinges becomes very high it leads to a reduction in hinge stiffness which can allow axial buckling caused by rotation and displacement of the compliant unit hinges. The stability of a nitinol stent unit can be increased by reducing the amount of transitional strain seen through the hinge during loading; this can be accomplished readily by changing the geometry of the stent repeating unit. It was also shown that reduced hinge angles can minimise the effect of this transitional strain effect. In summary this study provides significant new insights to the design process for self-expanding stents, giving guidance on design features to optimize stability during crimping and deployment.

A.2 Appendix 2

A.2.1 Stent Stiffness Post-buckling

In this section the effect of deploying a buckled stent in the respiratory tree is considered, which highlights some of the disadvantages associated with this type of buckling. In general tracheobronchial stents are deployed with an oversizing of around 20%. For a 15 mm diameter stent this corresponds to 12 mm. In Fig. A2.1 below the original stent is shown during computational radial force unloading at a diameter of 12 mm. The stent is still in its buckled configuration as it has not been allowed to return to its original diameter (where it would take up its symmetric, unbuckled configuration).

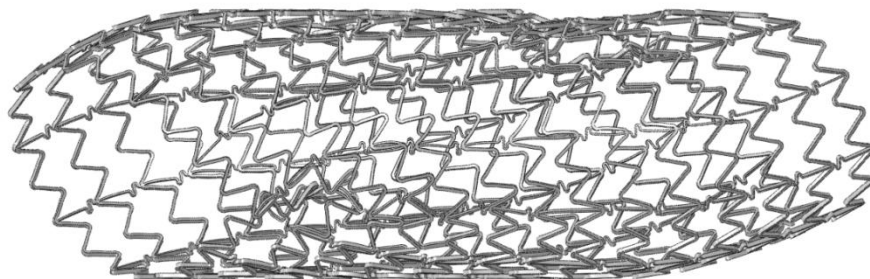


Fig. A2.1: Original stent at 12 mm during unload still in a buckled configuration.

While the stent can still conceivably provide scaffolding support in this configuration, it has a number of disadvantages. A buckled stent will have a lower overall radial stiffness than a non-buckled stent due to the reduction in geometric rigidity, resulting in a drop in mechanical support during extreme loading conditions (e.g. during coughing) which could lead to an increased chance of migration. To illustrate this a further analysis was performed where after crimping to 5 mm the stent was unloaded to 12 mm and then reloaded to 9 mm. From the corresponding radial force plot shown in Fig. A2.2 it can be seen that there is a significant reduction in stent stiffness during reloading which could potentially increase migration risk. Apart from this large strut deformations caused by the reduced stiffness could decrease the fatigue life of the stent owing to increased strain amplitudes, and additional axial displacement of stent rings could cause unnecessary irritation to the surrounding tissue causing unwanted inflammatory responses. So even though in theory this device could still

perform as a stent in the tracheobronchial region, these attributes are undesirable and should be removed from the design.

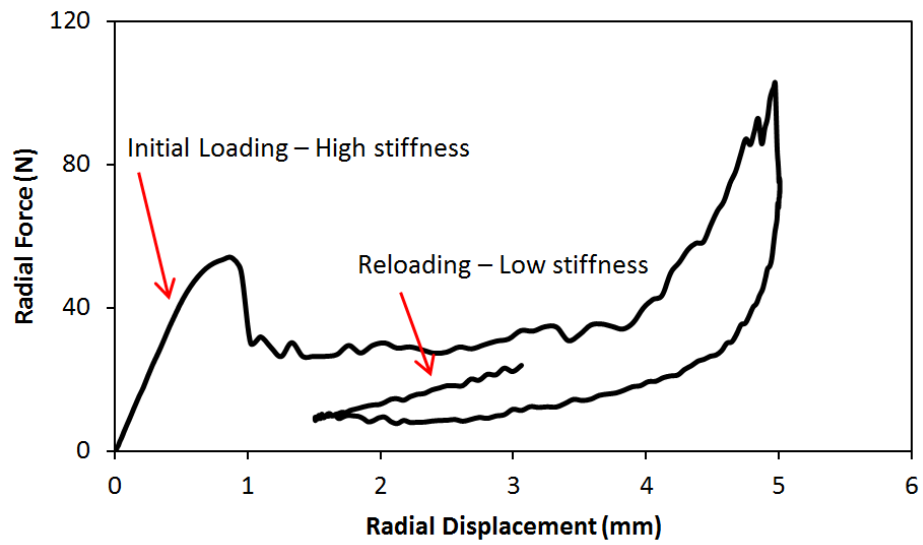


Fig. A2.2: Results of the reloading model. Stent crimped by 5 mm (to 5 mm OD) unloaded 3.5 mm (to 12 mm OD) and re-loaded 1.5 mm (to 9 mm OD).

References

- Asprone D, Auricchio F, Menna C, Morganti S, Prota A, Reali A (2013) Statistical finite element analysis of the buckling behavior of honeycomb structures. *Compos Struct* 105:240–255. doi: 10.1016/j.compstruct.2013.05.014
- Auricchio F, Taylor R, Lubliner J (1997) Shape-memory alloys: macromodelling and numerical simulations of the superelastic behavior. *Comput methods Appl* 146.3:281–312.
- Azaouzi M, Lebaal N, Makradi A, Belouettar S (2013) Optimization based simulation of self-expanding Nitinol stent. *Mater Des* 50:917–928. doi: 10.1016/j.matdes.2013.03.012
- Azaouzi M, Makradi A, Belouettar S (2012) Deployment of a self-expanding stent inside an artery: A finite element analysis. *Mater Des* 41:410–420. doi: 10.1016/j.matdes.2012.05.019
- Bolliger CT, Heitz M, Hauser R, Probst R, Perruchoud AP (1996) An Airway Wallstent for the treatment of tracheobronchial malignancies. *Thorax* 51:1127–9.
- Bolliger CT, Sutedja TG, Strausz J, Freitag L (2006) Therapeutic bronchoscopy with immediate effect: laser, electrocautery, argon plasma coagulation and stents. *Eur Respir J* 27:1258–71. doi: 10.1183/09031936.06.00013906
- Chen L, Jingfeng S, Bing C, Zhiyong X (2012) Numerical Analysis of the Influence of Stent Parameters on the Fatigue Properties. *Mod Appl Sci* 6:23–27. doi: 10.5539/mas.v6n4p23
- Chin CS, Litle V, Yun J, Weiser T, Swanson SJ (2008) Airway stents. *Ann Thorac Surg* 85:S792–6. doi: 10.1016/j.athoracsur.2007.11.051
- Chung WJ, Cho JW (1998) On the dynamic effects of explicit FEM in sheet metal forming analysis. *J Mater Process Manuf* 15:750–776.
- Donnelly EW, Bruzzi MS, Connolley T, McHugh PE (2007) Finite element comparison of performance related characteristics of balloon expandable stents. *Comput Methods Biomech Biomed Engin* 10:103–110. doi: 10.1080/10255840601086234
- Dooms C, De Keukeleire T, Janssens A, Carron K (2009) Performance of fully covered self-expanding metallic stents in benign airway strictures. *Respiration* 77:420–6. doi: 10.1159/000203364
- Duerig TW, Tolomeo DE, Wholey M (2000) An overview of superelastic stent design. *Minim Invasive Ther Allied Technol* 9:235–46. doi: 10.1080/13645700009169654
- Dumoulin C, Cochelin B (2000) Mechanical behaviour modelling of balloon-expandable stents. *J Biomech* 33:1461–70.
- Fernández-Bussy S, Majid A, Caviedes I, Akindipe O, Baz M, Jantz M (2011) Treatment of airway complications following lung transplantation. *Arch Bronconeumol* ((English Ed 47:128–133. doi: 10.1016/S1579-2129(11)70031-3
- Freitag L (2010) Airway stents. In: Strausz J, Bolliger CT (eds) *Interventional Pulmonology*. European Respiratory Society Journals Ltd, Sheffield, pp 190–217
- Furukawa K, Ishida J, Yamaguchi G, Usuda J, Tsutsui H, Saito M, Konaka C, Kato H (2010) The role of airway stent placement in the management of tracheobronchial stenosis caused

- by inoperable advanced lung cancer. *Surg Today* 40:315–20. doi: 10.1007/s00595-008-4058-2
- García A, Peña E, Martínez MA (2012) Influence of geometrical parameters on radial force during self-expanding stent deployment. Application for a variable radial stiffness stent. *J Mech Behav Biomed Mater* 10:166–75. doi: 10.1016/j.jmbbm.2012.02.006
- Ghriallais RN, Bruzzi M (2014) Self-expanding stent modelling and radial force accuracy. *Comput Methods Biomech Biomed Engin* 17:318–333. doi: 10.1080/10255842.2012.683427
- Gong X, Pelton A, Duerig TW, Rebelo N, Perry K (2004) Finite element analysis and experimental evaluation of superelastic Nitinol stent. SMST, Society, Menlo Park, CA
- Kleinstreuer C, Li Z, Basciano C a, Seelecke S, Farber M a (2008) Computational mechanics of Nitinol stent grafts. *J Biomech* 41:2370–8. doi: 10.1016/j.jbiomech.2008.05.032
- Lagaros ND, Papadopoulos V (2006) Optimum design of shell structures with random geometric, material and thickness imperfections. *Int J Solids Struct* 43:6948–6964. doi: 10.1016/j.ijsolstr.2006.02.019
- Madden BP, Park JES, Sheth A (2004) Medium-term follow-up after deployment of ultraflex expandable metallic stents to manage endobronchial pathology. *Ann Thorac Surg* 78:1898–902. doi: 10.1016/j.athoracsur.2004.05.062
- McGarry JP, O'Donnell BP, McHugh PE, McGarry JG (2004) Analysis of the mechanical performance of a cardiovascular stent design based on micromechanical modelling. *Comput Mater Sci* 31:421–438. doi: 10.1016/j.commatsci.2004.05.001
- Nagl F, Siekmeyer G, Quellmalz M, Schuessler A (2011) A comparison of different nitinol material data sources for finite element analysis. *J Mater Eng Perform* 20:737–744. doi: 10.1007/s11665-011-9910-7
- Otsuka K, Ren X (2005) Physical metallurgy of Ti–Ni-based shape memory alloys. *Prog Mater Sci* 50:511–678. doi: 10.1016/j.pmatsci.2004.10.001
- Rebelo N, Perry M (2000) Finite element analysis for the design of Nitinol medical devices. *Minim Invasive Ther Allied Technol* 9:75–80. doi: 10.3109/13645700009063053
- Rieu R, Barragan P, Masson C, Fuseri J, Garitey V, Silvestri M, Roquebert P, Sainsous J (1999) Radial force of coronary stents: a comparative analysis. *Catheter Cardiovasc Interv* 46:380–91. doi: 10.1002/(SICI)1522-726X(199903)46:3<380::AID-CCD27>3.0.CO;2-J
- Robertson SW, Pelton AR, Ritchie RO (2012) Mechanical fatigue and fracture of Nitinol. *Int Mater Rev* 57:1–37. doi: 10.1179/1743280411Y.0000000009
- Ryu YJ, Kim H, Yu C, Choi JC, Kwon YS, Kim J (2006) Comparison of natural and dumon airway stents for the management of benign tracheobronchial stenoses. 748–754. doi: 10.1111/j.1400-1843.2006.00955.x
- Saito Y, Imamura H (2005) Airway stenting. *Surg Today* 35:265–70. doi: 10.1007/s00595-004-2942-y
- Shen X, Yi H, Ni Z (2008) Effects of stent design parameters on radial force of stent. 2008 2nd Int Conf Bioinforma Biomed Eng 1:1712–1716. doi: 10.1109/ICBBE.2008.756

Stoeckel D, Pelton A, Duerig T (2004) Self-expanding nitinol stents: material and design considerations. *Eur Radiol* 14:292–301. doi: 10.1007/s00330-003-2022-5

Chapter 3

Evaluation of Cover Effects on Bare Stent Mechanical Response

Published in: The Journal of the Mechanical Behavior of Biomedical Materials, 2016
DOI: 10.1016/j.jmbbm.2016.04.023

Abstract

Covered tracheobronchial stents are used to prevent tumour growth from reoccluding the airways. In the present work a combination of experimental and computational methods are used to present the mechanical effects that adhered covers can have on stent performance. A prototype tracheobronchial stent is characterised in bare and covered configurations using radial force, flat plate and a novel non-uniform radial force test, while computational modelling is performed in parallel to extensively inform the physical testing. Results of the study show that cover configuration can have a significant structural effect on stent performance, and that stent response (bare or covered) is especially loading specific, highlighting that the loading configuration that a stent is about to be subjected to should be considered before stent implantation.

3.1 Introduction

Lung cancer was responsible for 24% of male and 14% of female cancer deaths worldwide in 2012 (Islami et al. 2015). Around 30% of all lung cancer patients progress to develop problems with central airway obstruction due to extrinsic or intrinsic tumour growth restricting airflow through the airways (Bolliger et al. 2006; Lee et al. 2010). Primary tumours causing obstruction in the airway are rare, occurring in less than 0.1% of cases (Ernst et al. 2004; Macchiarini 2006), the obstruction is most often caused due to extrinsic compression from bronchogenic,

oesophageal and thyroid carcinomas (Ernst et al. 2004). The majority of these patients present with impending suffocation with >50% airway obstruction, leaving tracheobronchial stenting as their only option (Bolliger et al. 2006). In these instances the stents are used for palliative purposes, but tracheobronchial stents are also extensively utilized for benign cases such as treating malacia (collapsing airways), supporting benign strictures and sealing fistulas (Freitag 2010).

Tracheobronchial stents are tubular scaffolds that restore patency to the blocked airways by providing support to the affected area. Three families of tracheobronchial stents are commercially available including: bare metal, covered metal and polymeric. Covered metal and polymeric stents are typically used in malignant cases to prevent reocclusion of the airway from tumour ingrowth through open stent struts (Freitag 2010). Although there is no favoured stent type, covered metal stents have the majority of the market share (Bolliger et al. 2006).

Typically covered metal stents are made from nitinol and covered with a flexible polymer. The superelastic properties of nitinol allow a stent to be crimped from a large freely expanded diameter to a small delivery diameter without plastic deformation. Upon crimping, the stents are placed in a delivery device which can be tracked to the diseased location using a flexible bronchoscope under local anaesthetic. Once positioned, the outer sheath is removed and the stent deploys into the airway using its inherent elasticity. The force exerted by the expanding stent pushes the stenosis against the airway wall and restores airflow to the affected region. Polymeric materials like PTFE (polytetrafluoroethylene), silicone and polyurethane (PU) are commonly used to cover metallic stents (Farhatnia et al. 2013). These biocompatible materials can be attached to the stent using processes such as suturing, electrospinning, moulding, casting or dip coating (Farhatnia et al. 2013), and can extend over the entire length of the stent or just cover a particular region. To allow a low profile for the crimped stent the cover needs to be relatively thin but still capable of preventing tumour ingrowth.

There is currently no ideal tracheobronchial stent as all commercially available designs are associated with high complication rates (Trisolini et al. 2006; Chung et al.

2008; Gildea et al. 2008; Dooms et al. 2009; Furukawa et al. 2010; Fernández-Bussy et al. 2011; Ost et al. 2012). In particular covered tracheobronchial stents suffer from high levels of migration and can be prone to fracture (Chung et al. 2008; Dooms et al. 2009; Chung et al. 2011; Sosa and Michaud 2012). The first aspect of the present study is concerned with understanding the effect that an adhered cover can have on stent mechanical response and its possible implications for stent design.

To date much work has been performed in the literature on the design and testing of bare stents for a range of applications in the body (for example (Rieu et al. 1999; Chen et al. 2012; García et al. 2012; Grogan et al. 2012; Azaouzi et al. 2012; Ghriallais and Bruzzi 2014; Boland et al. 2015b)), but fewer studies have focused on covered stents (for clarity it should be noted that the word “bare” in this chapter refers to an uncovered stent (i.e. a stent without a cover attached to it). Similarly, the word “covered” is used to describe a stent that has a cover attached to it.). Initial finite element evaluations of covered stents largely ignored the mechanical effects of covers on stent response due to their considerably lower stiffness in comparison to the stent structure (Kleinstreuer et al. 2008; Prasad et al. 2011; Prasad et al. 2013). De Bock et al. experimentally performed and computationally modelled radial force and flat plate tests on a number of commercially available stent grafts, and showed through computational modelling that stent covers can have an influence on stent response (De Bock et al. 2013). Another group has performed a number of studies in the area of stent graft modelling and used a more robust material model for the graft including in-plane elastic behaviour and bending behaviour (Demanget et al. 2012a; Demanget et al. 2012b; Demanget et al. 2013; Perrin et al. 2014; Perrin et al. 2015). These models were validated by comparing the stent centreline position during bending tests performed on commercially available stents, but mechanical attributes such as radial force and flat plate tests which are commonly used to evaluate stent performance were not assessed. All of the above studies used fully integrated shell element cover representations which allow for an accurate representation of the cover folding and cover-stent interaction that occurs during stent loading once the covers are considered suitably thin. To the best of the authors’ knowledge none of the above studies have experimentally compared bare and covered stent mechanics.

When specifically considering the computational modelling of covered tracheobronchial stents no previous work has been performed. Malvè et al. have performed fluid-solid interactions using bare metal and fully polymeric stent representations in the tracheal region (Malvè et al. 2010; Malvè et al. 2011c; Malvè et al. 2011a; Malvè et al. 2011b; Malvè et al. 2012; Malvè et al. 2014).

Another aspect of interest in tracheobronchial stenting is the physiological loading that the stent undergoes in the airways. *In-vivo* the stents are subjected to two loading configurations: loading from tissue deformation caused by gas flow through the lung and loading from the stenosis-airway arrangement. Unlike coronary arteries which experience a generally uniform deformation from pulsatile blood flow, the natural deformation of the airways is asymmetric. The upper airways are composed of c-shaped rings of cartilage inter-connected with soft membranous tissue; during coughing these rings allow the airways to collapse non-uniformly to increase air velocity and improve cough effectiveness (Irwin 1977; Lyubimov 2001). Stents are deployed when the stenosis occludes over 50% of the airway (Hugo Marquette et al. 1995; Bolliger et al. 2006) resulting in non-cylindrical loading configurations. This non-cylindrical geometry combined with non-uniform deformation leads to complex stent loading which can result in stent failure (Trisolini et al. 2006; Doods et al. 2009). Common test methods like radial force testing and crush testing as suggested by the Food and Drug Administration's (FDA) guidance for stent testing (Food and Drug Administration 2010) fail to capture this multifaceted *in-vivo* loading behaviour. The lack of sufficient detail in these guidelines has previously been commented on by Conway et al. (2012; 2014) in relation to the inadequate requirements for *in-silico* computational simulations.

More realistic stent loading conditions have been investigated for *in-vitro* testing using excised tissue in combination with pressure deformation and static loading techniques (Freitag et al. 1994; Freitag et al. 1995). However, these methods are difficult to repeat due to the natural variation in tissue properties. Animal models with surgically created benign stenoses have also been developed (Hugo Marquette et al. 1995; Bolliger et al. 1999; Korpela et al. 1999) to simulate the loading seen clinically, though useful for examining stent behaviour these methods are neither

repeatable nor practical for stent testing. The second aspect of this work investigates the use of a simple bench-top test that could be used to evaluate the effect of airway geometry and deformation on stent response.

The objective of the present study is to evaluate the mechanical effect that adhered covers can have on tracheobronchial stent response through the use of experimental and computational methods. This is accomplished by experimentally testing bare and adhered cover stents using commonly performed tests in combination with a novel non-uniform radial force test. Finite element models are developed in parallel to these tests to provide a more thorough understanding of the mechanical effect the adhered cover has on stent response.

3.2 Materials and Methods

3.2.1 Stent Fabrication

3.2.1.1 Bare Stents

Six prototype tracheobronchial stents were fabricated by Admedes Schuessler (Pforzheim, Germany). The stents were laser-cut from nitinol tubing with a 5.0 mm OD and a 0.23 mm thickness. Each stent was expanded and shape set using a cylindrical mandrel, and then electropolished. The expanded stent dimensions were approximately 15 x 30 x 0.195 mm (OD x Length x thickness) (Fig. 3.1 (a)).

3.2.1.2 Adhered Cover Stents

A Polycarbonate-Urethane (PCU) cover was adhered to the entire length of three stents in two steps. First a polyurethane adhesive was applied to the length of the bare stent to improve adhesion between the cover and stent. This process causes adhesive to form between the stent struts as shown in Fig. 3.1 (b). The PCU cover was then sprayed onto the stent using a spray atomization procedure of dissolved polyurethane as describes elsewhere (Nadzeyka et al. 2014). A rotating spindle and linearly translating spraying nozzle ensure uniform cover thickness. For coating the stents, a material flow rate of 2 ml/min, a pressure of 0.8 bar and a spraying duration of 3 minutes per stent was used. A fully covered stent is shown in Fig. 3.1 (b).

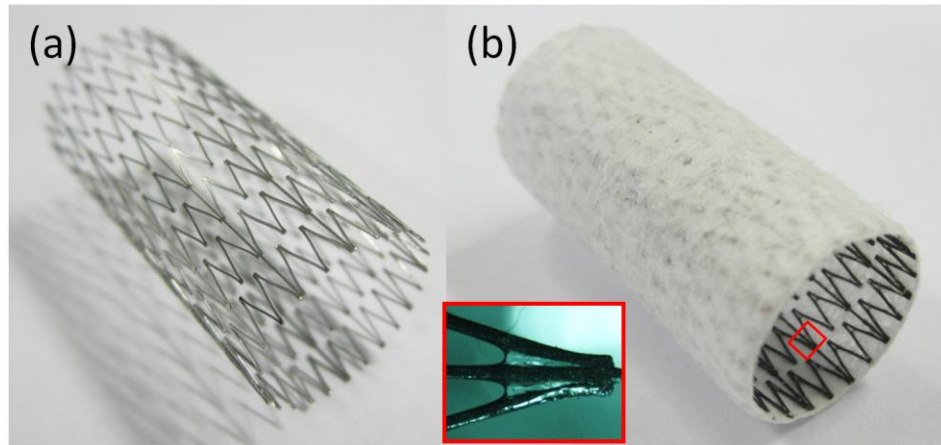


Fig. 3.1: (a) Bare stent (b) Covered stent. Inset shows detail of adhesive between stent struts.

3.2.2 Material Properties

3.2.2.1 Nitinol

Tensile testing at 37 °C was performed on cylindrical samples cut from the same tube used to fabricate the stents, and these results were used to calibrate the Aurrichio in-built nitinol constitutive model in Abaqus (DS SIMULIA, USA) as described previously in McGrath et al. (2014). Table 3.1 shows the parameters used for the nitinol material model assuming no plasticity and symmetric tensile and compressive properties, as is common in the literature (García et al. 2012; Ghriallais and Bruzzi 2014; McGrath et al. 2014). The material model fit is shown in Fig. 3.2.

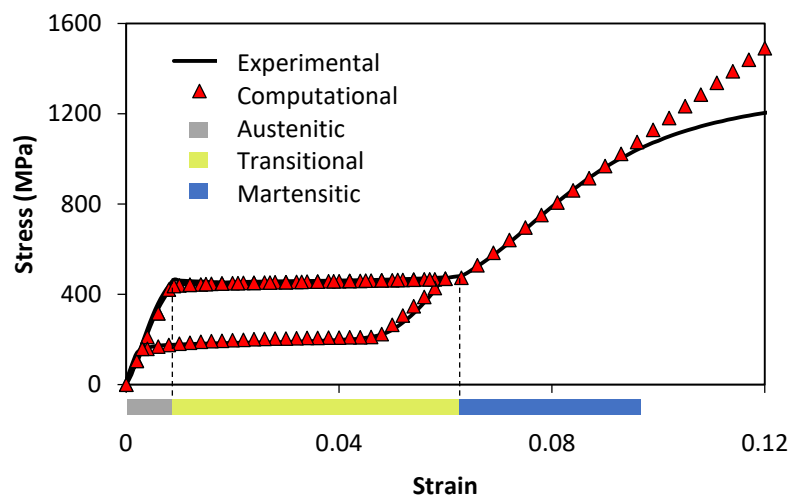


Fig. 3.2: Nitinol material model computational fit to average tensile data. The transitional stage of nitinol (yellow region) is characterised by a small increase in stress resulting in a large increase in strain. This is caused by the stress induced transformation from austenite (green region) to martensite (blue region).

Table 3.1: Nitinol material properties used in the Abaqus constitutive model.

Parameter	Value
Austenite Elasticity (MPa)	53001
Austenite Poisson's Ratio	0.3
Martensite Elasticity (MPa)	21500
Martensite Poisson's Ratio	0.3
Transformation Strain	0.038
Start of Transformation Loading (MPa)	434
End of Transformation Loading (MPa)	500
Reference Temperature (°C)	37
Start of Transformation Unloading (MPa)	210.3
End of Transformation Unloading (MPa)	138.7
Start of Transformation Stress During Loading in Compression (MPa)	434
Volumetric Transformation Strain	0.038

3.2.2.2 Stent Cover and Adhesive

Material properties for the cover were obtained by tensile testing samples sprayed directly onto a mandrel. Specimens were cut into 25 mm x 5 mm samples and uniaxially loaded at 10 mm/min using a Zwick biaxial tester in combination with a calibrated video extensometer. Tensile tests were performed at room temperature. Cover material properties are not expected to be significantly altered when at body temperature. The results were fit to a Neo-Hookean hyperelastic constitutive model (Fig. 3.3), where the strain energy potential is represented by:

$$U = C_{10}(\bar{I}_1 - 3) + \frac{1}{D_1} (J^{el} - 1)^2 \quad (3.1)$$

where C_{10} and D_1 are temperature-dependent material parameters, \bar{I}_1 is the first deviatoric strain invariant and J^{el} is the elastic volume ratio. Material coefficients are given in Table 3.2. Material properties for the adhesive were obtained from literature

(Sheikhy et al. 2013) and were also fit using the Neo-Hookean material model (Fig. 3.3), the coefficients of which are given in Table 3.2.

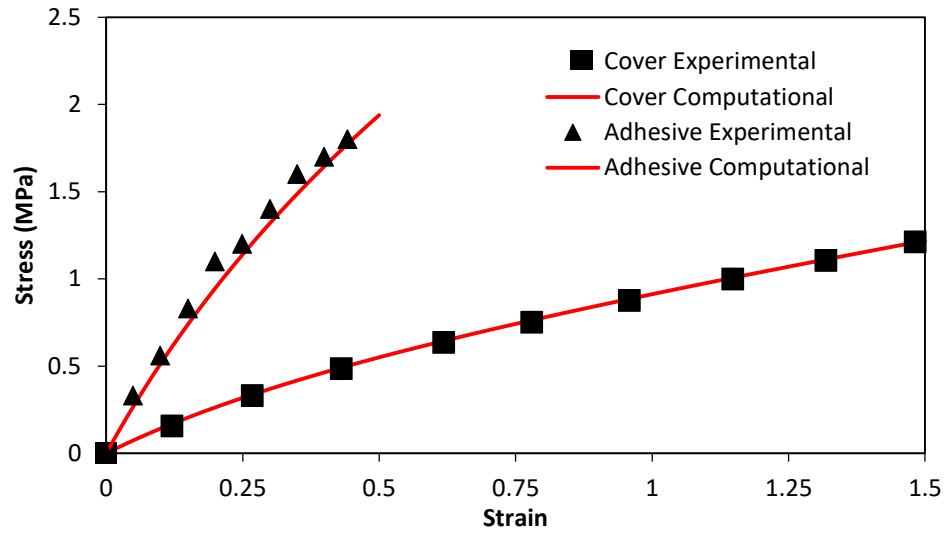


Fig. 3.3: Computational fits for the cover and adhesive constitutive models. Adhesive properties obtained from the literature (Sheikhy et al. 2013).

Table 3.2: Constitutive model coefficients for cover and adhesive.

Material	Material Model	D1	C10	Poisson's Ratio
Cover	Neo-Hookean	0.007681062	0.260554336	0.499
Adhesive	Neo-Hookean	0.211184593	1.01468441	0.499

3.2.3 Stent Experimental Testing

Three tests were undertaken to determine the effect the cover has on the mechanical response of the stent: a radial force test, a flat plate test and a non-uniform radial force test. The radial force test determined the radial stiffness of the stents, the flat plate test evaluated the effect on stent out-of-plane bending, and the non-uniform radial force test assessed the effect non-uniform loading has on stent response. Six stents were tested (3 bare and 3 covered) in each loading configuration.

3.2.3.1 Radial Force Testing

Each stent was radial force tested using an 8-faced crimping head (RCM-H60, MPT Europe) connected to a Zwick uniaxial tester with a 100N Xforce HP load cell (Zwick

Roell, GmbH & Co., Germany). The stents were crimped and unloaded from their nominal expanded diameter ≈ 15 mm to 7.5 mm at a rate of 0.1 mm/s at 37 °C. The effects of frictional forces within the crimping head are minimised by subtracting the results of a test performed with no device present (see Fig. A3.1 in Appendix 3). Dimensional accuracy is maintained through the use of pin gages.

3.2.3.2 Flat Plate Testing

A flat plate test was performed on each stent using an EnduraTEC (ELF 3200, Bose) in conjunction with an ET1 environmental chamber (Sun Electronic Systems, Inc.). Stents were placed between two flat platens, crushed to 3 mm and unloaded at a rate of 0.1 mm/s at 37 °C.

3.2.3.3 Non-uniform Radial Force Testing

Tracheobronchial stents can be deployed into especially non-circular configurations due to the nature of diseased airway geometries. A non-uniform radial force test was carried out to replicate the non-uniform loading that tracheobronchial stents experience from tumour growth or pressure variation *in-vivo*. To simulate the non-uniform loading a 4 mm diameter semi-circular steel rod was inserted into the radial force tester, and the stent was deployed into the crimper head at a fixed diameter of 12 mm corresponding to a 20% oversizing (Fig. 3.4). The non-uniformly loaded stent was then crimped to 10 mm at a rate of 0.1 mm/s at 37 °C to represent increased loading from tumour growth or inherent physiological tissue displacement. By performing a radial crimp on a non-circular deployed stent configuration it is possible to evaluate the effect that a combination of loading types can have on stent performance, which more accurately represents *in-vivo* loading. In reality the stenosis would compress somewhat against the airway wall and so this test corresponds to a worst case loading scenario. Other combinations of deployment diameter, rod geometry and material are not considered in this work.

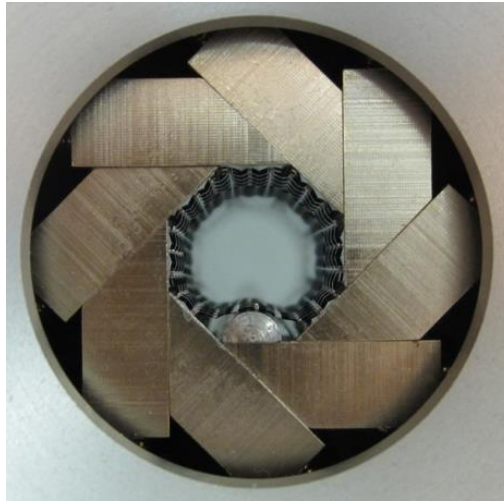


Fig. 3.4: Non-uniform test setup. Stent is deployed into crimper head at 12 mm with semi-circular rod positioned as shown.

3.2.4 Stent Computational Modelling

3.2.4.1 Stent Models

3.2.4.1.1 Bare Stent

The as-cut bare stent geometry was created in Abaqus from the dimensions used to fabricate the stents (Fig. 3.5 (a)). One radially repeating longitudinal stent length was first created and expanded from its as-cut OD of 5 mm to 14.96 mm using a rigid cylindrical section and symmetrical boundary conditions (Fig. 3.5 (b)). The expanded section was then “annealed” and radially patterned to create a stress-free fully expanded stent geometry (Fig. 3.6 (a)). The fully expanded bare stent consisted of 1,490,112 eight-noded linear brick elements (C3D8R) with enhanced hourglass control. A mesh sensitivity analysis was performed to ensure mesh convergence where the selected mesh converged to 0.02% Von Mises stress and 1.4% max principal strain with the densest mesh evaluated. A summary of the convergence study is provided in Table A3.1 in Appendix 3.

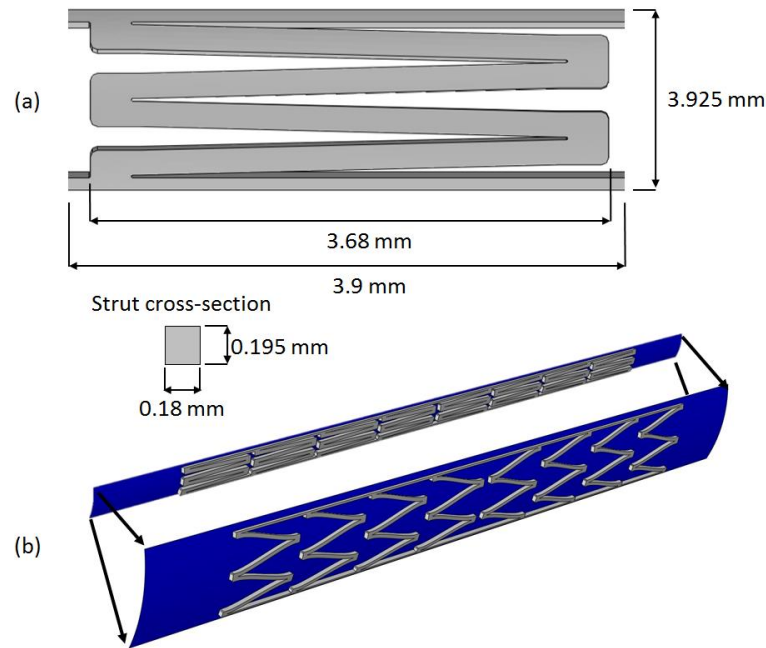


Fig. 3.5: (a) Unit cell geometry (b) Stent length expansion from as-cut diameter.

3.2.4.1.2 Adhered Cover Stent

Due to the complexity of attaching the stent cover to the bare stent, a different approach to the bare stent was used to create the adhered cover stent geometry. First, a radially repeating longitudinal length was expanded as described in Section 3.2.4.1.1. Measurements were taken from this expanded length (Fig. 3.5 (b)) to create a flat 2D pattern onto which an adhesive layer between the struts was introduced, and a uniform cover thickness of 100 μm was offset from the stent surface. This was then wrapped to create a stress-free cylindrical section of the entire assembly. In early work it was found that the adhesive between the stent struts had a significant effect on radial force results making it necessary to include in the computational model (Please see Appendix 3 for further details on the effects of the adhesion mediator). An average adhesive length was calculated from microscopy images and average cover thickness was measured using a micrometre. All adhered cover stent components (stent, cover and adhesive) are fully bonded at coincident nodes.

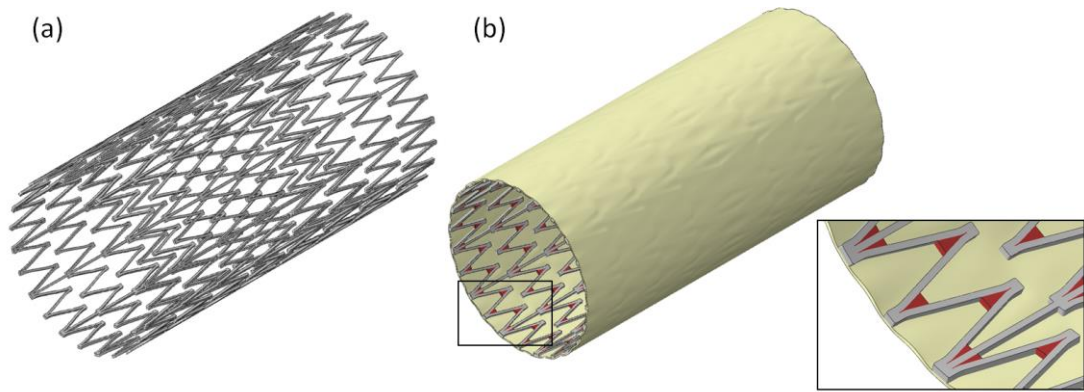


Fig. 3.6: (a) Expanded bare stent (b) Expanded covered stent. Inset showing detail of covered model. Red segments indicate adhesive regions.

To remove computational problems associated with cover compression due to perfect cylindricity, a small uniform pressure was applied to the outer surface of the cover to introduce slight folds in the cover. The final adhered cover stent configuration is shown in Fig. 3.6 (b). Linear eight-noded brick (C3D8R) elements with enhanced hourglass control were used to define the adhered cover components. The mesh contained 3,605,568 cover elements and 278,208 adhesive elements. Brick elements were selected to represent the cover instead of (more commonly used) shell elements due to an inadequate shell thickness to width ratio based on local stent geometrical limitations and the need to use less robust reduced integration shell elements in combination with hyperelastic material property definitions in Abaqus (Further information on cover element type selection is provided in Appendix 3). To select a suitable mesh for the stent cover a mesh convergence study was performed. Max radial force was used as the convergence criteria as this study does not investigate the stress or strain in the stent cover during loading as it does not reach levels high enough to damage the cover. The force was found to converge to within 1.7% of the densest mesh evaluated. A summary of the convergence analysis is given in Table A3.2 in Appendix 3. Four elements through the cover thickness ensure an adequate stress distribution and minimise hourglassing effects due to cover folding.

3.2.4.2 Computational Simulations

Each test configuration was computationally modelled using Abaqus/Explicit (V6.14) due to non-linearities caused by large amounts of contact and cover folding. The ratio

of kinetic to internal energy was maintained below 5% after initial contact between the device and rigid surfaces, and hourglassing energy was maintained below 10% of internal energy for all simulations. Semi-automatic mass scaling was used with a target time increment of $1\text{E-}6$ and a lowest stable time increment of $4.1\text{E-}8$. Simulation run times are given in Appendix 3.

3.2.4.2.1 Radial Force Testing

To simulate radial force testing the expanded stent geometry was placed in the centre of eight radially patterned rigid plates which were then radially displaced to 7.5 mm and returned to their initial configuration to load and unload the stent (Fig. 3.7 (a)). General contact using a penalty contact method is defined with penalty tangential contact with a coefficient of friction of 0.1 and hard normal contact. This contact definition includes contact between all components (stent, cover, adhesive and crimper plates) but contact between crimper plates is ignored. The same contact definition is used for each simulation. No boundary conditions are directly applied to the stent.

3.2.4.2.2 Flat Plate Testing

The flat plate test was replicated computationally by placing the stent geometry between two rigid body plates and displacing both plates until the stent was crushed to 3 mm. The plates' displacement was then reversed to unload the stent (Fig. 3.7 (b)).

3.2.4.3 Non-uniform Force Testing

Non-uniform force testing was simulated in three steps illustrated in Fig. 3.7 (c). Firstly, the stent was crimped to 7.5 mm using a rigid cylinder. It was then deployed into the crimper and rod assembly by displacing the rigid cylinder radially outward, allowing contact between the stent and crimper surfaces (including the semi-circular rod). Finally the stent was loaded from 12 mm to 10 mm, as was performed experimentally by radially displacing the rigid plates and semi-circular rod.

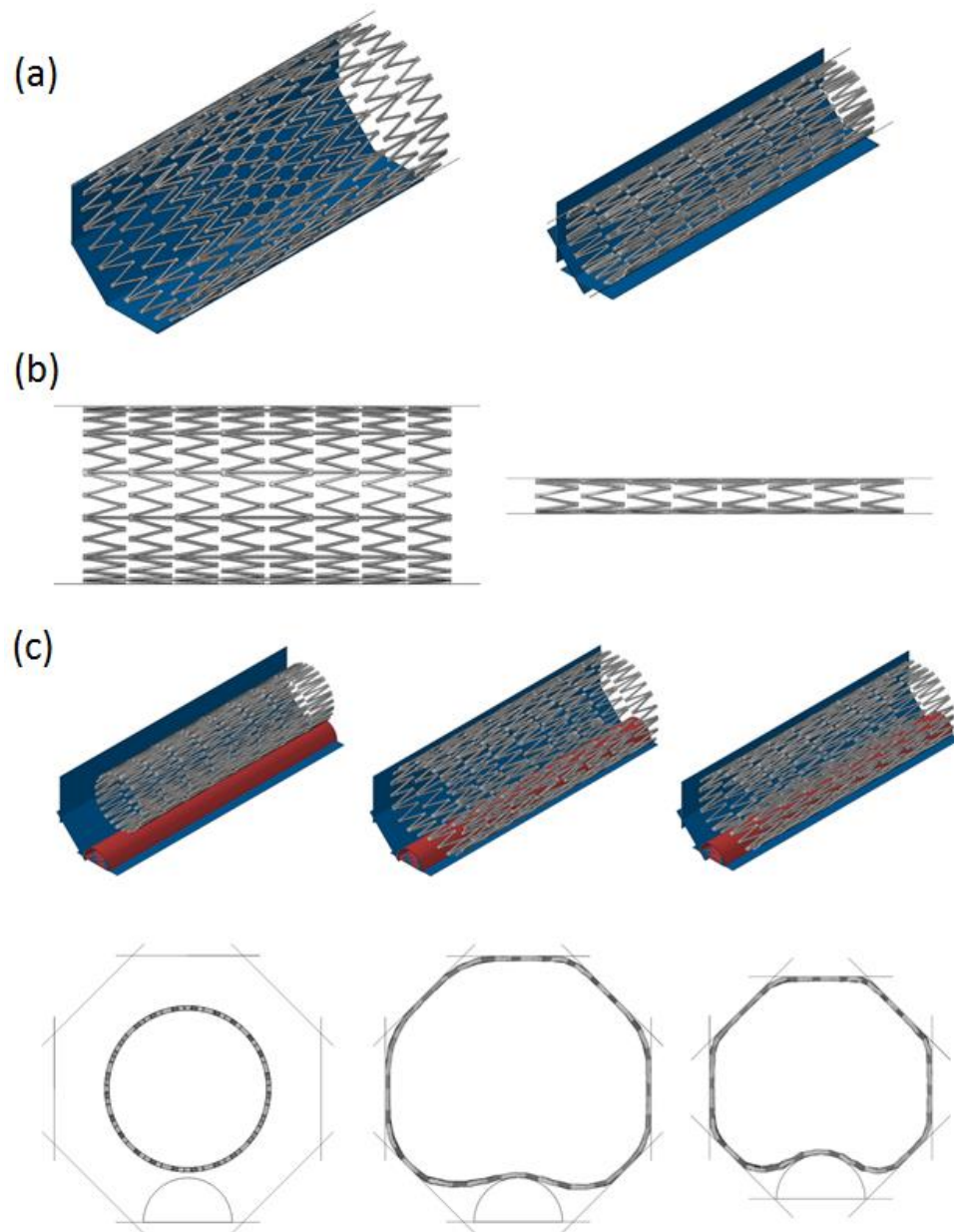


Fig. 3.7: (a) Radial force test at full expansion and full crimp (b) Flat plate test at full expansion and full crush. (c) Non-uniform radial force test showing three steps: stent crimping, stent deployment and non-uniform loading.

3.3 Results

3.3.1 Radial Force Testing

Experimental and computational radial force results are shown in Fig. 3.8 (a). Comparing the bare and covered experimental results it can be seen that there is a significant increase in radial force required to crimp the adhered cover stent. This corresponds to an increase in force of over 136% at full crimp. At 12 mm (or 20% oversizing) the chronic outward force (COF) for the adhered cover stent is only

12.47% higher than the bare stent. It should be noted that the abrupt drop in force observed directly after unload (≈ 7.5 mm) is caused by lag within the crimper head as a result of the change in test direction, and as such should be treated as a test artefact meaning a precise match with the computational models is not expected in the early portion of the unload curve (Further discussion on radial force result accuracy is provided in Appendix 3).

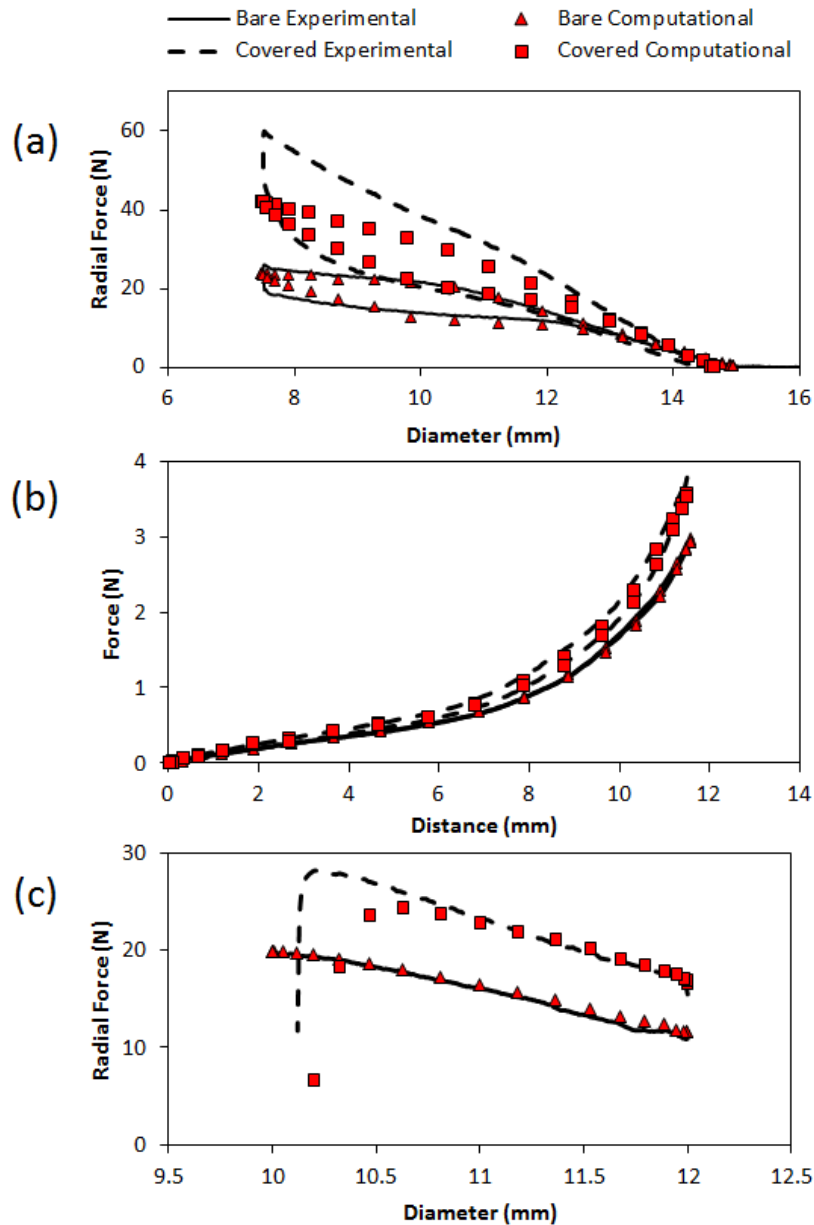


Fig. 3.8: Experimental and computational results for bare and covered stents: (a) radial force test (b) flat plate test (c) non-uniform radial force test. Note the experimental results of only one bare (Bare 1) and one covered (Covered 2) stent are shown in the interest of simplicity, summary data for all of the stents tested are given in Table 3.3.

Comparing the computational and experimental results for the bare stent a good match can be seen for the entirety of the radial resistive force (RRF) while the COF has a good match after 9 mm. There is a reasonably good match for the covered stent results, although the adhered cover model doesn't pick up the high radial force at low diameters (between 9.5 mm and 7.5 mm). This may be due to a higher value of experimental friction between the crimper surfaces and the stent cover, or possibly because the adhered cover components might have different material behaviour in compression (material constraints meant a compressive characterisation was not possible in the scope of this work).

Table 3.3: Selected experimental results for all stents tested.

Stent	Bare 1	Bare 2	Bare 3	Covered 1	Covered 2	Covered 3
Radial Force						
Max Force (N)	26.13	25.26	25.34	54.45	61.48	60.63
COF at 12 mm (N)	11.53	11.44	11.67	11.63	12.77	12.89
Flat Plate						
Max Force (N)	2.97	2.96	3.06	3.94	4.03	3.78
Non-Uniform						
Max Force (N)	19.81	19.48	20.23	24.60	28.26	28.79
Buckling Diameter (mm)	N/A	N/A	N/A	10.29	10.22	10.1

The effect the adhesive and cover have on stent hinge bending during crimping can be seen in Fig. 3.9. The bare stent struts bend near to the stent hinge where high localised strains are observed (marked by arrow in Fig. 3.9 (a) inset), while the covered stent struts bend further down the strut length (arrow in Fig. 3.9 (b) inset) with a lower, more evenly distributed strain range. The change in strain distribution is primarily due to the adhesive material between the stent struts causing the metal to bend further away from the hinge as a result of the added stiffness. However, the cover also effects local stent deformation due to the reduction in available space between struts caused by cover folding. This can clearly be seen in Fig. 3.9 where the

distance between struts on the crimped adhered cover stent is more uniform than those of the bare stent. The effect on strain distribution is additionally demonstrated in Fig. 3.10 (a) where the strain along a hinge length for both the bare and covered stents is plotted. At full crimp the bare stent hinge experiences levels of strain over twice that of the adhered cover stent. The strain distribution is spread out over a greater length for the adhered cover stent.

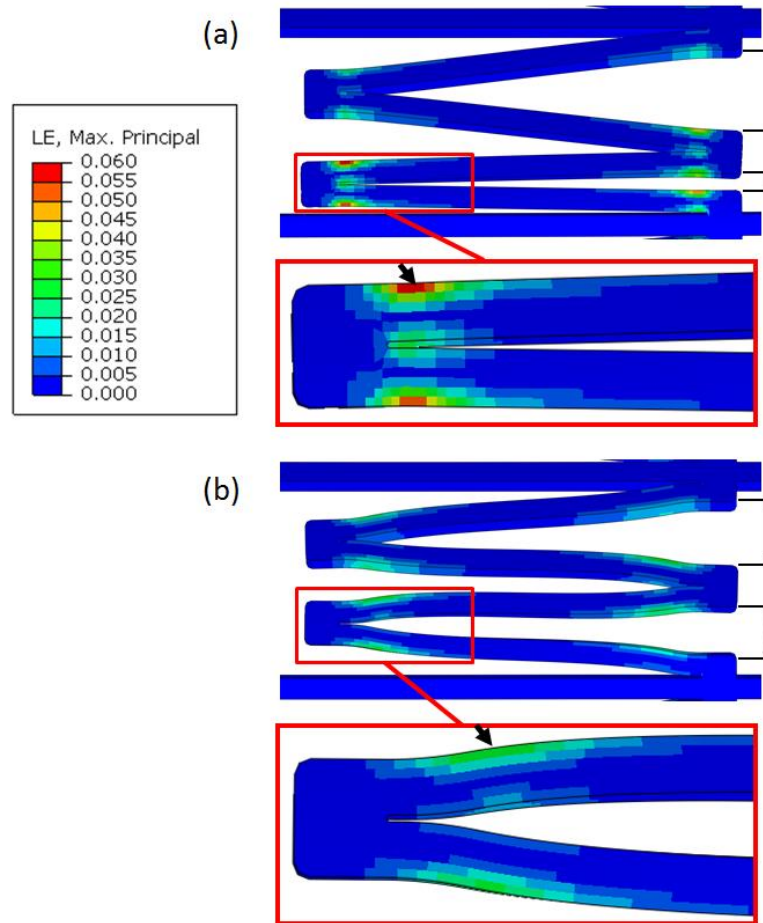


Fig. 3.9: Max principal logarithmic strain on fully crimped (a) bare stent (b) adhered cover stent (with adhesive and cover removed). Arrows on inset images indicate areas of highest strain on the outside surface of the hinge. Other arrows highlight difference in deformed distance between struts.

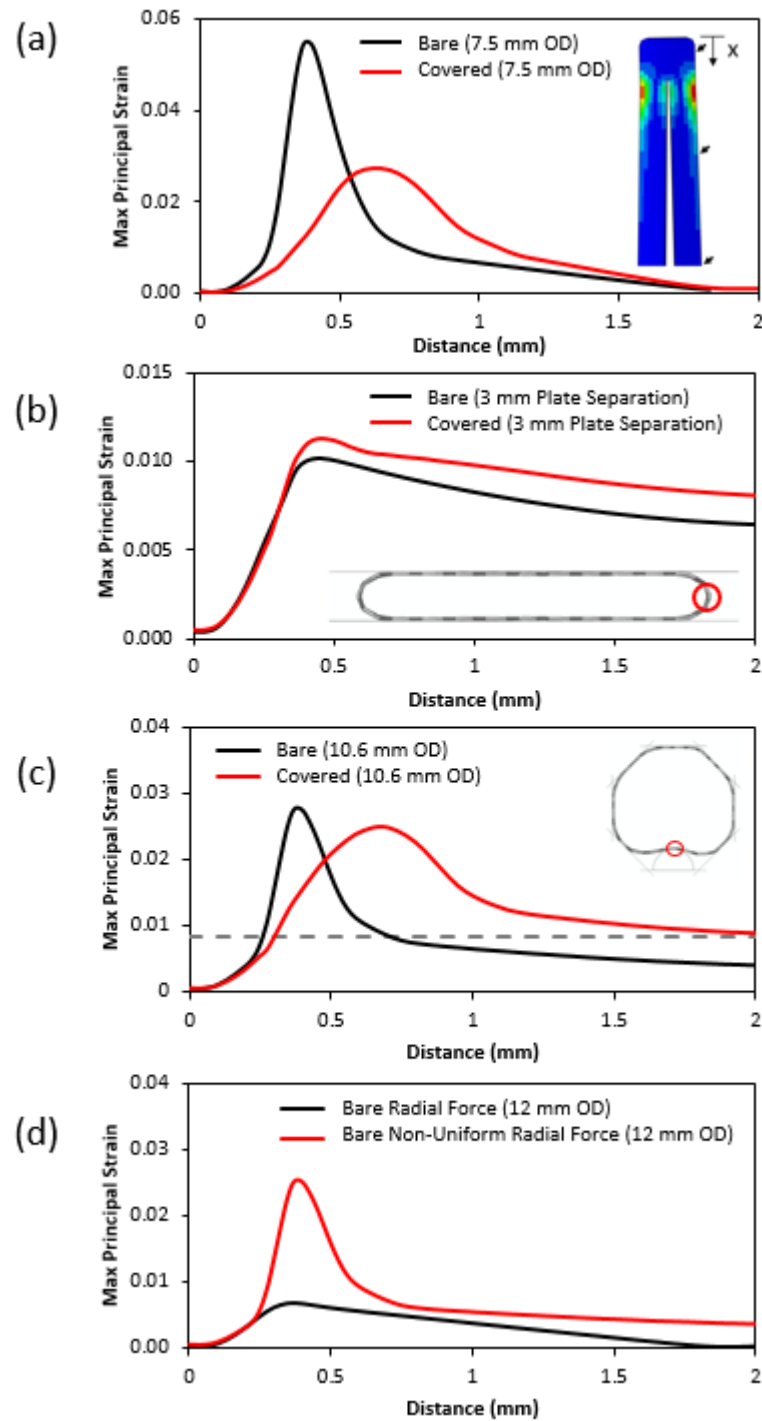


Fig. 3.10: Plots of the max principal logarithmic strain along a stent strut edge of the bare and adhered cover stent for: (a) Radial force test at full crimp. Inset arrows indicate the edge used to measure strain. (b) Flat plate test at full crush. Hinges selected at position of max strain along longitudinal position indicated by red circle in inset. (c) Non-uniform radial force test at diameter immediately before radial buckling of covered stent occurs (10.6 mm). Hinges selected along longitudinal position indicated by red circle in inset. Dashed black line specifies the start of the nitinol transitional strain region (Fig. 3.2). (d) Bare stent during radial force and non-uniform testing. Strain recorded at 12 mm diameter.

3.3.2 Flat Plate Testing

For the flat plate experiment the results in Fig. 3.8 (b) show a 27.3 % increase in the reaction force at full crush for the adhered cover stent compared to the bare stent. There is good agreement between the computational and experimental results for both the bare and adhered cover stents. The strain on the stent hinge edges at full crush is shown in Fig. 3.10 (b). There is a slight increase in the hinge strain for the adhered cover stent which is expected as the cover thickness causes the stent structure to be crushed by a marginally larger amount (Further detail is provided in Appendix 3). Otherwise the cover and adhesive have little effect on the stent response as they are orders of magnitude less stiff than the nitinol stent structure.

3.3.3 Non-uniform Force Testing

A qualitative comparison of cover folding before deployment is shown in Fig. 3.11 (a) and (b). The folded cover patterns on the outer surface and down the longitudinal axis correspond well with the model. This result is important as it indicates that the simulated cover is performing in a similar manner to the real cover, highlighting that the 8-noded linear brick elements are capable of capturing the complex behaviour of the cover.

Typical results for the non-uniform loading test are shown in Fig. 3.8 (c). The sharp decrease in force observed for the adhered cover stent occurs when the stent radially buckles, as shown in Fig. 3.11 (c). This type of stent failure results in rapid loss of radial support followed by stent migration or dyspnoea *in-vivo* and has been clinically observed (Trisolini et al. 2006). It can be seen in Table 3.3 that buckling occurs for all three adhered cover stents within 0.19 mm of one another. This suggests that the observed buckling behaviour is repeatable to some extent. No buckling occurs within the 12-10 mm test range for the bare stent. A marked difference in force can be seen between the two stents indicating a significant difference in stiffness even when loaded non-uniformly (Fig. 3.8 (c)). The computational results generally compare well to the experimental, with the adhered cover model following the same loading path until buckling, and no buckling occurring for the bare stent. The experimental buckling mode and buckled configuration is very well captured by the simulation (Fig. 3.11 (c)), however quantitatively, the covered simulation buckles sooner than the

experimental result (Fig. 3.8 (c)). Though a highly accurate prediction of the buckling point is not expected due to the random nature of buckling, the repeatability of the experiment suggests that the model prediction could be improved. The early onset of buckling may be due to the use of a low friction coefficient in the contact definition between the stent cover and the crimping plates.

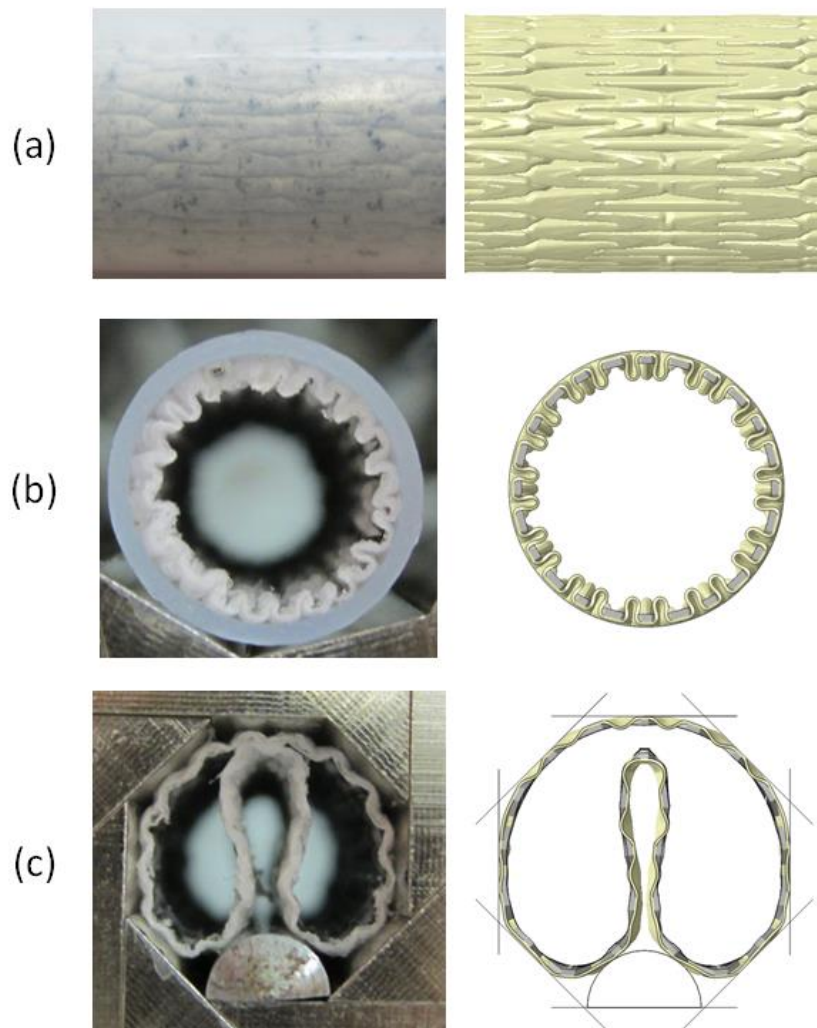


Fig. 3.11: Qualitative comparison of computational and experimental results. (a) Longitudinal view of cover folding. (b) Radial view of cover folding. (c) Radial view of cover buckling during non-uniform loading.

The max logarithmic strain along a strut edge for the non-uniform radial force models at the diameter just before buckling occurs in the adhered cover stent is shown in Fig. 3.10 (c). The strain distribution on the adhered cover stent edge is higher than the bare stent for the majority of the strut length. From the dashed black line in Fig. 3.10 (c) it can be seen that a high proportion of the adhered cover stent strut length

is within the nitinol transitional strain region (the plateau region of the tensile curve (Fig. 3.2)), which has been shown to reduce the stability of nitinol stents and make them more susceptible to buckling (McGrath et al. 2014).

The effect that the percentage of material in the transitional range has on stent stability can be seen more clearly in Fig. 3.12. As crimp displacement increases (diameter decreases), the percentage of material in the transitional region in the stent strut for the adhered cover stent increases; once this exceeds the 50% mark (indicated by the dashed black line) the stent begins to buckle. For the bare stent the average strain within the strut cross-section remains below 50% during the entire simulation.

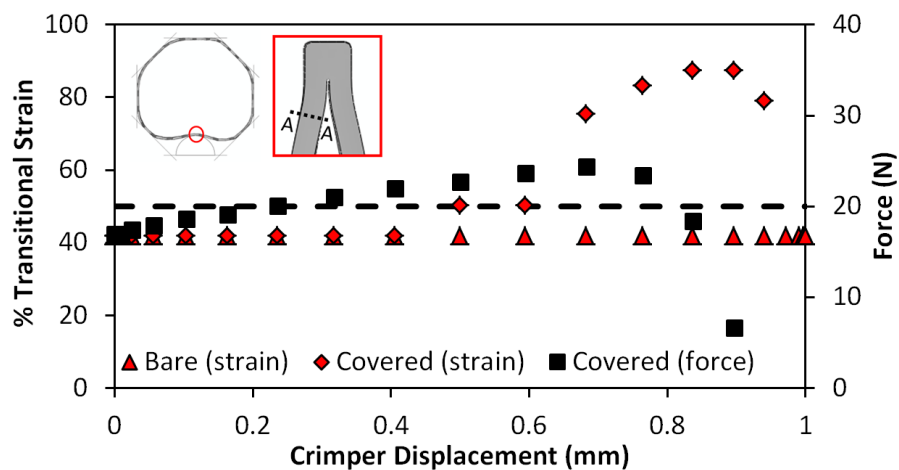


Fig. 3.12: Percentage transitional material (calculated using max principal logarithmic strain per element) through stent cross-section A-A (inset) plotted against crimp displacement for bare and covered stent. Covered non-uniform radial force is also shown for the covered stent. Dashed line indicates 50% of strut cross-section within transitional strain range.

Fig. 3.10 (d) shows a comparison of the maximum strain on the struts of the bare stent at 12 mm unload (corresponding to a typical 20% stent oversizing) for the radial force and non-uniform force test. It can clearly be seen that the non-uniform test has a higher strain distribution at this diameter.

3.4 Discussion

The objective of this study was to evaluate the effect that an adhered cover has on the mechanical response of a bare prototype tracheobronchial stent, through the use of experimental and computational means. Three tests were experimentally

performed and simulated including a radial force test, a flat plate test and a novel non-uniform radial force test. The non-uniform test was developed as a simplified representation of the multi-loading environment that the stent is subjected to *in-vivo*, where a semi-circular rod was used to represent stenotic compression, and radial displacement simulated the natural loading of the airways during breathing or coughing. To the best of the authors' knowledge it is the first time volume elements have been employed to describe the cover in a computational analysis. It is also the first study to experimentally examine the direct effect that a cover has on bare stent mechanics. Previous studies have not experimentally tested bare stents when evaluating covered stent designs, though De Bock et al. (2013) did perform a computational analysis on cover effects as part of a parameter study.

The introduction of the adhered cover resulted in a considerable increase in radial resistive force (Fig. 3.8 (a)). This is initially due to the adhesive material between the stent struts restricting hinge closure (Fig. 3.9) and, later due to the folding and pinching of the cover between the stent struts, which alters local strut deformation. The COF of the stent is much less affected by the adhered cover than the RRF which can be seen at 20% oversizing (12 mm) where the increase in force between the bare stent and the adhered cover stent is much lower for the COF than the RRF. The adhered cover also reduced the maximum strain seen in the stent struts by increasing the strain distribution along the strut length (Fig. 3.10 (a)). When the flat plate results (Fig. 3.8 (b)) are compared to the radial results it can be seen that the adhered cover has a markedly smaller effect on bending, which can be seen from the strain response of the covered stent in Fig. 3.10 (b). This is expected, due to the cover material's low stiffness in comparison to the nitinol stent structure. By just considering these two tests, as is common, it would appear that the adhered cover substantially improves the stent response by increasing both radial force and bending resistance, and decreasing the maximum strain throughout the stent struts. However, when the non-uniform radial force test results are considered it can be seen that the adhered cover stent is more likely to fail due to radial buckling (Fig. 3.8 (c)). The adhered cover stents buckled around 10.2 mm which is equivalent to $\approx 32\%$ oversizing, which is not uncommon in clinical practice. This is an important result as it highlights the

catastrophic effect that non-uniform loading can have on stent response, and suggests that the combination of radial force and crush testing which are routinely performed may not be fully capable of evaluating stent performance when considering multi-loading situations such as those that exist *in-vivo*. Radial collapse of stents *in-vivo* has been reported in at least one case (Trisolini et al. 2006).

The main mechanism responsible for the radial buckling observed in Fig. 3.8 (c) is due to a sudden increase in the amount of transitional material within the adhered cover stent strut (Fig. 3.10 (c), Fig. 3.12). This concept has previously been discussed in detail by McGrath et al. (2014). In short, a large increase in the volume of strut material within the transitional strain range of nitinol can cause a considerable reduction in stent stiffness. This is what happened in the present case, meaning that the stent was no longer able to support the load, and so buckling ensued.

At the lowest diameter in the radial force test the bare stent has a higher strain distribution than its adhered cover counterpart (Fig. 3.10 (a)), but the converse is seen during the non-uniform load test (Fig. 3.10 (c)) where the strains along the length of the adhered cover strut are significantly higher throughout the strut cross-section, even at a larger radial diameter (7.5 mm for the radial force test versus ≈ 10.6 mm for the non-uniform force test). Kleinstreuer et al. (2008) previously reported that the addition of graft materials to a nitinol stent can result in a reduction in strain amplitudes, but the results of the non-uniform test performed in this work suggests that the effect the cover has on strain distribution is largely dependent on the particular loading condition applied to the stent. Even though the loading condition has significant implications for the adhered cover stent in relation to whether or not the stent buckles, it also has important consequences on the bare stent in that the strains generated in the stent in the non-uniform test are considerably higher than for the radial force test (Fig. 3.10 (d)). Therefore, the loading condition significantly influences stent response whether it is covered or not. The implication of this is that to reduce possible complications the loading configuration that a particular stent design (bare or covered) is about to be subjected to should be considered before stent implantation.

The non-uniform test proposed in this work presents much promise as a simple, repeatable benchtop test that can be used to evaluate the stability or fatigue of stents under multi-loading conditions. The test performed adequately here, but a full characterisation (that is outside the remit of this present work) would need to be performed. This characterisation could allow for a more detailed analysis of the effect of deployment diameter (oversizing), stenosis shape and size, rod material, friction and cover materials on stent response. Ultimately the test method developed could be used to improve stent design and even create a safe deployment matrix for clinicians.

The loading dependent nature of these stents raises issues about the correct method for evaluating stent designs. It is clear that more effort is needed in the development of benchtop tests that can simulate a range of loading conditions that correspond to *in-vivo* conditions, but *in-silico* modelling is another tool that could be utilised more effectively for stent evaluation. The computational models developed in this study are capable of capturing complex device behaviour under different loading conditions. If validated *in-silico* models of the *in-vivo* state could be developed, then stents could be virtually evaluated in a realistic, repeatable manner in a way that cannot be accomplished through benchtop testing alone due to the inherent complexity involved. Much work is currently being performed on the development of more anatomically and physiologically realistic *in-vivo* loading models of stent devices (for example (Malvè et al. 2011c; Conway et al. 2012; Morlacchi et al. 2013; Conway et al. 2014; Ní Ghriallais and Bruzzi 2014; Gökgöl et al. 2015; Perrin et al. 2015; Boland et al. 2015a), and also as reviewed in (Morlacchi and Migliavacca 2013)), but interestingly it is not yet a significant requirement in FDA guidelines (Conway et al. 2012; Conway et al. 2014).

3.5 Conclusions

This study presents the effects that an adhered cover can have on the mechanical response of a bare prototype tracheobronchial stent through experimental and computational means. Classic stent characterisation tests were combined with a novel non-uniform test to contrast the macroscopic performance of the bare and covered devices, while computational modelling performed in parallel provided a

comprehensive insight into local device differences. A major conclusion that can be drawn from this work is that stent response (covered or bare) is highly loading specific, making it difficult to predict device performance in an *in-vivo* situation where loading conditions can differ considerably from patient to patient. It was shown that under perfectly radial loading conditions the adhered cover produced an overall reduction in strut strain, whereas the opposite was observed with non-uniform loading. With regard to this, improved bench-top testing and *in-silico* modelling should be regarded as key to more comprehensively evaluating stent performance. Another important conclusion is that the cover should be considered a fundamental input during the design of the stent structure as it can have a sizeable effect on device performance. For this particular stent-cover combination the cover produced an increase of over 136% in maximum radial force, while simultaneously reducing the stent stability under non-uniform loading. In this instance a significant portion of the increase in radial force is due to the adhesive material between the stent struts restricting hinge closure. The cover also provides an increase in radial force, but this is not as substantial.

A.3 Appendix 3

A.3.1 Mesh convergence and Simulation Run Times

Table A3.1: Summary of convergence results for bare and covered stent structures. Note the max stress and strain in the covered model is the max stress/strain in the cover. Mesh 2 was used for the stent structure and mesh A for the cover.

Stent	Bare			Covered	
	Mesh 1	Mesh 2	Mesh 3	Mesh A	Mesh B
Number of elements	52304	124176	490428	300464	601128
Max Von Mises stress (MPa)	473.8	483.4	483.3	0.568	0.564
Max principal logarithmic strain (%)	3.96	4.93	5.00	2.79	2.81
Max Radial Force (N)	-	-	-	3.51	3.45

Table A3.2: Simulation hours. All analyses were performed on a SGI ICE X HPC cluster using 3 or 4 nodes with each node having 2x12 core processors and 64 GB of RAM. (*) signifies 3 nodes were utilised.

Simulation	Bare	Covered
Radial Force (hrs)	64*	69
Flat Plate (hrs)	91	121
Non-uniform Radial Force (hrs)	55*	117

A.3.2 Raw Radial Force

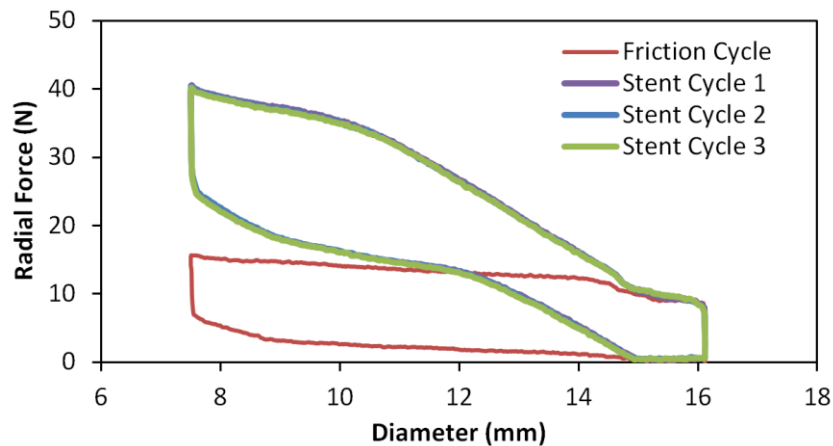


Fig. A3.1: Raw data of radial force test performed on one stent for three load and unload cycles where the friction curve for this test is also given. Three cycles are shown to highlight test repeatability.

A.3.3 Adhesive and Friction Effects on Stent Response

To determine the effect that the adhesive layer had on stent response a radial force test was simulated with a stent that only included a layer of adhesive between the stent hinges (the radial force simulation method is described in detail in Section 3.2.4.2.1). This was then compared to the bare and covered computational models as shown in Fig. A3.2. From these results it can be seen that the adhesive increases the maximum radial force of the bare stent by 53%, while the adhesive and the cover together cause an increase of 76%. This highlights that the adhesive has a significant impact on the mechanical response of the stent. However, the cover also has a sizeable effect.

To evaluate the effect of higher friction on radial force response the covered stent model was crimped using a coefficient of friction of 0.3. Previously the model had been run with a coefficient of friction of 0.1 (the contact definition is described in detail in Section 3.2.4.2.1). The effect of the friction can clearly be seen in Fig. A3.2, showing an increase in maximum radial force of 6%. This suggests that higher friction between the stent surfaces and the crimping plates may result in a higher force as observed experimentally (Fig. 3.8).

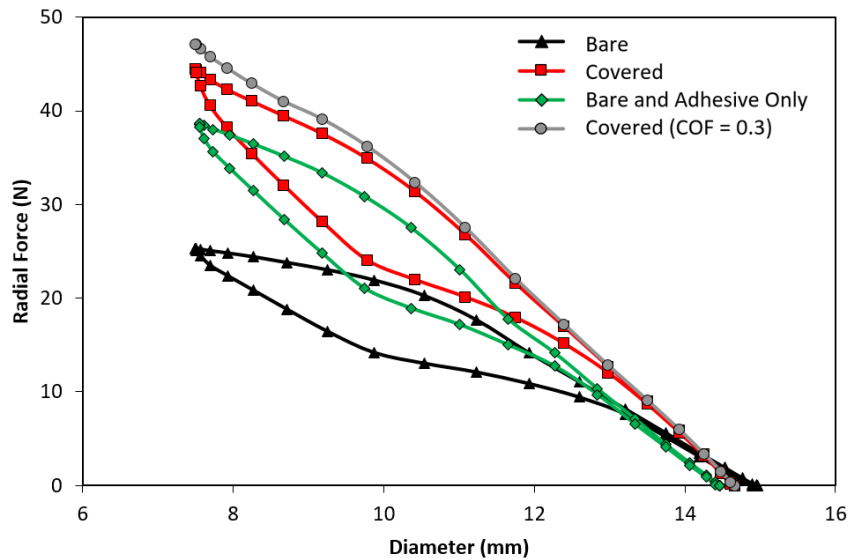


Fig. A3.2: Radial force comparison of computational models. Stent models are crimped from their freely expanded configuration to 7.5 mm. “Bare” refers to the bare stent without a cover. “Covered” refers to the stent with a PCU cover and adhesive. “Bare and Adhesive Only” refers to a stent with only the adhesive attached. “Covered (COF = 0.3)” refers to a covered stent model with a coefficient of friction of 0.3 between all surfaces.

A.3.4 Cover Element Type

As previously described in Chapter 3 the cover was modelled using brick elements (C3D8R) over the more commonly used shell element. Further analysis of brick element versus shell element is described in this section.

In this study the stent cover considered here is more than half the size of the stent strut thickness (100 μm and 195 μm respectively) making it difficult to refer to the membrane as thin relative to the stent struts. In all previous studies performed on covered stents (Demanget et al. 2012a; Demanget et al. 2012b; Demanget et al. 2013; De Bock et al. 2013; Perrin et al. 2014; Perrin et al. 2015) the ratio of stent wire diameter/thickness to cover thickness was higher than that used in this study, making the assumption of a thin membrane more reasonable (De Bock et al. for example had a ratio between 16 and 25 for their models, though they assumed a negligible cover thickness in their analyses).

A suitable representation of cover thickness is important in this work as it has an effect on the radial force results at lower crimping diameters. At lower diameters the cover folds and is compressed between the stent struts. Good contact definitions for the upper and lower surfaces of the cover are needed to calculate contributions from

cover contact and compression. This complex contact behaviour is difficult to capture using shell elements when the section is required to be so thick. Due to the thickness of the cover prescribed in this analysis an accurate surface thickness is impossible to describe using shell elements due to the limitations imposed by the contact algorithms in Abaqus/Explicit. The maximum thickness assigned to a shell element is controlled by the facet edge lengths or diagonal lengths of the element. The thickness must be below 20% to 60% of this length or automatic resizing occurs. This sizing does not affect the material attributes of the shell but only the contact thickness. Quite large element edge lengths in relation to the local stent geometry would be required to describe the cover elements with the desired thickness. This would result in only 3 cover elements across the mid-section of the stent strut/hinge (or 5 at the widest section) which is nowhere near enough to suitably capture cover folding. This means that it is not possible to use a shell representation to model the cover with the desired thickness. Previous studies have neglected cover thickness (De Bock et al. for example), but this is not suitable here as cover thickness effects the results.

Another difficulty associated with the use of shell elements in this work is the fact that fully integrated shell elements cannot be used in combination with hyperelastic material property representations in Abaqus. Instead, reduced integration elements must be used which introduces problems associated with hourglassing and this affects the in-plane bending results.

Computational simulations were run to compare shell and brick elements. A radial force test performed on a 1/12th section of the covered stent (with the cover discretised using C3D8R elements or S4R elements, both with enhanced hourglass control and with the same base mesh) using a rigid cylindrical section (Fig. A3.3). Radial displacement boundary conditions were placed on the cylindrical surface to crimp the stent from its initial configuration to 7.5 mm. Displacement in the theta direction along stent outer edges was held and a single node on the stent was held in the axial direction. The same material properties and contact definitions described in Chapter 3 were used. The shell cover thickness was set to 100 μm .

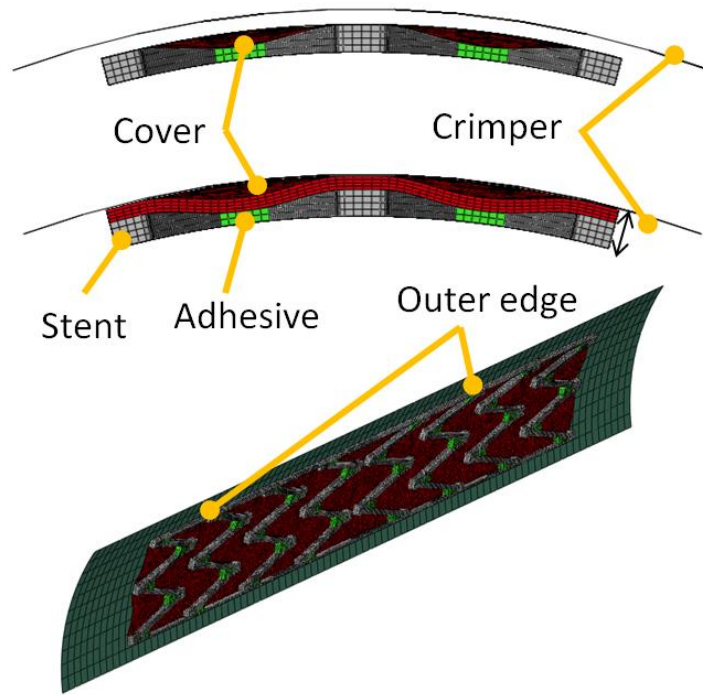


Fig. A3.3: Simulation setup showing radial view of shell (top) and brick (bottom) representations used.

Due to the thickness of the shell section automatic resizing of the shell offset for contact was performed. From Fig. A3.4 it can be seen that for an equivalent force of 3 N the shell element (S4R) simulation needed to displace 13% further than the brick element (C3D8R) run. The use of shell elements also resulted in a 10% lower prediction in maximum force at maximum crimper displacement (the equivalent experimental measurement). These are significant under-predictions that affect the nitinol stent response. The difference between the two models is derived from the reduced offset thickness in the shell model and can clearly be seen when considering the contact force along one stent unit edge as shown in Fig. A3.5. The contact force is higher in the solid model as it accounts for the full cover thickness. De Bock et al., 2013 reported that computational simulations that don't include a stent graft representation under-predict the force by between 10 to 30%, in the present work the use of a shell element representation would cause a similar under-prediction. The results of this analysis suggest that the effects of cover thickness are important at higher crimper displacements, but the use of shell elements at lower displacements where cover self-contact is smaller is more suitable.

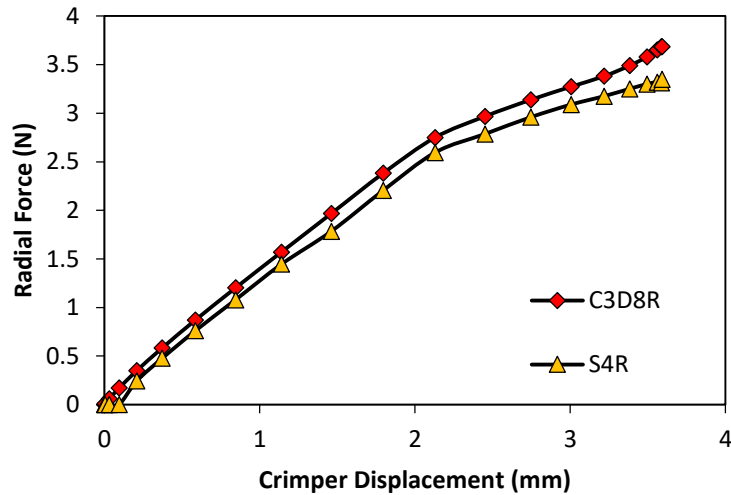


Fig. A3.4: Comparison of radial force using C3D8R or S4R elements.

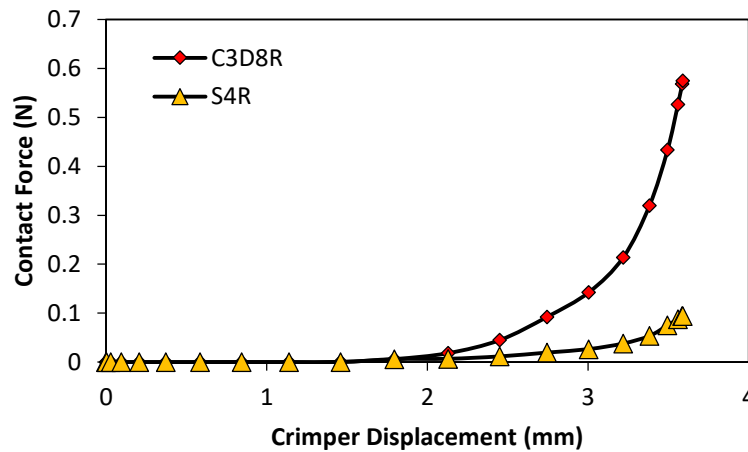


Fig. A3.5: Comparison of Contact force along the edges of one unit cell.

It is worth noting that the shell element model performed the analysis 31% faster than the brick analysis (Table A3.3), but considering the difference between the adhered cover and bare stent analyses were between 23% and 33% (Appendix A, Chapter 3) the use of a shell element representation would correspond to little overall improvement in computational efficiency for a full analysis (assuming a linear scaling).

Table A3.3: Simulation run time. Both analyses were performed on a SGI ICE X HPC cluster using 2 nodes with each node having 2x12 core processors and 64 GB of RAM.

Model	C3D8R	S4R
Run Time (hrs)	4	2.75

A.3.5 Radial Force Test Accuracy

The effect of internal friction in the radial force tester is minimised by performing a friction test before every sample is tested. To do this a radial force test is performed without any device present and the resulting force (caused by internal friction in the tester) is removed from the stent radial force result. In Chapter 3 an observed drop in force at unload was described as being caused by lag within the crimper head as a result of the change in test direction. We believe that this is caused by internal slippage in the load train associated with the change of loading direction. It is possible that during unload, slippage within the tester records a drop in force that isn't a valid result. From previous experience it is known that the stents used in this analysis don't suffer from such a sudden drop in force at unload (radial force tests performed by Admedes Schuessler on this bare stent design, using a radial force tester where each crimping plate is connected to an individual load cell and so negates internal friction discrepancies), and so it's more than likely a test artefact caused by lag in the system. In this case it only affects the early portion of the unload curve (7.5 – 9 mm) and so can be ignored. The important result in this area of the test curve is the maximum force during crimp which is captured here, which is important from a delivery device design perspective. The main region of interest on the unload curve is around the 20% oversizing mark (12 mm) which would be the expected deployment diameter of this stent and this is suitably captured in the experiment.

The effect of a friction factor on radial force results was considered to evaluate whether it had an influence on the observed experimental hysteresis. Here, the friction test is removed from the device test as previously described (Chapter 3) and the resulting force is multiplied by a small factor, which is then subtracted from the device force. Fig. A3.6 below shows the effect that this approach has for one radial force curve. It compares the subtraction (and addition) of a 0.1 and 0.05 friction factor from a radial force curve with the friction run removed. As can be seen the desired effect is obtained at max crimp where the large drop at unload is reduced somewhat, but conversely (and more importantly) it causes an "overlap" in the 12 – 15 mm region of the test curve where the loading and unloading curves no longer match. Here it can be seen that the unload curve for both the 0.05 and 0.1 factors

are higher than the loading curve which is not physical (Fig. A3.6 (Bottom)). This suggests that there is no link between radial force and friction force in the system, as otherwise this section of the curve would not match, as it does for the simple subtraction of the friction force run that is currently used.

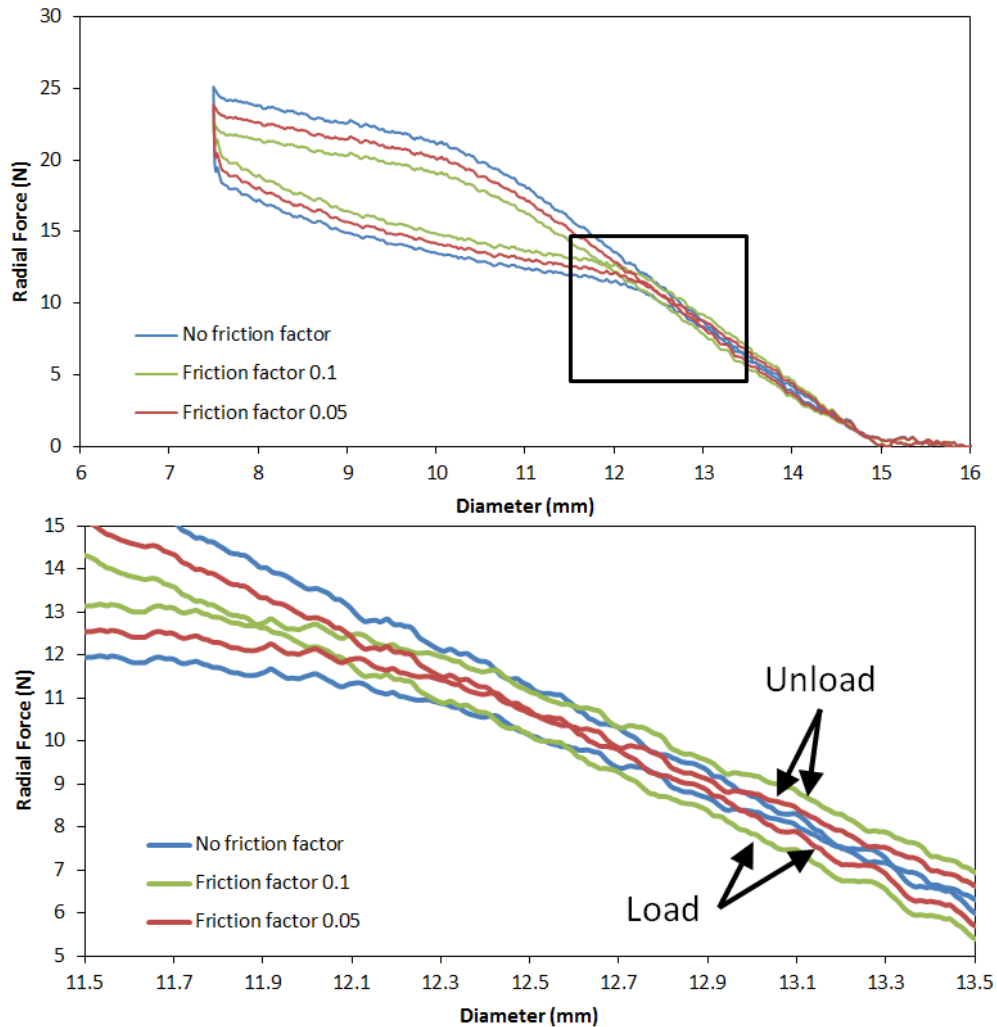


Fig. A3.6: (Top) Three radial force curves with friction force and various friction factors subtracted/added from/to the raw data. (Bottom) Enhanced view of the overlap. Arrows indicate load and unload overlap for 0.1 and 0.05 curves.

A.3.6 Flat Plate Strain Comparison

A comparison of flat plate strain along a strut edge between the covered and bare stent is shown in Fig. A3.7. The strain at full crush is shown for the bare and covered stents, along with the strain for the covered stent with the stent surface at an equivalent OD to the bare stent. Here it can be seen that when the stents are at an equivalent diameter (i.e. accounting for the increased thickness due to the cover)

that the strain profiles are quite similar, which further highlights that the cover has a limited effect on stent response in the flat plate test.

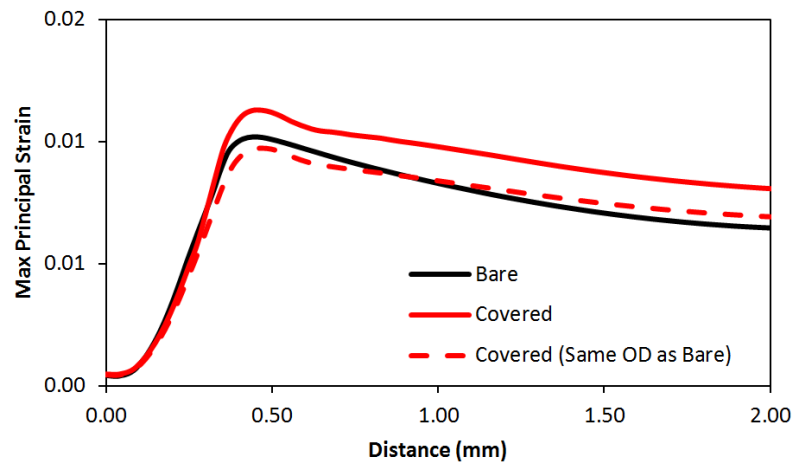


Fig. A3.7: Plot of max principal logarithmic strain along a stent strut edge of the bare and adhered cover stent for the flat plate test at full crush. The strain along an adhered cover stent edge at the same OD as the bare stent at full crush is also given.

References

- Azaouzi M, Makradi A, Belouettar S (2012) Deployment of a self-expanding stent inside an artery: A finite element analysis. *Mater Des* 41:410–420. doi: 10.1016/j.matdes.2012.05.019
- Boland EL, Grogan JA, Conway C, McHugh PE (2015a) Computer simulation of the mechanical behaviour of implanted biodegradable stents in a remodelling artery. *JOM* 34:8049. doi: 10.1007/s11837-015-1761-5
- Boland EL, Shine R, Kelly N, Sweeney CA, McHugh PE (2015b) A review of material degradation modelling for the analysis and design of bioabsorbable stents. *Ann Biomed Eng*. doi: 10.1007/s10439-015-1413-5
- Bolliger CT, Sutedja TG, Strausz J, Freitag L (2006) Therapeutic bronchoscopy with immediate effect: laser, electrocautery, argon plasma coagulation and stents. *Eur Respir J* 27:1258–71. doi: 10.1183/09031936.06.00013906
- Bolliger CT, Wyser C, Wu X, Hauser R, Studer W, Dalquen P, Perruchoud AP (1999) Evaluation of a new self-expandable silicone stent in an experimental tracheal stenosis. *Chest* 115:496–501. doi: 10.1378/chest.115.2.496
- Chen L, Jingfeng S, Bing C, Zhiyong X (2012) Numerical analysis of the influence of stent parameters on the fatigue properties. *Mod Appl Sci* 6:23–27. doi: 10.5539/mas.v6n4p23
- Chung FT, Chen HC, Chou CL, Yu CT, Kuo CH, Kuo HP, Lin SM (2011) An outcome analysis of self-expandable metallic stents in central airway obstruction: a cohort study. *J Cardiothorac Surg* 6:46. doi: 10.1186/1749-8090-6-46
- Chung FT, Lin SM, Chen HC, Chou CL, Yu CT, Liu CY, Wang CH, Lin HC, Huang CD, Kuo HP (2008) Factors leading to tracheobronchial self-expandable metallic stent fracture. *J Thorac Cardiovasc Surg* 136:1328–1335. doi: 10.1016/j.jtcvs.2008.05.039
- Conway C, McGarry JP, McHugh PE (2014) Modelling of atherosclerotic plaque for use in a computational test-bed for stent angioplasty. *Ann Biomed Eng* 42:2425–2439. doi: 10.1007/s10439-014-1107-4
- Conway C, Sharif F, McGarry JP, McHugh PE (2012) A computational test-bed to assess coronary stent implantation mechanics using a population-specific approach. *Cardiovasc Eng Technol* 3:374–387. doi: 10.1007/s13239-012-0104-8
- De Bock S, Iannaccone F, De Beule M, Van Loo D, Vermassen F, Verheghe B, Segers P (2013) Filling the void: a coalescent numerical and experimental technique to determine aortic stent graft mechanics. *J Biomech* 46:2477–82. doi: 10.1016/j.jbiomech.2013.07.010
- Demanget N, Avril S, Badel P, Orgéas L, Geindreau C, Albertini JN, Favre JP (2012a) Computational comparison of the bending behavior of aortic stent-grafts. *J Mech Behav Biomed Mater* 5:272–282. doi: 10.1016/j.jmbbm.2011.09.006
- Demanget N, Duprey A, Badel P, Orgéas L, Avril S, Geindreau C, Albertini J-N, Favre J-P (2013) Finite element analysis of the mechanical performances of 8 marketed aortic stent-grafts. *J Endovasc Ther* 20:523–35. doi: 10.1583/12-4063.1
- Demanget N, Latil P, Orgéas L, Badel P, Avril S, Geindreau C, Albertini JN, Favre JP (2012b)

- Severe bending of two aortic stent-grafts: an experimental and numerical mechanical analysis. *Ann Biomed Eng* 40:1–13. doi: 10.1007/s10439-012-0618-0
- Dooms C, De Keukeleire T, Janssens A, Carron K (2009) Performance of fully covered self-expanding metallic stents in benign airway strictures. *Respiration* 77:420–6. doi: 10.1159/000203364
- Ernst A, Feller-Kopman D, Becker HD, Mehta AC (2004) Central airway obstruction. *Am J Respir Crit Care Med* 169:1278–1297. doi: 10.1164/rccm.200210-1181SO
- Farhatnia Y, Tan A, Motiwala A, Cousins BG, Seifalian AM (2013) Evolution of covered stents in the contemporary era: clinical application, materials and manufacturing strategies using nanotechnology. *Biotechnol Adv* 31:524–42. doi: 10.1016/j.biotechadv.2012.12.010
- Fernández-Bussy S, Majid A, Caviedes I, Akindipe O, Baz M, Jantz M (2011) Treatment of airway complications following lung transplantation. *Arch Bronconeumol* ((English Ed 47:128–133. doi: 10.1016/S1579-2129(11)70031-3
- Food and Drug Administration (2010) Non-clinical engineering tests and recommended labeling for intravascular stents and associated delivery systems.
- Freitag L (2010) Airway stents. In: Strausz J, Bolliger CT (eds) *Interventional Pulmonology*. European Respiratory Society Journals Ltd, Sheffield, pp 190–217
- Freitag L, Eicker K, Donovan TJ, Dimov D (1995) Mechanical properties of airway stents. *J Bronchol* 2:270–278. doi: 10.1097/00128594-199510000-00003
- Freitag L, Eicker R, Linz B, Greschuchna D (1994) Theoretical and experimental basis for the development of a dynamic airway stent. *Eur Respir J* 7:2038–2045. doi: 10.1183/09031936.94.07112038
- Furukawa K, Ishida J, Yamaguchi G, Usuda J, Tsutsui H, Saito M, Konaka C, Kato H (2010) The role of airway stent placement in the management of tracheobronchial stenosis caused by inoperable advanced lung cancer. *Surg Today* 40:315–20. doi: 10.1007/s00595-008-4058-2
- García A, Peña E, Martínez MA (2012) Influence of geometrical parameters on radial force during self-expanding stent deployment. Application for a variable radial stiffness stent. *J Mech Behav Biomed Mater* 10:166–75. doi: 10.1016/j.jmbbm.2012.02.006
- Ghriallais RN, Bruzzi M (2014) Self-expanding stent modelling and radial force accuracy. *Comput Methods Biomech Biomed Engin* 17:318–333. doi: 10.1080/10255842.2012.683427
- Gildea TR, Downie G, Eapen G, Herth F, Jantz M, Freitag L (2008) A prospective multicenter trial of a self-expanding hybrid stent in malignant airway obstruction. *J Bronchol* 15:221–224. doi: 10.1097/LBR.0b013e31818859b9
- Gökgöl C, Diehm N, Nezami FR, Büchler P (2015) Nitinol stent oversizing in patients undergoing popliteal artery revascularization: a finite element study. *Ann Biomed Eng*. doi: 10.1007/s10439-015-1358-8
- Grogan J a, Leen SB, McHugh PE (2012) Comparing coronary stent material performance on a common geometric platform through simulated bench testing. *J Mech Behav Biomed*

Mater 12:129–38. doi: 10.1016/j.jmbbm.2012.02.013

Hugo Marquette C, Mensier E, Copin MC, Desmidt A, Freitag L, Witt C, Petyt L, Ramon P (1995) Experimental models of tracheobronchial stenoses: A useful tool for evaluating airway stents. *Ann Thorac Surg* 60:651–656. doi: 10.1016/0003-4975(95)00460-3

Irwin RS (1977) Cough. *Arch Intern Med* 137:1186. doi: 10.1001/archinte.1977.03630210060019

Islami F, Torre LA, Jemal A (2015) Global trends of lung cancer mortality and smoking prevalence. *Transl lung cancer Res* 4:327–38. doi: 10.3978/j.issn.2218-6751.2015.08.04

Kleinstreuer C, Li Z, Basciano CA, Seelecke S, Farber MA (2008) Computational mechanics of Nitinol stent grafts. *J Biomech* 41:2370–8. doi: 10.1016/j.jbiomech.2008.05.032

Korpela A, Aarnio P, Sariola H, Törmälä P, Harjula A (1999) Bioabsorbable self-reinforced poly-l-lactide, metallic, and silicone stents in the management of experimental tracheal stenosis. *Chest* 115:490–495. doi: 10.1378/chest.115.2.490

Lee P, Kupeli E, Mehta AC (2010) Airway stents. *Clin Chest Med* 31:141–150. doi: 10.1016/j.ccm.2009.08.002

Lyubimov GA (2001) The physiological function of the posterior tracheal wall. *Dokl Biol Sci* 380:421–423.

Macchiarini P (2006) Primary tracheal tumours. *Lancet Oncol* 7:83–91. doi: 10.1016/S1470-2045(05)70541-6

Malvè M, Barreras I, López-Villalobos JL, Ginel A, Doblaré M (2012) Computational fluid-dynamics optimization of a human tracheal endoprosthesis. *Int Commun Heat Mass Transf* 39:575–581. doi: 10.1016/j.icheatmasstransfer.2012.03.014

Malvè M, Pérez del Palomar A, Chandra S, López-Villalobos JL, Finol E a, Ginel A, Doblaré M (2011a) FSI analysis of a human trachea before and after prosthesis implantation. *J Biomech Eng* 133:71003. doi: 10.1115/1.4004315

Malvè M, Pérez del Palomar A, Chandra S, López-Villalobos JL, Mena A, Finol E a, Ginel A, Doblaré M (2011b) FSI Analysis of a healthy and a stenotic human trachea under impedance-based boundary conditions. *J Biomech Eng* 133:21001. doi: 10.1115/1.4003130

Malvè M, Pérez del Palomar A, López-Villalobos JL, Ginel A, Doblaré M (2010) FSI analysis of the coughing mechanism in a human trachea. *Ann Biomed Eng* 38:1556–65. doi: 10.1007/s10439-010-9951-3

Malvè M, Pérez del Palomar A, Mena A, Trabelsi O, López-Villalobos JL, Ginel A, Panadero F, Doblaré M (2011c) Numerical modeling of a human stented trachea under different stent designs. *Int Commun Heat Mass Transf* 38:855–862. doi: 10.1016/j.icheatmasstransfer.2011.04.012

Malvè M, Serrano C, Peña E, Fernández Parra R, Lostalé F, De Gregorio M a., Martínez M a. (2014) Modelling the air mass transfer in a healthy and a stented rabbit trachea: CT-images, computer simulations and experimental study. *Int Commun Heat Mass Transf* 53:1–8. doi: 10.1016/j.icheatmasstransfer.2014.02.001

- McGrath DJ, O'Brien B, Bruzzi M, McHugh PE (2014) Nitinol stent design - understanding axial buckling. *J Mech Behav Biomed Mater* 40:252–263. doi: 10.1016/j.jmbbm.2014.08.029
- Morlacchi S, Colleoni SG, Cárdenes R, Chiastra C, Diez JL, Larrabide I, Migliavacca F (2013) Patient-specific simulations of stenting procedures in coronary bifurcations: Two clinical cases. *Med Eng Phys* 35:1272–1281. doi: 10.1016/j.medengphy.2013.01.007
- Morlacchi S, Migliavacca F (2013) Modeling stented coronary arteries: where we are, where to go. *Ann Biomed Eng* 41:1428–1444. doi: 10.1007/s10439-012-0681-6
- Nadzeyka I, Gabler C, Erarslan D, Safi Y, Steinseifer U (2014) Manufacturing of biocompatible nonwoven structures by using spray atomization of dissolved polymers. *Polym Eng Sci* 54:867–873. doi: 10.1002/pen.23622
- Ní Ghriallais R, Bruzzi M (2014) A computational analysis of the deformation of the femoropopliteal artery with stenting. *J Biomech Eng* 136:71003. doi: 10.1115/1.4027329
- Ost DE, Shah AM, Lei X, Godoy MCB, Jimenez C a, Eapen G a, Jani P, Larson AJ, Sarkiss MG, Morice RC (2012) Respiratory infections increase the risk of granulation tissue formation following airway stenting in patients with malignant airway obstruction. *Chest* 141:1473–81. doi: 10.1378/chest.11-2005
- Perrin D, Badel P, Orgeas L, Geindreau C, Dumenil A, Albertini J-N, Avril S (2015) Patient-specific numerical simulation of stent-graft deployment: validation on three clinical cases. *J Biomech* 48:1868–1875. doi: 10.1016/j.jbiomech.2015.04.031
- Perrin D, Demanget N, Badel P, Avril S, Orgéas L, Geindreau C, Albertini JN (2014) Deployment of stent-grafts in curved aneurysmal arteries: Towards a predictive numerical tool. *Int j numer method biomed eng*. doi: 10.1002/cnm.2698
- Prasad A, To LK, Gorrepati ML, Zarins CK, Figueroa CA (2011) Computational analysis of stresses acting on intermodular junctions in thoracic aortic endografts. *J Endovasc Ther* 18:559–568. doi: 10.1583/11-3472.1
- Prasad A, Xiao N, Gong X-Y, Zarins CK, Figueroa CA (2013) A computational framework for investigating the positional stability of aortic endografts. *Biomech Model Mechanobiol* 12:869–887. doi: 10.1007/s10237-012-0450-3
- Rieu R, Barragan P, Masson C, Fuseri J, Garitey V, Silvestri M, Roquebert P, Sainsous J (1999) Radial force of coronary stents: a comparative analysis. *Catheter Cardiovasc Interv* 46:380–91. doi: 10.1002/(SICI)1522-726X(199903)46:3<380::AID-CCD27>3.0.CO;2-J
- Sheikhy H, Shahidzadeh M, Ramezanzadeh B, Noroozi F (2013) Studying the effects of chain extenders chemical structures on the adhesion and mechanical properties of a polyurethane adhesive. *J Ind Eng Chem* 19:1949–1955. doi: 10.1016/j.jiec.2013.03.008
- Sosa AF, Michaud GC (2012) Metallic stents in the airway: should we continue to use them and can we remove them? *Curr Respir Care Rep* 2:54–60. doi: 10.1007/s13665-012-0036-7
- Trisolini R, Piaoli D, Fornario V, Lazzari Agli L, Grosso D, Patell M (2006) Collapse of a new type of self-expanding metallic tracheal stent. *Monaldi Arch Chest Dis - Pulm Ser* 65:56–58.

Chapter 4

An Ovine *in-vivo* Framework for Tracheobronchial Stent Analysis

Published in: Biomechanics and Modeling in Mechanobiology, 2017

DOI: 10.1007/s10237-017-0904-8

Abstract

Tracheobronchial stents are most commonly used to restore patency to airways stenosed by tumour growth. Currently all tracheobronchial stents are associated with complications such as stent migration, granulation tissue formation, mucous plugging and stent strut fracture. The present work develops a computational framework to evaluate tracheobronchial stent designs *in-vivo*. Pressurised computed tomography (CT) is used to create a biomechanical lung model which takes into account the *in-vivo* stress state, global lung deformation and local loading from pressure variation. Stent interaction with the airway is then evaluated for a number of loading conditions including normal breathing, coughing and ventilation. Results of the analysis indicate that three of the major complications associated with tracheobronchial stents can potentially be analysed with this framework, which can be readily applied to the human case. Airway deformation caused by lung motion is shown to have a significant effect on stent mechanical performance, including implications for stent migration, granulation formation and stent fracture.

4.1 Introduction

Tracheobronchial stents are used for many applications in the lung, with the most common being for the restoration of patency to airways stenosed by benign or malignant tumour compression (Freitag 2010). Around 30% of all lung cancer patients go on to develop problems with central airway obstruction (Lee et al. 2010),

typically presenting with blockages of >50% signifying imminent suffocation and the immediate need for stenting (Bolliger et al. 2006). Currently there exists no ideal tracheobronchial stent as all commercially available devices are associated with complications, which include stent migration, granulation tissue formation, mucous plugging, and stent strut fracture (Gildea et al. 2008; Dooms et al. 2009; Razi et al. 2010; Freitag 2010; Fernández-Bussy et al. 2011; Jeong et al. 2012; Ost et al. 2012; Marchese et al. 2015; Park et al. 2016).

Tracheobronchial stents are tubular devices that restore airway patency to diseased airways by providing scaffolding support. Commercially available tracheobronchial stents can generally be divided into three families: bare metal, covered metal and polymeric. Some bare and covered metal stents include the Ultraflex stent, Aero stent and Taewoong stent, while common polymeric stents include the Dumon stent, Montgomery T stent and Polyflex stent (Freitag 2010). Typically, covered metal and polymeric stents are used to prevent airway reocclusion caused by malignant tumour ingrowth through open struts (Freitag 2010). Many metal stents are fabricated from nitinol, a superelastic alloy of Nickel and Titanium. The superelastic properties allow nitinol to reach strains in excess of 10% without plastically deforming, permitting stents to be crimped and deployed in a self-expanding manner (Stoeckel et al. 2004). Stents are crimped from a freely expanded state to a small diameter and placed into a delivery device, which, with the aid of a flexible bronchoscope can be tracked to the desired location. Once positioned, the stent is deployed by removing an outer sheath which allows the stent to expand using its inherent elasticity. Airflow is returned to the diseased region by the stent pushing against the occluding stenosis.

Stent migration is believed to occur in at least 10% of malignant cases, and is thought even higher for benign stenoses (Freitag 2010). Dooms et al. (2009) found that migration occurred in 65% of stents placed for benign airway strictures, while Ost et al. (2012) observed 14% migration for stents deployed to counteract malignant airway obstruction. Granulation tissue formation, another common complication is understood to occur from repetitive motion trauma caused by friction at the stent ends and by excessive pressure from stent oversizing (Hautmann et al. 1999; Schmääl et al. 2003; Saad et al. 2003; Hu et al. 2011; Ost et al. 2012). Granulation tissue

formation can cause large stenoses that hamper airflow resulting in the need for secondary intervention. Fernández-Bussy et al. (2011) identified that 57% of lung transplant patients requiring stents experienced granulation formation. Both Saad et al. (2003) and Chung et al. (2011) found granulation formation in 15% of cases for benign and malignant indications. Cyclic loading from normal breathing and large deformation from coughing cause stent fractures to occur in all metal airway stents (Freitag 2010). Chung et al. (2008) and Dooms et al. (2009) reported stent fracture in 12% and 15% of cases respectively.

Numerous studies have been published on improving stent designs through computational means for many applications in the body (Gastaldi et al. 2010; García et al. 2012; Conway et al. 2012; Prasad et al. 2013; Ní Ghriallais and Bruzzi 2014; Petrini et al. 2016), however, few have examined tracheobronchial devices and their associated complications. McGrath et al. (2016) investigated tracheobronchial stent mechanical performance through *in-vitro* means. Using a combination of bench testing and computational modelling it was shown that stent response is especially loading specific, making it difficult to predict device *in-vivo* performance with bench-top testing alone. Other studies have evaluated the effect of stenting on tracheal deformation and local tissue response *in-silico* using fluid solid interaction (FSI) modelling (Malvè et al. 2010; Malvè et al. 2011c; Malvè et al. 2014; Chaure et al. 2016), proposing a method to estimate the susceptibility of a stent to migrate (Malvè et al. 2011c) and, suggesting that granulation formation is more likely caused by the high stresses induced from stent deployment rather than the effects of fluid dynamics (Chaure et al. 2016). While these studies provide valuable insights into stress locations and tissue granulation, relatively simplified stent representations were used that do not fully elucidate the stress magnitude or complex interactions that can occur in the airways.

The motion of the lungs during respiration is a complex mechanism controlled by the interaction of the pleurae, diaphragm and intercostal muscles. Each lung is encased within a thin, fluid-filled sac called a pleura, which also lines the diaphragm and mediastinum. The fluid-filled space (called the pleural cavity) allows frictionless motion between the lung and thoracic cavity, and keeps the lung inflated at all times

due to a negative intrapleural pressure (Lai Fook 2004). Respiratory motion occurs when the diaphragm and intercostal muscles contract, causing an increase in the volume of the thoracic cavity and a reduction in intrapleural pressure, which initiates air flow into the lungs (West 2012). In effect, the lungs remain passive and inflate and deflate with the expansion and contraction of the thoracic cavity (Werner et al. 2009). The lung has a large range of motion resulting in considerable deformation of the airways. The ability to capture this motion may be important in better understanding stent performance *in-vivo*. Much work has been performed in the area of lung motion modelling for applications such as tumour tracking for improved radiotherapy treatment (McClelland et al. 2013). In general, the techniques used to predict this complex motion can be divided into two groups: image registration and biomechanical modelling. Both groups make use of time dependant image data such as 4D CT or 4D magnetic resonance imaging (MRI). Deformable image registration procedures map lung motion by matching features between data sets obtained at different time points (Crum et al. 2004). However, these non-rigid deformations neglect tissue mechanics and so are undesirable for stenting analyses, but have been used to simulate airway deformation during respiratory motion for other applications (Yin et al. 2013; Ibrahim et al. 2015). Biomechanical modelling in contrast, makes use of physiological parameters, controlling lung motion by either projecting one lung surface onto another (Tawhai et al. 2009; Al-Mayah et al. 2010; Tehrani et al. 2015) or by applying a pressure to the lung or other surfaces (Villard et al. 2005; Werner et al. 2009; Eom et al. 2010; Fuerst et al. 2015). Surfaces from other respiratory phases commonly limit the deformation of the lung. Generally, the lung is considered a homogenous unit, with the parenchyma, airways and arterial network described by a single linear or non-linear material representation (Werner et al. 2009; Tawhai et al. 2009; Al-Mayah et al. 2011). Al-Mayah et al. (2010) evaluated the effects of a shell element representation of the bronchial tree on airway positioning using a linear elastic constitutive model, and found that the assumption of homogeneity is suitable for capturing global lung deformation. The application of a suitable pre-stress to account for negative intrapleural pressure acting on the lung surface is normally neglected, though Tawhai et al. (2009) did account for it using a uniform volume scaling method. This method is not suitable for inhomogeneous assemblies where

the deformation of parts such as the airways and parenchyma are not uniform. Ní Ghriallais and Bruzzi (2014) previously showed that femoropopliteal artery stenting can lead to changes in global deformation characteristics and have major effects on vessel deformation. None of these biomechanical models have been used to analyse the effect of lung motion on stent performance, or on the effect that stenting has on global lung deformation. Other models have been developed that investigate the local effects of fluid dynamics on tracheal tissue response using FSI modelling (Malvè et al. 2010; Malvè et al. 2011d; Malvè et al. 2011b). In these studies models of the trachea include cartilage and muscle representations which describe the principal structures in the tracheal airway. Anisotropic material constitutive models and realistic pressure and velocity conditions allow for the accurate capture of trachea collapsibility during breathing and coughing (Malvè et al. 2010). The effect of stent loading on local tissue response has also been performed in these analyses (Malvè et al. 2011a; Malvè et al. 2014; Chaure et al. 2016). However, due to the intricacy of FSI modelling these studies simplify the complex interaction between the stent and tissue wall. The effect of swallowing on the stent-tissue interaction in the trachea has also been performed for a variety of stents (Trabelsi et al. 2011; Trabelsi et al. 2015), but similarly simplify the stent representations.

The objective of this study is to develop a finite element framework that can be used to evaluate tracheobronchial stent performance *in-vivo*. Firstly, to accomplish this objective a physiologically realistic finite element ovine lung model capable of capturing biomechanical loading from lung deformation and pressure variation during respiration is generated. The deployment of tracheobronchial stents into the bronchial tree is then simulated to evaluate the effect of realistic physiological loading on stent and tissue response, with the aim of informing future stent designs.

4.2 Materials and Methods

4.2.1 Imaging Data

All procedures used conform to the “Guide for the care and use of laboratory animals” (8th ed., Washington, DC: Natl. Acad. Press, 2011). The described procedure was part of a study evaluated and approved by the North Rhine Westphalian State

Agency for Nature, Environment and Consumer Protection under number 84-02.04.2013.A452. As part of the PulmoStent project pressurised CT data was obtained for a healthy adult female sheep with a body weight of 50 kg (Thiebes et al. 2017). The sheep was pre-medicated with intramuscular 1% atropine sulphate (0.1-0.15 mg/kg, Dr. Franz Köhler Chemie, Germany) and 2% xylazine (1 mg/kg, Vexylan, Ceva, Germany) and endotracheally intubated. Anaesthesia was maintained by ventilation with isoflurane (1–2 vol%)-oxygen mixture. The sheep thorax was then imaged at fixed gauge pressures of 0, 15 and 30 cmH₂O using a Siemens Somatom Definition Flash scanner with a pixel resolution of 0.78 mm. It is assumed that at 0 cmH₂O (atmospheric pressure) the lung is at a volume similar to that at the end of passive expiration, which relates to the functional residual capacity (FRC) of the lung. The 30 cmH₂O pressure is considered the maximum volume that the lung can expand to during maximal inhalation, and is referred to as total lung capacity (TLC). Finally, the 15 cmH₂O pressure is referred to as mid capacity (MC) due to its midway position between the minimum and maximum pressure points in this analysis. Due to practical considerations the scan was performed with the animal in the lateral position. Body position can affect lung volume and shape at the measured pressures (Moreno and Lyons 1961; Hoffman 1985), and so ideally scanning should have been performed in the prone position. This will have affected the recorded airway deformation so that it may not precisely represent the natural deformation of the airways, but should still provide an adequate approximation.

4.2.2 Lung Geometry

Lung geometry is extracted and assembled from the *in-vivo* data sets using Mimics and 3-Matic (Materialise, Belgium). The left lung parenchyma is removed as a continuous surface neglecting separate lobes. A partial length of the trachea (cut above the most cranial surface of the left lung) and all major bronchi visible from the CT are extracted using the airway cavity as tissue thickness is not discernible from CT. This includes branches as low as the ninth generation, though the average branch generation is the fifth. A uniform thickness of 1 mm (based on measurements performed in Section 4.2.5.1) is offset from the obtained airway cavity to produce the airway tissue geometry. The FRC lung assembly is created by inserting the FRC

airway into the corresponding parenchyma surface and subtracting the airway cavity (Fig. 4.1). This leaves only the airway tissue and parenchyma with an unobstructed airway channel which allows for stent deployment. The airway tissue and parenchyma volumes are meshed with a high quality tetrahedral mesh using TetGen (Si and Gärtner 2015). All airway nodes in contact with the lung are fully bonded at coincident nodes, excepting those approximately 1 mm from where the main bronchus enters the lung. This ensures that lung surface deformation does not excessively distort the displacement of the bronchus at the interface between the two components. In this work only the left lung and airway is modelled to improve computational efficiency. The same modelling approach can be applied to both lungs simultaneously if required.

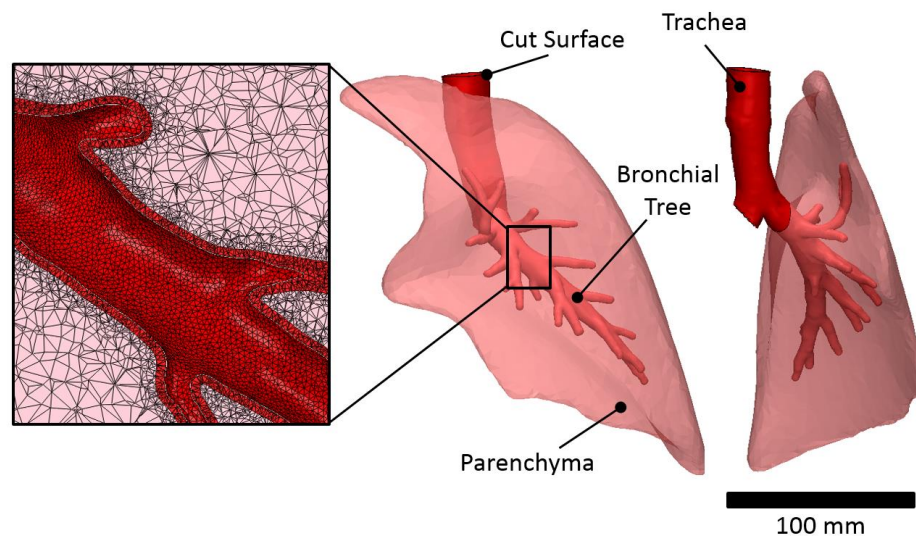


Fig. 4.1: FRC lung assembly including mesh detail.

Mesh convergence was performed by deploying a stent section into a pre-strained cylindrical tube representing an airway section. Various mesh densities were investigated using total contact force on the tissue surface as the convergence criteria. The selected mesh converged to within 2.2% of a mesh over three times denser. The lung parenchyma and airway sections of the selected mesh contained 365,198 and 342,242 elements respectively. A section of the mesh is shown in Fig. 4.1.

4.2.3 Zero-pressure Assembly

Negative intrapleural pressure maintains continuous lung expansion, which results in the lungs being in a constant state of tension *in-vivo*, and consequently all lung geometries from *in-vivo* CT contain inbuilt pre-stresses which should be considered when simulating lung mechanics. Typically, in biomechanical lung modelling the physiological stress state of the *in-vivo* lung data has either been ignored by assuming the acquired data contains no pre-stress (Werner et al. 2009; Al-Mayah et al. 2011; Fuerst et al. 2015), or accounted for only by applying a uniform scaling of a homogenous lung volume (Tawhai et al. 2009), which is unsuitable when considering the inhomogeneity caused by the lung's airways. However, much work has been performed on *in-vivo* stress states in other applications, primarily in the vascular system, where various methods have been utilised (Lu et al. 2007; Gee et al. 2009; Alastrué et al. 2010; Bols et al. 2013; Nestola et al. 2017). In this work, an inverse method adapted from the algorithm presented by Bols et al. (2013) is employed to obtain a suitable zero-pressure (ZP) lung assembly. Note a zero-pressure state is defined in this work as the state the lung would be in if there was zero (or atmospheric) pressure everywhere in the lung. The proposed approach does not account for residual stresses in the lung.

In the proposed method the ZP assembly is obtained over two steps: a forward step, and a backward step. For the forward step, lung motion from FRC to TLC is simulated assuming no pre-stress is present in the lung assembly at FRC. Over the forward motion the displacement of each node on the lung assembly is recorded to form the displacement vector field (DVF). The backward step is then performed to obtain the ZP assembly by deflating the lung from FRC to ZP by assuming that the FRC assembly unloads along the reverse path of the DVF. This is accomplished through updating the FRC assembly's nodal coordinate field (NCF) by uniformly scaling the DVF and subtracting it from the NCF. Using this method a physiologically relevant deformation is used to acquire the ZP assembly.

Lung motion from FRC to TLC is simulated in the forward step using a pleural surface method adapted from Tawhai et al. (2009). The outer surface of the parenchyma of the lung assembly is constrained to remain in frictionless contact with a surface (the

pleural surface) containing an identical mesh to the outer surface of the parenchyma. When the nodes on the pleural surface are deformed, the lung assembly deforms accordingly by remaining in contact and freely sliding on the pleural surface. Lung motion is captured in a physiologically realistic manner by allowing the parenchyma to slide in this way. The nodal displacement of the pleural surface is calculated by projecting the pleural surface at FRC onto the corresponding surface at TLC. This is achieved using an incremental expansion and smoothing method implemented in Matlab (MathWorks, USA) and Abaqus (V6.14, DS Simulia, USA). During simulation of lung motion the nodes on the cut surface of the trachea (Fig. 4.1) are held in all directions to represent the fixation at the larynx, and to remove rigid body motion. The forward displacement vector of each node in the lung assembly is recorded to create the lung assembly DVF using

$$u_f = x_{TLC} - x_{FRC} \quad (4.1)$$

Where u_f is the nodal forward displacement vector, x_{TLC} and x_{FRC} are the coordinates of the same node at TLC and FRC respectively.

In the backward step the ZP assembly is obtained by assuming the lung deflates backward along the determined DVF. To ensure the deformation applied is physiologically relevant an appropriate scaling must be applied. Meaning that the deformation should be related to the intrapleural pressure required to maintain the lung at FRC *in-vivo*. Here, the intrapleural pressure is set to 6.84 cmH₂O which is what has previously been measured in sheep lying in the (left) lateral position (Hurewitz et al. 1984). An appropriate deflation of the lung is then determined by linearly scaling the DVF, based on the ratio of intrapleural pressure (6.84 cmH₂O) to the pressure difference between FRC and TLC (30 cmH₂O), which corresponds to 23% of the DVF. Thus, the NCF of the ZP assembly is determined using nodal positioning described by

$$x_{SF} = x_{FRC} - ku_f \quad (4.2)$$

Where x_{SF} is a ZP nodal coordinate, and k is a scalar variable used to uniformly scale the corresponding vector displacement with a value of 0.23. After nodal coordinates have been updated the ZP assembly volume mesh is remeshed due to the effects the

large backward displacements have on mesh quality. All structural surfaces are maintained during this process. With the ZP lung assembly obtained, appropriate physiological stresses at FRC can be applied by re-inflating the assembly. It should be noted that this method does not produce a unique solution, which would require a far more complex approach.

4.2.4 Stent Model

The stent design used in this analysis consists of a repeating segmented geometry joined by alternating connectors based on the nitinol laser-cut Cordis SMART stent. To determine the effect of stent length on mechanical performance in the airways two 15 mm diameter stents with a length of 25 mm (short stent) and 51 mm (long stent) respectively are modelled. Dimensions for the stents are given in Fig. 4.2. The stents are meshed with 2400 and 4832 Timoshenko beam elements (B31) respectively. Mesh sensitivity shows the Von Mises stress and max principal strain to agree to 1.6% and 3.1% respectively for a mesh 4.6 times denser than the selected mesh. The stents are designed to have a chronic outward force (COF) within the range of other commercial devices of the same diameter (McGrath et al. 2014; Thiebes et al. 2017). The normalised radial force of the stents per unit length is shown in Fig. 4.3.

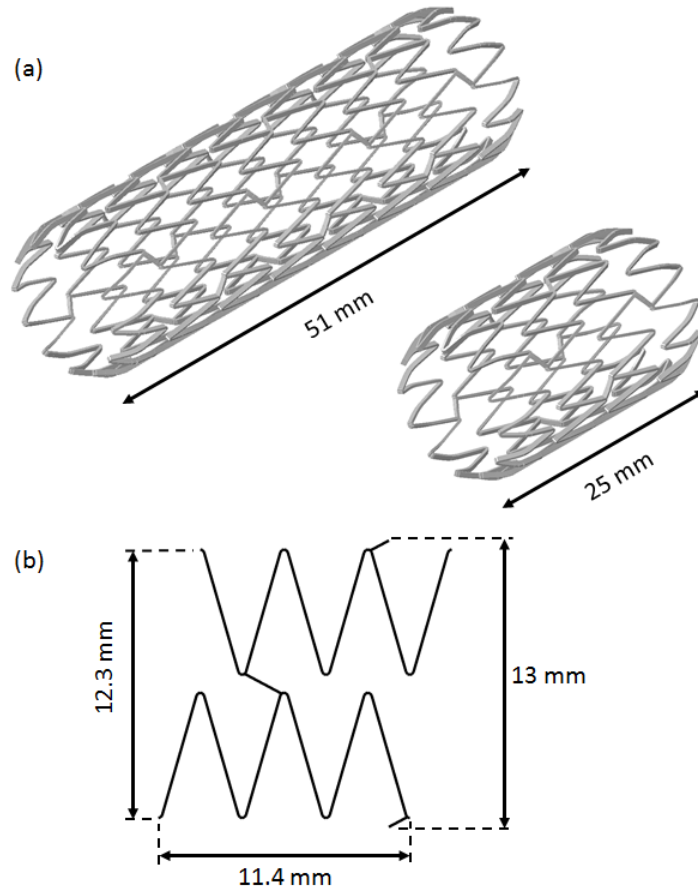


Fig. 4.2: (a) 3D Stent designs for both stents. (b) Periodic stent unit dimensions. Both stents have the same repeating unit.

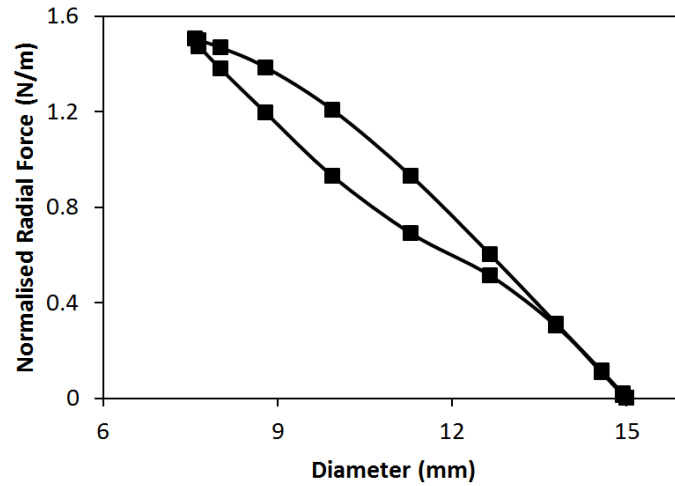


Fig. 4.3: Normalised radial force for the short stent. The curve for the other stent is not shown as the stents have a similar normalised force.

4.2.5 Material Properties

4.2.5.1 Tissue Properties

Preliminary airway properties were obtained from tensile testing of ovine main bronchi samples. Rectangular samples 5 x 40 mm were cut from the bronchi tissue in the circumferential direction. After recording sample thickness uniaxial tensile testing was performed on a Zwick biaxial testing machine with a 500 N load cell and a calibrated video extensometer camera. Samples were cyclically loaded to 0.1 mN for five cycles, and then tensile tested to failure at a rate of 1 mm/min. Tests were performed at room temperature and within 24 hours of sacrifice. Results of a representative sample were fit to a second order reduced polynomial constitutive model, where the strain energy potential is represented by

$$U = \sum_{i=1}^2 C_{i0} (\bar{I}_1 - 3)^i + \sum_{i=1}^2 \frac{1}{D_i} (J^{el} - 1)^{2i} \quad (4.3)$$

where C_{i0} and D_i are temperature-dependent material parameters, \bar{I}_1 is the first deviatoric strain invariant and J^{el} is the elastic volume ratio. The experimental and computational tensile results are displayed in Fig. 4.4 (Computational fit is discussed in more detail in Appendix 4). As airway diameter decreases, airway tissue thickness decreases (Kamm 1999), resulting in a reduction in section stiffness that should be accounted for in a computational representation. As the airway geometry used in this analysis contains a constant thickness, a reduction in section stiffness is instead achieved by linearly scaling the constitutive model coefficients fit to the experimental data based on the assumption of a constant relationship for the ratio of airway diameter to thickness. This relationship can be observed in the airways down to at least the sixteenth branching generation (Kamm 1999). To limit the number of material representations required to vary the section stiffness in this way the airways were split into four equal diameter ranges (M1-M4) and assigned a material property according to the median diameter for each group. A ratio of 15.6 was used to vary the material properties based on the average measured thickness of the main bronchi (1 mm) and the corresponding diameter in the lung-assembly geometry (15.6 mm). Material properties for the designated sections are given in Table 4.1. Though the airways contain a combination of smooth muscle and cartilage, material

properties are assumed homogenous. There is no consensus in the literature on appropriate parenchymal constitutive models as properties can vary widely (Zeng et al. 1987). In this study baseline properties were obtained from Rausch et al. (2011) and fit to a second order reduced polynomial. The determined constants were then linearly scaled until the pressure to expand the ZP lung assembly from FRC to TLC was close to 30 cmH₂O (lung expansion is described in Section 4.2.6.1). Material properties are shown in Table 4.1. Rayleigh damping with an α coefficient of 8000 was applied to a thin layer of shell elements offset from the lung and airway surfaces to reduce unrealistic fluctuations during lung motion.

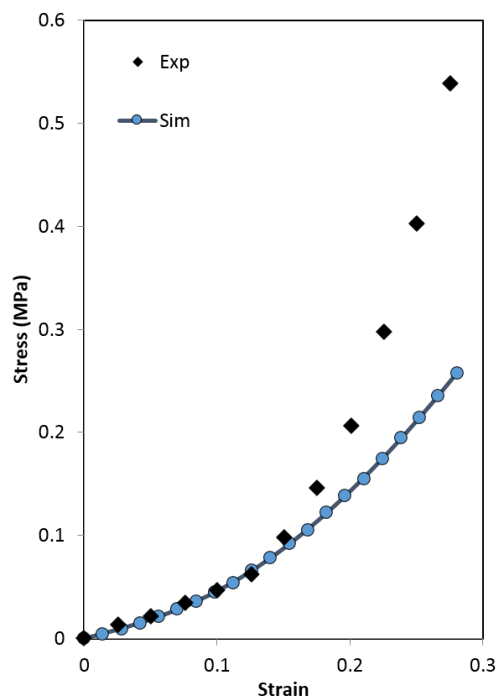


Fig. 4.4: Experimental and computational results for circumferential bronchial section.

4.2.5.2 Stent Properties

The inbuilt Auricchio nitinol constitutive model in Abaqus is utilized for the stent properties (Auricchio et al. 1997). Parameters used are shown in Table 4.2 which are obtained from McGrath et al. (2014), where further details on testing and fit can be found.

Table 4.1: Constitutive model coefficients. M1 to M4 refer to airway materials and L1 refers to the parenchymal material. A Poisson's ratio of 0.42 and 0.3 was used for airway and parenchyma properties respectively. The selected airway Poisson's ratio was used to help with model convergence issues.

Parameter	M1	M2	M3	M4	L1
Scale	1.33	0.98	0.64	0.34	0.37
D1	2.099	2.848	4.361	8.210	1365.218
D2	0	0	0	0	0
C ₁₀	0.081	0.059	0.038	0.021	0.00034
C ₂₀	0.874	0.644	0.421	0.223	0.0014

Table 4.2: Nitinol material properties used in the Abaqus constitutive model. *Nitinol non-symmetric properties in tension and compression were used to capture hysteresis effect using B31 elements.

Parameter	Value
Austenite Elasticity (MPa)	53001
Austenite Poisson's Ratio	0.3
Martensite Elasticity (MPa)	21500
Martensite Poisson's Ratio	0.3
Transformation Strain	0.038
Start of Transformation Loading (MPa)	434
End of Transformation Loading (MPa)	500
Reference Temperature (°C)	37
Start of Transformation Unloading (MPa)	210.3
End of Transformation Unloading (MPa)	138.7
Start of Transformation Stress During Loading in Compression (MPa)	634*
Volumetric Transformation Strain	0.038

4.2.6 Computational Experiments

All computational analyses are performed using Abaqus/Explicit (V6.14) due to large deformations and non-linearities caused by contact. The ratio of kinetic to internal

energy was maintained below 5% for all simulations. Semi-automatic mass scaling was used with a target time increment of 1E-6 and a lowest stable time increment of 5.4E-9.

4.2.6.1 Airway Positioning

Lung expansion is first simulated without stent loading to evaluate airway positioning. Simulations are performed with and without the inclusion of a pre-stress. For the model with no pre-stress (referred to as model A1, see Table 4.3) the FRC lung assembly previously obtained is expanded to TLC using the pleural surface method. During lung expansion, uniformly distributed pressure is applied directly to the inner surface of the airways according to the pressure-volume distribution in Fig. 4.5 (a). This represents the change in pressure caused by inflation of the lung during CT acquisition which helps capture local effects of airway deformation. For the pre-stress simulation (model A2) a nodal displacement method is used to simulate lung motion. Using the nodal coordinates obtained for the parenchyma surface at FRC and TLC from model A1, displacement boundary conditions are applied directly to the nodes on the outer surface of the ZP assembly parenchyma to inflate the lung to FRC (to apply the pre-stress), and then to TLC. The cut surface of the trachea is held in all directions and pressure is applied to the inner surface of the airways as before. This method of lung motion is employed to simplify the model without significantly affecting model accuracy (This is further discussed in Appendix 4). The nodal displacement method is used for all models using the ZP assembly.

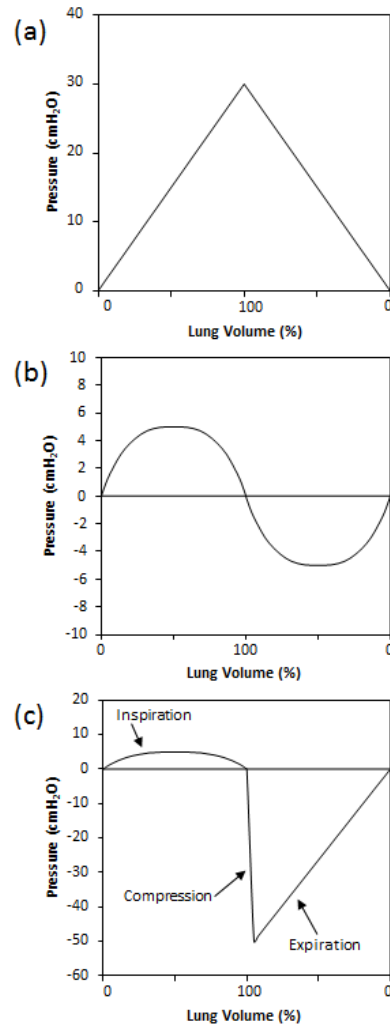


Fig. 4.5: Pressure-volume relationship for (a) ventilator loading, (b) breathing (Wall and Rabczuk 2008) and (c) coughing (McCool 2006). Volume is shown as a percentage of the tidal volume (the difference between FRC and TLC volumes). It should be noted that the ventilator and coughing conditions are simplified representations of more complex loads.

4.2.6.2 Stent Deployment and Loading

Stent deployment is simulated over a series of steps as illustrated in Fig. 4.6. The ZP lung assembly is first deformed to FRC (Fig. 4.6 (a)). A rigid cylinder representing the outer tube of a stent delivery system (aligned with the airway centreline at FRC) is then expanded from a diameter of 5 mm to 8 mm to straighten the airway to allow for stent deployment (Fig. 4.6 (b)). Following this, the stent is crimped from its freely expanded diameter of 15 mm to 7.5 mm using a rigid cylinder (Fig. 4.6 (c)). The stent is then deployed into the airway by radially expanding the crimper, while simultaneously reducing the diameter of the outer tube, and allowing the outer surface of the stent to contact the airway inner surface (Fig. 4.6 (d)). Before lung

motion is simulated, contact is removed for everything except the stent and airway surfaces (Fig. 4.6 (e)). General contact with a coefficient of friction of 0.1 is used to describe all contact in the simulation. No boundary conditions are directly applied to the stent geometry. Both stents are deployed at the same midpoint, which corresponds to the same deployment position selected for the insertion of a prototype stent with a 15 mm diameter as part of the PulmoStent project (Thiebes et al. 2017). Airway diameter in the region of stent deployment tapers from 14.1 mm to 9.8 mm, with an average diameter of 12.4 mm corresponding to a stent oversizing of 17%. Stent oversizing is used to guarantee a suitable lumen gain and to secure the device against migration (Freitag 2010; Gökgöl et al. 2015).

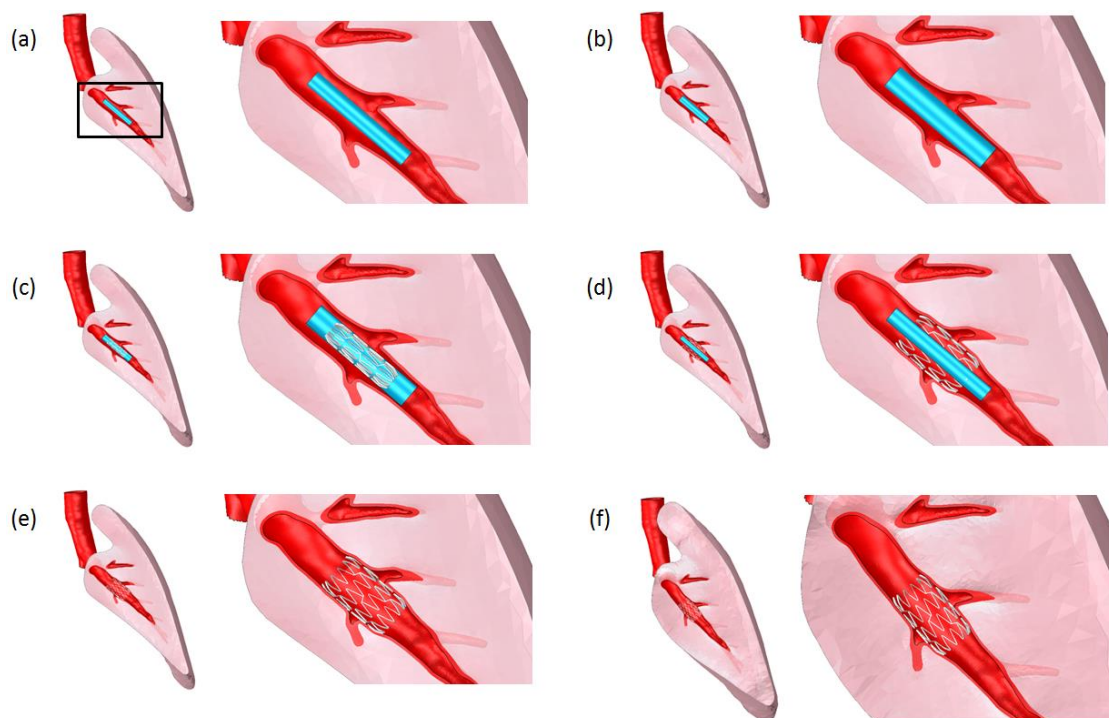


Fig. 4.6: Summary of stent deployment and physiological loading. (a) Lung assembly at FRC. (b) Delivery system outer expanded. (c) Stent crimped. (d) Stent deployed and outer crimped. (e) Stent deployed before respiratory loading. (f) Lung assembly and stent at TLC.

The influence of local and global physiological deformations is evaluated by performing a mix of stented analyses that include combinations of local pressure and global lung motion conditions. Local pressure effects are accounted for by applying a uniformly distributed pressure to the inner surface of the airways. Global motion is accounted for by expanding the lung using either a pleural surface method or nodal displacement method.

Global motion is modelled between FRC and TLC only. Three local pressure conditions are investigated for the stented bronchial tree: ventilation, breathing and coughing. The pressure-volume relationship associated with each condition is shown in Fig. 4.5. Ventilation loading (Fig. 4.5 (a)) is represented by a linear pressure-volume ramp for inspiration and expiration, based on the ventilation pressures applied for CT imaging. Breathing (Fig. 4.5 (b)) is simulated by applying a sinusoidal pressure-volume association obtained from Wall and Rabczuk (2008). Lastly, for coughing (Fig. 4.5 (c)) three steps are performed including inspiration, compression and expiration which relate to the three states of coughing (McCool 2006). For the compression step of coughing the lung volume at TLC is unloaded to 95% of the tidal volume based on a pressure increase of 50 cmH₂O. Each of the described loading conditions is simulated for both stents. Other loading conditions are also performed to illustrate the effect of local deformation and global lung motion. These include simulating ventilation, normal breathing and coughing without applying a global motion and simulating lung motion without a local pressure. All simulations are summarised in Table 4.3. It should be noted that the pressure conditions used to describe normal breathing and ventilation are acquired from human data due to the unavailability of suitable ovine data in the literature. However, as sheep lung function is considered similar to human lung function (Scheerlinck et al. 2008; Bähr and Wolf 2012) the influence of this on results should be relatively small. The pressure-volume relationships described here are simplified representations of very complex interactions. To properly represent the effects of lung deformation coupled with pressure variations a FSI model would need to be considered which is outside the scope of this work. For both the normal breathing and coughing analyses pressures are only applied to the bronchial tree due to collapse of the trachea during coughing.

Table 4.3: Summary of simulations performed. If no pre-stress is applied then global lung motion is controlled by the pleural surface method, otherwise the nodal displacement method is employed. Local Pressure refers to the specific local uniform pressure condition applied to the airway surface (described in Fig. 4.5). Global Motion refers to whether or not lung motion is applied to the lung assembly.

Model	Pre-stress	Stent	Local	Global Motion
	Y/N		Pressure	Y/N
A1	N	None	Ventilation	Y
A2	Y	None	Ventilation	Y
A3	Y	Short	None	Y
A4	Y	Short	Breathing	N
A5	Y	Short	Breathing	Y
A6	Y	Short	Coughing	N
A7	Y	Short	Coughing	Y
A8	Y	Short	Ventilation	Y
A9	Y	Long	Breathing	N
A10	Y	Long	Breathing	Y
A11	Y	Long	Coughing	N
A12	Y	Long	Coughing	Y
A13	Y	Long	Ventilation	Y

4.3 Results

4.3.1 Lung Deformation Results

4.3.1.1 Pressure-Volume Relationship

The relationship between lung pressure and volume change from FRC to TLC is shown in Fig. 4.7. The simulation pressure at TLC matches the *in-vivo* data closely as expected due to the experimental design. The model predicts a linear pressure-volume relationship which appears to adequately represent the loading response observed at MC.

4.3.1.2 Airway Positioning

A qualitative comparison of airway positioning at FRC and TLC is demonstrated in Fig. 4.8, with CT output shown in Fig. 4.8 (a) and corresponding computational predictions shown in Fig. 4.8 (b) and (c). The first thing to note is that the pre-stressed airways at FRC qualitatively match the *in-vivo* condition well (Fig. 4.8 (b)). A similar result can be seen for the simulation prediction at TLC, though there is a more distinct misalignment between CT and model positioning (Fig. 4.8 (c)).

Airway deformation accuracy is quantitatively assessed by comparing simulation branch point positioning to the corresponding CT data at FRC, MC and TLC. From Table 4.4 it can be seen that at TLC model A1 (no pre-stress) has a smaller average residual error (16.7%) than model A2 (pre-stress) (17.9%), though there is no significant difference between the two models ($p < 0.05$). Model A2 overcompensates for branch point motion with an average of 16.5 mm compared to the recorded motion of 16.2 mm. The average residual error at MC for model A2 is 30.8%, and the average branch point motion is 0.4 mm lower than the corresponding CT result. It should be noted that the pre-stress introduces a positioning error to model A2 with an average residual error of 1.1 ± 0.6 mm.

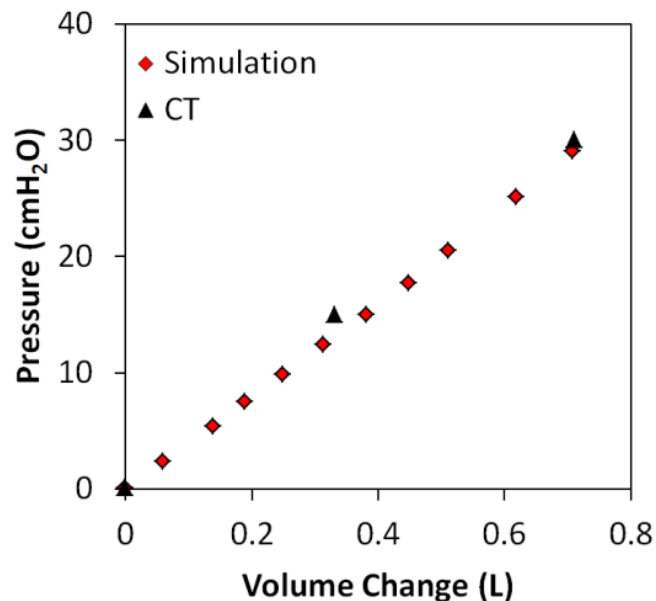


Fig. 4.7: Pressure versus volume change for model A2 compared to CT data. Change in volume from FRC to TLC.

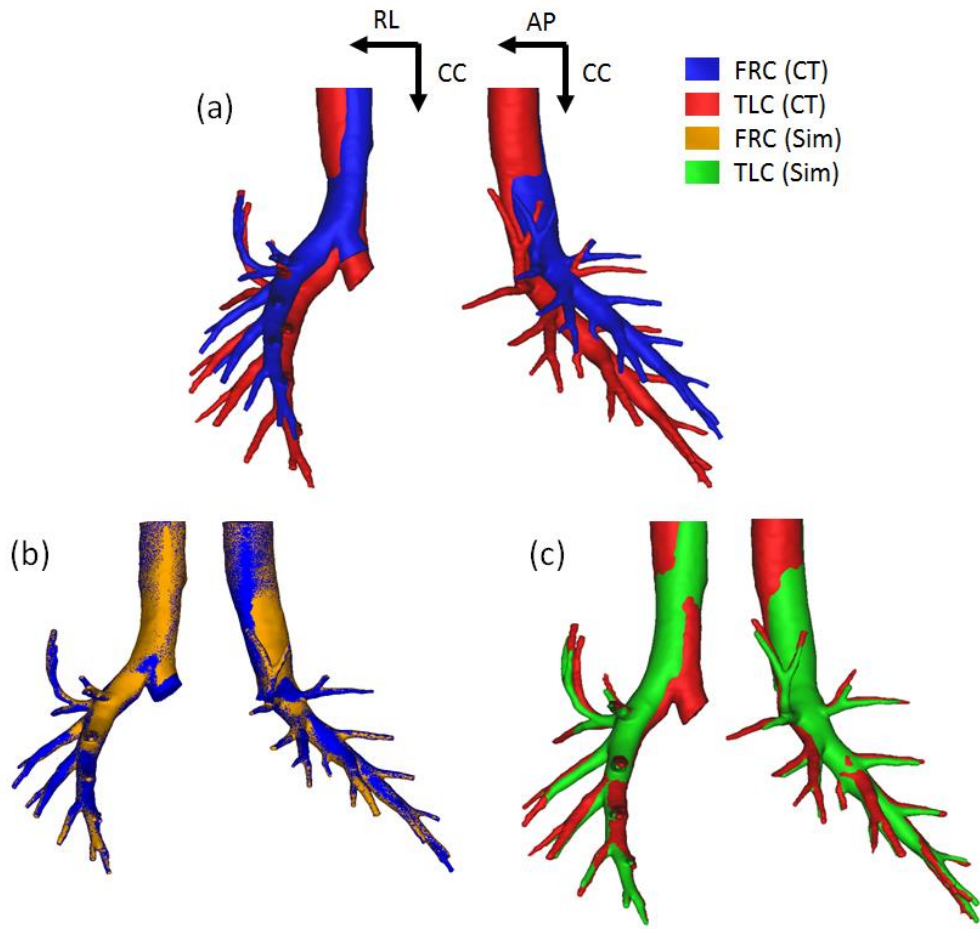


Fig. 4.8: (a) Airway positioning from CT at FRC and TLC. (b) Model A2 prediction of airway positioning compared to CT at FRC after pre-stress application (c) Model A2 prediction of airway positioning compared to CT at TLC. CC, AP and RL refer to the craniocaudal (head to toe), anteroposterior (front to back) and lateral (right to left) directions respectively.

Table 4.4: Airway branch point positioning. V is the lung volume position that measurements are recorded at, $\|R\|$ is the average residual error, R_{CC} , R_{AP} , and R_{RL} are the residuals in the craniocaudal, anteroposterior and lateral directions respectively. Negative values denote model overestimation in caudal, anterior and leftward directions. $\|\Delta P\|$ is the average branch point displacement from CT data and finite element models.

Model	V	$\ R\ $ (mm)	R_{CC} (mm)	R_{AP} (mm)	R_{RL} (mm)	$\ \Delta P_{CT}\ $ (mm)	$\ \Delta P_{FE}\ $ (mm)
A1	TLC	2.7 ± 1.3	-0.4 ± 1.7	1.0 ± 1.1	-1.6 ± 1.6	16.2	16.1
A2	TLC	2.9 ± 1.3	-0.9 ± 1.7	1.2 ± 1.2	-1.2 ± 1.5	16.2	16.5
A2	MC	2.8 ± 1.4	-0.3 ± 1.8	2.0 ± 1.3	-1.1 ± 1.1	9.1	8.7
A2	FRC	1.1 ± 0.6	0.1 ± 0.7	-0.1 ± 0.7	0.1 ± 0.6	-	-

4.3.2 Stenting Results

4.3.2.1 Effect on Airway Positioning

The effect of stent loading on airway positioning at TLC is graphically presented in Fig. 4.9. Here it can be seen that the short stent (Fig. 4.9 (a)) has a noticeably smaller global effect than the long stent (Fig. 4.9 (b)), where the influence extends from the trachea down to the most distal end of the airways. It is interesting to note that the shorter stent has regions of greater local deformation (highlighted by the black arrows) which suggests that it may be less constrained by the local geometry. The large deformation occurring at the distal end of the long stent is due to airway tapering over the stent length.

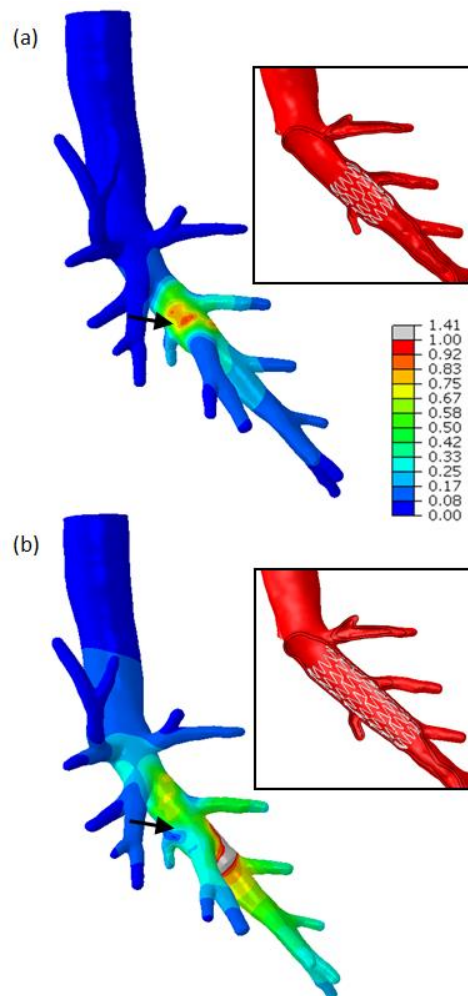


Fig. 4.9: Magnitude difference in nodal position at TLC between the unstented model (A2) and the (a) short stent model (A8), (b) long stent model (A13). Insets show stent positioning in airway. Black arrows highlight local differences in airway positioning between the two models. Values are given in mm.

4.3.2.2 Stent Reaction Force

Stent reaction force is determined by summing the normal contact force magnitude at each node on the stent. This corresponds to the force the stent exerts on the airway tissue. The reaction force of the short stent is displayed in Fig. 4.10 (a). The results show great variability between loading conditions, with coughing having the most significant impact, producing a difference of 0.13 N/mm (Note all reaction forces are normalised against stent length) between minimum inspiration and maximum expiration force. Ventilation loading also considerably affects the reaction force with a 0.07 N/mm range. Global lung motion with no local pressure effected stent response the least, causing a difference of only 0.01 N/mm. The influence of breathing with and without lung motion for both stents is shown in Fig. 4.10 (b). Although normalised against stent length, upon deployment the longer stent produces a force 1.4 times greater than the shorter stent. The effect of global lung deformation on stent reaction force is visible in different ways for the two stent types. The short stent produces a 33% higher force range than the pressure-only model, which is characterised by an overall drop in force during inspiration. Alternatively the long stent shows a mean drop in force for the lung deformation model, combined with an end expiration force that is significantly lower than the force at deployment which is not observed for the pressure-only simulation. Similar results are observed for coughing simulations shown in Fig. 4.10 (c), though the force range of the short stent is less affected by lung deformation in this case due to the more significant local pressure load.

4.3.2.3 Strain Analysis

Constant-life diagrams for breathing and coughing on both stent types are shown in Fig. 4.11. The results indicate that the global motion models produce higher strain amplitudes than the pressure-only models, although this is significantly less of a factor for the short stent under cough loading. Considering the local pressure-only analyses, it is shown that the maximum strain amplitudes for both stents are quite similar under the same loading conditions, but this is not the case for the local pressure and global motion results. Both long stent constant-life diagrams show that the global motion has a significant effect on strain amplitude results. However, even

with the inclusion of global motion the maximum strain amplitude remains well below 0.4% which is generally considered safe for stent loading under 10^7 cycles (Pelton et al. 2008), and so stent fracture is not to be expected. It should be noted that as the stent models are defined using beam elements the strain analysis is only performed to comment on general observations.

The effect of simulated coughing on stent displacement is qualitatively presented in Fig. 4.12. For the shorter stent the loading configuration appears to have little effect on stent displacement, suggesting that the stent is relatively well fixated. Conversely, the proximal migration of the long stent under local pressure and global motion is considerably more evident, implying that the positioning of the longer stent is much less stable.

Stent axial displacement is quantitatively presented for each simulation in Fig. 4.13. It can be seen that the long stent can displace over nine times more than the shorter stent when global motion is accounted for, but little axial displacement is observed with local pressure loading alone. Another observation is that comparable loading conditions affect the displacement of the stent types differently. The short stent displaces further under ventilation loading, while simulated coughing causes the longer stent to displace the greatest.

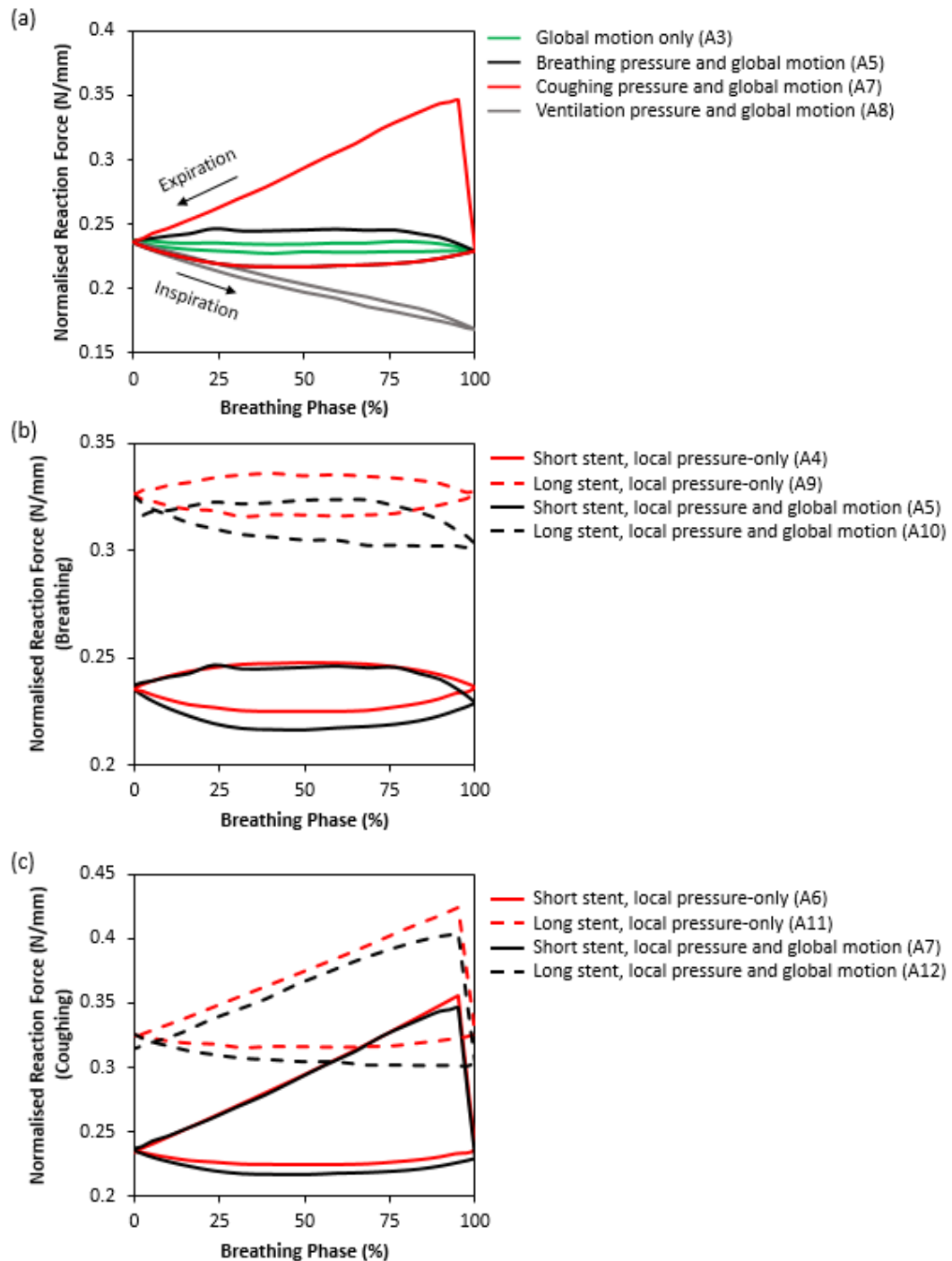


Fig. 4.10: Stent normalised reaction force during lung loading. 0% represents the lung volume at FRC and 100% is at TLC. (a) Typical results for the different local pressure loading types with global motion on short stent. (b) Results for breathing cycles with (models A5, A10) and without (models A4, A9) global motion applied to both stent types. (c) Results for coughing cycles with (models A7, A12) and without (models A6, A11) global motion applied to both stent types. Reaction force normalised against stent length.

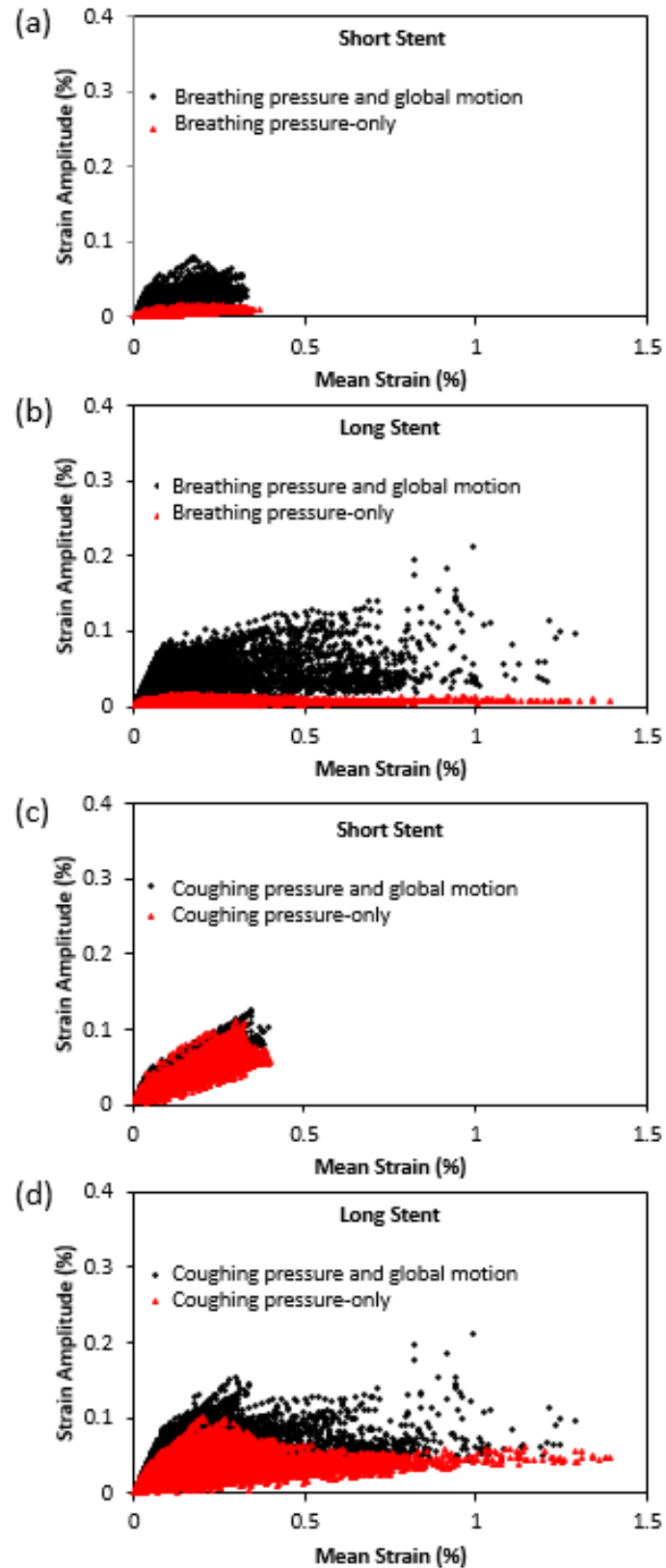


Fig. 4.11: Constant-life diagrams for normal breathing: (a) short stent, models A4 and A5 (b) long stent, models A9 and A10. Constant-life diagrams for simulated coughing: (c) short stent, models A6 and A7 (d) long stent, models A11 and A12.

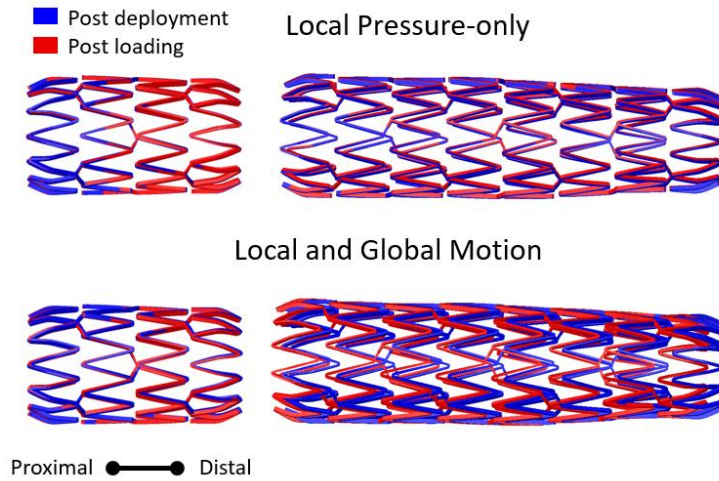


Fig. 4.12: Comparison of stent position after deployment at FRC (Blue) and after simulated coughing at FRC (Red). (Left): Short stent models A6 and A7. (Right): Long stent models A11 and A12. Proximal direction is leftwards.

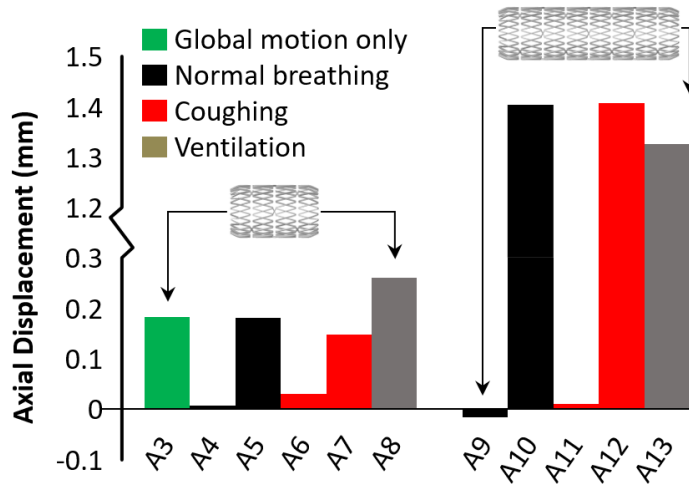


Fig. 4.13: Stent axial displacement between deployment and simulated loading at FRC. Values determined using average nodal displacement along stent axis. Positive values indicate proximal stent movement.

4.3.3 Tissue Interaction

Results shown in Fig. 4.14 compare stented bronchi stress states at maximum inspiration and minimum expiration pressures for simulated coughing. The contours in Fig. 4.14 (a) and (b) highlight the minute effect that pressure change alone has on the stented airway stress state. Fig. 4.14 (c) and (d) indicate that global motion has a greater effect due to the axial stretching of the airway during lung motion. These results signify that maximum principal stress can vary significantly in the airways under natural lung motion.

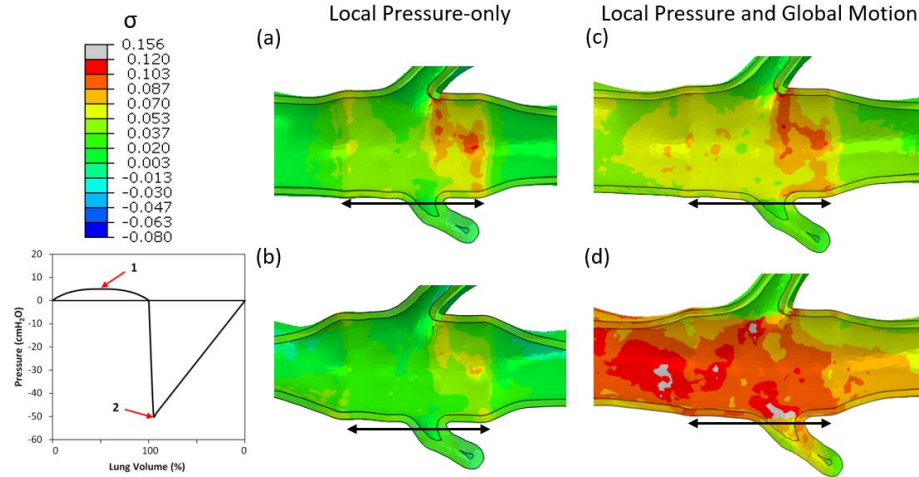


Fig. 4.14: Max principal stress in airway with the short stent. (a) Model A6 max inspiration. (b) Model A6 min expiration. (c) Model A7 max inspiration. (d) Model A7 min expiration. Number 1 and 2 refer to the max inspiration and max expiration pressure points respectively. Black arrows indicate stented region of the airway. Stresses are shown in MPa.

Another way of investigating the stent-tissue interaction is to evaluate the variation in contact pressure locally applied to the tissue surface by the stent. This is accomplished here by computing the mean contact pressure and the contact pressure change experienced by the airway surface. Mean contact pressure is calculated using

$$P_m = \frac{P_{max} + P_{min}}{2} \quad (4.4)$$

where P_m is the mean contact pressure at an individual node on the tissue surface, and P_{max} and P_{min} are the maximum and minimum nodal normal contact pressures on the airway tissue over the loading cycle. Contact pressure change is calculated using

$$P_\Delta = P_{max} - P_{min} \quad (4.5)$$

where P_Δ is the contact pressure change at an individual node. Stent-tissue contact pressure for the short stent under coughing conditions is illustrated in Fig. 4.15. The mean contact pressure for the pressure only model (Fig. 4.15 (a)), and displacement and pressure model (Fig. 4.15 (b)) show very similar contact patterns. Nevertheless, when considering the contact pressure change (Fig. 4.15 (c) and (d)) it becomes apparent that global motion results in larger changes in pressure, occurring over a

larger area. This indicates more localised stent motion against the tissue wall due to global lung deformation.

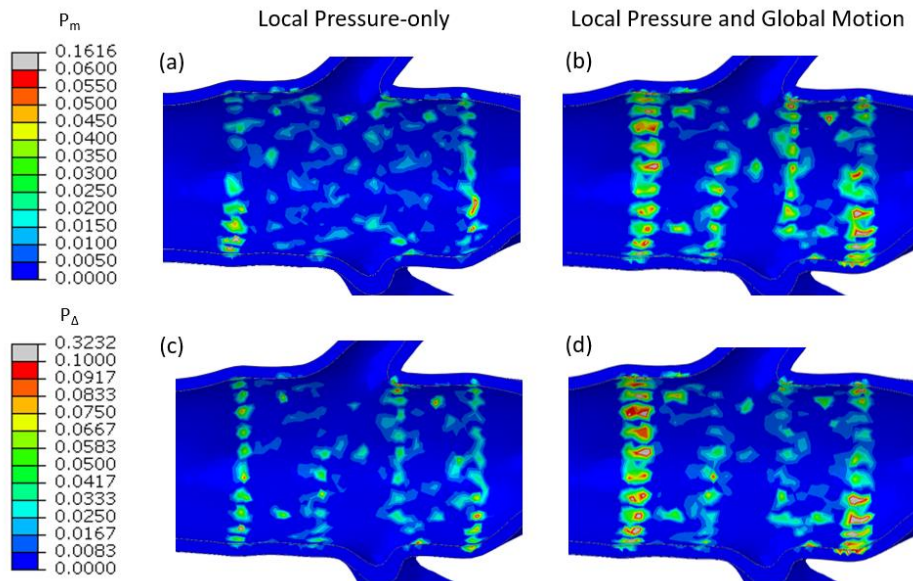


Fig. 4.15: Mean contact pressure and contact pressure change contours for the short stent under simulated coughing. (a) Model A6 mean force, (b) Model A7 mean force, (c) Model A6 force range, (d) Model A7 force range. Pressures are shown in MPa.

Fig. 4.16 visualises the contact pressure changes above 0.05 MPa to remove noise caused by small pressure variations and allow the effect of contact variation on airway tissue to be captured more effectively. The local pressure-only models record very few regions greater than 0.05 MPa (Fig. 4.16 (a) and (b)), while in contrast the global motion and local pressure models show a considerable area of tissue that experiences these sizeable swings in pressure (Fig. 4.16 (c) and (d)). There is a noticeable difference between the short stent (Fig. 4.16 (c)) and the long stent (Fig. 4.16 (d)) results, with much of the variation in force focused at the stent ends for the shorter stent, and throughout the length of the longer stent.

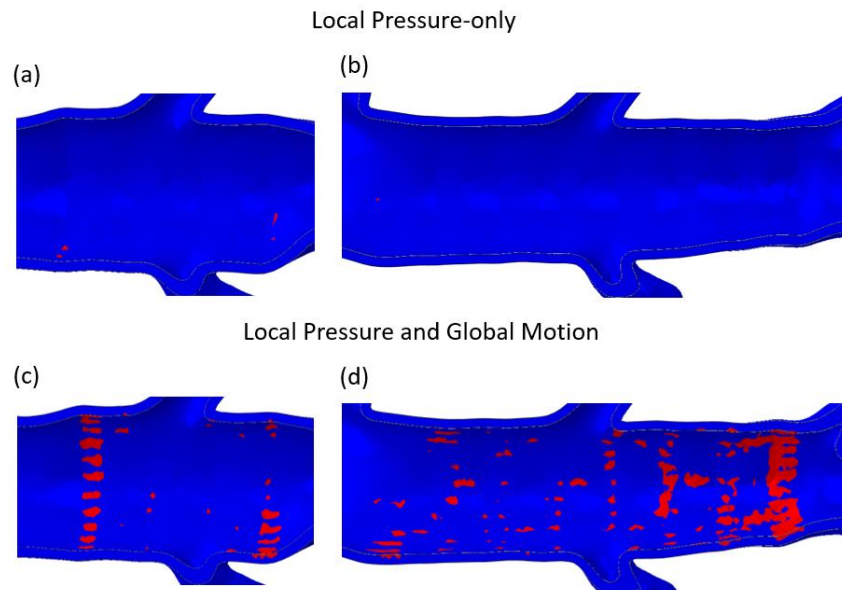


Fig. 4.16: Contact pressure change greater than 0.05 MPa (Red) for stent both stents under simulated coughing. Local pressure-only: (a) model A6, (b) model A11. Local pressure and global motion: (c) model A7, (d) model A12.

4.4 Discussion

The objective of this study was to develop a finite element framework that can be used to evaluate tracheobronchial stent performance *in-vivo*. This was accomplished by first developing a biomechanical ovine lung model capable of capturing realistic physiological loading, including pre-stress state, global lung motion and local pressure loading. Stent deployment and loading under ventilation, breathing and coughing conditions were then simulated.

An important aspect of this work is the ability of the biomechanical model to appropriately describe airway deformation so that suitable loading is applied to the stented region. Qualitatively it can be seen that the model is capable of capturing airway positioning from FRC to TLC quite well (Fig. 4.8), and quantitatively the average residual error of 2.9 ± 1.3 mm at TLC (Table 4.4) is within the 2.7 – 3.3 mm range reported in the literature for human biomechanical lung models (Werner et al. 2009; Al-Mayah et al. 2010). A similar error is observed at MC (Table 4.4), suggesting that the model is adept at capturing the airway deformation to some degree of accuracy throughout the lung motion. It should be noted however, that while this error is typical of biomechanical lung models it could be deemed relatively

high when considering 2.9 mm is around 20% of the average branch point displacement. This may have some effect on the ability of the model to accurately capture the stent-tissue interaction, but as the general motion of the lung is well captured this should not be significant. Although the application of a pre-stress is necessary to accurately model stent interaction with the airway, it is interesting to note that it had no significant effect on airway positioning when compared to the biomechanical model without pre-stress (Model A1) in Table 4.4. This implies that the inclusion of a pre-stress in lung models where the stress-state is not critical (such as in radiation therapy analyses) may not be necessary.

At first glance it would appear that local pressure loading conditions possess the most dominant effect on stent mechanical performance. This is evident in Fig. 4.10 where the change in stent reaction force is almost entirely determined by the particular pressure condition applied. However, when considering the other measured quantities it becomes apparent that airway deformation due to global motion has a significant effect on localised stent mechanical response. The inclusion of lung deformation in the analysis increases the maximum strain amplitudes for both stents under both breathing and coughing conditions (Fig. 4.11), a result that is also observed for stent axial displacement in Fig. 4.12 and Fig. 4.13, and similarly higher tissue contact force ranges are more prevalent in the models that include global lung motion (Fig. 4.16). These results suggest that the inclusion of global motion is necessary in order to suitably capture important aspects of stent-tissue interaction in the lung. Nevertheless, it should be noted that the application of local pressure-only conditions could be useful when first evaluating a stent design by ensuring a suitable radial force is obtained.

The models presented here appear to be able to indicate migration in the form of axial displacement. Results suggest that stent migration could be driven more by airway deformation caused by global lung motion rather than the effects of local pressure deformation alone, and that radial force may not be the only significant factor in maintaining stent position. The longer stent was shown to displace further than the short stent (Fig. 4.13) even though the former applied a greater normalised radial force upon deployment (Fig. 4.10 (b)). One reason for the improved fixation of

the shorter device may be due to geometrical considerations. This stent is able to expand uniformly (Fig. 4.12) and sit in between two bronchi branches (Fig. 4.9 (a)). The radial force applied by the stent expands the airway and essentially anchors it between the two branching points. Conversely, the longer stent does not gain fixation from geometrical features proximally due to the combination of its increased length and the airway taper, and this results in it being more vulnerable to migrate under the large deformations involved in global lung motion. These findings indicate that stent sizing (both radially and longitudinally) may be important in preventing stent migration and highlight the significant impact airway anatomy can have on stent response.

Granulation tissue formation is thought to initiate due to irritation caused by the repetitive motion of the stent rubbing against the airway tissue, or by excessive stent expansion forces (Hautmann et al. 1999; Schmäl et al. 2003; Saad et al. 2003; Hu et al. 2011; Ost et al. 2012). In previous computational analyses excessive expansion forces have been used to indicate granulation formation by highlighting areas of maximum tissue stress created by stent introduction (Malvè et al. 2014; Chaure et al. 2016). This may be a suitable predictor if the stresses generated by the stent are significantly higher than those experienced naturally by the tissue, but between Fig. 4.14 (c) and (d) it can be seen that the maximum stresses induced by the short stent are similar to those naturally experienced (due to the large deformations associated with global lung motion), and so, granulation formation owing to excessive stent expansion is not to be expected. However, granulation tissue is also thought to form due to the irritation caused by the stent rubbing against the tissue wall (Saad et al. 2003; Ost et al. 2012). Here, it is proposed that the change in contact pressure over a loading cycle can be used to indicate tissue irritation due to stent rubbing. Using this comparison the results in Fig. 4.16 (c) appear to indicate irritation at the stent ends, which is where granulation tissue tends to form (Schmäl et al. 2003; Freitag 2010). This is most likely caused by cyclic stretching of the airway tissue during lung motion. The longer stent shows a much larger area of the tissue experiencing high levels of irritation Fig. 4.16 (c). This is probably due to the effects of stent migration (Fig. 4.12). The results presented here show promise at being able to predict

granulation formation, but further work will need to be performed to be able to validate this indicator.

Another principal complication associated with airway stents is stent fracture. Although beam elements are not ideal for fatigue analysis, they can be used to indicate stress and strain trends. The results presented here suggest that the inclusion of global lung deformation increases the strain amplitude experienced by the stents for all loading scenarios. This could potentially be of more use in a diseased model where non-uniform tumour loading can have a more significant effect on stent response (McGrath et al. 2016). It should be noted that due to the differences in stent response between stent loading conditions that fatigue analyses should be performed for combinations of coughing and ventilation loading in order to capture the loading variability involved. If fatigue analyses are to be performed it would also be advisable to perform the analysis using more robust elements.

Finally, it should be noted that all of the methods used in the presented work are directly applicable to the human case. Patient-specific CT data can be used to obtain the lung assembly and global lung deformation as described. Typical lung function tests such as spirometry can be used to attain patient specific data for local pressure deformation. Airway material properties are readily available from the literature, and patient-specific parenchyma properties can be estimated as performed in this study. This means that the entire framework, or smaller aspects such as the determination of the ZP lung assembly can be easily implemented in analyses of human biomechanical lung modelling and tracheobronchial stenting.

4.5 Limitations

A major limitation of this study is the use of just one animal. Although the primary objective was to develop a framework for stent testing which was performed, some observations made could be better informed with a larger cohort. The simplification of tissue properties is another principal limitation of this study. An isotropic material representation is used to describe the airways, even though in reality they contain anisotropic properties in the axial and circumferential directions. The airways are also composed of a combination of smooth muscle and cartilage, which is also

neglected in this study. While this is deemed suitable for the lower airways where cartilage is randomly distributed it will have a significant effect on the tracheal response where c-shaped cartilage rings offer sizeable structural support to the airway, and so the model in its current form is not suitable for modelling tracheal stenting. This would require the inclusion of separate cartilaginous and smooth muscled regions which could be introduced if necessary. Moreover, airway thickness is assumed constant throughout the bronchial tree, though four scaled material ranges are assumed to account for this it results in stress continuities at material boundaries. These simplifications have implications for stresses observed in the tissue and would have some effect on the stent-tissue interaction. Similarly, an unphysical linear pressure-volume response is obtained when loading the parenchyma material in this study. Further work needs to be performed to obtain a more realistic material response. The application of a uniformly distributed pressure in the presented model does not accurately capture the effects of dynamic pressure that are present during breathing and coughing. To properly model the fluid interaction and its effect on the stent-tissue interaction a FSI analysis would be required. For the normal breathing analyses the inclusion of FSI would not be expected to have a significant effect on the presented results as fluid dynamics associated with breathing have previously been shown to have a limited effect (Chaure et al. 2016). The dynamic effects associated with coughing may have more noticeable implications. However, the simulation of the presented work using FSI is technically challenging, and previous airway stenting studies have been unable to adequately capture the stent-tissue interaction due to the limitations imposed (Malvè et al. 2011a; Malvè et al. 2014; Chaure et al. 2016), and so, practically speaking this may not currently be a viable option. It should also be pointed out that the applied pressure conditions were not animal specific, and were based instead on human data. However, animal specific pressure data was not available, and suitable ovine related data was not found in the literature. Another limitation is the use of static CT data which doesn't capture the dynamic effects of the lungs. The coefficient of friction between the stent and airway is assumed to be 0.1. A different coefficient could significantly affect stent loading results. A linear pressure-displacement relationship is assumed to calculate the pre-stress. In reality there are no straight

lines in the body and so this leads to a slight underprediction of the pre-stress used in this analysis. Another limitation is the use of just one respiration cycle in the analyses; continued cycling could shed more light on migration, granulation and constant-life results.

4.6 Summary and Conclusions

This study presents a computational framework that can be used to evaluate tracheobronchial stent designs using realistic *in-vivo* loading conditions. An ovine biomechanical lung model was developed that was capable of capturing realistic physiological loading with the inclusion of *in-vivo* stress states, global lung deformation and local pressure conditions. Stent deployment was simulated and a comprehensive study on tissue-stent interaction was performed for a variety of stent types and loading combinations. Results indicate that three of the primary complications associated with tracheobronchial stents including stent migration, granulation tissue formation and stent fracture could be investigated with this framework.

A major conclusion of this work is that airway deformation caused by global lung motion can have a significant impact on stent mechanical performance, and should be accounted for in biomechanical modelling. Another conclusion that can be drawn is that varying respiratory pressure conditions can produce considerably different responses, meaning that to suitably evaluate a stent design, coughing and ventilation conditions must both be considered to properly capture the stent loading range. Similarly, results indicate that stent deployment can have global implications for airway deformation. It was also shown that airway tree structure appears to play an important role in maintaining stent positioning, and should be considered when sizing stents. Finally, results were shown to agree with clinical observations that cyclic stretching of the airway could promote granulation formation through irritation caused by stent friction.

A.4 Appendix 4

A.4.1 Airway Tissue Computational Fit

In Fig. 4.4 the stress-strain relationship for the experimentally obtained bronchial tissue is compared to the used computational fit. A good agreement with the experimental is found below a strain of 15%, but above this the material fit diverges. The divergence is due to the use of a compressible material with an equivalent Poisson's ratio of 0.42. When fitting a hyperelastic material in Abaqus it assumes incompressibility and so Poisson effects are not considered. This was only realised post publication. To determine the effect of using a material with such a reduced stiffness computational models using the second order reduced polynomial with an effective Poisson's ratio of 0.49 (almost incompressible) and a Yeoh material model (third order reduced polynomial) with a Poisson's ratio of 0.49 were performed. The corresponding material fits are provided in Fig. A4.1.

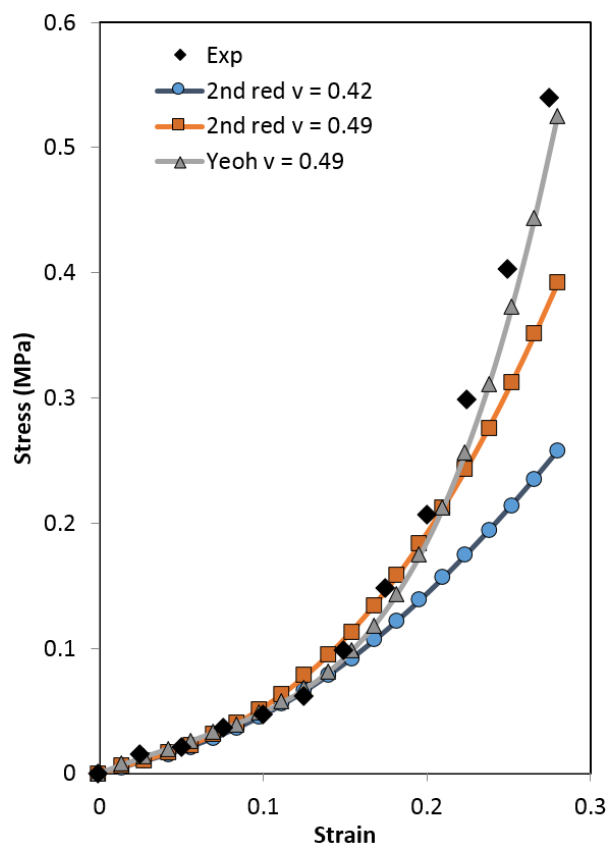


Fig. A4.1: Comparison of computational and experimental fits using different material models.

The model consisted of deploying the S1 stent at FRC and simulating lung expansion under normal breathing conditions to TLC. In Fig. A4.2 the maximum principal stress

distribution in the airway at TLC is compared for each model. As can be seen from the figure the inclusion of a lower Poisson's ratio results in an underprediction of the maximum principal stress on the tissue by up to a maximum of 53%. However, the stress distributions within the tissue are largely similar with areas of high stress predicted in the more accurate models similarly being predicted in the utilised model.

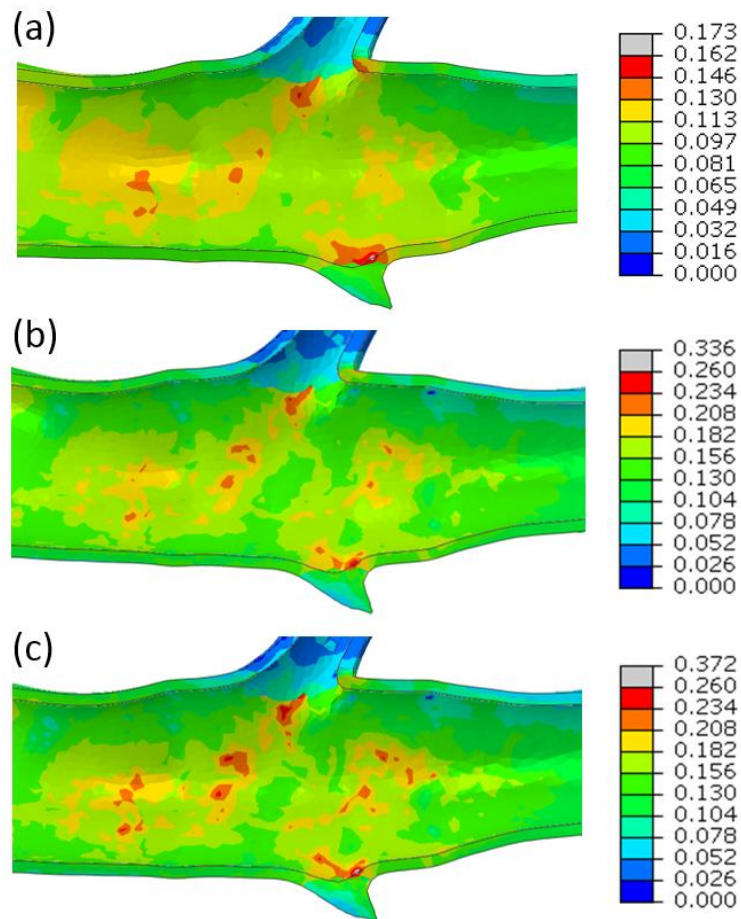


Fig. A4.2: Comparison of stress induced in airway tissue when using different constitutive models and fits with stent S1 deployed at TLC. (a) Second order reduced polynomial with Poisson's ratio = 0.42, (b) second order reduced polynomial with Poisson's ratio = 0.49, (c) Yeoh model with Poisson's ratio = 0.49. Maximum principal stress shown in MPa. No pressure is applied to the model.

Fig. A4.3 considers the distribution of maximum principal stress within the airway tissue. It can be determined from this that 95.5% of the volume in the stented region experiences stress levels below 0.113 MPa, which corresponds to an estimated maximum over-prediction of strain of <10% (i.e. a strain value around 0.015). If the entire airway tree is considered then 94.9% of the airway volume experiences stresses below 0.097 MPa, which corresponds to an estimated under-prediction of

<6% (i.e. a strain value around 0.009). This will inevitably affect the interaction between the tissue and the stent, but should not overly influence the resulting trends and presented conclusions.

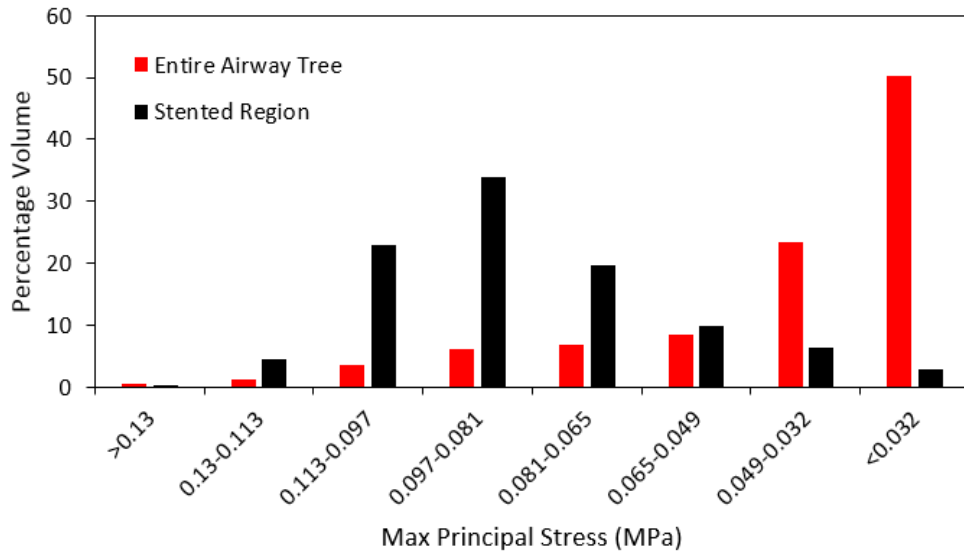


Fig. A4.3: Maximum principal stress distribution in airway tissue for the entire airway tree and the stented region at TLC. The stented region corresponds to the area shown in Fig. A4.2.

A.4.2 Nodal Displacement Method Accuracy

Lung motion is realised in two distinct but related ways in this work. The first method (the pleural surface method) indirectly deforms the lung assembly between two known lung volumes using a sliding contact condition, while the second method (nodal displacement method) deforms the lung assembly by displacing nodes on the outer surface of the lung parenchyma to nodal positions previously determined by the pleural surface method. As only the displacement of the outer nodes on the parenchyma are controlled, the rest of the parenchyma and the airways of the lung assembly are free to deform as before. In this study the nodal displacement method is used to deform the zero-pressure assembly to FRC and then to TLC. It is employed to simplify the model for the stent loading analyses by removing the need for contact (which removes convergence issues associated with deforming the zero-pressure assembly and improves model efficiency) without substantially affecting the accuracy of the model. This is observed from the average residual error shown between models A1 and A2 in Table 4 (Chapter 4) (2.7 ± 1.3 mm and 2.9 ± 1.3 mm respectively). Similarly, if the total force to expand the lung assemblies are compared

(Fig. 4.17) it can be seen that the ZP assembly follows along a similar path as the FRC assembly. This suggests that the nodal deformation method does not significantly affect the local deformation of the assembly elements, as considerably higher forces would be expected.

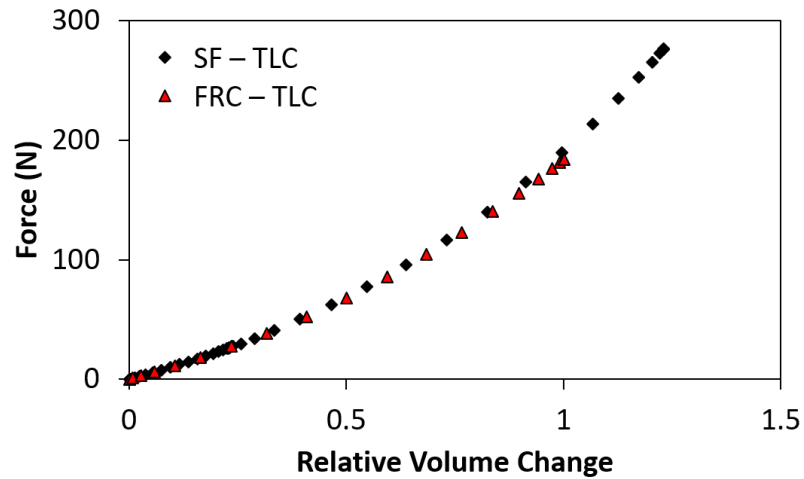


Fig. 4.17: Comparison of total nodal reaction force to expand the FRC lung assembly and ZP lung assembly to TLC using the nodal displacement method. Relative volume change based on volume change from FRC to TLC.

References

- Al-Mayah A, Moseley J, Velec M, Brock K (2011) Toward efficient biomechanical-based deformable image registration of lungs for image-guided radiotherapy. *Phys Med Biol* 56:4701–13. doi: 10.1088/0031-9155/56/15/005
- Al-Mayah A, Moseley J, Velec M, Hunter S, Brock K (2010) Deformable image registration of heterogeneous human lung incorporating the bronchial tree. *Med Phys* 37:4560–4571. doi: 10.1118/1.3471020
- Alastrué V, Garía A, Peña E, Rodríguez JF, Martínez MA, Doblaré M (2010) Numerical framework for patient-specific computational modelling of vascular tissue. *Int j numer method biomed eng* 26:35–51. doi: 10.1002/cnm.1234
- Auricchio F, Taylor R, Lubliner J (1997) Shape-memory alloys: macromodelling and numerical simulations of the superelastic behavior. *Comput methods Appl ...* 146.3:281–312.
- Bähr A, Wolf E (2012) Domestic animal models for biomedical research. *Reprod Domest Anim* 47:59–71. doi: 10.1111/j.1439-0531.2012.02056.x
- Bolliger CT, Sutedja TG, Strausz J, Freitag L (2006) Therapeutic bronchoscopy with immediate effect: laser, electrocautery, argon plasma coagulation and stents. *Eur Respir J* 27:1258–71. doi: 10.1183/09031936.06.00013906
- Bols J, Degroote J, Trachet B, Verhegghe B, Segers P, Vierendeels J (2013) A computational method to assess the in vivo stresses and unloaded configuration of patient-specific blood vessels. *J Comput Appl Math* 246:10–17. doi: 10.1016/j.cam.2012.10.034
- Chaure J, Serrano C, Fernández-Parra R, Peña E, Lostalé F, De Gregorio MA, Martínez MA, Malvè M (2016) On studying the interaction between different stent models and rabbit tracheal tissue: numerical, endoscopic and histological comparison. *Ann Biomed Eng* 44:368–381. doi: 10.1007/s10439-015-1504-3
- Chung FT, Chen HC, Chou CL, Yu CT, Kuo CH, Kuo HP, Lin SM (2011) An outcome analysis of self-expandable metallic stents in central airway obstruction: a cohort study. *J Cardiothorac Surg* 6:46. doi: 10.1186/1749-8090-6-46
- Chung FT, Lin SM, Chen HC, Chou CL, Yu CT, Liu CY, Wang CH, Lin HC, Huang CD, Kuo HP (2008) Factors leading to tracheobronchial self-expandable metallic stent fracture. *J Thorac Cardiovasc Surg* 136:1328–1335. doi: 10.1016/j.jtcvs.2008.05.039
- Conway C, Sharif F, McGarry JP, McHugh PE (2012) A computational test-bed to assess coronary stent implantation mechanics using a population-specific approach. *Cardiovasc Eng Technol* 3:374–387. doi: 10.1007/s13239-012-0104-8
- Crum WR, Hartkens T, Hill DLG (2004) Non-rigid image registration: theory and practice. *Br J Radiol* 77:S140–S153. doi: 10.1259/bjr/25329214
- Dooms C, De Keukeleire T, Janssens A, Carron K (2009) Performance of fully covered self-expanding metallic stents in benign airway strictures. *Respiration* 77:420–6. doi: 10.1159/000203364
- Eom J, Xu XG, De S, Shi C (2010) Predictive modeling of lung motion over the entire respiratory cycle using measured pressure-volume data, 4DCT images, and finite-element analysis. *Med Phys* 37:4389. doi: 10.1118/1.3455276

- Fernández-Bussy S, Majid A, Caviedes I, Akindipe O, Baz M, Jantz M (2011) Treatment of airway complications following lung transplantation. *Arch Bronconeumol* ((English Ed 47:128–133. doi: 10.1016/S1579-2129(11)70031-3
- Freitag L (2010) Airway stents. In: Strausz J, Bolliger CT (eds) *Interventional Pulmonology*. European Respiratory Society Journals Ltd, Sheffield, pp 190–217
- Fuerst B, Mansi T, Carnis F, Salzle M, Zhang J, Declerck J, Boettger T, Bayouth J, Navab N, Kamen A (2015) Patient-specific biomechanical model for the prediction of lung motion from 4-D CT images. *IEEE Trans Med Imaging* 34:599–607. doi: 10.1109/TMI.2014.2363611
- García A, Peña E, Martínez MA (2012) Influence of geometrical parameters on radial force during self-expanding stent deployment. Application for a variable radial stiffness stent. *J Mech Behav Biomed Mater* 10:166–75. doi: 10.1016/j.jmbbm.2012.02.006
- Gastaldi D, Morlacchi S, Nichetti R, Capelli C, Dubini G, Petrini L, Migliavacca F (2010) Modelling of the provisional side-branch stenting approach for the treatment of atherosclerotic coronary bifurcations: Effects of stent positioning. *Biomech Model Mechanobiol* 9:551–561. doi: 10.1007/s10237-010-0196-8
- Gee MW, Reeps C, Eckstein HH, Wall WA (2009) Prestressing in finite deformation abdominal aortic aneurysm simulation. *J Biomech* 42:1732–1739. doi: 10.1016/j.jbiomech.2009.04.016
- Gildea TR, Downie G, Eapen G, Herth F, Jantz M, Freitag L (2008) A prospective multicenter trial of a self-expanding hybrid stent in malignant airway obstruction. *J Bronchol* 15:221–224. doi: 10.1097/LBR.0b013e31818859b9
- Gökgöl C, Diehm N, Nezami FR, Büchler P (2015) Nitinol stent oversizing in patients undergoing popliteal artery revascularization: a finite element study. *Ann Biomed Eng*. doi: 10.1007/s10439-015-1358-8
- Hautmann H, Rieger J, Huber RM, Pfeifer KJ (1999) Elastic deformation properties of implanted endobronchial wire stents in benign and malignant bronchial disease: A radiographic in vivo evaluation. *Cardiovasc Intervent Radiol* 22:103–8.
- Hoffman EA (1985) Effect of body orientation on regional lung expansion: a computed tomographic approach. *J Appl Physiol* 59:468–80.
- Hu HC, Liu YH, Wu YC, Hsieh MJ, Chao YK, Wu CY, Ko PJ, Liu CY (2011) Granulation tissue formation following dumon airway stenting: the influence of stent diameter. *Thorac Cardiovasc Surg* 59:163–168.
- Hurewitz AN, Sidhu U, Bergofsky EH, Chanana AD (1984) How alterations in pleural pressure influence esophageal pressure. *J Appl Physiol* 56:1162–1169.
- Ibrahim G, Rona A, Hainsworth S V. (2015) Modeling the nonlinear motion of the rat central airways. *J Biomech Eng* 138:11007. doi: 10.1115/1.4032051
- Jeong BH, Um SW, Suh GY, Chung MP, Kwon OJ, Kim H, Kim J (2012) Results of interventional bronchoscopy in the management of postoperative tracheobronchial stenosis. *J Thorac Cardiovasc Surg* 144:217–222. doi: 10.1016/j.jtcvs.2012.03.077
- Kamm RD (1999) Airway wall mechanics. *Annu Rev Biomed Eng* 1:47–72. doi:

10.1146/annurev.bioeng.1.1.47

- Lai Fook SJ (2004) Pleural mechanics and fluid exchange. *Physiol Rev* 84:385–410. doi: 10.1152/physrev.00026.2003
- Lee P, Kupeli E, Mehta AC (2010) Airway stents. *Clin Chest Med* 31:141–150. doi: 10.1016/j.ccm.2009.08.002
- Lu J, Zhou X, Raghavan ML (2007) Inverse elastostatic stress analysis in pre-deformed biological structures: Demonstration using abdominal aortic aneurysms. *J Biomech* 40:693–696. doi: 10.1016/j.jbiomech.2006.01.015
- Malvè M, Pérez del Palomar A, Chandra S, López-Villalobos JL, Finol E a, Ginel A, Doblaré M (2011a) FSI analysis of a human trachea before and after prosthesis implantation. *J Biomech Eng* 133:71003. doi: 10.1115/1.4004315
- Malvè M, Pérez del Palomar A, Chandra S, López-Villalobos JL, Mena A, Finol E a, Ginel A, Doblaré M (2011b) FSI Analysis of a healthy and a stenotic human trachea under impedance-based boundary conditions. *J Biomech Eng* 133:21001. doi: 10.1115/1.4003130
- Malvè M, Pérez del Palomar A, López-Villalobos JL, Ginel A, Doblaré M (2010) FSI analysis of the coughing mechanism in a human trachea. *Ann Biomed Eng* 38:1556–65. doi: 10.1007/s10439-010-9951-3
- Malvè M, Pérez del Palomar A, Mena A, Trabelsi O, López-Villalobos JL, Ginel A, Panadero F, Doblaré M (2011c) Numerical modeling of a human stented trachea under different stent designs. *Int Commun Heat Mass Transf* 38:855–862. doi: 10.1016/j.icheatmasstransfer.2011.04.012
- Malvè M, Pérez del Palomar A, Trabelsi O, López-Villalobos JL, Ginel A, Doblaré M (2011d) Modeling of the fluid structure interaction of a human trachea under different ventilation conditions. *Int Commun Heat Mass Transf* 38:10–15. doi: 10.1016/j.icheatmasstransfer.2010.09.010
- Malvè M, Serrano C, Peña E, Fernández Parra R, Lostalé F, De Gregorio M a., Martínez M a. (2014) Modelling the air mass transfer in a healthy and a stented rabbit trachea: CT-images, computer simulations and experimental study. *Int Commun Heat Mass Transf* 53:1–8. doi: 10.1016/j.icheatmasstransfer.2014.02.001
- Marchese R, Poidomani G, Paglino G, Crimi C, Lo Nigro C, Argano V (2015) Fully covered self-expandable metal stent in tracheobronchial disorders: Clinical experience. *Respiration* 89:49–56. doi: 10.1159/000368614
- McClelland JR, Hawkes DJ, Schaeffter T, King AP (2013) Respiratory motion models: A review. *Med Image Anal* 17:19–42. doi: 10.1016/j.media.2012.09.005
- McCool FD (2006) Global physiology and pathophysiology of cough: ACCP evidence-based clinical practice guidelines. *Chest* 129:48S–53S. doi: 10.1378/chest.129.1_suppl.48S
- McGrath DJ, O'Brien B, Bruzzi M, Kelly N, Clauser J, Steinseifer U, McHugh PE (2016) Evaluation of cover effects on bare stent mechanical response. *J Mech Behav Biomed Mater* 61:567–580. doi: 10.1016/j.jmbbm.2016.04.023
- McGrath DJ, O'Brien B, Bruzzi M, McHugh PE (2014) Nitinol stent design - understanding axial

- buckling. *J Mech Behav Biomed Mater* 40:252–263. doi: 10.1016/j.jmbbm.2014.08.029
- Moreno F, Lyons HA (1961) Effect of body posture on lung volumes. *J Appl Physiol* 16:27–9.
- Nestola MGC, Faggiano E, Vergara C, Lancellotti RM, Ippolito S, Antona C, Filippi S, Quarteroni A, Scrofani R (2017) Computational comparison of aortic root stresses in presence of stentless and stented aortic valve bio-prostheses. *Comput Methods Biomech Biomed Engin* 20:171–181. doi: 10.1080/10255842.2016.1207171
- Ní Ghriallais R, Bruzzi M (2014) A computational analysis of the deformation of the femoropopliteal artery with stenting. *J Biomech Eng* 136:71003. doi: 10.1115/1.4027329
- Ost DE, Shah AM, Lei X, Godoy MCB, Jimenez C a, Eapen G a, Jani P, Larson AJ, Sarkiss MG, Morice RC (2012) Respiratory infections increase the risk of granulation tissue formation following airway stenting in patients with malignant airway obstruction. *Chest* 141:1473–81. doi: 10.1378/chest.11-2005
- Park J-H, Kim PH, Shin JH, Tsao J, Kim MT, Cho YC, Kim JH, Song H-Y (2016) Removal of Retrievable Self-Expandable Metallic Tracheobronchial Stents: An 18-Year Experience in a Single Center. *Cardiovasc Intervent Radiol*. doi: 10.1007/s00270-016-1420-4
- Pelton AR, Schroeder V, Mitchell MR, Gong XY, Barney M, Robertson SW (2008) Fatigue and durability of Nitinol stents. *J Mech Behav Biomed Mater* 1:153–164. doi: 10.1016/j.jmbbm.2007.08.001
- Petrini L, Trotta A, Dordoni E, Migliavacca F, Dubini G, Lawford P V., Gosai JN, Ryan DM, Testi D, Pennati G (2016) A computational approach for the prediction of fatigue Behaviour in peripheral stents: application to a clinical case. *Ann Biomed Eng* 44:536–547. doi: 10.1007/s10439-015-1472-7
- Prasad A, Xiao N, Gong XY, Zarins CK, Figueroa CA (2013) A computational framework for investigating the positional stability of aortic endografts. *Biomech Model Mechanobiol* 12:869–887. doi: 10.1007/s10237-012-0450-3
- Rausch SMK, Martin C, Bornemann PB, Uhlig S, Wall W a (2011) Material model of lung parenchyma based on living precision-cut lung slice testing. *J Mech Behav Biomed Mater* 4:583–92. doi: 10.1016/j.jmbbm.2011.01.006
- Razi SS, Lebovics RS, Schwartz G, Sancheti M, Belsley S, Connery CP, Bhora FY (2010) Timely airway stenting improves survival in patients with malignant central airway obstruction. *Ann Thorac Surg* 90:1088–1093. doi: 10.1016/j.athoracsur.2010.06.093
- Saad CP, Murthy S, Krizmanich G, Mehta AC (2003) Self-expandable metallic airway stents and flexible bronchoscopy. *Chest* 124:1993–1999. doi: 10.1378/chest.124.5.1993
- Scheerlinck JPY, Snibson KJ, Bowles VM, Sutton P (2008) Biomedical applications of sheep models: from asthma to vaccines. *Trends Biotechnol* 26:259–266. doi: 10.1016/j.tibtech.2008.02.002
- Schmäl F, Fegeler W, Terpe HJ, Hermann W, Stoll W, Becker K (2003) Bacteria and granulation tissue associated with Montgomery T-tubes. *Laryngoscope* 113:1394–1400. doi: 10.1097/00005537-200308000-00024
- Si H, Gärtner K (2015) Meshing piecewise linear complexes by constrained delaunay

- tetrahedralizations. In: Proceedings of the 14th International Meshing Roundtable. Springer-Verlag, Berlin/Heidelberg, pp 147–163
- Stoeckel D, Pelton A, Duerig T (2004) Self-expanding nitinol stents: material and design considerations. *Eur Radiol* 14:292–301. doi: 10.1007/s00330-003-2022-5
- Tawhai MH, Nash MP, Lin CL, Hoffman EA (2009) Supine and prone differences in regional lung density and pleural pressure gradients in the human lung with constant shape. *J Appl Physiol* 107:912–20. doi: 10.1152/jappphysiol.00324.2009
- Tehrani JN, Yang Y, Werner R, Lu W, Low D, Guo X, Wang J (2015) Sensitivity of tumor motion simulation accuracy to lung biomechanical modeling approaches and parameters. *Phys Med Biol* 60:8833–8849. doi: 10.1088/0031-9155/60/22/8833
- Thiebes AL, Kelly N, Sweeney CA, McGrath DJ, Clauser J, Kurtenbach K, Gesche VN, Chen W, Kok RJ, Steinseifer U, Bruzzi M, O'Brien BJ, McHugh PE, Jockenhoevel S, Cornelissen CG (2017) PulmoStent: in vitro to in vivo evaluation of a tissue engineered endobronchial stent. *Ann Biomed Eng* 45:873–883. doi: 10.1007/s10439-016-1737-9
- Trabelsi O, Malve M, Mena Tobar A, Doblare M (2015) Simulation of swallowing dysfunction and mechanical ventilation after a Montgomery T-tube insertion. *Comput Methods Biomech Biomed Engin* 18:1596–1605. doi: 10.1080/10255842.2014.930448
- Trabelsi O, Pérez del Palomar A, Mena Tobar A, López-Villalobos JL, Ginel A, Doblare M (2011) FE simulation of human trachea swallowing movement before and after the implantation of an endoprosthesis. *Appl Math Model* 35:4902–4912. doi: 10.1016/j.apm.2011.03.041
- Villard PF, Beuve M, Shariat B, Baudet V, Jaillet F (2005) Simulation of lung behaviour with finite elements: influence of bio-mechanical parameters. In: Third International Conference on Medical Information Visualisation--BioMedical Visualisation. IEEE, pp 9–14
- Wall WA, Rabczuk T (2008) Fluid–structure interaction in lower airways of CT-based lung geometries. *Int J Numer Methods Fluids* 57:653–675. doi: 10.1002/flid.1763
- Werner R, Ehrhardt J, Schmidt R, Handels H (2009) Patient-specific finite element modeling of respiratory lung motion using 4D CT image data. *Med Phys* 36:1500. doi: 10.1118/1.3101820
- West JB (2012) *Respiratory physiology: the essentials*. Lippincott Williams & Wilkins
- Yin Y, Choi J, Hoffman EA, Tawhai MH, Lin C-L (2013) A multiscale MDCT image-based breathing lung model with time-varying regional ventilation. *J Comput Phys* 244:168–192. doi: 10.1016/j.jcp.2012.12.007
- Zeng YJ, Yager D, Fung YC (1987) Measurement of the mechanical properties of the human lung tissue. *J Biomech Eng* 109:169–174.

Chapter 5

Evaluating the Interaction of a Tracheobronchial Stent in an Ovine *in-vivo* Model

Submitted to: Biomechanics and Modeling in Mechanobiology, 2017

Abstract

Tracheobronchial stents are used to restore patency to stenosed airways. However, these devices are associated with many complications such as migration, granulation tissue formation, mucous plugging and stent strut fracture. This study evaluates the effect of stent interaction on granulation formation in an ovine model. Animal data is used to develop a biomechanical lung model capable of capturing the lung *in-vivo* stress state and physiological loading from respiration. Stenting is simulated using a validated model of a prototype covered laser-cut tracheobronchial stent, and physiological loading is performed. Computational predictions are then compared to pre-clinical stenting results after a six week implantation period. Results of the analysis indicate an apparent correlation between contact pressure variation and granulation tissue formation, where the change in contact pressure provides a quantitative assessment of tissue irritation due to stent interaction.

5.1 Introduction

As much as 30% of lung cancer cases develop difficulties associated with central airway obstruction, which is mostly caused by benign or malignant tumour compression (Lee et al. 2010; Freitag 2010). When other options such as surgical resection fail, tracheobronchial stents are used to relieve the blockage. These devices are used as a last resort as they are associated with numerous complications, with granulation tissue formation in particular being one of the most common (Hu et al. 2011; Fernández-Bussy et al. 2011; Ost et al. 2012).

Tracheobronchial stents are tubular devices that return patency to diseased airways by scaffolding stenosed regions. A suitable stent is selected based on a number of factors including healthy and diseased airway diameters, and stenosis length and type (Freitag 2010). The selected stent is then tracked through the airway to the desired location using a delivery catheter, a bronchoscope and fluoroscopic imaging. Once positioned, the stent is deployed and opens the stenosed airway by pushing out against the blockage. An extensive variety of commercial tracheobronchial stents are available which can generally be divided into three families: bare metal, covered metal and polymeric. Bare metal stents consist solely of a metal mesh which provides better fixation and improved clearance of secretions (Saito and Imamura 2005; Guibert et al. 2015), but can have negative long-term effects with incorporation into the airway wall and granulation tissue formation (Murthy et al. 2004; Godoy et al. 2014). Covered metal stents are comprised of a bare metal structure attached to a polymeric cover which partially or completely seals off the open structure of the stent to prevent airway reocclusion caused by malignant tumour ingrowth through open struts and stent incorporation. Typically metal stents are fabricated from nitinol, a superelastic alloy of nickel and titanium which allows strains in excess of 10% without plastic deformation (Stoeckel et al. 2004). These superelastic properties allow the stents to be crimped and deployed in a self-expanding manner. The Ultraflex, Wallstent, Aero stent and Taewoong stent are examples of bare and covered devices. Common polymeric stents include the Dumon stent, Montgomery T stent and Polyflex stent (Freitag 2010), and are typically fabricated from tubes of material that resist tumour ingrowth.

All commercially available tracheobronchial stents are associated with complications (Freitag 2010). The four primary complications are granulation tissue formation, stent migration, stent fracture and mucous plugging. Stent migration is thought to be in the order of 10% for malignant cases and even higher for benign stenoses (Freitag 2010). Stent fracture is observed in all metal airway stents with reported fracture rates between 2% and 55% (Chung et al. 2008; Doms et al. 2009; Fernández-Bussy et al. 2011; Ost et al. 2012). Mucous plugging has been observed in a range between 4% and 30% of cases for a variety of stent types and indications

(Razi et al. 2010; Fernández-Bussy et al. 2011; Jeong et al. 2012). Granulation tissue formation was identified in 57% of lung transplant patients requiring stents in one study (Fernández-Bussy et al. 2011), while for benign and malignant indications it has been detected in a range between 10% and 33% (Saad et al. 2003; Doms et al. 2009; Chung et al. 2011; Jeong et al. 2012).

Granulation tissue formation is the complication that most often requires intervention after stent placement (Hu et al. 2011; Fernández-Bussy et al. 2011; Ost et al. 2012). Severe granulation formation can cause large stenoses that hamper airflow resulting in the need for secondary treatment which can include electrocauterization, cryotherapy, laser photocoagulation, radiofrequency ablation, balloon dilatation, stent removal, or secondary stent implantation (Fernández-Bussy et al. 2011; Chung et al. 2011). A combination of mechanical irritation and bacterial infection is believed to initiate its formation (Schmäl et al. 2003; Ost et al. 2012), which typically occurs at the stent ends (Schmäl et al. 2003; Freitag 2010; Hu et al. 2011). Excessive expansion forces and cyclic motion between the stent and the airway wall is thought to cause trauma that results in inflammation and granulation tissue formation (Schmäl et al. 2003; Saad et al. 2003; Grewe et al. 2005; Ost et al. 2012). Little is known about preventing its formation, but poor stent sizing is widely believed to play an important role, with oversizing applying excessive force and undersizing allowing increased stent motion (Saad et al. 2003; Hu et al. 2011; Ost et al. 2012). Other factors that might affect granulation formation include strong bronchial mucosal inflammation in certain patients (Saad et al. 2003) and tortuous airways (Chung et al. 2008).

Lung motion during respiration is an intricate process where the lung maintains a passive role, being driven instead by the relationships between the pleurae, diaphragm and intercostal muscles. The pleurae surround the lungs, and line the mediastinum and diaphragm, forming thin fluid-filled sacs that allow frictionless motion between the lung and thoracic cavity. A negative intrapleural pressure maintained within the pleural cavity ensure the lungs remain inflated at all times. The contraction of the intercostal muscles and diaphragm cause a reduction in intrapleural pressure which inflates the lungs and initiates airflow. The prediction of

lung motion has been modelled computationally using a number of methods including deformable image registration and biomechanical modelling (Werner et al. 2009; Brock 2010; Al-Mayah et al. 2011; Murphy et al. 2011). Biomechanical modelling is the preferred method when considering tissue mechanics as it makes use of physiological parameters. This method typically controls lung motion by either projecting one lung surface onto another (Tawhai et al. 2009; Al-Mayah et al. 2010; Tehrani et al. 2015; McGrath et al. 2017) or by applying a negative pressure to a surface (Villard et al. 2005; Werner et al. 2009; Fuerst et al. 2015), in both cases lung deformation is usually limited by other respiratory phases. For the most part biomechanical lung modelling has focused on the prediction of tumour motion during respiration for more efficient radiation therapy application. In these instances the studies have been more motivated on the global deformation of the lung caused by organ inflation and deflation during respiration (to predict tumour motion) than on the local airway deformation caused by pressure changes associated with gaseous flow. Therefore, the lung is generally considered a homogenous unit where the parenchyma, airways and arterial network is defined by a single material representation (Werner et al. 2009; Al-Mayah et al. 2011). Al-Mayah et al. (2010) evaluated the effect of inhomogeneity caused by the inclusion of a bronchial tree (represented by shell elements) and found that it had little effect on capturing global lung movements, but was shown to have more localised effects. Other studies have evaluated the effect of in-plane, local deformation on stent and tissue response in isolated tracheal airways, using FSI (fluid solid interaction) modelling to assess the effects of fluid dynamics on stented or unstented airway geometries (Malvè et al. 2011a; Malvè et al. 2014; Chaure et al. 2016). These studies use realistic structural representations of the trachea's cartilage rings and smooth muscle components in combination with anisotropic material constitutive models to accurately capture local tissue mechanics. Malvè et al. (2011a) proposed that high stresses detected at the stent ends were a possible indication of future granulation formation. The observation of high stress levels at peek expiration was later shown to correlate with granulation formation throughout the stent implantation site in a rabbit model (Malvè et al. 2014). A later study conducted by Chaure et al. (2016) also highlighted a relationship between high stress and granulation formation in another rabbit

model. In this instance the stresses associated with stent deployment were shown to have a more significant effect than the accompanying fluid dynamics, as the stresses related to stent deployment had not previously been accounted for. Other studies have considered the consequences of tracheobronchial stenting on swallowing using finite element analyses (Perez del Palomar et al. 2010; Trabelsi et al. 2011; Trabelsi et al. 2015). The effect on the longitudinal extension of the trachea was evaluated, and high stresses were again detected after stent implantation which were associated with granulation formation observed *in-vivo*. These previous studies simplified the stent-tissue interaction by neglecting to consider stent mechanical performance. Stents were either rigidly deformed to an expanded state which led to an unrealistically stiff stent response, or modelled in the expanded configuration where a stress-free condition existed between the stent and tissue in the deployed configuration. More recently, McGrath et al. (2017) assessed the combined effects of local and global loading on stent-tissue interactions in the bronchi. An ovine biomechanical lung model was developed which included representations of the tracheobronchial tree and parenchyma, and accounted for the physiological stress state of the lung *in-vivo*. To better capture stent-tissue interactions stent deployment was simulated by crimping and releasing a stent with suitably representative mechanical properties. Results of the study indicated that airway stretching caused by global lung deformation can have a significant effect on stent mechanical performance. In particular, it was proposed that this cyclic stretching of the airway might promote granulation formation through irritation caused by stent contact. However, as the stent implantation was only performed computationally, no direct correlation between the simulated prediction and clinical observations was possible.

The overall objective of this study is to correlate pre-clinical observations of granulation tissue formation with computational predictions. To accomplish this, animal data pre- and post-stent implantation in a sheep is utilized in combination with stent experimental data. A validated covered stent model is developed and stent deployment and physiological loading in the ovine airway is simulated in a semi-specific biomechanical lung model. Experimentally observed granulation formation is then compared to computational predictions.

5.2 Materials and Methods

5.2.1 Animal Work

All procedures used conform to the “Guide for the care and use of laboratory animals” published by the US National Institutes of Health. The described procedure was part of a study evaluated and approved by the North Rhine Westphalian State Agency for Nature, Environment and Consumer Protection under number 84-02.04.2013.A452. As part of the PulmoStent project (Thiebes et al. 2017) twelve healthy adult sheep were implanted with prototype covered laser-cut and braided tracheobronchial stents for time periods between six weeks and six months. The stenting procedure is described in detail elsewhere (Thiebes et al. 2017). However, a brief summary is provided here. The sheep were first anesthetized and intubated, and computed tomography (CT) of the thorax was obtained. CT was performed using a Siemens Somatom Definition Flash scanner with the sheep placed on its side. Afterwards, bronchoscopy was performed to visually inspect the airways. Stents were then implanted with a deployment catheter with an outer diameter (OD) of 8.5 mm under fluoroscopic guidance. Stent positioning was evaluated by bronchoscopy following deployment. Afterwards, anaesthesia was concluded and the animal was extubated upon commencing spontaneous breathing. For one animal (Sheep A) implanted with a laser-cut stent for six weeks, CT was again performed pre-euthanasia with the sheep breathing normally. Pressurised CT data for a second sheep (Sheep B) with no stent present was also acquired at 0, 15 and 30 cmH₂O inflation pressures (McGrath et al. 2017). For simplicity, the 0 and 30 cmH₂O pressure points are referred to as functional residual capacity (FRC) and total lung capacity (TLC) respectively. FRC relates to the volume of the lung at the end of passive expiration and TLC describes the maximum volume that the lung can expand to during maximal inhalation. After euthanasia the lungs were dissected and the stented bronchi were removed to record stent positioning and granulation formation. Histological samples were prepared by first dividing the stented bronchi into proximal, medial and distal sections. The sections were fixed and cut into 10-30 µm thick samples by a cutting-grinding technique and stained with haematoxylin and

eosin (H&E). More information on histological methodology can be obtained from (Thiebes et al. 2017).

5.2.2 Stent Fabrication

In this study only the laser-cut prototype stent is considered. Prototype tracheobronchial stents were laser-cut from nitinol tubing with a 5.0 mm OD and a 0.23 mm thickness. Each stent was expanded and shape set using a cylindrical mandrel, and then electropolished. The expanded stent dimensions were approximately 15 x 30 x 0.195 mm (OD x Length x thickness) with a flare OD of 17 mm. A 20 mm long and 100 μ m thick polycarbonate-urethane (PCU) cover was then adhered to the central portion of the bare stents using a polyurethane (PU) adhesive and PCU spray atomization procedure (Fig. 5.1(a)). Further details on the stent covering procedure are provided elsewhere (Nadzeyka et al. 2014; Chen et al. 2016).

5.2.3 Stent Modelling

5.2.3.1 Geometry and Material Properties

The covered stent geometry included representations of the three structural components: the nitinol stent, the PU adhesive and the PCU cover (Fig. 5.1 (b)). Eight-noded linear brick (C3D8R) elements with enhanced hourglass control were used to mesh the stent and PU adhesive. To increase computational efficiency the PCU cover was meshed with 4-noded shell (S4R) elements with enhanced hourglass control. The final mesh consisted of 811,968 and 364,896 C3D8R and S4R elements respectively. The methods used to create the final stent geometry are detailed in McGrath et al. (2016).

The in-built Auricchio nitinol constitutive model in Abaqus (DS SIMULIA, USA) (Auricchio et al. 1997) was used to model the superelastic behaviour of the stent material. Model constitutive parameters were calibrated using tensile tests performed on cylindrical samples of the same tube used in stent fabrication (McGrath et al. 2014). Table 5.1 shows the parameters used for the model assuming no plasticity, and symmetric tensile and compressive properties, as is common in the literature (García et al. 2012; Ghriallais and Bruzzi 2014; McGrath et al. 2014). PCU cover material properties were similarly obtained from tensile testing of samples

(McGrath et al. 2016), and PU adhesive material properties were acquired from the literature (Sheikhy et al. 2013). Both polymeric materials were fit to a Neo-Hookean hyperelastic constitutive model, the coefficients of which are given in Table 5.2. Due to limitations associated with shell facet edge length to thickness ratio the cover was modelled with a reduced thickness of 20 μm . To account for this reduction, the material stiffness was increased accordingly, similar to that performed by De Bock et al. (2013) where shell thickness was neglected.

5.2.3.2 Stent Model Validation

To validate the suitability of the stent model, radial force testing was performed experimentally and computationally. A single stent was radial force tested between its nominal expanded diameter and a diameter of 7.5 mm using an eight-faced crimping head (RCM-H60, MPT Europe) connected to a Zwick uniaxial tensile tester (Zwick Roell, GmbH & Co.). The test was performed at 37 °C at a rate of 0.1 mm/s. To simulate the experimental test the stent model was situated in the centre of eight radially patterned rigid plates which were radially displaced to 7.5 mm and returned to their initial configuration (Fig. 5.2). General contact was defined with penalty tangential contact with a coefficient of friction of 0.1 and hard normal contact. No boundary conditions were directly applied to the stent. Further details on stent testing and simulation can be obtained in McGrath et al. (2016).

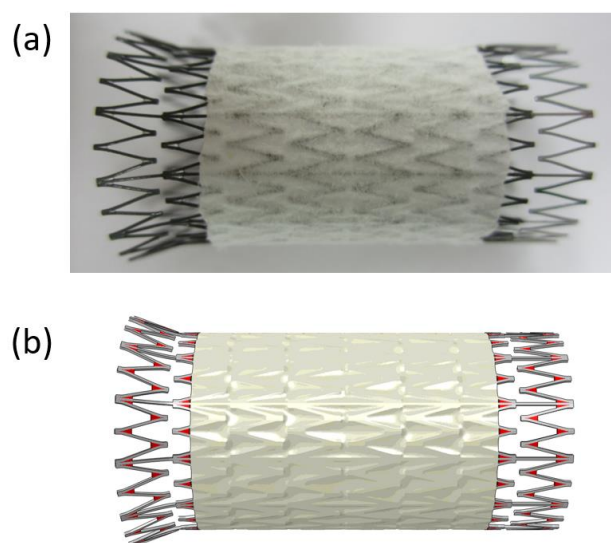


Fig. 5.1: (a) Covered stent geometry. (b) Computational model of covered stent with adhesive shown in red.

Table 5.1: Nitinol material properties used in the Abaqus constitutive model.

Parameter	Value
Austenite Elasticity (MPa)	53001
Austenite Poisson's Ratio	0.3
Martensite Elasticity (MPa)	21500
Martensite Poisson's Ratio	0.3
Transformation Strain	0.038
Start of Transformation Loading (MPa)	434
End of Transformation Loading (MPa)	500
Reference Temperature (°C)	37
Start of Transformation Unloading (MPa)	210.3
End of Transformation Unloading (MPa)	138.7
Start of Transformation Stress During Loading in Compression (MPa)	434
Volumetric Transformation Strain	0.038

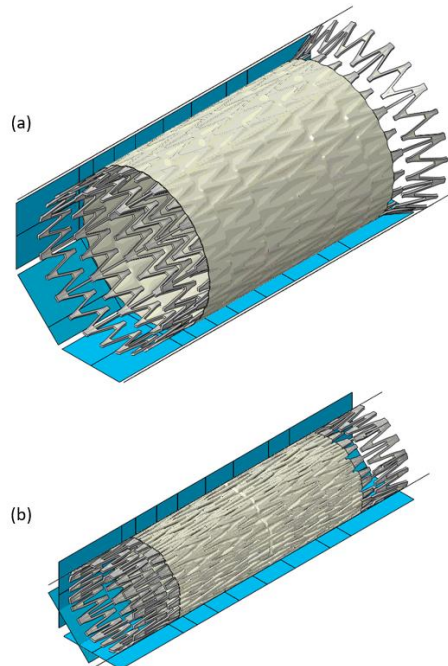
**Fig. 5.2:** Computational radial force test setup (a) at full expansion (b) at full crimp of 7.5 mm.

Table 5.2: Constitutive model coefficients for cover and adhesive. Cover properties are from McGrath et al. (2016) and adhesive properties are from (Sheikhy et al. 2013).

Material	Material Model	D1	C10
Cover	Neo-Hookean	0.007681062	0.260554336
Adhesive	Neo-Hookean	0.211184593	1.01468441

5.2.4 Lung Modelling

This section describes the development of the lung model zero-pressure assembly, physiological loading and material properties. The steps used in this process are summarised in Fig. 5.3. As the majority of the methods performed in this work have been discussed in detail elsewhere (McGrath et al. 2017) only a brief summary of the primary steps are given.

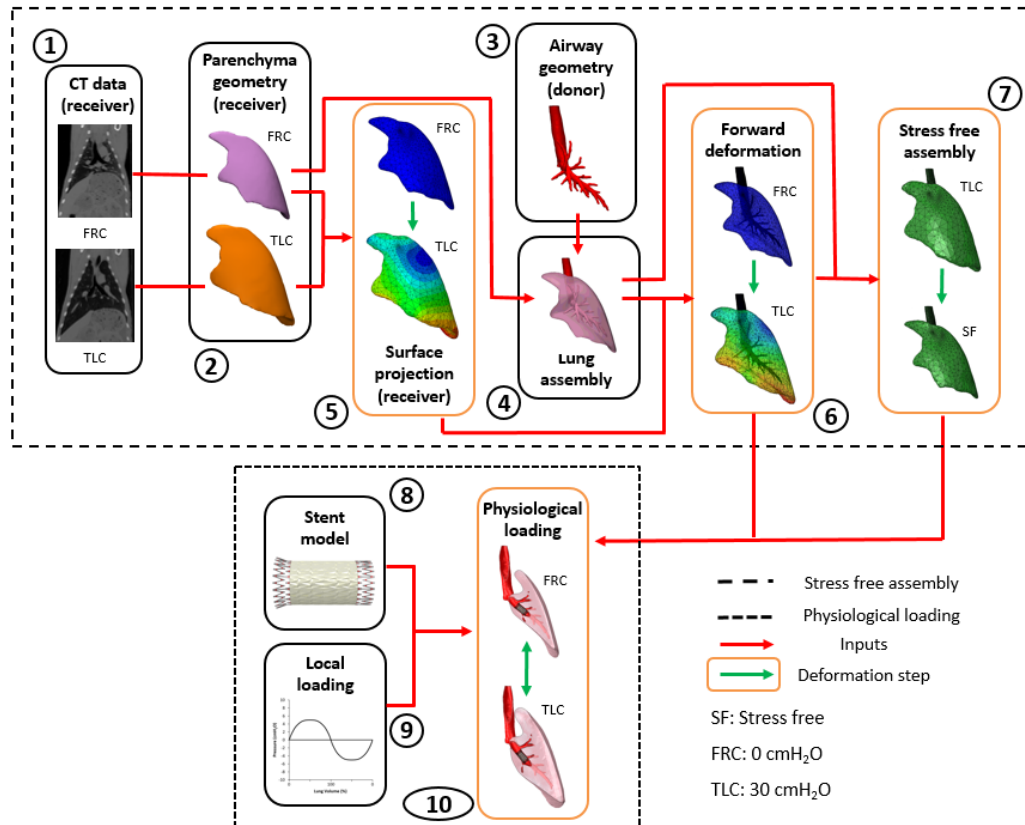


Fig. 5.3: Flow chart summarising the steps to obtain a zero-pressure assembly and apply physiological loading. (1) Pressurised CT data from Sheep B. (2) Parenchymal geometry created at FRC and TLC. (3) Airway geometry obtained from Sheep A. (4) FRC lung assembly created from combining airway and parenchyma geometry. (5) Sheep B FRC parenchyma is projected onto the TLC parenchyma geometry. (6) Forward deformation step performed displacing lung assembly from FRC to TLC to obtain nodal deformation. (7) zero-pressure assembly obtained from backward step where lung is deflated using reverse displacement. (8) Stent model created. (9) Local loading defined. (10) Stent deployment and physiological motion simulated.

5.2.4.1 Initial Lung Assembly

In a previous study it was shown that the axial stretching of airways caused by global lung motion significantly affected stent-tissue interactions (McGrath et al. 2017). In the present work no pressurised CT data was available for the stented sheep (Sheep A). In order to include this motion a donor-receiver method was employed to create the initial lung assembly. To accomplish this the airway geometry from Sheep A (the donor) is orientated within the lung parenchyma of Sheep B (the receiver) at FRC. The pressurised parenchymal data of Sheep B can then be utilised to apply a representative global deformation to the airways of Sheep A. While this method is not ideal, it allows for a suitable representation of the natural physiological loading that occurs within the airways. It is assumed that at the time of CT capture for Sheep A the lung was at FRC.

Mimics and 3-Matic (Materialise, Belgium) was used to extract and assemble the lung geometry. The airway geometry for Sheep A was composed of a partial length of the trachea and all observable bronchi from the CT data. A uniform thickness of 1 mm was assigned to the airways. For Sheep B the lung parenchyma geometry at FRC and TLC was obtained as a continuous surface where separate lobes were neglected. The initial donor-receiver lung assembly was formed by inserting the airway of Sheep A into the FRC parenchyma surface of Sheep B (Fig. 5.4). Using TetGen (Si and Gärtner 2015) the resulting airway and parenchyma volumes were meshed with a high quality tetrahedral mesh. Only the left lung and airway is modelled in this work. However, the modelling approach is easily extended to the right side if necessary. Mesh convergence was performed using the maximum Von Mises stress at a number of discrete points in a simulated stent deployment in a tubular section. The selected mesh was found to converge to below 5% of a mesh twice as dense. The final mesh contained 405,252 and 407,788 elements for the lung parenchyma and airway respectively.

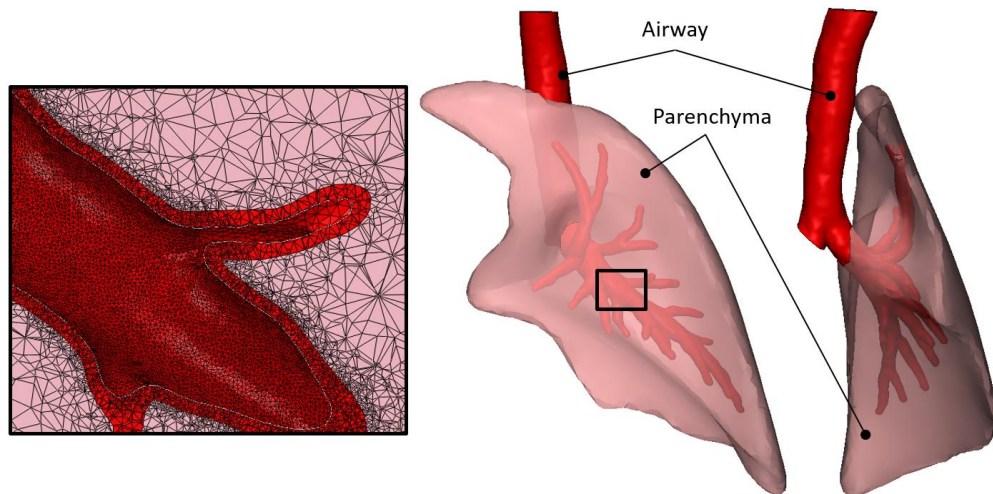


Fig. 5.4: Initial lung assembly with donor airway embedded in receiver parenchyma. Inset shows final mesh detail in stent deployment region.

5.2.4.2 Zero-pressure Lung Assembly

As the acquired CT data of the *in-vivo* lung contains pre-stresses due to negative intrapleural pressure a zero-pressure (ZP) lung model is required. This is attained by utilising an inverse method developed in McGrath et al. (2017) and loosely based on the method presented by Bols et al. (2013). Briefly, the method uses a forward step, followed by a backward step to obtain the ZP assembly. In the first step lung motion is simulated between FRC and TLC where it is assumed no pre-stress is present at the FRC position. The forward motion is simulated using a pleural surface method adapted from Tawhai et al. (2009), where the outer surface of the lung assembly parenchyma is constrained to remain in frictionless contact with a surface representing the deforming pleural cavity. Deformation of the pleural surface is determined by projecting the pleural surface at FRC onto the corresponding surface at TLC. All nodes on the cut surface of the trachea are held in all directions. The displacement of each node in the lung assembly is recorded to create a displacement vector field (DVF). After obtaining the DVF the backward step is executed. In this step it is assumed that a pre-stressed lung at FRC deflates to a ZP position along the reverse path of the DVF. A uniform scaling based on the ratio of an assumed intrapleural pressure of 6.84 cmH₂O (Hurewitz et al. 1984) at FRC and the pressure difference between FRC and TLC (30 cmH₂O) is applied to the DVF. This is then subtracted from the FRC assembly nodal coordinate field (NCF) to obtain the

resulting ZP assembly NCF. This method employs a physiologically relevant deformation to obtain the ZP assembly. Further details on the application of the method can be obtained in McGrath et al. (2017).

5.2.4.3 Physiological Loading

Physiological motion is applied to the lung to simulate normal breathing through a combination of global and local deformation. The global deformation is applied to the ZP assembly by displacing the nodes on the outer surface of the lung parenchyma, firstly, to FRC to apply a pre-stress, and then to TLC to capture the full range of motion of the lung. Finally, the lung is returned to FRC to complete the respiratory cycle. Local deformation is applied to represent the effects pressure variation has in the vicinity of the airways. This is applied using a uniform pressure on the airway surface which follows the sinusoidal pressure-volume association shown in Fig. 5.5 which represents normal breathing conditions. Due to the unavailability of appropriate ovine data in the literature human information was used to describe the pressure conditions. However, as ovine lung function falls within typical human ranges (Scheerlinck et al. 2008; Bähr and Wolf 2012) this should not overly impact the results of the study.

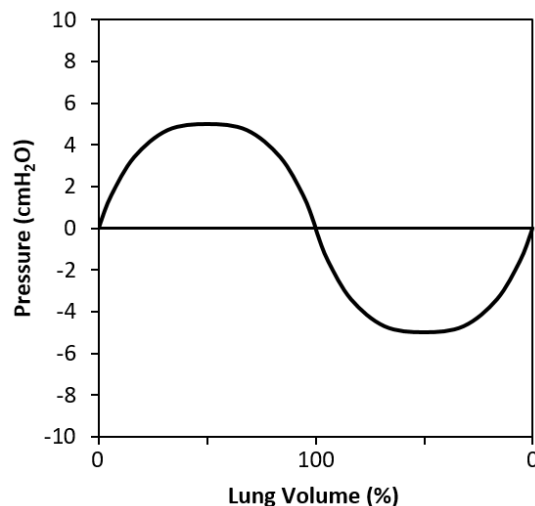


Fig. 5.5: Pressure-volume relationship for normal breathing adapted from (Wall and Rabczuk 2008; West 2012). Lung volume is considered at 0% at FRC and 100% at TLC.

5.2.4.4 Lung Material Properties

Preliminary airway properties were obtained from tensile testing of main bronchi tissue and fit to a second order reduced polynomial, where the strain energy potential is represented by

$$U = \sum_{i=1}^2 C_{i0} (\bar{I}_1 - 3)^i + \sum_{i=1}^2 \frac{1}{D_i} (J^{el} - 1)^{2i} \quad (5.1)$$

where C_{i0} and D_i are temperature-dependent material parameters, \bar{I}_1 is the first deviatoric strain invariant and J^{el} is the elastic volume ratio. To account for the natural variation in airway wall thickness four material properties were utilised where the constitutive model coefficients were linearly scaled by assuming a constant relationship between airway diameter and thickness (McGrath et al. 2017). Material properties are given in Table 5.3. Though the airways contain a combination of constituents including cartilage and smooth muscle the material properties are assumed homogenous and isotropic. Parenchyma properties were initially fit to results from Rausch et al. (2011) using a second order reduced polynomial. The determined constants were then linearly scaled until the pressure to expand the ZP lung from FRC to TLC was similar to the pressure measured at TLC. Further details on material data can be obtained from McGrath et al. (2017).

Table 5.3: Tissue constitutive model coefficients. M1 to M4 refer to airway materials and L1 refers to the parenchymal material. A Poison's ratio of 0.42 and 0.3 was used for airway and parenchyma respectively.

Parameter	M1	M2	M3	M4	L1
Scale	1.33	0.98	0.64	0.34	0.37
D1	2.099	2.848	4.361	8.210	1365.218
D2	0	0	0	0	0
C ₁₀	0.081	0.059	0.038	0.021	0.00034
C ₂₀	0.874	0.644	0.421	0.223	0.0014

5.2.5 Stenting Analyses

All simulations were run using Abaqus/Explicit (V6.14) due to large deformations and non-linearities caused by contact. The ratio of kinetic to internal energy was

maintained below 5% for all simulations. Semi-automatic mass scaling was used with a target time increment of $1\text{E-}6$ and a lowest stable time increment of $2.55\text{E-}8$. Stent deployment is simulated over a number of steps as indicated in Fig. 5.6. Firstly, the ZP assembly is deformed to FRC (Fig. 5.6 (a)) where the stent delivery system is positioned based on a combination of bronchoscopy and CT images. A rigid cylinder acting as the outer tube of the stent delivery system is then expanded from 5 mm to 8 mm to straighten the airway and allow stent deployment (Fig. 5.6 (b)). Simultaneously, the stent is crimped to 7.5 mm using a rigid cylinder. Afterwards, stent deployment is simulated by radially expanding the rigid cylinder restraining the stent, while at the same time returning the outer tube to its original diameter, and allowing the stent to make contact with the inner surface of the airway (Fig. 5.6 (c)). At this point the only contact in the model is between the stent and airway surfaces which allows for deformation between FRC and TLC (Fig. 5.6 (d)). One inspiration and expiration cycle is executed using the physiological loading previously described. The average diameter of the airway at the implantation site is 12.8 mm, though the diameter tapers from 14.1 mm at the proximal end to 11.7 mm at the most distal stent portion. A simulation of normal breathing between FRC and TLC is also performed without including stent deployment for comparative purposes.

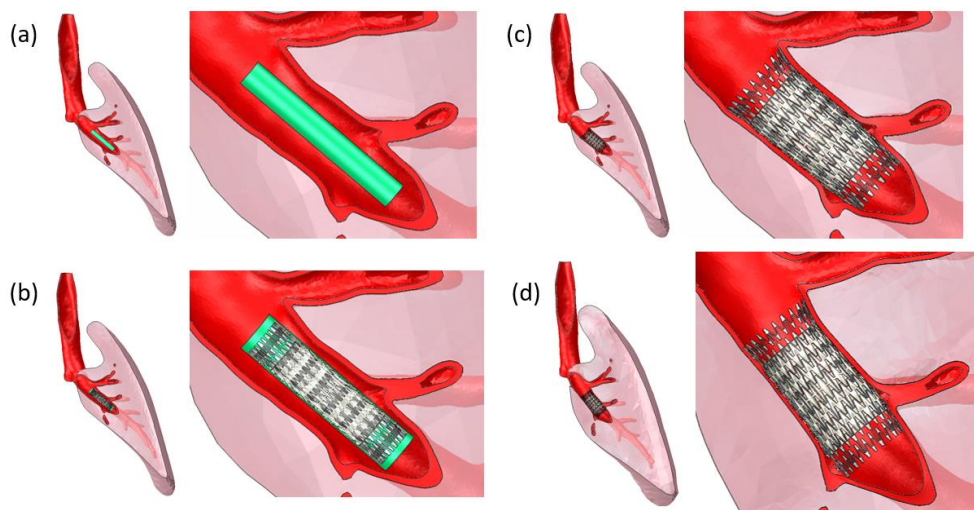


Fig. 5.6: Summary of stent deployment and physiological loading steps. (a) Lung assembly is deformed to FRC. Delivery system outer (green) is shown at its initial diameter of 5 mm. (b) Stent crimped and delivery system outer expanded to 8 mm. (c) Stent deployed. (d) Physiological loading applied with lung assembly at TLC.

5.3 Results

5.3.1 Animal Study Results

A combination of CT data pre-euthanasia and excised tissue images post-euthanasia are shown in Fig. 5.7. In the CT slice shown in Fig. 5.7 (b) the distal and medial regions of the stented airway appear granulation free, while granulation tissue formation is observed proximally. This observation is repeated in the axial CT sections shown in Fig. 5.7 (c), (d) and (e), with Fig. 5.7 (c) showing granulation formation around the circumference of the proximal stent end, including a slightly larger formation on the left side of the airway. Fig. 5.7 (f) and (g) show proximal and distal images of the excised stented bronchus. Proximally, granulation formation corresponding to that observed in the CT data can be seen, while in the distal region slight airway thickening is also observed. The diameters presented in Table 5.4 highlight the significant growth at the proximal end with a maximum to minimum diameter ratio of 2.72. The distal end shows a slightly higher ratio to the medial portion of 1.27 and 1.10 respectively.

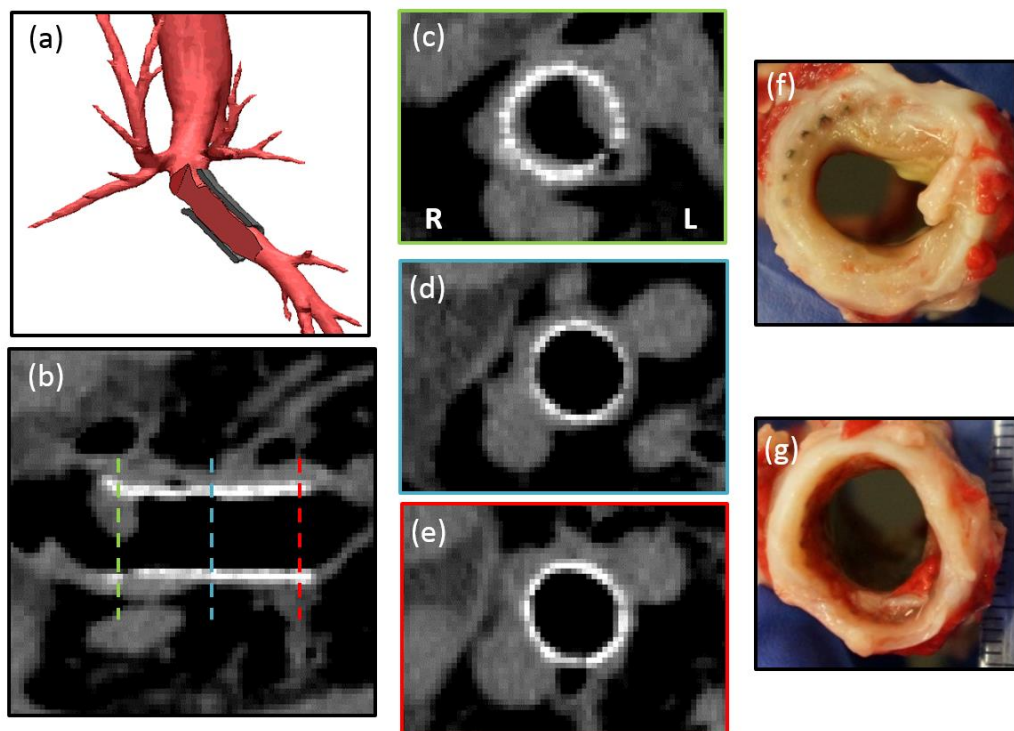


Fig. 5.7: CT pre-euthanasia and excised tissue images. (a) Reconstructed CT of the left stented airway with cut section. (b) Longitudinal CT slice of stented airway with proximal (green), medial (blue) and distal (red) section lines. (c) Proximal cross-section. (d) Medial cross-section. (e) Distal cross-section. (f) Proximal excised tissue section. (g) Distal excised airway section. L and R refer to Left and right.

Table 5.4: Minimum and maximum airway diameters measured from CT at proximal, medial and distal positions of stented airway.

Diameter	Proximal	Medial	Distal
Minimum (mm)	5.49	11.97	10.8
Maximum (mm)	14.93	13.13	13.76
Diameter Ratio	2.72	1.10	1.27

The excised stented left bronchus is shown in Fig. 5.8. It can be seen that granulation formation is primarily observed at the proximal stent edge in the uncovered region, where a large amount of newly formed tissue exists. Distally, there is some inflammation with part of the uncovered stent end embedded in the new tissue.

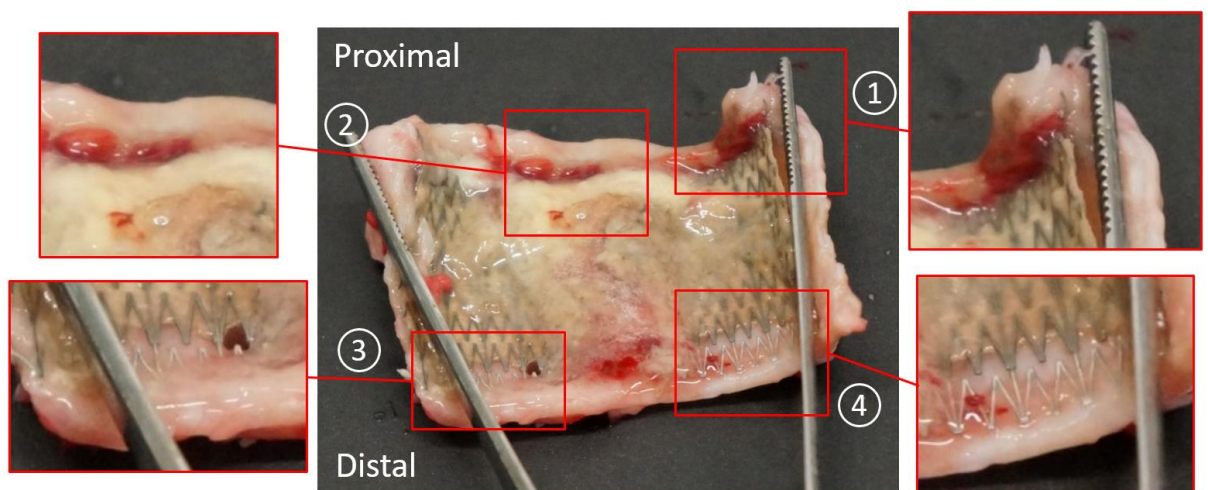


Fig. 5.8: Excised stented bronchus highlighting regions of interest. (1) Proximal section of bare stent struts embedded in granulation tissue. (2) Granulation tissue formed over proximal bare stent struts. (3) Granulation tissue formed over distal bare stent struts. (4) Bare stent struts visible distally.

The histological H&E stained sections in Fig. 5.9 provide further information on the state of the tissue in different regions of the stented and unstented bronchus. The unstented control section in Fig. 5.9 (a) provides a good example of a healthy airway, with the epithelium, lamina propria, submucosa and cartilage all visible. Similar structures are also observed in the medial section of the stented airway with no apparent thickening (Fig. 5.9 (c)), however, the epithelial layer is less visible, which is probably due to interaction with the PCU cover. At the proximal and distal sections (Fig. 5.9 (b) and (d)) granulation tissue is clearly visible with collagen fibres and dense

connective tissue surrounding the stent struts, and no discernible epithelial layer. It can be seen that qualitatively the proximal end produces the largest inflammatory response (Fig. 5.9 (b)), followed by the distal section (Fig. 5.9 (d)) and no obvious response in the medial section (Fig. 5.9 (c)). It should be noted that embedding of the stent does not occur in the proximal histology image (Fig. 5.9 (b)) as the section is taken from the covered portion close to the proximal end.

5.3.2 Simulation Results

5.3.2.1 Stent Validation

Experimental and computational results of stent radial force are shown in Fig. 5.10, where a suitable agreement is observed. The computational model accurately captures the experimental radial force over a large range of diameters between 15 and 9 mm. Below 9 mm the stent model does not predict as well, but this is acceptable as the stent is deployed into an airway with an average diameter of 12.34 mm and a minimum of 11.7 mm. Reduction in shell thickness may account in part for the inability to capture the higher forces observed at lower diameters.

5.3.2.2 Physiological Loading

5.3.2.2.1 Lung Deformation

Lung assembly deformation between ZP and TLC is shown in Fig. 5.11. A maximum displacement of 39.5 mm occurs along the inferior parenchymal surface corresponding to the large motions associated with the diaphragm. The airways undergo large displacement by up to 32.0 mm, with the deformation between ZP and FRC accounting for almost 20% of the total displacement.

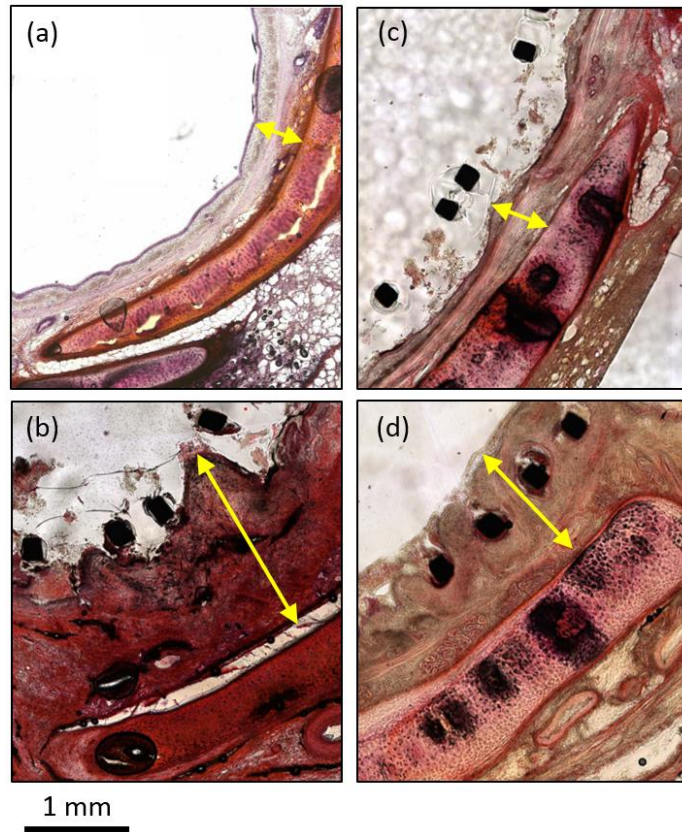


Fig. 5.9: Histological sections with H&E staining. (a) Control, (b) proximal section, (c) medial section, (d) distal section.

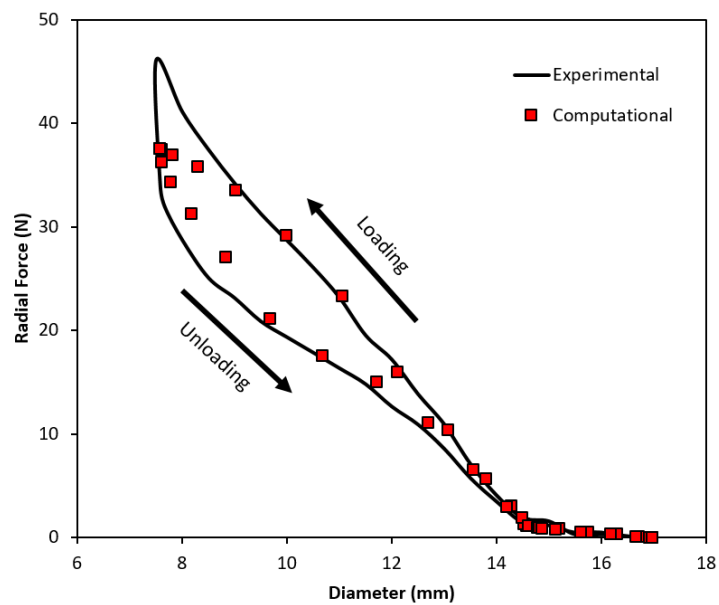


Fig. 5.10: Experimental and computational results of stent radial force.

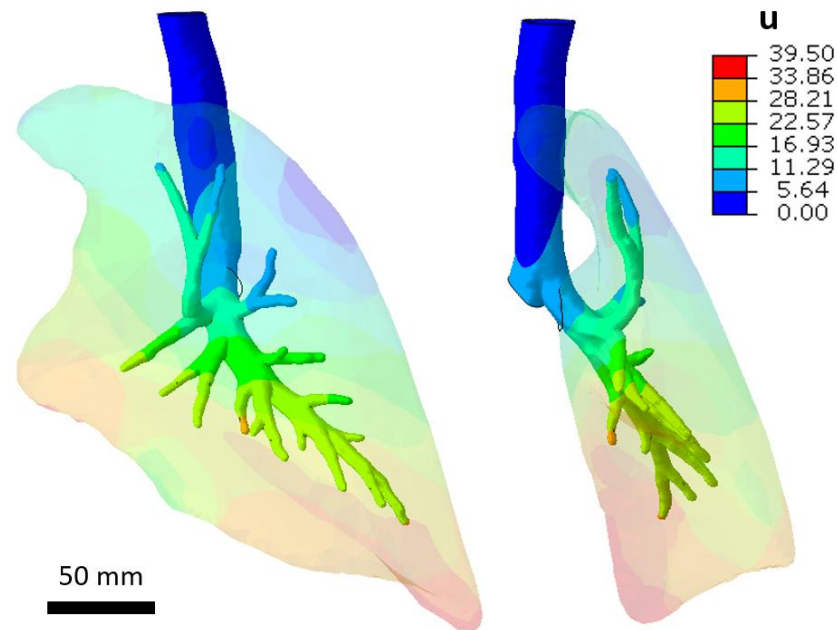


Fig. 5.11: Visualisation of the deformation the lung assembly undergoes between ZP and TLC. Displacement in mm.

5.3.2.2.2 *Stress Results*

Maximum principal stress contours of the stented region are shown in Fig. 5.12. At FRC (Fig. 5.12 (a)) the stent increases the local tissue stress across the length of the device due to oversizing. A higher concentration of increased stress occurs in the distal portion. When lung motion is simulated to TLC the stress increases across the entirety of the stented region with the highest stresses observed at the bronchi branch points and at the distal stent end (Fig. 5.12 (b)). The stress at TLC in an unstented simulation is shown in (Fig. 5.12 (c)) with stresses in a similar range to those found in the stented model. While it is evident that the stent increases the stress experienced by the tissue across the length of the device, it only causes the maximum principal stress to increase by just over 4%. The large increase in stress seen in the unstented model is due to the deformation of the airways between FRC and TLC naturally increasing the stress in the tissue. The axial stretching of the airways and the relative positioning of the stent over the breathing cycle can be observed in Fig. 5.12 (a) and (b) (red arrows).

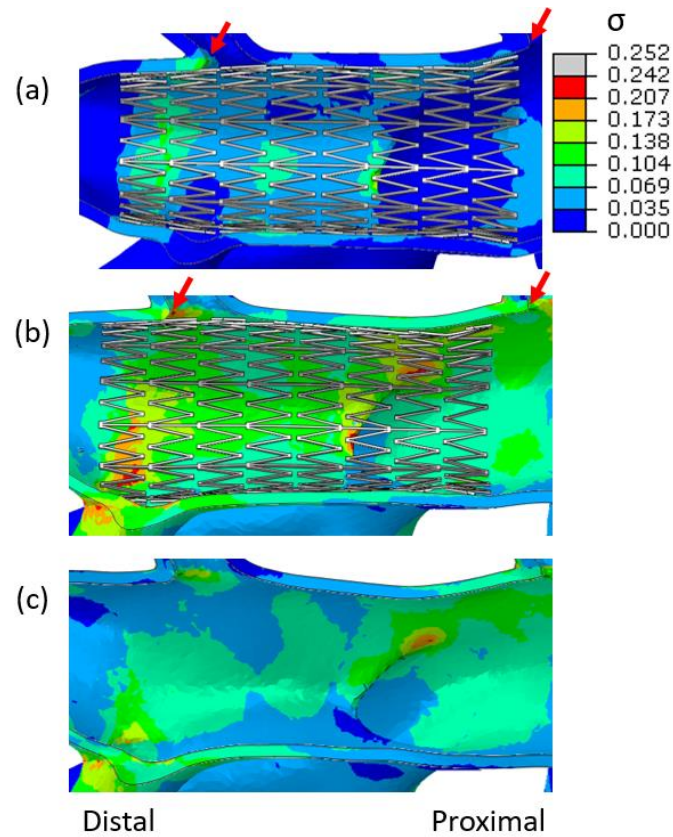


Fig. 5.12: Maximum principal stress around stented airway section at (a) FRC, (b) TLC, (c) TLC with a simulation that did not include a stent. Arrows indicate the positioning of two branch points to illustrate the stretching that occurs in the airway. Maximum principal stress shown in MPa. Views are of inner surface of bronchi on the left side.

To solely consider the stress contribution the stent imparts on the airway tissue (i.e. remove the effects of airway deformation due to lung motion), the maximum principal stress for each element in the unstented tissue at TLC is subtracted from the corresponding elemental stress in the stented model (Fig. 5.13). The greatest change is observed at a medial branching point (Fig. 5.13 (a)), followed by a distal branch point. A general increase in stress is observed across the length of the stented region, although a reduction in stress is observed at the proximal end.

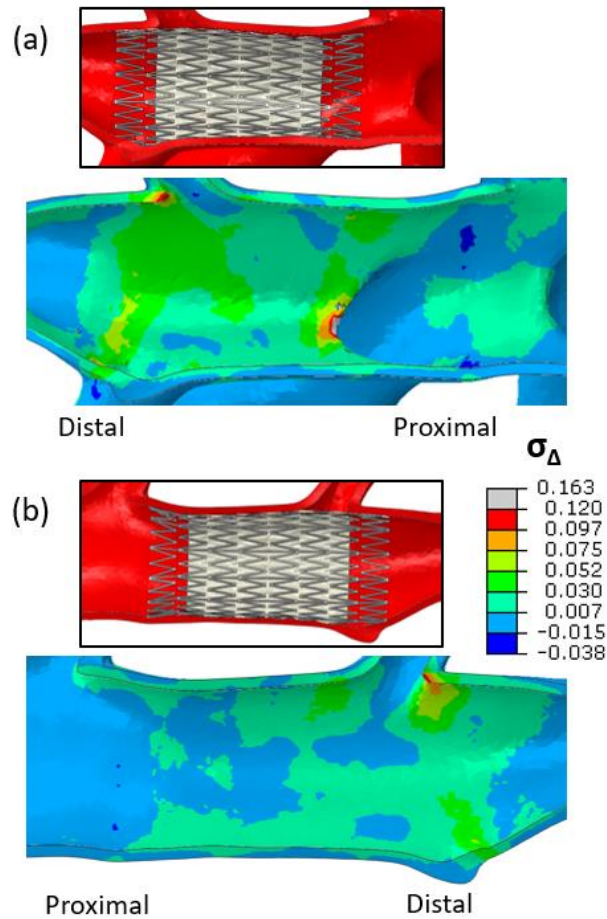


Fig. 5.13: Difference in maximum principal stress between an unstented airway and stented airway at TLC. (a) Leftward side of stented airway (b) Rightward side of stented airway. Stress difference shown in MPa.

5.3.2.2.3 Contact Pressure Results

Repetitive motion injury is believed to be one of the primary causes of granulation tissue formation which is caused by sustained friction between the implant and the airway during respiratory motion (Saad et al. 2003; Ost et al. 2012). One method to evaluate this interaction which has previously been proposed by McGrath et al. (2017) is to record the variation in contact pressure across the stented airway surface over a full respiratory cycle, where large variation in pressure highlights relative motion between two surfaces in contact. Here the contact pressure change is calculated using

$$P_{\Delta} = P_{max} - P_{min} \quad (5.2)$$

Where P_{max} and P_{min} are the maximum and minimum nodal contact pressures on the airway tissue over a respiratory cycle. The variation in contact pressure on the

airway surface over a respiratory cycle is shown in Fig. 5.14 for both sides of the stented bronchus. In Fig. 5.14 (a) it can be seen that higher contact pressure ranges are experienced proximally at the stent end, though some large contact pressure variation is also observed at the lower distal end. Throughout the medial section of the left side of the airway there is a relatively low variation in contact force. On the right side of the airway a relatively low variation in force is observed throughout the length of the stented region (Fig. 5.14 (b)). It should be noted that small variations in contact pressure will also be observed due to changes in stent reaction force, but these are expected to be minor due to low overall force variation.

A qualitative comparison of the surface area occupied by different contact pressure ranges is shown in Fig. 5.15, where it can be observed that only small regions, primarily at the stent ends experience contact pressure variations greater than 50 kPa (Fig. 5.15 (a) and (b)). At ranges above 10 kPa the covered area is much more widespread (Fig. 5.15 (d)). Most of the stented airway surface experiences contact pressure ranges in excess of 1 kPa.

Quantitative measures of stent radial force, stent OD and average contact pressure change at proximal, medial and distal positions, along with the total average is shown in Fig. 5.16. Stent reaction force is calculated at FRC after stent deployment (Fig. 5.16 (a)). The highest force is observed at the most distal stent ring with a value of 1.15 N, which is expected due to the airway taper. Correspondingly, the lowest diameter at FRC is observed distally (Fig. 5.16 (b)). The average regional contact pressure change over a respiratory cycle is shown in Fig. 5.16 (c) where the proximal end exhibits the highest variation with a range of 69.5 kPa, followed by the distal end with 43.2 kPa and the medial region with 12.1 kPa. The average over the entire length of the stented tissue was 15.8 kPa.

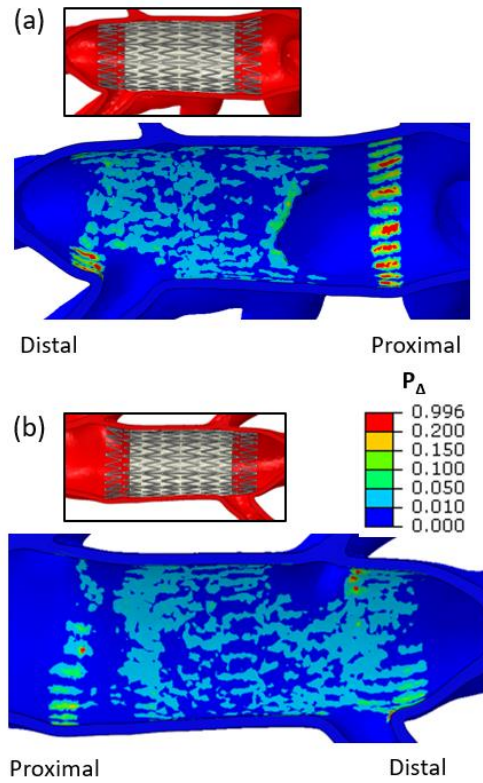


Fig. 5.14: Airway contact pressure change contours showing (a) leftward side of stented airway (b) rightward side of stented airway. Stent positioning shown in insets. Contact pressure ranges shown in MPa.

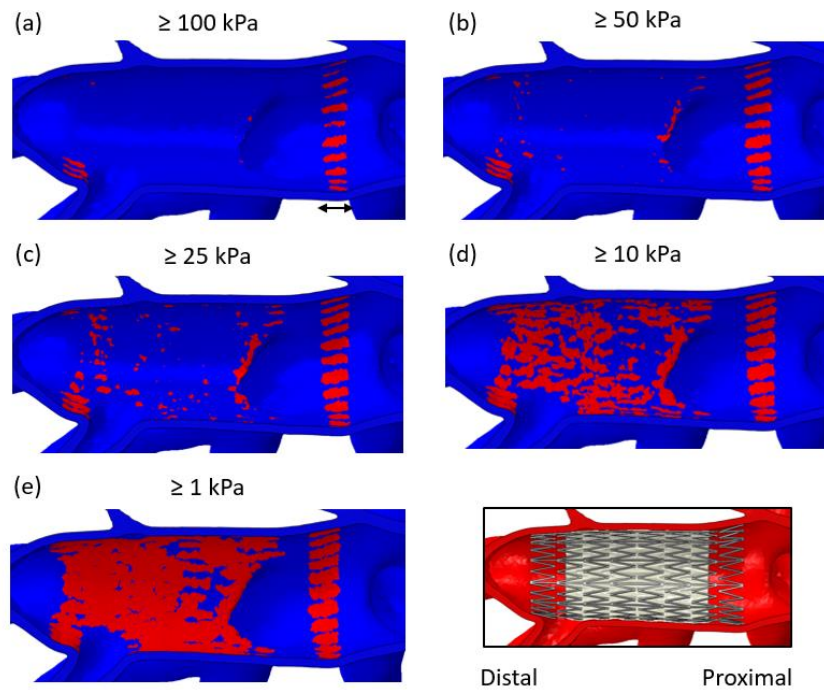


Fig. 5.15: Contact pressure range above (a) 100 kPa (b) 50 kPa (c) 25 kPa (d) 10 kPa (e) 1 kPa. Inset showing stent positioning. Note the average proximal contact change is 2.53 mm long for ranges above 100 kPa (arrow in (a)).

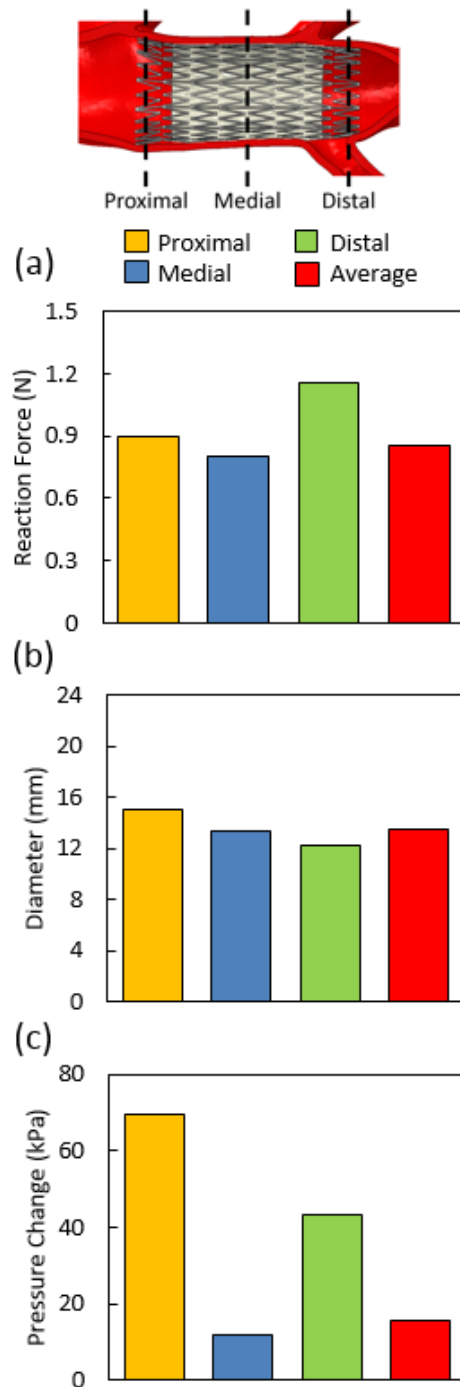


Fig. 5.16: Regional measures of (a) stent reaction force at FRC, (b) stent expanded diameter at FRC, (c) average contact pressure change over the respiratory cycle.

5.3.2.2.4 Stent Migration

A common complication associated with airway stenting is migration. The positioning of the stent at FRC directly after deployment and after cyclic loading is illustrated in Fig. 5.17. The stent migrated proximally by an average of 0.82 mm after the loading cycle.

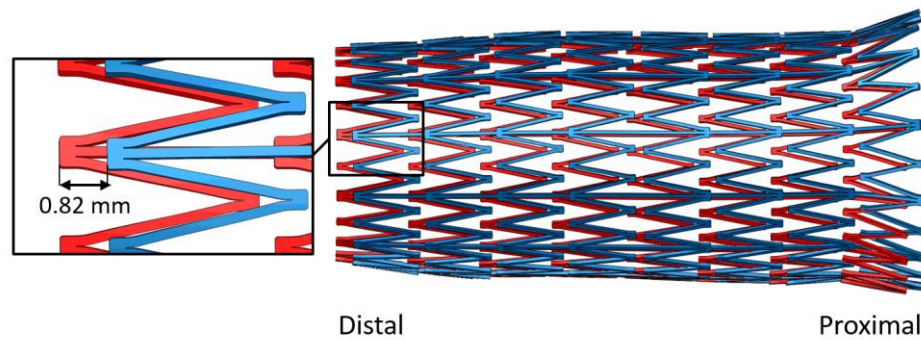


Fig. 5.17: Stent positioning at FRC post deployment (red) and post respiratory cycle (blue). The average difference in axial position is 0.82 mm. Note the stent is shown without cover and adhesive for simplicity.

5.4 Discussion

The inflammatory response that drives the formation of granulation tissue is a complex process that is thought to be initiated by a combination of mechanical irritation and bacterial infection (Schmäl et al. 2003; Ost et al. 2012). Excessive force caused by stent expansion and irritation due to repetitive motion at the stent ends are understood to be the main mechanical instigators of granulation formation (Hautmann et al. 1999; Saad et al. 2003; Noppen et al. 2005; Hu et al. 2011; Ost et al. 2012). Excessive force from the stent presumably cuts off blood flow through the capillaries which causes ischemic necrosis followed by granulation tissue formation (Diaz-Jimenez and Rodriguez 2013). Repetitive motion at the stent ends damages the epithelial surface which can result in granulation tissue formation. Granulation tissue is most often reported at the stent ends (Burningham et al. 2002; Zakaluzny et al. 2003; Lemaire et al. 2005; Hu et al. 2011; Godoy et al. 2014; Thiebes et al. 2017), which is consistent with what is observed in Fig. 5.8 and Fig. 5.9 with granulation tissue at both ends, and no observable thickening in the central portion of the stented region. More inflammation is seen proximally, followed by the distal region, with little observed medially.

A common predictor of granulation formation in the literature has been regions of high stress caused by stent introduction inducing trauma in the tracheal tissue (Perez del Palomar et al. 2010; Trabelsi et al. 2011; Malvè et al. 2011b; Malvè et al. 2011a; Malvè et al. 2014; Chaure et al. 2016). Most notably, studies by Pérez del Palomar et al. (2010), Trabelsi et al. (2011), and Chaure et al. (2016) all correlated areas of

significantly increased maximum principal stress (>100%) with clinical observations of tissue growth. However, in this study the stent implantation only increases the maximum principal stress by around 4% at TLC (Fig. 5.12), suggesting that high stresses may not be responsible for the observed tissue reaction.

Other studies have similarly reported stent implantations having little effect on the stresses experienced by the airway tissue during swallowing due to the large motions involved in airway deformation (Perez del Palomar et al. 2010; Trabelsi et al. 2011). Interestingly, while there is a general increase in stress throughout the length of the stented tissue (Fig. 5.13), reductions in maximum principal stress are recorded at the proximal end where the largest *in-vivo* reaction was observed.

A better correlation is observed in this study between the change in contact pressure over the respiratory cycle and the experimental observations of granulation tissue formation. In Fig. 5.16 (c) the average contact pressure change in the proximal region is 4.4 times higher than the overall average of the stented region. The distal end is 2.7 times higher than the average, while the medial section is 1.3 times smaller. These results suggest that a more significant inflammatory response may be expected proximally, followed by a reduced response in the distal region, which is what is found experimentally. Here, the change in contact pressure is being used as a quantitative measure of the irritation the stent causes the airway tissue due to the repetitive friction between the two surfaces during respiratory motion. This has previously been proposed as a possible cause of granulation formation in clinical settings (Saad et al. 2003; Ost et al. 2012). The change in contact pressure is driven by the same axial stretching of the airways that causes the increase in stress in the bronchial tree (Fig. 5.12). As the airways stretch the tissue rubs against the expanded stent which itself resists axial stretching. The motion of the airways relative to the stent can be seen between Fig. 5.12 (a) and (b) where the distance between the proximal stent end and the proximal branch point (red arrow) increases between FRC and TLC. This rubbing motion results in a change in contact pressure, which is most evident at the stent ends. It should be noted that stent migration may have an influence on the contact pressure range results as high levels of contact pressure variation will be recorded at the stent ends. However, if this were to influence the

results in this study then higher contact pressure variation would be expected in the distal region due to the higher radial force applied by the distal section of the stent (Fig. 5.16 (a)), which is not the case.

A noteworthy result of the presented work is that the stent reaction force does not appear to influence the contact pressure change over the respiratory cycle as one would expect. In Fig. 5.16 (a) the distal portion of the stent applies the most force on the airway tissue, but the highest average contact pressure change is observed in the proximal region (Fig. 5.16 (c)). One would expect the higher reaction force to have more influence on the pressure change as the pressure exerted on the tissue from the stent should be greater distally. This may be explained by the lower proximal reaction force allowing additional movement of the proximal stent end (Fig. 5.12) during respiration which results in the recording of a higher change in contact pressure proximally.

The results of the study also indicate that a certain magnitude of contact pressure variation may be required to initiate an inflammatory response. No apparent mucosal thickening was noted in the medial section of the airway (Fig. 5.9 (c)) despite there being an average contact pressure change of 12.1 kPa in this region (Fig. 5.16 (c)). From Fig. 5.15 (e) it can be seen that the majority of the stented surface experiences contact pressure changes of at least 1 kPa, and a significant area also encounters values greater than 10 kPa (Fig. 5.15 (d)). This suggests that a certain amount of contact pressure variation may be tolerated by the tissue before inflammation is initiated. In this instance it appears that values around 12 kPa are “safe”, though further analysis will need to be performed to further evaluate this assertion.

An important aspect of the current study is the use of an experimentally validated stent model. Previous studies have neglected to consider the mechanical performance of the stenting device which could lead to incorrect estimation of tissue stresses due to stent interaction. The findings of the analysis appear to suggest that contact pressure change may be a suitable predictor for granulation formation, and

the framework utilised in the current study may aid with the improvement of future tracheobronchial stent designs.

5.5 Limitations

The model developed in this work contains a number of limitations. The use of a donor-receiver method to apply a suitable global deformation to the bronchial tree through lung motion simulation is not ideal as it does not apply animal-specific loading. Instead, it applies an animal-specific loading to another animal's airway tree. A better approach, if patient-specific pressurised CT data or 4D CT data is not available, would be to use a mean motion model similar to those proposed by Ehrhardt et al. (Ehrhardt et al. 2008; Ehrhardt et al. 2011). However, this data is not available for ovine models and would require method conversion from deformable image registration to a biomechanical approach. Additionally, the use of just one animal in this study means that further analysis will need to be performed to further confirm the correlations obtained.

Another limitation of this study is the simplification of tissue properties. The airway tissue is considered an isotropic and homogenous material even though it is composed of (among other components) a combination of cartilage and smooth muscle, and exhibits anisotropic properties (Codd et al. 1994; Trabelsi et al. 2010). This assumption may be suitable for the smaller bronchial airways where cartilage is randomly orientated, but it will have a more noticeable effect in the larger airways where c-shaped cartilage rings structurally support the airway. This means that the model is not suitable for tracheal stenting analyses in its current guise. However, cartilaginous representations could be introduced as in Malvè et al. (2014) if necessary. Similarly, the use of constant airway thickness and a range of material properties to describe the naturally reducing thickness results in stress continuities at material boundaries which are not ideal.

To determine the pre-stress a linear pressure-displacement relationship is utilised, which slightly underpredicts the level of pre-stress necessitated. A coefficient of friction of 0.1 between the stent and bronchial tree is utilised. Altering this coefficient could affect the obtained results.

5.6 Summary and Conclusions

In this work pre- and post-stenting data was obtained for a sheep that received a prototype covered laser-cut stent for a period of six weeks. Image and experimental data was used to develop a semi-specific biomechanical lung model that captured the lung *in-vivo* stress state and physiological loading conditions under normal respiration. Stent deployment in the bronchial airway was simulated using a validated stent model. Results of the computational analysis were then correlated with pre-clinical observations. The major conclusion of this work is that there appears to be a correlation between the change in contact pressure applied to the stented airway and granulation tissue formation. The change in contact pressure in this instance represents the irritation experienced by the tissue due to the introduction of the device. Interestingly, there was no apparent correlation between principal stress and granulation formation. The presented framework may eventually lead to improved stent designs for tracheobronchial applications.

References

- Al-Mayah A, Moseley J, Velec M, Brock K (2011) Toward efficient biomechanical-based deformable image registration of lungs for image-guided radiotherapy. *Phys Med Biol* 56:4701–13. doi: 10.1088/0031-9155/56/15/005
- Al-Mayah A, Moseley J, Velec M, Hunter S, Brock K (2010) Deformable image registration of heterogeneous human lung incorporating the bronchial tree. *Med Phys* 37:4560–4571. doi: 10.1118/1.3471020
- Auricchio F, Taylor R, Lubliner J (1997) Shape-memory alloys: macromodelling and numerical simulations of the superelastic behavior. *Comput methods Appl ...* 146.3:281–312.
- Bähr A, Wolf E (2012) Domestic animal models for biomedical research. *Reprod Domest Anim* 47:59–71. doi: 10.1111/j.1439-0531.2012.02056.x
- Bols J, Degroote J, Trachet B, Verhegghe B, Segers P, Vierendeels J (2013) A computational method to assess the in vivo stresses and unloaded configuration of patient-specific blood vessels. *J Comput Appl Math* 246:10–17. doi: 10.1016/j.cam.2012.10.034
- Brock KK (2010) Results of a multi-institution deformable registration accuracy study (MIDRAS). *Int J Radiat Oncol Biol Phys* 76:583–596. doi: 10.1016/j.ijrobp.2009.06.031
- Burningham AR, Wax MK, Andersen PE, Everts EC, Cohen JI (2002) Metallic tracheal stents: complications associated with long-term use in the upper airway. *Ann Otol Rhinol Laryngol* 111:285–90.
- Chaure J, Serrano C, Fernández-Parra R, Peña E, Lostalé F, De Gregorio MA, Martínez MA, Malvè M (2016) On studying the interaction between different stent models and rabbit tracheal tissue: numerical, endoscopic and histological comparison. *Ann Biomed Eng* 44:368–381. doi: 10.1007/s10439-015-1504-3
- Chen W, Clauser J, Thiebes AL, McGrath DJ, McHugh PE, Steinseifer U, Jockenhoevel S, Hennink WE, Kok RJ (2016) Selection and fabrication of a non-woven polycarbonate urethane cover for a tissue engineered airway stent. *Int J Pharm* 514:255–262. doi: 10.1016/j.ijpharm.2016.06.047
- Chung FT, Chen HC, Chou CL, Yu CT, Kuo CH, Kuo HP, Lin SM (2011) An outcome analysis of self-expandable metallic stents in central airway obstruction: a cohort study. *J Cardiothorac Surg* 6:46. doi: 10.1186/1749-8090-6-46
- Chung FT, Lin SM, Chen HC, Chou CL, Yu CT, Liu CY, Wang CH, Lin HC, Huang CD, Kuo HP (2008) Factors leading to tracheobronchial self-expandable metallic stent fracture. *J Thorac Cardiovasc Surg* 136:1328–1335. doi: 10.1016/j.jtcvs.2008.05.039
- Codd SL, Lambert RK, Alley MR, Pack RJ (1994) Tensile stiffness of ovine tracheal wall. *J Appl Physiol* 76:2627–2635.
- De Bock S, Iannaccone F, De Beule M, Van Loo D, Vermassen F, Verhegghe B, Segers P (2013) Filling the void: a coalescent numerical and experimental technique to determine aortic stent graft mechanics. *J Biomech* 46:2477–82. doi: 10.1016/j.jbiomech.2013.07.010
- Diaz-Jimenez JP, Rodriguez AN (2013) *Interventions in Pulmonary Medicine*. Springer New York, New York, NY
- Dooms C, De Keukeleire T, Janssens A, Carron K (2009) Performance of fully covered self-

- expanding metallic stents in benign airway strictures. *Respiration* 77:420–6. doi: 10.1159/000203364
- Ehrhardt J, Werner R, Schmidt-Richberg A, Handels H (2011) Statistical modeling of 4D respiratory lung motion using diffeomorphic image registration. *IEEE Trans Med Imaging* 30:251–265. doi: 10.1109/TMI.2010.2076299
- Ehrhardt J, Werner R, Schmidt-Richberg A, Schulz B, Handels H (2008) Generation of a mean motion model of the lung using 4D – CT image data. *EurographicsWorkshop Vis Comput Biomed*. doi: 10.2312/VCBM/VCBM08/069-076
- Fernández-Bussy S, Majid A, Caviedes I, Akindipe O, Baz M, Jantz M (2011) Treatment of airway complications following lung transplantation. *Arch Bronconeumol* ((English Ed 47:128–133. doi: 10.1016/S1579-2129(11)70031-3
- Freitag L (2010) Airway stents. In: Strausz J, Bolliger CT (eds) *Interventional Pulmonology*. European Respiratory Society Journals Ltd, Sheffield, pp 190–217
- Fuerst B, Mansi T, Carnis F, Salzle M, Zhang J, Declerck J, Boettger T, Bayouth J, Navab N, Kamen A (2015) Patient-specific biomechanical model for the prediction of lung motion from 4-D CT images. *IEEE Trans Med Imaging* 34:599–607. doi: 10.1109/TMI.2014.2363611
- García A, Peña E, Martínez MA (2012) Influence of geometrical parameters on radial force during self-expanding stent deployment. Application for a variable radial stiffness stent. *J Mech Behav Biomed Mater* 10:166–75. doi: 10.1016/j.jmbbm.2012.02.006
- Ghriallais RN, Bruzzi M (2014) Self-expanding stent modelling and radial force accuracy. *Comput Methods Biomech Biomed Engin* 17:318–333. doi: 10.1080/10255842.2012.683427
- Godoy MCB, Saldana DA, Rao PP, Vlahos I, Naidich DP, Benveniste MF, Erasmus JJ, Marom EM, Ost D (2014) Multidetector CT evaluation of airway stents: what the radiologist should know. *RadioGraphics* 34:1793–1806. doi: 10.1148/rg.347130063
- Grewe PH, Müller KM, Lindstaedt M, Germing A, Müller A, Mügge A, Deneke T (2005) Reaction patterns of the tracheobronchial wall to implanted noncovered metal stents. *Chest* 128:986–990. doi: 10.1378/chest.128.2.986
- Guibert N, Mazieres J, Marquette CH, Rouviere D, Didier A, Hermant C (2015) Integration of interventional bronchoscopy in the management of lung cancer. *Eur Respir Rev* 24:378–391. doi: 10.1183/16000617.00010014
- Hautmann H, Rieger J, Huber RM, Pfeifer KJ (1999) Elastic deformation properties of implanted endobronchial wire stents in benign and malignant bronchial disease: A radiographic in vivo evaluation. *Cardiovasc Intervent Radiol* 22:103–8.
- Hu HC, Liu YH, Wu YC, Hsieh MJ, Chao YK, Wu CY, Ko PJ, Liu CY (2011) Granulation tissue formation following dumon airway stenting: the influence of stent diameter. *Thorac Cardiovasc Surg* 59:163–168.
- Hurewitz AN, Sidhu U, Bergofsky EH, Chanana AD (1984) How alterations in pleural pressure influence esophageal pressure. *J Appl Physiol* 56:1162–1169.
- Jeong BH, Um SW, Suh GY, Chung MP, Kwon OJ, Kim H, Kim J (2012) Results of interventional

- bronchoscopy in the management of postoperative tracheobronchial stenosis. *J Thorac Cardiovasc Surg* 144:217–222. doi: 10.1016/j.jtcvs.2012.03.077
- Lee P, Kupeli E, Mehta AC (2010) Airway stents. *Clin Chest Med* 31:141–150. doi: 10.1016/j.ccm.2009.08.002
- Lemaire A, Burfeind WR, Toloza E, Balderson S, Petersen RP, Harpole DH, D’Amico TA (2005) Outcomes of tracheobronchial stents in patients with malignant airway disease. *Ann Thorac Surg* 80:434–438. doi: 10.1016/j.athoracsur.2005.02.071
- Malvè M, Pérez del Palomar A, Chandra S, López-Villalobos JL, Finol E a, Ginel A, Doblaré M (2011a) FSI analysis of a human trachea before and after prosthesis implantation. *J Biomech Eng* 133:71003. doi: 10.1115/1.4004315
- Malvè M, Pérez del Palomar A, Chandra S, López-Villalobos JL, Mena A, Finol E a, Ginel A, Doblaré M (2011b) FSI Analysis of a healthy and a stenotic human trachea under impedance-based boundary conditions. *J Biomech Eng* 133:21001. doi: 10.1115/1.4003130
- Malvè M, Serrano C, Peña E, Fernández Parra R, Lostalé F, De Gregorio MA, Martínez MA (2014) Modelling the air mass transfer in a healthy and a stented rabbit trachea: CT-images, computer simulations and experimental study. *Int Commun Heat Mass Transf* 53:1–8. doi: 10.1016/j.icheatmasstransfer.2014.02.001
- McGrath DJ, O’Brien B, Bruzzi M, Kelly N, Clauser J, Steinseifer U, McHugh PE (2016) Evaluation of cover effects on bare stent mechanical response. *J Mech Behav Biomed Mater* 61:567–580. doi: 10.1016/j.jmbbm.2016.04.023
- McGrath DJ, O’Brien B, Bruzzi M, McHugh PE (2014) Nitinol stent design - understanding axial buckling. *J Mech Behav Biomed Mater* 40:252–263. doi: 10.1016/j.jmbbm.2014.08.029
- McGrath DJ, Thiebes AL, Cornelissen CG, O’Shea MB, O’Brien B, Jockenhoevel S, Bruzzi M, McHugh PE (2017) An ovine in vivo framework for tracheobronchial stent analysis. *Biomech Model Mechanobiol*. doi: 10.1007/s10237-017-0904-8
- Murphy K, van Ginneken B, Reinhardt JM, Kabus S, Kai Ding, Xiang Deng, Kunlin Cao, Kaifang Du, Christensen GE, Garcia V, Vercauteren T, Ayache N, Commowick O, Malandain G, Glocker B, Paragios N, Navab N, Gorbunova V, Sporring J, de Bruijne M, Xiao Han, Heinrich MP, Schnabel JA, Jenkinson M, Lorenz C, Modat M, McClelland JR, Ourselin S, Muenzing SEA, Viergever MA, De Nigris D, Collins DL, Arbel T, Peroni M, Rui Li, Sharp GC, Schmidt-Richberg A, Ehrhardt J, Werner R, Smeets D, Loeckx D, Gang Song, Tustison N, Avants B, Gee JC, Staring M, Klein S, Stoel BC, Urschler M, Werlberger M, Vandemeulebroucke J, Rit S, Sarrut D, Pluim JPW (2011) Evaluation of registration methods on thoracic CT: the EMPIRE10 challenge. *IEEE Trans Med Imaging* 30:1901–1920. doi: 10.1109/TMI.2011.2158349
- Murthy SC, Gildea TR, Mehta AC (2004) Removal of self-expandable metallic stents: is it possible? *Semin Respir Crit Care Med* 25:381–385. doi: 10.1055/s-2004-832711
- Nadzeyka I, Gabler C, Erarslan D, Safi Y, Steinseifer U (2014) Manufacturing of biocompatible nonwoven structures by using spray atomization of dissolved polymers. *Polym Eng Sci* 54:867–873. doi: 10.1002/pen.23622
- Noppen M, Stratakos G, D’Haese J, Meysman M, Vinken W (2005) Removal of covered self-expandable metallic airway stents in benign disorders: indications, technique, and

outcomes. *Chest* 127:482–7. doi: 10.1378/chest.127.2.482

Ost DE, Shah AM, Lei X, Godoy MCB, Jimenez C a, Eapen G a, Jani P, Larson AJ, Sarkiss MG, Morice RC (2012) Respiratory infections increase the risk of granulation tissue formation following airway stenting in patients with malignant airway obstruction. *Chest* 141:1473–81. doi: 10.1378/chest.11-2005

Perez del Palomar A, Trabelsi O, Mena A, Lopez-Villalobos JL, Ginel A, Doblare M (2010) Patient-specific models of human trachea to predict mechanical consequences of endoprosthesis implantation. *Philos Trans R Soc A Math Phys Eng Sci* 368:2881–2896. doi: 10.1098/rsta.2010.0092

Rausch SMK, Martin C, Bornemann PB, Uhlig S, Wall W a (2011) Material model of lung parenchyma based on living precision-cut lung slice testing. *J Mech Behav Biomed Mater* 4:583–92. doi: 10.1016/j.jmbbm.2011.01.006

Razi SS, Lebovics RS, Schwartz G, Sancheti M, Belsley S, Connery CP, Bhora FY (2010) Timely airway stenting improves survival in patients with malignant central airway obstruction. *Ann Thorac Surg* 90:1088–1093. doi: 10.1016/j.athoracsur.2010.06.093

Saad CP, Murthy S, Krizmanich G, Mehta AC (2003) Self-expandable metallic airway stents and flexible bronchoscopy. *Chest* 124:1993–1999. doi: 10.1378/chest.124.5.1993

Saito Y, Imamura H (2005) Airway stenting. *Surg Today* 35:265–70. doi: 10.1007/s00595-004-2942-y

Scheerlinck JPY, Snibson KJ, Bowles VM, Sutton P (2008) Biomedical applications of sheep models: from asthma to vaccines. *Trends Biotechnol* 26:259–266. doi: 10.1016/j.tibtech.2008.02.002

Schmäl F, Fegeler W, Terpe HJ, Hermann W, Stoll W, Becker K (2003) Bacteria and granulation tissue associated with Montgomery T-tubes. *Laryngoscope* 113:1394–1400. doi: 10.1097/00005537-200308000-00024

Sheikhy H, Shahidzadeh M, Ramezanzadeh B, Noroozi F (2013) Studying the effects of chain extenders chemical structures on the adhesion and mechanical properties of a polyurethane adhesive. *J Ind Eng Chem* 19:1949–1955. doi: 10.1016/j.jiec.2013.03.008

Si H, Gärtner K (2015) Meshing piecewise linear complexes by constrained delaunay tetrahedralizations. In: *Proceedings of the 14th International Meshing Roundtable*. Springer-Verlag, Berlin/Heidelberg, pp 147–163

Stoeckel D, Pelton A, Duerig T (2004) Self-expanding nitinol stents: material and design considerations. *Eur Radiol* 14:292–301. doi: 10.1007/s00330-003-2022-5

Tawhai MH, Nash MP, Lin CL, Hoffman EA (2009) Supine and prone differences in regional lung density and pleural pressure gradients in the human lung with constant shape. *J Appl Physiol* 107:912–20. doi: 10.1152/jappphysiol.00324.2009

Tehrani JN, Yang Y, Werner R, Lu W, Low D, Guo X, Wang J (2015) Sensitivity of tumor motion simulation accuracy to lung biomechanical modeling approaches and parameters. *Phys Med Biol* 60:8833–8849. doi: 10.1088/0031-9155/60/22/8833

Thiebes AL, Kelly N, Sweeney CA, McGrath DJ, Clauser J, Kurtenbach K, Gesche VN, Chen W, Kok RJ, Steinseifer U, Bruzzi M, O'Brien BJ, McHugh PE, Jockenhoevel S, Cornelissen CG

- (2017) PulmoStent: in vitro to in vivo evaluation of a tissue engineered endobronchial stent. *Ann Biomed Eng* 45:873–883. doi: 10.1007/s10439-016-1737-9
- Trabelsi O, Malve M, Mena Tobar A, Doblare M (2015) Simulation of swallowing dysfunction and mechanical ventilation after a Montgomery T-tube insertion. *Comput Methods Biomech Biomed Engin* 18:1596–1605. doi: 10.1080/10255842.2014.930448
- Trabelsi O, Pérez del Palomar A, López-villalobos JL, Ginel A, Doblare M (2010) Experimental characterization and constitutive modeling of the mechanical behavior of the human trachea. *Med Eng Phys* 32:76–82. doi: 10.1016/j.medengphy.2009.10.010
- Trabelsi O, Pérez del Palomar A, Mena Tobar A, López-Villalobos JL, Ginel A, Doblare M (2011) FE simulation of human trachea swallowing movement before and after the implantation of an endoprosthesis. *Appl Math Model* 35:4902–4912. doi: 10.1016/j.apm.2011.03.041
- Villard PF, Beuve M, Shariat B, Baudet V, Jaillet F (2005) Simulation of lung behaviour with finite elements: influence of bio-mechanical parameters. In: *Third International Conference on Medical Information Visualisation--BioMedical Visualisation*. IEEE, pp 9–14
- Wall WA, Rabczuk T (2008) Fluid–structure interaction in lower airways of CT-based lung geometries. *Int J Numer Methods Fluids* 57:653–675. doi: 10.1002/flid.1763
- Werner R, Ehrhardt J, Schmidt R, Handels H (2009) Patient-specific finite element modeling of respiratory lung motion using 4D CT image data. *Med Phys* 36:1500. doi: 10.1118/1.3101820
- West JB (2012) *Respiratory physiology: the essentials*. Lippincott Williams & Wilkins
- Zakaluzny SA, Lane JD, Mair EA (2003) Complications of tracheobronchial airway stents. *Otolaryngol Head Neck Surg* 128:478–88. doi: 10.1016/mhn.2003.107

Chapter 6

Conclusions and recommendations

6.1 Introduction

This chapter summarises and discusses the work presented in this thesis. In Section 6.2 a summary of the main findings of the technical chapters (Chapters 2-5) is given and a discussion on their possible application towards future stent design is provided. This is followed by recommendations for future research (Section 6.3) and final concluding remarks (Section 6.4).

6.2 Thesis Summary

Tracheobronchial stents are associated with numerous complications. The focus of this thesis is on the development of a computational and experimental framework that can be used to better understand the mechanical performance of these devices, with the aim of being able to facilitate the improvement of future generations of stent designs. This is accomplished in this work by developing an array of tools that can evaluate stent performance from the bench-top to implantation.

The large deformations required of self-expanding nitinol tracheobronchial stents can make them difficult to design. In Chapter 2 the influence of the transitional stage of nitinol loading on stent stability was investigated for the first time. A computational and experimental analysis showed that the amount of transitional strain within the hinges of a stent can considerably influence stent mechanical performance. Increased levels of transitional strain significantly reduced repeating unit stiffness which initiated stent axial buckling. Through the use of an instability analysis and a proposed instability parameter (I_U) the effect of transitional strain on repeating unit mechanics was evaluated and eliminated from the design. The analysis indicated that a reduction in the percentage of material in the transitional strain range leads to increased stent stability. Geometric dimensional changes and material property variation were utilised to obtain a reduction in transitional strain. While

material property variation is not easily replicated in real-world conditions, its use was capable of validating that the observed effects were from the transitional strain and not caused by geometric effects due to dimensional modifications. Further validation was obtained in Chapter 3, where a link between radial buckling and transitional strain was also exhibited. Conventional wisdom suggests increasing strut thickness to combat the effects of radial buckling (Duerig et al. 2000). However, this may not have the desired affect if critical regions of the stent are already within the transitional strain range due to the radial compression associated with stent deployment. Instead, radial buckling could be improved by utilising the techniques developed here. In Chapter 2 increasing strut length was shown to reduce the percentage of the cross-section within the transitional range. However, this had a large impact on stent radial force. In response to this, it was demonstrated that relatively small changes to the repeating unit hinges and strut width could increase radial force while simultaneously increasing stent stability, demonstrating that there are multiple options available to improve stability while maintaining stent mechanical functionality. Another noteworthy result from Chapter 2 was the geometric effect observed with extended strut length. An increased strut length causes a reduction in hinge angle which inadvertently improves stent stability due to the limited room afforded to the unit in which to axially displace. This study highlights the need to consider nitinol's complex material properties when developing a self-expanding stent, and provides guidance that may be useful for stent designers tackling issues with these devices.

In Chapter 3 classic stent characterisation tests (radial force and flat plate) were combined with a novel non-uniform radial force test to contrast the mechanical performance of a bare and covered stent. In parallel, computational modelling was performed to provide a comprehensive insight into local device behaviour. The non-uniform test in this work was developed as a simplified representation of the multi-loading environment that a tracheobronchial stent is subjected to *in-vivo*, capturing representative non-uniform disease compression and radial compression associated with natural functioning of the airways. Results of the investigation showed that adhered covers can significantly affect stent mechanical function and should be

taken into consideration during the design of the metallic scaffolding structure. A principal conclusion of the work was that stent response (covered or bare) is highly loading specific, which makes it challenging to predict stent performance *in-vivo* from benchtop testing alone, as loading conditions can differ considerably from case to case. This was particularly evident for the covered devices where the classic stent characterisation tests produced very favourable results, but the non-uniform test introduced increased local strut strains and catastrophic failure in the form of radial buckling. The work performed in Chapter 3 highlights the importance of considering *in-vivo* loading conditions, and the need for improved bench-top testing and *in-silico* modelling to more comprehensively evaluate stent performance.

Following on from the recommendations of Chapter 3 an analysis of tracheobronchial stent performance *in-vivo* was considered in Chapter 4. In this chapter a computational framework that can be utilised to evaluate tracheobronchial stent performance using realistic *in-vivo* loading conditions was presented for the first time. The developed ovine biomechanical lung model was capable of capturing physiological loading from a number of differing lung motions, and included *in-vivo* stress states, global lung motion and local pressure loading. It was the first computational analysis to consider stent deployment within the bronchial tree, to evaluate the effect of global lung motion on stent performance, and to utilise stent representations with realistic mechanical performance. While the model developed was of a sheep, the presented framework is easily transferable to human cases. The error associated with the deformation of the airways during simulated lung motion was found to fit within the ranges reported in the literature for other biomechanical lung models. Realistic stent deployment and functional loading, which considered both stent and tissue mechanics, and the interaction between them was simulated. The results of the analysis indicated that stent migration, granulation tissue formation and stent fracture could all be investigated with the proposed framework. A major conclusion of the work undertaken in Chapter 4 was that lung motion drives respiratory tree deformation that can have a considerable impact on stent mechanical performance in all areas evaluated, and so needs to be accounted for in biomechanical modelling. Similarly, when considering the different physiological

loading conditions evaluated (including normal breathing, coughing and ventilation) it was shown that substantially different stent reactions are obtained, which suggests that to suitably evaluate a stent design a variety of loading conditions should be considered in order to appropriately capture stent mechanical performance *in-vivo*. This follows on directly from the conclusions drawn from Chapter 3 where stent performance was shown to be loading dependant. Results from Chapter 4 also indicated that stent radial force may not be the only significant factor in sustaining stent placement as the respiratory tree structure appears to be able to play a valuable role in sustaining stent positioning. An interesting result of the study was that stent deployment appears to have global implications on airway motion, with noticeable effects down to the most distal bronchi in the model. A final observation from the analysis was that while large stresses in the airway tissue due to stent implantation were not observed, results were shown to agree with clinical observations that cyclic stretching of the airway could possibly promote granulation tissue formation through irritation caused by stent friction. This has not previously been considered in computational tracheobronchial stenting analyses.

In Chapter 5 the effect of stent interaction on granulation tissue formation in an ovine model was investigated. In this work a semi-specific biomechanical lung model was developed for a healthy sheep that received a prototype covered laser-cut tracheobronchial stent for a six week period. A computational stent model representing the device deployed in the animal was validated against experimental testing and deployed *in-silico*. The effects of stent loading over a normal respiratory cycle were considered and results of the computational analysis were then compared to experimental observations from the stented animal. The major conclusion of this work was that a correlation appears to exist between the change in contact pressure experienced by the airway tissue and granulation formation. Here, the contact pressure change represents the irritation experienced by the tissue due to the friction between the airway and the stent, caused by the cyclic loading of the airways during lung motion. Interestingly, the local stent reaction force (i.e. the force the stent applies to the tissue in the proximal, medial and distal regions) didn't appear to influence the pressure change over the respiratory cycle in this instance.

Correspondingly, there was no apparent link between the maximum principal stress experienced by the tissue and granulation formation. The observations from this study may prove useful in the optimisation of future stent designs for the reduction of granulation tissue formation.

In Chapters 2-5 an array of tools was developed that can be used to evaluate various aspects of stent functionality. In Chapters 2 and 3 experimental bench-top tests such as radial force, flat plate and non-uniform radial force testing were considered. These can be used to assess stent mechanical performance *in-vitro* and to validate stent computational analyses. Likewise, computational analyses of the benchtop tests can be performed to optimise a device design. The non-uniform radial test proposed in Chapter 3 could prove useful when developing a stent for highly deformed geometries. The computational instability analysis introduced in Chapter 2 can be used to analyse the stability of stent designs during the initial design phase or at any point during design optimisation. Similarly, a more simplified analysis of the transitional strain within critical regions of a full 3D stent model could be performed to ensure stent safety. An obvious application for the biomechanical lung models developed in Chapters 4 and 5 is in stent design optimisation. In their current form, the models could be used to improve stent design, for granulation formation, stent migration and stent strut fracture in patient-specific cases. However, if the models were adapted to consider differing population based disease states they could also be used to improve the general functioning of tracheobronchial stents or used for the classification of stents for differing disease types. The *in-vivo* biomechanical lung models not only have applications in design but with further development could also be utilised in clinical practice. Possible outcomes of stent deployment could be evaluated in patient-specific scenarios, providing additional information for the physician on suitable stent types and sizing. While in reality this is some way out, it is still within the realm of possibility.

6.3 Recommendations for Future Research

The instability analysis performed in Chapter 2 considered the effect of the transitional strain range on stent repeating unit stability. While this approach was effective for the analysed stent, further analysis of the effects of transitional strain

on stent response could improve the functionality of the analysis. In the proposed approach the stability analysis consisted of performing a crimp simulation to determine levels of transitional strain within a unit cross-section, and a sensitivity model to determine the sensitivity of the unit to buckling. Only the strain through a single cross-section is considered, but it may be more informative to consider the amount of transitional strain within a particular volume of stent material. This is because the large deformations required for instabilities to occur depend on a certain volume of material being within the transitional plateau, which cannot be accurately determined from a single cross-section. It may be more useful to develop a relation between transitional strain volume and strut dimensions so that the likelihood of stent unit failure due to reducing material stiffness could be determined during a regular 3D analysis (such as radial force) which could then inform the designer that the stent should be considered for sensitivity analysis.

A further evaluation of the non-uniform radial force test described in Chapter 3 could prove useful. The test was performed using a 4 mm diameter semi-circular steel rod positioned in a radial force tester at 12 mm. However, other combinations of deployment diameter, rod geometry and material were not considered. An interesting continuation of this study would be to investigate the different *in-vivo* disease states and replicate them with corresponding non-uniform test setups. An evaluation of different disease types for which stents are required would need to be carried out and representative geometries and loading conditions would need to be developed. An array of benchtop tests specific to a particular disease state could then be used to better evaluate stent design and choice for implantations.

Another area of possible future research is in the further development of the biomechanical lung models introduced in Chapters 4 and 5. One of the major limitations of the biomechanical models is the lack of anisotropy and tissue inhomogeneity. Tissue inhomogeneity could be addressed with the inclusion of representations of different structural components of the airways including cartilage, smooth muscle and annular ligaments, as considered in other studies (Trabelsi et al. 2011; Malvè et al. 2011; Chaure et al. 2016). Similarly, the anisotropic properties of smooth muscle could also be included to better capture the effects of axial and radial

deformation on airway stresses. While this can be implemented easily into the tracheal section of the model where structures like the c-shaped cartilage rings are generally predictable, the random orientation of cartilage in the lower airways may prove more difficult to accurately represent in the bronchial tree. The increased detail in such large models could significantly amplify model run times. Instead, multiscale analyses could be considered. Large scale macro analyses similar to those performed in Chapters 4 and 5 could be combined with more detailed models that consider tissue micromechanics. Boundary conditions determined from the larger macro scale models could be used to load the local geometry allowing more accurate results to be obtained with less computational effort. It would also be worthwhile computing a tangential component with regards to the correlation between contact pressure change and granulation tissue formation. The method proposed in this thesis does not adequately capture shear effects which are expected to be the primary cause of granulation tissue formation from repetitive motion injury.

An important area of future consideration is on the evaluation of stent mechanical performance when loaded under different states *in-vivo*. The creation of biomechanical lung models that consider different physiological loading conditions such as extrinsic or intrinsic compression of an airway, or conditions such as tracheomalacia could further help improve and assess stent designs. These disease states could either be implemented directly from patient-specific data as in Malvè et al. (2011), or modifications to healthy airways could be introduced as in Xi et al. (2015). An aspect that has not previously been considered in this area is the effect of tissue properties on stent mechanical performance. Lung tissue is known to stiffen with age and disease (Panitch et al. 1989; Rains et al. 1992; Faffe and Zin 2009; Mariappan et al. 2011), and this could have implications for stent functionality *in-vivo*.

The conversion of the ovine models presented in this work to human based models is an additional area of future research. The framework used to develop the ovine biomechanical lung models can be directly implemented using human data. As more data is available on human lung conditions, and the stent designer is more interested in the effect of stents in human patients than in animals, the conversion to human

based models should be a priority. Ideally, with further enhancements the human based models could be used in a clinical setting to assist physicians to select suitable stent types, which is similar to methods being developed for tumour tracking in radiation therapy (McClelland et al. 2013).

Additionally, the semi-specific biomechanical lung model described in Chapter 5 could be further enhanced by considering mean motion models (Ehrhardt et al. 2008; Ehrhardt and Lorenz 2013). Following this framework the global lung deformation can be applied to the model based on average lung deformations for a large population of patients which would be more accurate than the method employed in Chapter 5. This could allow for reasonably accurate models to be developed without the need for multiple CT scans that increase the amount of harmful radiation exposure experienced by the patient.

6.4 Concluding Remarks

In conclusion, the focus of this thesis was on the development of a computational and experimental framework that can be used to improve our understanding of the functional performance of tracheobronchial stents, with the overall aim of being able to facilitate the improvement of future stent designs. This was accomplished through the analysis of tracheobronchial stent mechanical performance in *in-vitro* benchtop studies which considered different aspects of stent functionality, and in *in-vivo* biomechanical lung models where various stent related complications were considered. Out of these analyses an array of tools was developed that can be directly applied to improve future generations of tracheobronchial stents.

The following specific conclusions can be drawn from the work performed in this thesis:

- The amount of transitional strain within critical areas of a nitinol stent structure (such as hinges, struts, etc.) can considerably influence device mechanical performance. Increased amounts through a cross-section can reduce regional stiffness and induce stent failure through buckling.
- The addition of an adhered cover to a stent structure can modify stent mechanical response by altering how the stent unit distributes strain. This can

positively or negatively affect the performance of a stent depending on the specific loading it is subjected to.

- The three primary stenting complications investigated (granulation tissue formation, stent migration and stent strut fracture) appear to be negatively influenced by airway stretching caused by cyclic lung motion.
- Different *in-vivo* load cases (coughing, ventilation, etc.) result in substantially different stent responses, suggesting that a variety of loading conditions should be considered to appropriately capture stent performance *in-vivo*.
- Airway tree geometry appears to help reduce stent migration by allowing stents to lodge between stiff structures. This suggests that a high radial force may not be the only factor that should be considered to ensure stents maintain position after deployment.
- There is an apparent correlation between the change in contact pressure experienced by airway tissue and granulation tissue formation due to stent interaction.

References

- Chaure J, Serrano C, Fernández-Parra R, Peña E, Lostalé F, De Gregorio MA, Martínez MA, Malvè M (2016) On studying the interaction between different stent models and rabbit tracheal tissue: numerical, endoscopic and histological comparison. *Ann Biomed Eng* 44:368–381. doi: 10.1007/s10439-015-1504-3
- Duerig TW, Tolomeo DE, Wholey M (2000) An overview of superelastic stent design. *Minim Invasive Ther Allied Technol* 9:235–46. doi: 10.1080/13645700009169654
- Ehrhardt J, Lorenz C (2013) 4D modeling and estimation of respiratory motion for radiation therapy.
- Ehrhardt J, Werner R, Schmidt-Richberg A, Schulz B, Handels H (2008) Generation of a mean motion model of the lung using 4D – CT image data. *EurographicsWorkshop Vis Comput Biomed*. doi: 10.2312/VCBM/VCBM08/069-076
- Faffe DS, Zin WA (2009) Lung parenchymal mechanics in health and disease. *Physiol Rev* 89:759–775. doi: 10.1152/physrev.00019.2007
- Malvè M, Pérez del Palomar A, Chandra S, López-Villalobos JL, Finol E a, Ginel A, Doblaré M (2011) FSI analysis of a human trachea before and after prosthesis implantation. *J Biomech Eng* 133:71003. doi: 10.1115/1.4004315
- Mariappan YK, Glaser KJ, Hubmayr RD, Manduca A, Ehman RL, McGee KP (2011) MR elastography of human lung parenchyma: Technical development, theoretical modeling and in vivo validation. *J Magn Reson Imaging* 33:1351–1361. doi: 10.1002/jmri.22550
- McClelland JR, Hawkes DJ, Schaeffter T, King AP (2013) Respiratory motion models: A review. *Med Image Anal* 17:19–42. doi: 10.1016/j.media.2012.09.005
- Panitch HB, Allen JL, Ryan JP, Wolfson MR, Shaffer TH (1989) A comparison of preterm and adult airway smooth muscle mechanics. *J Appl Physiol* 66:1760–5.
- Rains JK, Bert JL, Roberts CR, Paré PD (1992) Mechanical properties of human tracheal cartilage. *J Appl Physiol* 72:219–25.
- Trabelsi O, Pérez del Palomar A, Mena Tobar A, López-Villalobos JL, Ginel A, Doblaré M (2011) FE simulation of human trachea swallowing movement before and after the implantation of an endoprosthesis. *Appl Math Model* 35:4902–4912. doi: 10.1016/j.apm.2011.03.041
- Xi J, Kim J, Si XA, Corley RA, Kabilan S, Wang S (2015) CFD modeling and image analysis of exhaled aerosols due to a growing bronchial tumor: towards non-invasive diagnosis and treatment of respiratory obstructive diseases. *Theranostics* 5:443–455. doi: 10.7150/thno.11107

Appendix 5

A. Appendix 5

A.5 Appendix 5: Roles of Co-Authors

Referred to in the Declaration of Originality Section.

All the work completed and presented in this thesis was completed primarily by the author, Donnacha McGrath. The work was undertaken as part of PulmoStent, a project funded under the Seventh Framework Programme which involved collaboration between several European institutions. It is in this context that additional co-authors have been included in the articles that form the backbone of this thesis. The roles of co-authors (other than the student's supervisors) are described below for each Chapter (and associated paper).

A.5.1 Chapter 2: Nitinol Stent Design – Understanding Axial Buckling

Additional co-authors: Dr. Barry O'Brien.

Institution: Biomechanics Research Centre (BMEC), Biomedical Engineering, College of Engineering and Informatics, NUI Galway, Ireland.

Role: Dr. Barry O'Brien is included in this article as a co-author for supervision and technical aid provided.

A.5.2 Chapter 3: Evaluation of Cover Effects on Bare Stent Mechanical Response

Additional co-authors: Dr. Barry O'Brien¹, Dr. Nicola Kelly¹, Ms. Johanna Clauser², Dr. Ulrich Steinseifer².

Institutions: ¹Biomechanics Research Centre (BMEC), Biomedical Engineering, College of Engineering and Informatics, NUI Galway, Ireland. ²Department of Cardiovascular Engineering, Institute of Applied Medical Engineering, Helmholtz Institute, RWTH Aachen University, Aachen, Germany.

Roles: Dr. Barry O'Brien is included in this article as a co-author for supervision and technical aid provided. Dr. Nicola Kelly aided with polymeric sample testing. Ms. Johanna Clauser and Dr. Ulrich Steinseifer performed the stent covering and provided information on the procedure.

A.5.3 Chapter 4: An Ovine *in-vivo* Framework for Tracheobronchial Stent Analysis

Additional co-authors: Dr. Barry O'Brien¹, Ms. Mary B. O'Shea¹, Dr. Anja Lena Thiebes², Dr. Christian G. Cornelissen^{2,3}, Dr. Stefan Jockenhoevel².

Institutions: ¹Biomechanics Research Centre (BMEC), Biomedical Engineering, College of Engineering and Informatics, NUI Galway, Ireland. ²Department of Biohybrid & Medical Textiles (BioTex) at AME-Helmholtz Institute for Biomedical Engineering, ITA-Institut für Textiltechnik, RWTH Aachen University and at AMIBM Maastricht University, The Netherlands, Pauwelsstr. 20, 52074 Aachen, Germany. ³Department for Internal Medicine – Section for Pneumology, Medical Faculty, RWTH Aachen University, Pauwelsstr. 30, 52074 Aachen, Germany.

Roles: Dr. Barry O'Brien is included in this article as a co-author for supervision and technical aid provided. Ms. Mary B. O'Shea performed the tissue testing. Dr. Anja Lena Thiebes, Dr. Christian G. Cornelissen and Dr. Stefan Jockenhoevel performed the animal trial work and provided the relevant information.

A.5.4 Chapter 5: Evaluating the Interaction of a Tracheobronchial Stent in an Ovine *in-vivo* Model

Additional co-authors: Dr. Barry O'Brien¹, Dr. Anja Lena Thiebes², Dr. Christian G. Cornelissen^{2,3}, Dr. Stefan Jockenhoevel².

Institutions: ¹Biomechanics Research Centre (BMEC), Biomedical Engineering, College of Engineering and Informatics, NUI Galway, Ireland. ²Department of Biohybrid & Medical Textiles (BioTex) at AME-Helmholtz Institute for Biomedical Engineering, ITA-Institut für Textiltechnik, RWTH Aachen University and at AMIBM Maastricht University, The Netherlands, Pauwelsstr. 20, 52074 Aachen, Germany.

³Department for Internal Medicine – Section for Pneumology, Medical Faculty, RWTH Aachen University, Pauwelsstr. 30, 52074 Aachen, Germany.

Roles: Dr. Barry O'Brien is included in this article as a co-author for supervision and technical aid provided. Dr. Anja Lena Thiebes, Dr. Christian G. Cornelissen and Dr. Stefan Jockenhoewel performed the animal trial work and provided the relevant information.